

NORTHWESTERN UNIVERSITY

Biological and Environmental Implications and Applications of Two-Dimensional Layered  
Nanomaterials

A DISSERTATION

SUBMITTED TO THE GRADUATE SCHOOL  
IN PARTIAL FULFILLMENT OF THE REQUIREMENTS

for the degree

DOCTOR OF PHILOSOPHY

Field of Materials Science and Engineering

By

Linda M. Guiney

EVANSTON, ILLINOIS

June 2018

© Copyright by Linda M. Guiney 2018

All Rights Reserved

## **ABSTRACT**

### **Biological and Environmental Implications and Applications of Two-Dimensional Layered Nanomaterials**

Linda M. Guiney

To accelerate the implementation of technologies enabled by two-dimensional (2D) nanomaterials, the human health and environmental implications of these materials need to be addressed. Fundamental studies which elucidate the mechanisms of toxicity and environmental fate will allow for the safer design of these materials and promote their widespread use. This thesis presents a multidisciplinary approach to assess the potential hazards of 2D nanomaterials by establishing structure-activity relationships between the properties of the 2D nanomaterials to biological outcomes. In particular, interactions with the cell or bacterial membrane, cellular uptake, and intracellular localization and processing are investigated using a library of graphene oxide (GO) nanomaterials. By systematically varying GO surface oxidation and lateral size, we successfully deduce the toxicological mechanisms in mammalian and bacterial systems.

Next, the environmental fate of GO nanomaterials is studied by measuring the influence of pH, ionic strength, ion valence, and presence of natural organic matter (NOM) on the aggregation and stability of GO nanomaterials in aquatic environments. A similar library of GO nanomaterials is used to determine the influence of surface oxidation on both the aggregation as well as the chemical degradation under direct sunlight. Based on the observed interactions of GO with NOM, the antifouling properties of GO are investigated by observing the deposition kinetics of bacteria and NOM. Based on our findings with GO, we further expand our studies to other 2D materials, such

as molybdenum disulfide ( $\text{MoS}_2$ ). The attachment efficiency of foulants on both 2D nanomaterial functionalized surfaces is significantly lower than that of a control polymer surface, encouraging the potential use of GO and  $\text{MoS}_2$  for antifouling water filtration membrane technologies.

The environmental instability of black phosphorus (BP), a 2D layered nanomaterial which decomposes in the presence of oxygen and water, is studied in detail to encourage the development biodegradable constructs for a wide range of biomedical applications. Aqueous dispersions of few-layer BP nanosheets are prepared and the chemical and dispersion stability are studied by controlling the type of surfactants and overall flake size and thickness. Furthermore, the stability of the BP dispersions is investigated in biologically relevant media; environmental factors such as dissolved oxygen, temperature, and ionic strength are considered for their role in the stability of the BP nanosheets. These results will enable improved efficacy and lifetime of potential BP constructs for biomedical applications, as well as provide a foundation for investigating the biological impact of these nanomaterials.

Finally, we demonstrate the incorporation of a 2D layered material into a biocompatible polymer composite for potential applications in bioelectronics. Hexagonal boron nitride (hBN)—a thermally conductive yet electrically insulating two-dimensional layered material—is dispersed at high concentrations in the presence of a biocompatible polymer, which can be 3D printed at room temperature through an extrusion process to form complex architectures with features as small as 100  $\mu\text{m}$ . These robust, free-standing constructs can have high solids content while maintaining their mechanical integrity when flexed and stretched. Furthermore, the presence of hBN within the matrix results in enhanced thermal conductivity. The high cytocompatibility of these constructs makes them potentially suitable for use in the field of printed bioelectronics.

Overall this work contributes to a better understanding of the behavior and interactions of 2D nanomaterials at the nano-bio interface, allowing for the safe design and implementation of these materials into a wide range of biomedical applications.

## ACKNOWLEDGEMENTS

I would like to thank my advisor, Mark Hersam, for his guidance and support throughout the entirety of my Ph.D. I am grateful for the opportunity to learn from and work with such a brilliant and motivated scientist. His drive, efficiency, and leadership lift all those around him to new levels of achievement. He has been an excellent advisor and role model, and I look forward to continuing to work with him on new and exciting projects.

I would also like to thank Professor Ramille Shah for giving me the opportunity to become a part of her research group and for being a wonderful advisor over the past three years. Ramille's commitment to her research and to her students has been inspirational. She has assembled an incredibly creative and talented team and I am very grateful to have had the opportunity to work with all of them.

I would also like to thank my committee members, Professor Ken Shull and Professor Wes Burghardt, for their contributions to my research. They have provided meaningful feedback which has helped to shape the directions of my Ph.D. research.

I have been very fortunate to collaborate with many research groups across the country through the University of California Center for Environmental Implications of Nanotechnology. In particular, I would like to thank Dr. André Nel, Dr. Dermont Bouchard, Prof. Tian Xia, Prof. Indranil Chowdhury, Prof. Sharon Walker, and Prof. Trish Holden and members of their labs: Dr. Xiang Wang, Dr. Ruibin Li, Dr. Ivy Ji, Dr. Cathy Chen, Dr. Jacob Lanphere, Drew Story, Dr. Monika Mortimer, Mehnaz Shams, and Iftaykhairul Alam for their contributions to this work.

At Northwestern, I have many people to thank. First and foremost, I would like to thank Dr. Niki Mansukhani Kogar for her contributions to this work. I am very fortunate to have been able

to work alongside this creative and exceptional scientist for the majority of my Ph.D. This thesis would not have been possible without her mentorship and support. I also want to thank my officemates Dr. Jade Balla and Dr. Joohoon Kang who have been a constant source of support and ideas. I also thank the Northwestern research staff, especially Dr. Keith MacRenaris, Becky Sponenburg, Dr. Carla Schute, and Dr. Xinqi Chen for their help and research insights. I thank my collaborators in the Hersam lab, Dr. Jae-Hyeok Lee, Peter Kim, Mani Ramesh, and Yichao Zhao for their contributions to this work. I would like to thank all the members of the Hersam group, past and present, for their collaborations and support, especially Sarah Clark, Erika Swartz, Amanda Walker, Dr. Heather Arnold, Dr. Yujin Shin, Dr. Kan-Sheng Chen, Dr. Jian Zhu, Dr. Ted Seo, Dr. Tejas Shastry, Dr. Kyle Luck, David Lam, Shay Wallace, Nathan Bradshaw, Dr. Ethan Secor and Dr. Karl Putz.

I also thank the members of the Shah research group for welcoming me into their lab and for their collaborations. I would especially like to thank Dr. Adam Jakus for his contributions to this work. His creativity and enthusiasm for fun science always made it a pleasure to work with and learn from him. I would also like to thank Dr. Alexandra Rutz, Nick Geisendorfer, Phillip Lewis, Jimmy Su, and Danielle Duggins of the Shah lab for their support and for creating a fun and collaborative lab space.

I am also very grateful for the teachers and mentors who helped me to get to this point in my career. I would like to thank the chemistry faculty at Wellesley College, especially Dr. Nolan Flynn who advised me both during my tenure at Wellesley and afterwards as I navigated my early career and path to graduate school. I would also like to thank my team at Semprus BioSciences, especially

Dr. André Weinstock for his guidance, support, and friendship, and for encouraging me to pursue this Ph.D.

On a more personal note, I would like to thank my friends who have brightened my time in Chicago and filled my life here with laughter and love, especially Amy Plunk, Lam-Kiu Fong, and Katie Mauck. I would also like to thank my entire North Shore rugby family, especially Noby Takaki, Claire Herdeman, Joy Tull, Brittany Biedenbender, Dawn McKenzie, and Nicole Fisch, for their friendship and encouragement. I want to thank Maryska Kaczmarek for always being there for me, for the countless video chats, and for all of her visits to Chicago. She has always believed in me and pushed me to pursue my dreams and I am so grateful to have her in my life. I also want to thank Dr. Kavita Chandra for making my day-to-day life during my Ph.D. brighter and happier in every way. She has been by my side for my best and worst times and I cannot imagine having made this journey without her.

Most importantly, I want to thank my parents for being the most generous, selfless and loving people I know. Everything that I have accomplished in life is a direct result of their encouragement and support. I am so grateful to them for raising four strong, independent women and for helping us to follow our passions. I also thank my sisters, Michelle, Mary, and Bridget, for continuously raising the bar of excellence and for always being there for me. Finally, I want to thank Ed Kluender for being my person, for encouraging me in everything that I do, for pushing me outside of my comfort zone, and for all of his love and support.

**LIST OF ABBREVIATIONS**

2D	Two-dimensional
3D	Three-dimensional
AM	Additive manufacturing
APTES	(3-aminopropyl) triethoxysilane
AR	Antibiotic resistant
AFM	Atomic force microscopy
BP	Black phosphorus
BSA	Bovine serum albumin
CVD	Chemical vapor deposition
DBP	Dibutyl phthalate
DCM	Dichloromethane
$D_h$	Hydrodynamic diameter
DMEM	Dulbecco's modified Eagle's medium
DSC	Differential scanning calorimetry
EGBE	Ethylene glycol monobutyl ether
EPM	Electrophoretic mobility
EPR	Electron paramagnetic resonance
F68	Pluronic F68
FTIR	Fourier transform infrared spectroscopy
GO	Graphene oxide
hBN	Hexagonal boron nitride

hGO	Hydrated graphene oxide
hMSC	Human mesenchymal stem cells
HTS	High throughput screening
IC	Ion chromatography
IS	Ionic strength
MoS <sub>2</sub>	Molybdenum disulfide
NMP	<i>N</i> -methyl-2-pyrrolidone
NOM	Natural organic matter
PBS	Phosphate buffered saline
PLGA	Poly(lactic- <i>co</i> -glycolic acid)
QCM-D	Quartz crystal microbalance with dissipation monitoring
rGO	Reduced graphene oxide
ROS	Reactive oxygen species
SARs	Structure-activity relationships
SDS	Sodium dodecyl sulfate
SEM	Scanning electron microscopy
TEM	Transmission electron microscopy
TGA	Thermogravimetric analysis
TMDC	Transition metal dichalcogenide
UV	Ultra violet
Vis	Visible
XPS	X-ray photoelectron spectroscopy

*For my parents*

## TABLE OF CONTENTS

<b>ABSTRACT .....</b>	<b>3</b>
<b>ACKNOWLEDGEMENTS .....</b>	<b>6</b>
<b>LIST OF ABBREVIATIONS .....</b>	<b>9</b>
<b>TABLE OF CONTENTS .....</b>	<b>12</b>
<b>LIST OF FIGURES .....</b>	<b>16</b>
<b>LIST OF TABLES .....</b>	<b>31</b>
<b>CHAPTER 1 : INTRODUCTION.....</b>	<b>32</b>
1.1 Two-dimensional materials.....	33
1.1.1 Graphene-family nanomaterials.....	33
1.1.2 Transition metal dichalcogenides .....	34
1.1.3 Hexagonal boron nitride .....	36
1.1.4 Black phosphorus.....	36
1.2 Synthesis of 2D materials .....	37
1.3 Hazard assessment of 2D materials .....	40
1.3.2 Composition.....	42
1.3.3 Exfoliation.....	43
1.3.4 Lateral size and thickness .....	47
1.3.5 Physical forms.....	50
1.3.6 Surface functionalization .....	52
1.3.7 Environmental stability and chemical dissolution .....	55

	13
1.3.8 Crystal structure .....	58
1.4 Introduction to 3D printing .....	60
1.4.1 Additive manufacturing methods.....	61
1.4.2 Biological applications of 3D printing.....	62
<b>CHAPTER 2 : HAZARD ASSESSMENT AND ANTIBACTERIAL APPLICATIONS OF GRAPHENE OXIDE NANOMATERIALS.....</b>	<b>64</b>
2.1 Background .....	65
2.2 Results and discussion .....	68
2.2.1 Varying the physicochemical properties of graphene oxide.....	68
2.2.2 Pulmonary toxicity of graphene oxide nanomaterials .....	76
2.2.3 Toxicity of graphene oxide nanomaterials in liver cells .....	83
2.2.4 Antibacterial effects of graphene oxide nanomaterials.....	100
2.3 Experimental methods .....	105
2.3.1 Preparation of graphene oxide nanomaterial library.....	105
2.3.2 Physicochemical characterization of GO library .....	106
2.3.3 Determination of pulmonary toxicity.....	107
2.3.4 Determination of cytotoxicity in liver cells .....	108
2.3.5 Determination of bactericidal effects.....	112
2.4 Summary .....	113
<b>CHAPTER 3 : ENVIRONMENTAL STABILITY AND APPLICATIONS OF 2D NANOMATERIALS.....</b>	<b>115</b>
3.1 Background .....	116

3.2	Results and discussion .....	121
3.2.1	Aqueous stability of graphene oxide nanomaterials .....	121
3.2.2	Photodegradation of graphene oxide nanomaterials .....	132
3.2.3	Antifouling properties of graphene oxide and molybdenum disulfide functionalized membranes .....	142
3.2.4	Foulant removal from graphene oxide and molybdenum disulfide functionalized membranes .....	150
3.3	Experimental methods .....	156
3.3.1	Preparation of graphene oxide nanomaterial library .....	156
3.3.2	Physicochemical characterization of GO library .....	157
3.3.3	Environmental stability of GO nanomaterials .....	157
3.3.4	Photodegradation of GO nanomaterials .....	158
3.3.5	Antifouling properties of GO and MoS <sub>2</sub> functionalized surfaces .....	159
3.4	Summary .....	160
<b>CHAPTER 4 : AQUEOUS STABILITY OF EXFOLIATED BLACK PHOSPHORUS ...</b>		<b>164</b>
4.1	Background .....	165
4.2	Results and discussion .....	167
4.2.1	Aqueous liquid phase exfoliation of black phosphorus .....	167
4.2.2	Effects of surfactant selection .....	171
4.2.3	Stability of BP in biological media .....	173
4.2.4	Processing and environmental factors affecting stability .....	177
4.2.5	Degradation products of black phosphorus .....	183

4.3	Experimental methods .....	185
4.3.1	Liquid phase exfoliation of BP .....	185
4.3.2	BP dispersion characterization.....	185
4.3.3	Determination of degradation products .....	186
4.4	Summary .....	188
<b>CHAPTER 5 : 3D PRINTING OF LAYERED 2D MATERIALS .....</b>		<b>189</b>
5.1	Background .....	190
5.2	Results and discussion .....	193
5.2.1	3D printable ink formulation .....	193
5.2.2	Mechanical properties of 3D printed hBN .....	197
5.2.3	Thermal conductivity of 3D printed hBN .....	202
5.2.4	Cytocompatibility of 3D printed hBN .....	204
5.3	Experimental methods .....	206
5.3.1	Ink preparation and printing.....	206
5.3.2	Mechanical characterization .....	207
5.3.3	Thermal characterization .....	207
5.3.4	In vitro cytocompatibility .....	208
5.4	Summary .....	209
<b>CHAPTER 6 : FUTURE OUTLOOK.....</b>		<b>210</b>
<b>REFERENCES.....</b>		<b>217</b>
<b>CURRICULUM VITAE.....</b>		<b>249</b>

## LIST OF FIGURES

**Figure 1.1:** (A) Schematic structure of a TMDC where M represents a transition metal atom and X represents a chalcogen atom. Figure adapted from reference<sup>27</sup>. (B) Schematics of different structural polytypes of TMDCs. Figure adapted from reference<sup>17</sup>. ..... 35

**Figure 1.2:** Solution-phase exfoliation methods. (A) Chemical exfoliation using intercalation of small ionic species, followed by agitation such as sonication. (B) Ion exchange exfoliation, which employs the exchange of small naturally occurring ions with larger ions to weaken the interlayer attraction, followed by agitation to exfoliate the layers. (C) Sonication-assisted exfoliation which uses solvents of appropriate surface energy to effectively disperse the 2D sheets in solution. This method can also employ surfactants to stabilize the 2D materials following exfoliation. Adapted from reference<sup>105</sup>. ..... 39

**Figure 1.3:** Physicochemical properties of 2D nanomaterials that affect their toxicity. Complete characterization of these properties is needed to accurately assess the hazard of the specific nanomaterials. Figure adapted from references<sup>103,120,127–132</sup>. ..... 41

**Figure 1.4:** Effects of aqueous exfoliation methods on the pulmonary hazard potential of MoS<sub>2</sub>. (A) SEM micrograph of aggregated MoS<sub>2</sub> and AFM images of (B) chemically exfoliated MoS<sub>2</sub> using a lithiation process and (C) MoS<sub>2</sub> exfoliated by ultrasonication in the presence of Pluronic F87. (D) Cellular content of molybdenum (Mo) and (E) TNF- $\alpha$  production in THP-1 cells 24 hours after exposure to 50  $\mu\text{g mL}^{-1}$  of the MoS<sub>2</sub> materials. (F) Acute pulmonary effects of MoS<sub>2</sub> materials in mice after 40 hours. The H&E-stained histological images indicate that aggregated MoS<sub>2</sub> is

capable of inducing inflammation in the lung while the exfoliated MoS<sub>2</sub> materials show little or no effect. Figure adapted from reference<sup>140</sup>. 45

**Figure 1.5:** Effects of lateral size and thickness on the hazard potential of exfoliated black phosphorus (BP) nanomaterials. Representative TEM micrographs of flakes from three different sized BP dispersions—BP-1 (A), BP-2 (B) and BP-3 (C)—and corresponding photographs of the dispersions (insets). (D) Size measurements of the three BP dispersions in 10% FBS supplemented cell culture medium as determined by DLS. (E) Cell viability of NIH-3T3 cells after 24 hours exposure to the BP nanomaterials via RTCA. (F) Intracellular detection of reactive oxygen species in NIH-3T3 cells after exposure to 10 µg mL<sup>-1</sup> of BP nanomaterials for 4 hours. Figure adapted from reference<sup>150</sup>. 49

**Figure 1.6:** Cytotoxicity of 2D nanomaterial-modified glass substrates. (A) Schematic of the experimental design. Human adipose-derived mesenchymal stem cells (hADMSCs) were seeded onto glass substrates which have been modified with a thin film of various 2D nanomaterials, including molybdenum disulfide (MoS<sub>2</sub>), tungsten disulfide (WS<sub>2</sub>) and hexagonal boron nitride (hBN). (B-D) Cell viability of modified substrates after 2 days and 7 days as determined by growth rate using a CCK-8 assay. Figure adapted from reference<sup>131</sup>. 51

**Figure 1.7:** Effects of chemical modification on the toxicity of BP. (A) Synthesis scheme of the surface coordination of the titanium sulfonate ligand (TiL<sub>4</sub>) to BP to generate TiL<sub>4</sub>@BP. (B) Cell viability of raw 264.7 and J774A.1 cells after 24 hours exposure to bare BP and TiL<sub>4</sub>@BP as determined by an ATP assay. (C) TNF-α production from raw 264.7 cells after 12 hours exposure to 10 µg mL<sup>-1</sup> of the BP materials. (D) Confocal microscopy images of J774A.1 cells stained with

Magic Red to show Cathepsin B location after exposure to BP materials after 6 hours. In the control cells, cathepsin B appear as concentrated dots, localized within the lysosomes. After exposure to bare BPs, the lysosomes appear swollen, while this inflammatory effect is not observed after exposure to  $\text{TiL}_4\text{@BP}$ . Figure adapted from reference<sup>129</sup> ..... 54

**Figure 1.8:** Biodistribution and fate of PEGylated TMDCs. (A) In vivo biodistribution of PEGylated  $\text{MoS}_2$ ,  $\text{WS}_2$  and  $\text{TiS}_2$  in major organs of mice after intravenous injection for up to 30 days. All materials accumulated mainly in the liver and spleen but after 30 days  $\text{MoS}_2$  was cleared from the system while  $\text{WS}_2$  and  $\text{TiS}_2$  persisted. (B) Clearance of the PEGylated TMDCs from the liver over 30 days. (C) Schematic illustrating the chemical transformation the PEGylated TMDCs.  $\text{MoS}_2$  dissolves and forms soluble  $\text{MoO}_4^{2-}$  which is excreted.  $\text{TiS}_2$  oxidizes to form  $\text{TiO}_2$ , which is insoluble in aqueous solution and the aggregates are retained.  $\text{WS}_2$  undergoes some oxidation but its chemical stability leads to its retention in the organs. Figure adapted from reference<sup>127</sup> ..... 57

**Figure 1.9:** Stability and dissolution of 1T and 2H phases of  $\text{MoS}_2$ . (A) Illustration of the 1T and 2H phases of  $\text{MoS}_2$ . Chemical exfoliation of  $\text{MoS}_2$  (ce- $\text{MoS}_2$ ) results in a phase change to the 1T phase while ultrasonication-assisted exfoliation (ue- $\text{MoS}_2$ ) maintains the 2H phase. (B) XPS spectra and fitting of the Mo 3d and S 2p peaks of ce- $\text{MoS}_2$  and ue- $\text{MoS}_2$ . ue- $\text{MoS}_2$  is in the 2H phase while ce- $\text{MoS}_2$  contains both 1T and 2H phase materials. (C) UV-Vis spectra and pictures of ue- $\text{MoS}_2$  and ce- $\text{MoS}_2$ . ue- $\text{MoS}_2$  demonstrates the exciton peaks intrinsic to the 2H phase of the material. (D) Dissolution of ce- $\text{MoS}_2$  and ue- $\text{MoS}_2$  in HEPES buffer (pH 7), showing a significantly faster rate of dissolution for the ce- $\text{MoS}_2$ . Figure adapted from reference<sup>175</sup> ..... 59

**Figure 2.1:** Schematic of GO nanomaterial library synthesis. GO was synthesized by a modified Hummers' method. rGO-1 and rGO-2 were synthesized by solvothermal reduction of GO in NMP at 150 °C for 1 or 5 h, respectively. To prepare hGO-1 and hGO-2, GO was hydrated in aqueous alkalized solution at 50 °C or 100 °C for 24 h. Reaction of the epoxy groups with nucleophiles leads to the opening of the epoxy rings and the generation of hydroxyl groups (as well as carbon radicals as shown in Figure 2.3). ..... 71

**Figure 2.2:** XPS spectra and quantification of oxygen-containing groups on the GO surface. XPS was performed by the stepwise (50 meV) acquisition of high resolution spectra of the C 1s region. .... 72

**Figure 2.3:** Detection of carbon radicals on GO surface by EPR. (A) Schematic illustrating the formation of carbon radicals on the GO surface as a result of the hydration process. (B) EPR spectra of all GO nanomaterials. (C) Carbon radical content of all GO nanomaterials as determined by EPR. EPR was used to assess the carbon radical density on GO surface by testing 5 mg of each of the dried GO samples by an X-band Bruker ELEXYS 580 spectrometer with  $g$  value of 2.0091. .... 73

**Figure 2.4:** Raman spectroscopy of GO nanomaterials. Signature D and G bands of GO were detected using a 785 nm near-infrared diode and a 50x objective lens. Spectra are an average of 2 scans with 10 second exposure in the 500-2000  $\text{cm}^{-1}$  range. .... 74

**Figure 2.5:** AFM images of GO nanomaterials. AFM images were obtained by placing a drop of the GO solution (10  $\mu\text{g/mL}$ ) on silicon wafers that were pretreated with a 2.5 mM APTES aqueous

solution. After washing with water and drying with N<sub>2</sub>, AFM images were obtained using a nAsylum Research Cypher ES AFM. .... 75

**Figure 2.6:** Visualizing the interactions of GO with THP-1 cells by TEM. After exposure to rGO-2, GO or hGO-2 for 16 h, the cells were washed, fixed and stained for TEM viewing. .... 77

**Figure 2.7:** Assessment of the lipid peroxidation by GO nanosheets. To assess lipid peroxidation, THP-1 cells were treated with 100 µg/mL GO for 16 h or 10 µM cumene hydroperoxide (positive control) for 1 h. Cells were stained with 10 µM Image-iT® Lipid Peroxidation Sensor Lipid Peroxidation Sensor according to the manufacturer's instructions. Flow cytometry analysis was carried out in a FACS Vantage SE flow cytometer. .... 78

**Figure 2.8:** Cell viability assessment in (A) BEAS-2B and (B) THP-1 cells by the MTS assay. For cellular viability assessment, a MTS assay was used to assess the impact of 0-200 µg/mL of each GO suspension in THP-1 or BEAS-2B cells over 48h. .... 79

**Figure 2.9:** Calculation of the correlation coefficient of the cytotoxicity results versus carbon radical measurement for (A) BEAS-2B and (B) THP-1 cells..... 80

**Figure 2.10:** Lipid peroxidation of primary macrophages in the BALF after GO exposure by oropharyngeal aspiration. Animal exposure to rGO-2, GO and hGO-2 nanosheets was performed by using oropharyngeal aspiration of 2 mg/kg of each of the samples. Animals were sacrificed after 40 h to collect primary alveolar macrophages. Flow cytometry analysis was used to quantify the percentage of cells undergoing lipid peroxidation. .... 81

**Figure 2.11:** AFM images of GO nanomaterial library (top) and corresponding XPS spectra of the C 1s region. .... 85

**Figure 2.12:** Cytotoxicity of GO and rGO in liver cells. CellTox Green (top) and ATP (bottom) assays were used to determine cell death and cell viability, respectively, in Kup5, LSEC and Hepa 1-6 cells. Zinc oxide nanoparticles were used as a positive control in both assays..... 87

**Figure 2.13:** Cell death mechanisms of GO and rGO in liver cells. Flow cytometry with fluorescein isothiocyanate (FITC)-conjugated Annexin V and propidium iodide (PI) staining was used to determine the cell death mechanism—apoptosis or necrosis—induced by GO and rGO after 16 h in (A) Kup5 and (B) LSEC cells. Caspase-3/-7 activity in (C) Kup5 and (D) LSEC cells. .... 89

**Figure 2.14:** Cellular uptake of GO and rGO in (A) Kup5, (B) LSEC, and (C) Hepa 1-6 cells as measured by side scatter flow cytometry using GO/rGO labeled with FITC conjugated to BSA. .... 90

**Figure 2.15:** Effects of SR-B1 signaling on cellular uptake of GO and rGO in (A) LSEC and (B) Hepa 1-6 cells. Cellular uptake of GO and rGO was measured with and without treatment of BLT-1, a selective inhibitor for SR-B1. .... 91

**Figure 2.16:** Lipid peroxidation induced by GO and rGO in (A) Kup5, (B) LSEC, and (C) Hepa 1-6 cells using the BODIPY 581/591 C11 reagent and an Image-iT kit. .... 93

**Figure 2.17:** Pro-inflammatory effects of GO and rGO in liver cells. (A) Lysosomal damage in Kup5 cells as demonstrated by the release of Cathepsin B (red) after cellular uptake. Monosodium

urate (MSU) was used as a positive control. Significant increases in the IL-1 $\beta$  production in (B) Kup5, (C) LSEC, and (D) Hepa 1-6 cells are indicative of a pro-inflammatory response. .... 95

**Figure 2.18:** (A) TNF- $\alpha$  production induced by GO and rGO in Kup5, LSEC, and Hepa 1-6 cells. Treatment with the (B) TLR-4 or (C) NF- $\kappa$ B inhibitor illustrates that the pro-inflammatory response of GO is dependent on TLR-4 activation through the NF- $\kappa$ B signaling pathway in Kup5 cells. .... 98

**Figure 2.19:** Cytotoxic effects of GO and rGO nanomaterials are due to distinct membrane interactions, cellular uptake, and cellular localization and processing, which are dictated by the physicochemical properties of the nanomaterials, including oxidation and lateral size. .... 99

**Figure 2.21:** Inhibition of AR bacterial growth by hGO-2 covalently attached to the surface of a silicone catheter. (A) Schematic to describe hGO-2 coating of catheters as well as product images. (B)  $\beta$ -Galactosidase release from bacteria grown on coated catheters. The  $\beta$ -galactosidase release from embedded bacteria on catheter surfaces was determined after 2 h incubation. (C) Assessing the growth of bacteria retrieved from the coated catheter surfaces. After bacteria settled on catheter surfaces, they were incubated for 1, 3, and 6 h. The images show the growing colonies from uncoated or hGO-2-coated surfaces at each time point at same dilutions. .... 103

**Figure 2.22:** Schematic image to explain the bactericidal effect of GO including membrane association and lipid peroxidation. .... 104

**Figure 3.1:** AFM and XPS characterization of GO nanomaterials. Each column shows the characterization data of one of three GO and rGO samples: GO, rGO-2h, and rGO-5h, respectively,

from left to right. A representative AFM image (top row) and the flake size histograms of each (middle row) show that physical dimensions of the GO remain comparable despite the reduction process. Representative XPS spectra of each sample are shown in the bottom row, highlighting the stark drop in carbon-oxygen peaks and rise in the carbon-carbon peak as GO is reduced..... 123

**Figure 3.2:** FT-IR spectra of GO nanomaterials. .... 124

**Figure 3.3:** (A) Electrophoretic mobilities (EPM) and (B) hydrodynamic diameter ( $D_h$ ) of GO nanomaterials in DI water. Error bars are one standard deviation of at least three samples. .... 125

**Figure 3.4:** Electrophoretic mobilities and hydrodynamic diameter of GO nanomaterials as a function of pH in the presence of NaCl, without (black) and with background  $\text{CaCl}_2$  (red) and  $\text{MgCl}_2$  (green). EPM of (A) GO, (B) rGO-1h, (C) rGO-2h; hydrodynamic diameter of (D) GO, (E) rGO-1h, (F) rGO-2h. Error bars are one standard deviation of at least three samples. .... 127

**Figure 3.5:** Long-term stability of GO nanomaterials in natural and artificial water. Normalized rGO concentrations in the presence of (A) Call's Creek; (B) synthetic surface water; (C) synthetic surface water with 5 mg/L SRHA; (D) synthetic groundwater; (E) Oconee effluent wastewater; and (F) synthetic wastewater. .... 131

**Figure 3.6:** AFM images of GO showing degradation of particles before and after irradiation. .... 133

**Figure 3.7:** (A) Hydrodynamic diameter and (B) total organic carbon analysis of GO, rGO-2h and rGO-5h as a function of irradiation time..... 134

**Figure 3.8:** Images of (A) GO, (B) rGO-2h, and (C) rGO-5h dispersions as a function of time after irradiation, from left ( $t = 0$  hours) to right ( $t = 168$  hours). ..... 135

**Figure 3.9:** Chemical degradation of GO nanomaterials. XPS spectra of initial dispersions of (A) GO, (C) rGO-2h, and (E) rGO-5h prior to irradiation and (B) GO, (D) rGO-2h, and (F) rGO-5h after 72 hours of irradiation. .... 137

**Figure 3.10:** Optical absorbance spectra of irradiated (a) GO, (b) rGO-2h (c) rGO-5h samples. The shift in the major peak from 230 nm to 270 nm in GO implies the restoration of graphene lattice and disappearance of the peak at 300 nm indicates the removal of oxygen containing functional groups in GO. No significant changes are observed in the optical absorbance spectra for the rGO materials after irradiation. .... 139

**Figure 3.11:** Proposed mechanisms for the photodegradation of GO nanomaterials as a function of surface oxidation. Oxygen-containing functional groups on the basal plane of GO (top) such as hydroxyl and epoxy groups will react first after exposure to sunlight, initiating the degradation of the GO and creating holes in the graphene lattice, which further accelerates the GO breaking apart into smaller and smaller flakes. rGO (bottom) contains significantly fewer oxygen-containing functional groups on the basal plane resulting in less hole formation and higher overall stability. .... 141

**Figure 3.12:** AFM images of GO and MoS<sub>2</sub> on SiO<sub>2</sub>. The flakes are mainly monolayer or bilayer with a range of lateral sizes. .... 143

**Figure 3.13:** Attachment efficiency of NOM on GO and MoS<sub>2</sub> functionalized surfaces in (A) the absence of salts and in the presence of (B) monovalent cations and (C) divalent cations. (D) Attachment efficiency of *E. coli* in the presence of monovalent and divalent cations. .... 146

**Figure 3.14:** Schematic illustrating the proposed antifouling and self-cleaning mechanisms of GO- and MoS<sub>2</sub>-functionalized surfaces upon application of an external voltage. .... 150

**Figure 3.15:** Attachment efficiency of BSA on GO and MoS<sub>2</sub> functionalized surfaces. .... 151

**Figure 3.16:** (A) Deposition behavior of BSA under positive and negative potential. Reduced deposition of the BSA is observed upon application of  $-0.5 V_{Ag/AgCl}$  on PPy and MoS<sub>2</sub>-PPy surfaces. Deposition is reported in terms of the EQCM-D frequency shift. (B) Attachment efficiency of the BSA molecules on GO-PPy and MoS<sub>2</sub>-PPy surfaces under positive and negative potential. Higher attachment efficiency of BSA on the PPy-GO surface indicates faster deposition during negative bias application. However, efficiencies of  $<1$  suggest that both the modified surfaces perform better than the bare polymer surface under negative potential. .... 153

**Figure 3.17:** (A) Initial and (B) average release rates of BSA under different concentrations of NaCl and SSW electrolysis treatment under  $+0.74 V_{Ag/AgCl}$ . .... 154

**Figure 4.1:** Characterization of BP in DI-water prepared by LPE. (A) AFM image of BP nanosheets. (B) XPS analysis of the P 2p doublet and (C) Raman spectrum for BP demonstrating no oxidation or chemical changes. (D) Optical absorbance spectra of BP nanosheets dispersed in DI-water at varying concentrations and the mass extinction coefficient of exfoliated BP in DI-water as determined by the Beer-Lambert law (inset). .... 168

**Figure 4.2:** AFM height (A) and lateral size (B) histograms for solution-processed BP nanosheets.

..... 169

**Figure 4.3:** (A) Suspension stability and (B) chemical stability of aqueous dispersion of BP nanosheets after exposure to ambient conditions over time. Suspension stability was measured by the optical absorbance at 460 nm. Chemical stability was measured using XPS analysis. .... 170

**Figure 4.4:** Dispersion and chemical stability of BP nanosheets with different surfactants. (A) Optical absorbance spectra and photographs (inset) of BP exfoliated in DI water (black), 2% w v<sup>-1</sup> SDS (red) and 2% w v<sup>-1</sup> Pluronic F68 (blue) using identical preparation conditions. (B) Dispersion stability of BP dispersions after exposure to air under ambient conditions. (C) XPS spectra of the P 2p region for the BP dispersions immediately after processing, 1, and 7 days. 172

**Figure 4.5:** Stability of BP nanosheets in DI-water (A), 2% w v<sup>-1</sup> SDS-water (B), and in 2% w v<sup>-1</sup> F68-water (C) dispersions after dilution into native (oxygen-containing) DI-water, PBS, and DMEM. All measurements are normalized optical absorbance intensities at 460 nm. .... 174

**Figure 4.6:** Size distributions of BP nanosheets after dilution into native biological media (DI-water, PBS, and DMEM) after 1 hour (A) and 48 hours (B) as measured by NTA. .... 175

**Figure 4.7:** XPS spectra of BP nanosheets after dilution into native (oxygen-containing) DI-water (A) and native PBS (B) after 1 day and 28 days. .... 176

**Figure 4.8:** Factors affecting the degradation rate of aqueous dispersions of BP nanosheets. (A) Stability of BP in DI-water at room temperature (24 °C) and body temperature (37 °C). (B) Stability of BP in DI-water with different centrifugation conditions. (C) Stability of BP in native

DI-water and deoxygenated DI-water. All measurements are normalized optical absorbance intensities at 460 nm. .... 179

**Figure 4.9:** Degradation of BP dispersions as a function of ionic strength. Stability of BP in DI-water after dilution into native (oxygen-containing) solutions of varying concentrations of (A) KCl and (B) NaCl. Reported values are normalized optical absorbance intensities at 460 nm. .... 181

**Figure 4.10:** Stability of BP dispersion in phosphate buffers at varying pH: (A) pH 5.9, (B) pH 6.5, (C) pH 7.1, (D) pH 8.1. All measurements are normalized optical absorbance intensities at 460 nm. .... 182

**Figure 4.11:** Degradation products of black phosphorus. Ion chromatography analysis of degradation products of BP dispersions in (A) 1 mM KCl and (B) 1 mM NaCl after 7, 30 and 60 days. .... 184

**Figure 4.12:** Ion chromatography method for the determination of phosphate species. (A) Example chromatogram for 0.05 mg mL<sup>-1</sup> standard containing hypophosphite (H<sub>2</sub>PO<sub>2</sub><sup>-</sup>), phosphite (HPO<sub>3</sub><sup>2-</sup>), phosphate (PO<sub>4</sub><sup>3-</sup>), and pyrophosphate (P<sub>2</sub>O<sub>7</sub><sup>4-</sup>) using ion chromatography. Method details (B) and concentration curves for the determination of (C) hypophosphite, (D) phosphite, (E) phosphate, and (F) pyrophosphate anions using ion chromatography. .... 187

**Figure 5.1:** (a) Scanning electron microscopy (SEM) and (b) atomic force microscopy (AFM) images of the hBN powder, showing the characteristic particle lateral size (0.1–2 μm) and thickness (10–100 nm). .... 194

**Figure 5.2:** 3D printed hBN nanocomposite structures. (a) Photograph of complex structures including a small lumbar spine replica (left) and a double helix (right) that were 3D printed using a 60% vol. hBN nanocomposite ink. (b) Photograph and (c-e) scanning electron micrographs of a 3D printed 40% vol. hBN scaffold. The 3D printed strands are highly uniform and can be printed consistently over relatively large areas and heights. The printed strands can span gaps as seen in the grid inner structure in both the photograph and scanning electron micrographs as well as in the bridge structures of the double helix. The surface morphology is relatively smooth since the PLGA polymer uniformly coats and disperses the hBN flakes within the polymer matrix..... 195

**Figure 5.3:** Cross-sectional SEM images of the 3D printed hBN nanocomposites as a function of hBN loading: (a) 20% vol.; (b) 40% vol.; (c) 60% vol..... 196

**Figure 5.4:** Mechanical properties of 3D printed hBN. (A) Images of a single 3D printed 40% vol. hBN gridded sheet that has been cut, rolled and folded but still maintains its mechanical integrity. (B) Stress-strain curves for 3D printed samples with varying hBN content resulting from tensile testing. Corresponding modulus (C), strain to failure (D), and tensile strength (E) values ( $n \geq 3$ ) for the stress-strain curves shown in (B). Tensile strength and modulus are significantly different ( $p < 0.05$ ) for each composition. Strain to failure of 40% vol. and 60% vol. samples are significantly higher ( $p < 0.05$ ) than the strain to failure for 20% vol. and 70% vol. samples. Error bars represent one standard deviation. .... 198

**Figure 5.5:** Thermogravimetric analysis (TGA) scans of 3D printed hBN with varying hBN:PLGA composition ratios. PLGA curve is the raw PLGA polymer pellets used in the ink formulations (no

solvents). Samples were heated from 30°C to 600°C at a heating rate of 5°C/minute in a nitrogen environment. .... 199

**Figure 5.6:** Powder X-ray diffraction (PXRD) scans of (a) raw PLGA, (b) raw hBN powder, and (c) 3D printed hBN with varying hBN:PLGA composition ratios to determine the relative crystallinity of the PLGA polymer matrix. The relative crystallinity of the 3D printed structures was determined by normalizing the PXRD spectra to the primary hBN peak at 26.7° and then measuring the intensity of the primary PLGA peak at 16.9°. This intensity was then corrected for the amount of PLGA present in the hBN composite with the corrected intensity values provided in (d), which shows the highest relative crystallinity in the 20% vol. hBN and the lowest relative crystallinity in the 70% vol. hBN. .... 201

**Figure 5.7:** Thermal conductivity (A) and porosity (B) of 3D printed constructs (n = 3) at varying hBN content. Thermal conductivity for 20%, 30% and 40% vol. hBN are significantly different from each other ( $p < 0.05$ ), while there is no significant difference between 20%, 60% and 70% vol. hBN samples. Porosity is significantly higher ( $p < 0.05$ ) in 60% and 70% vol. hBN constructs, while the porosity does not vary significantly between the 20%, 30% and 40% vol. hBN constructs. Thermal conductivity increases as a function of hBN content until a significant increase in the porosity of the scaffolds causes a disruption in the thermally conductive network. Porosity was determined by comparison of the theoretical density to the experimentally measured density of the constructs. Error bars represent one standard deviation. .... 203

**Figure 5.8:** Cytocompatibility of 3D printed hBN. (A) Top down view reconstructions from scanning laser confocal microscopy of live (green) and dead (red) stained human mesenchymal

stem cells (hMSCs) on a 40% vol. hBN scaffold 1, 7, 14 and 28 days after seeding. (B) SEM micrographs of hMSCs seeded onto a 40% vol. hBN scaffold 1 day and 28 days after seeding. (C) DNA quantification of hMSCs seeded onto 40% vol. hBN scaffolds (n=3) over 28 days. Error bars represent one standard deviation. Scale bars for all images are 100  $\mu\text{m}$ . ..... 205

**Figure 5.9:** Live/dead confocal fluorescence imaging of 20% vol. hBN and 60% vol. hBN scaffolds after seeding with hMSCs. Live cells appear green, and dead cells appear red. Almost no dead cells were observed on the scaffolds, but it is hypothesized that dead cells tend to fall off the scaffold and thus are not observed attached to the scaffolds in these top-down reconstructions. The cells showed consistent growth and proliferation over the 28 day period. Scale bars for all images are 100  $\mu\text{m}$ . ..... 206

## LIST OF TABLES

<b>Table 2.1:</b> XPS summary showing relative amounts of functional groups on GO nanomaterials. .....	85
<b>Table 2.2:</b> Hydrodynamic sizes and zeta potential of GO and r-GO after suspension in cell media. .....	86
<b>Table 2.3:</b> Hydrodynamic sizes of GO and r-GO after suspension in PSF for 6h. ....	96
<b>Table 3.1:</b> XPS summary showing relative amounts of functional groups on GO nanomaterials. .....	124
<b>Table 3.2:</b> XPS summary showing atomic % (at.%) of oxygen and carbon associated with different functional groups on GO nanomaterials after 72 hours irradiation. ....	138
<b>Table 4.1:</b> Exfoliation yield of BP nanosheets in different surfactants. Final BP concentration is calculated from the mass extinction coefficient shown in Figure 4.1D. ....	173
<b>Table 5.1:</b> Compositions of 3D printed hBN based on the TGA scans shown in Figure 5.5. The volume percent reported in the last two columns of the table takes into account only the solid components of the 3D printed hBN (i.e., hBN and PLGA). ....	199

## **CHAPTER 1:**

### **INTRODUCTION**

This chapter is based, in part, on the research described in the following publication:

Guiney, L. M.; Wang, X.; Xia, T.; Nel, A. E.; Hersam, M. C. “Assessing the hazard potential of two-dimensional nanomaterials” *ACS Nano* 2018, under review

## 1.1 Two-dimensional materials

Two-dimensional (2D) materials have gained widespread interest in the research community due to interesting physicochemical properties that emerge as the materials approach single-atom thicknesses, an interest first sparked by the isolation of graphene in 2004.<sup>1-3</sup> The 2D materials which have been explored since encompass a broad range of mechanical, electrical, and optical properties. In order to realize and commercialize 2D nanomaterial-enabled technologies, the biological and environmental hazards of the materials need to be well-established. Specifically, 2D nanomaterials present new compositions, chemistries, and physicochemical properties to consider in their toxicological profile.

### 1.1.1 *Graphene-family nanomaterials*

Graphene is increasingly being used for a broad range of applications in electronics, energy, sensors, and catalysis due to its high electronic and thermal conductivity, high surface area, and extraordinary mechanical properties.<sup>4,5</sup> However, graphene suffers from poor aqueous dispersibility due to its hydrophobic nature and requires the use of surfactants to stably disperse the nanosheets in water.<sup>6,7</sup> In contrast, the graphene derivative graphene oxide (GO) exhibits excellent dispersibility, colloidal properties and the potential to use surface functionalization to render the material attractive for use in biomedicine, including tissue engineering,<sup>8</sup> antimicrobial agents,<sup>9</sup> bioimaging,<sup>10</sup> and drug delivery.<sup>11</sup> This disruption in the  $sp^2$  network leads to a loss in electrical conductivity.<sup>4,12</sup> Using chemical or thermal reduction processes, the graphene lattice can be restored, but many structural defects will still be present in the basal plane of this reduced graphene oxide (rGO). However, this process still represents a scalable and low-cost method for production of graphene-like nanosheets.<sup>13</sup> As GO and rGO represent the most likely forms of the

material to be used on an industrial scale, the successful translation of these materials to commercialized products will rely on a complete understanding of their safety and environmental impact.<sup>14,15</sup>

### ***1.1.2 Transition metal dichalcogenides***

TMDCs are a class of layered materials that gained a lot of interest after graphene because of the wide range of band structures available, which provide more opportunities for the use of 2D nanomaterials in electronic applications.<sup>16–18</sup> Similar to graphene, these materials in the 2D form exhibit interesting properties different from those of the bulk material.<sup>16,17,19–21</sup> TMDCs are layered materials with a stoichiometry of  $\text{MX}_2$ , where M represents a group IV, V or VI transition metal and X represents a chalcogen such as sulfur, selenium or tellurium (Figure 1.1).<sup>17</sup> The intralayer bonding is covalent while the layers are held together by van der Waals forces. This weak interlayer bonding allows for easy exfoliation of the bulk material into few-layer or monolayer form.<sup>22</sup> Thus far, the most widely studied of the TMDCs is molybdenum disulfide ( $\text{MoS}_2$ ).  $\text{MoS}_2$  undergoes a transition from an indirect band gap in the bulk to a direct band gap in the monolayer form that gives rise to unique optical properties such as photoluminescence.<sup>23–26</sup> The semiconducting nature of  $\text{MoS}_2$  allows for potential use in field-effect transistors and other similar devices, while the optical properties make it useful for optoelectronic as well as biomedical applications. Although  $\text{MoS}_2$  in the monolayer form is a direct gap semiconductor, other TMDCs exhibit a wide range of electronic properties including metallic (e.g.,  $\text{NdS}_2$ ), semimetallic (e.g.,  $\text{WTe}_2$ ) and insulating (e.g.,  $\text{Bi}_2\text{Te}_3$ ).<sup>17</sup>

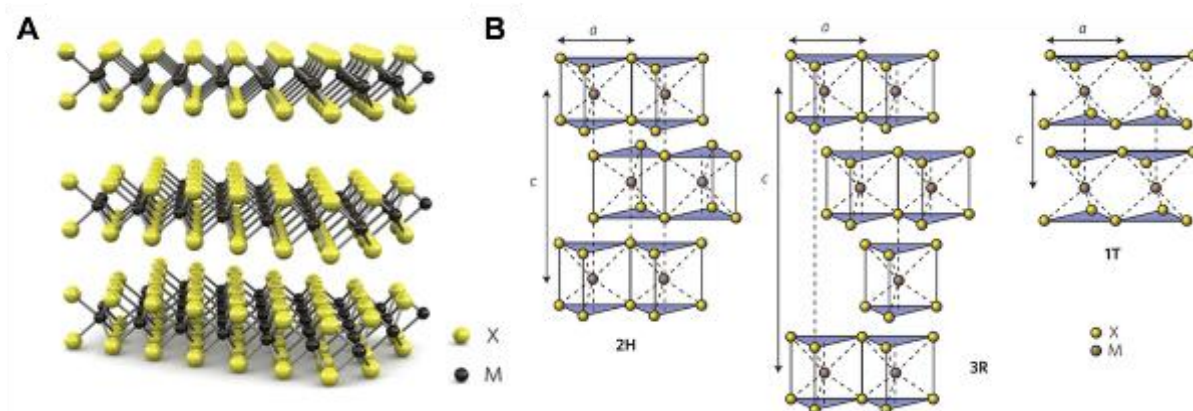


**Figure 1.1:** (A) Schematic structure of a TMDC where M represents a transition metal atom and X represents a chalcogen atom. Figure adapted from reference<sup>27</sup>. (B) Schematics of different structural polytypes of TMDCs. Figure adapted from reference<sup>17</sup>.

The high surface area and greater chemical reactivity of TMDCs compared to graphene has enabled the development of a wide range of biomedical applications, such as the functionalization and use of these 2D materials as drug delivery carriers.<sup>28,29</sup> This high surface to volume ratio also makes TMDCs highly sensitive to adsorbed molecules, enabling their use for biosensors.<sup>30–36</sup> The intrinsic photoluminescence of some TMDCs allows for their use as imaging agents.<sup>37–40</sup> Novel photothermal therapies can also make use of the optical properties of TMDCs, such as the absorption of light in the near infrared range as well as the high photothermal conversion efficiency of a wide range of TMDCs including MoS<sub>2</sub>, titanium disulfide (TiS<sub>2</sub>), tin sulfide (SnS), rhenium disulfide (ReS<sub>2</sub>), and molybdenum diselenide (MoSe<sub>2</sub>).<sup>41–50</sup>

### **1.1.3 Hexagonal boron nitride**

Hexagonal boron nitride (hBN) is a layered material similar to graphene, in that the boron and nitrogen atoms are arranged in a hexagonal  $sp^2$  bonded 2D lattice, resulting in a material that is highly chemically stable. In contrast to graphene, hBN has a band gap of approximately 6 eV, making it an insulating material.<sup>51–53</sup> As an insulator, hBN can also be used as a component of electronic systems for thermal management<sup>54–56</sup> or as a dielectric material.<sup>53,57,58</sup> In particular, hBN has lower cytotoxicity in comparison to its carbon analogue.<sup>59–62</sup> This observed increased biocompatibility *in vitro* has resulted in a surge of studies on potential biomedical applications of this material, including drug delivery, fluorescent labeling in cells, and tissue engineering.<sup>63–69</sup>

### **1.1.4 Black phosphorus**

Finally, elemental 2D nanomaterials comprised of atoms of a single element are also gaining popularity in the field of materials science. Unlike graphene, these 2D nanomaterials generally need to be synthesized using highly controlled bottom-up approaches because they do not occur naturally in their bulk form.<sup>70</sup> Black phosphorus (BP) is one exception, in that the bulk form of the material can be synthesized from other naturally occurring allotropes of phosphorus.<sup>71</sup> As a result, BP, a semiconducting, anisotropic material with a layer-dependent band structure, has been extensively studied in the last few years for its use in electronics, optoelectronics, and most recently biomedical applications.<sup>72–79</sup> However, BP demonstrates environmental instability under ambient conditions, chemically degrading in the presence of oxygen and water.<sup>80–85</sup> While this degradation is considered a challenge in the application of BP for electronics and optoelectronics, the same chemical degradation presents opportunities to create a biodegradable 2D nanomaterial

construct. As a result, research on the use of BP for biological imaging, sensing and therapeutics has accelerated significantly in the last two years.<sup>86–95</sup>

## 1.2 Synthesis of 2D materials

A variety of preparation methods exist for monolayer or few-layer 2D nanomaterials, which can generally be separated into either bottom-up or top-down approaches. Bottom-up approaches involve the use of precursors to grow the 2D nanomaterial. For example, chemical vapor deposition (CVD) of MoS<sub>2</sub> requires solid precursors of molybdenum, usually in the form of molybdenum oxide (MoO<sub>3</sub>), and sulfur to be vaporized by heating and subsequently deposited onto a substrate to form mostly monolayer MoS<sub>2</sub>.<sup>96–98</sup> Solution-phase synthesis methods such as hydrothermal synthesis<sup>99</sup> or combining precursors such as molybdic acid and thiourea at high temperature and pressure<sup>100</sup> can be used to prepare some TMDCs, such as MoS<sub>2</sub>. These solution-based methods produce highly polydisperse samples, both in lateral dimensions of the flakes as well as in number of layers.

Top-down approaches involve the isolation of 2D materials from bulk layered crystals. The most well-known of these approaches is micromechanical cleavage, more commonly referred to as the Scotch tape method.<sup>1,26,27,101</sup> However, due to the low yield of micromechanical cleavage, significant research effort has been devoted to liquid phase exfoliation methods because they are more scalable and enable easier post-processing in manufacturing settings (Figure 1.2).<sup>102–105</sup> Liquid phase exfoliation methods often use small ionic species, such as lithium, to intercalate between the layers in the bulk material, ultimately facilitating exfoliation.<sup>25,106,107</sup> In particular, the addition of water reacts with intercalated lithium ions, liberating hydrogen gas that weakens the interlayer van der Waals forces, resulting in exfoliation into 2D sheets. For the case of MoS<sub>2</sub>, while

this process produces monolayer sheets in solution with high yield, the aggressive chemical conditions drive MoS<sub>2</sub> to undergo a phase transformation from trigonal prismatic (2H-MoS<sub>2</sub>) to octahedral (1T-MoS<sub>2</sub>) (Figure 1.1). Since 1T-MoS<sub>2</sub> is a metastable metallic material, it can be partially converted back to 2H-MoS<sub>2</sub> through thermal annealing or laser-assisted phase reversion,<sup>19,25,108</sup> although the final structure and properties differ from pristine exfoliated 2H-MoS<sub>2</sub>.

Another top-down liquid phase method that has been studied extensively utilizes ultrasonication or shear mixing to exfoliate 2D materials.<sup>7,104,109–115</sup> To achieve optimal exfoliation yields, the liquid needs to contain a surface energy that is well-matched to the targeted 2D material or additional additives, such as surfactants or stabilizing polymers, need to be added to the solution. While this method is amenable to scale-up and generally yields chemically pristine 2D materials, the resulting flakes are generally small in lateral dimensions and possesses high polydispersity, with the majority of the flakes being few-layer instead of monolayer.<sup>104</sup> Despite these drawbacks, top-down approaches are being most commonly pursued in early-stage industrial efforts due to the low costs involved.<sup>116</sup> Additionally, post-processing methods such as density gradient ultracentrifugation can be used to sort and isolate monodisperse populations of the 2D materials following liquid phase exfoliation.<sup>57,103,111</sup> In addition, some top-down approaches can be carried out in aqueous media, which eliminates the need for environmentally unfriendly organic solvents.<sup>109,117–122</sup> Consequently, aqueous and biocompatible synthesis and processing have become increasingly important for the application of 2D materials in biomedical contexts.

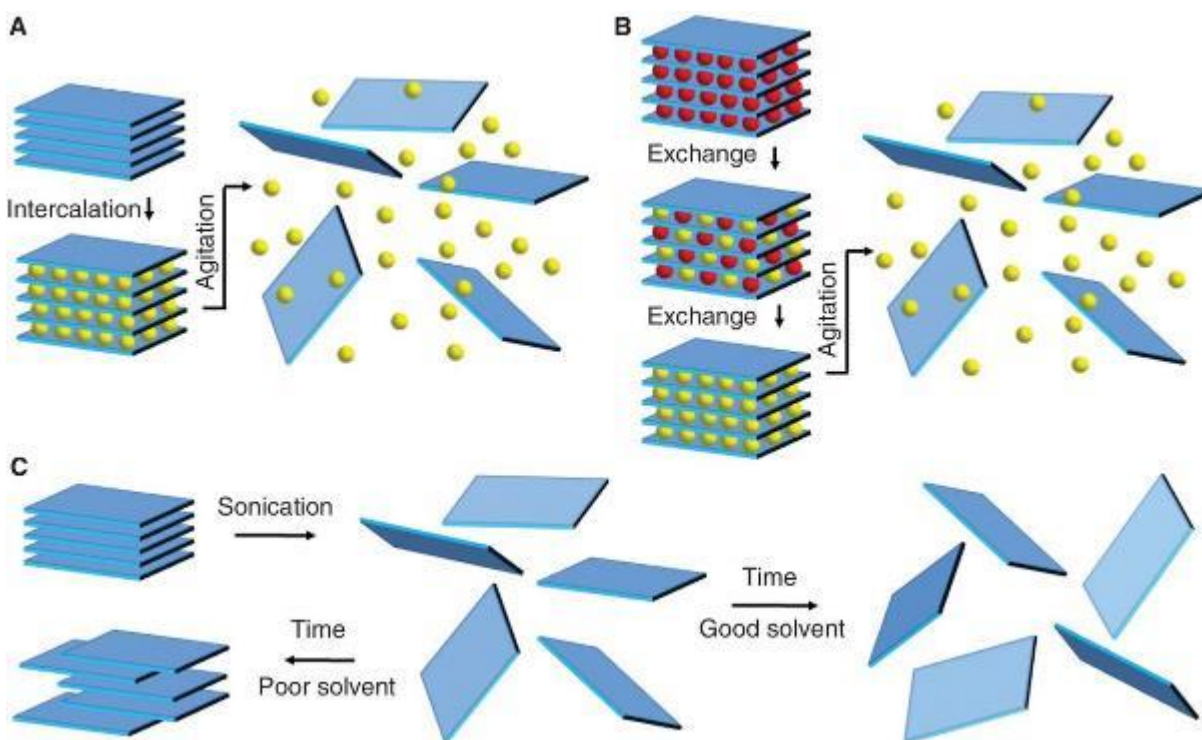


**Figure 1.2:** Solution-phase exfoliation methods. (A) Chemical exfoliation using intercalation of small ionic species, followed by agitation such as sonication. (B) Ion exchange exfoliation, which employs the exchange of small naturally occurring ions with larger ions to weaken the interlayer attraction, followed by agitation to exfoliate the layers. (C) Sonication-assisted exfoliation which uses solvents of appropriate surface energy to effectively disperse the 2D sheets in solution. This method can also employ surfactants to stabilize the 2D materials following exfoliation. Adapted from reference<sup>105</sup>.

### **1.3 Hazard assessment of 2D materials**

The growing interest in the use of 2D nanomaterials in electronics, optoelectronics, energy capture and storage, and biomedical applications necessitates the need to understand the health and environmental implications of exposure to these nanomaterials. These biological and environmental interactions of 2D nanomaterials will be dictated by the physicochemical properties of the material.<sup>123–126</sup> Here, several important factors are reviewed, including composition, exfoliation, flake size and thickness, surface functionalization, physical forms and chemical dissolution, which play a role in the interactions at the nano-bio interface (Figure 1.3). Without a complete understanding of these properties, it is not possible to designate the hazard potential of a 2D nanomaterial construct.

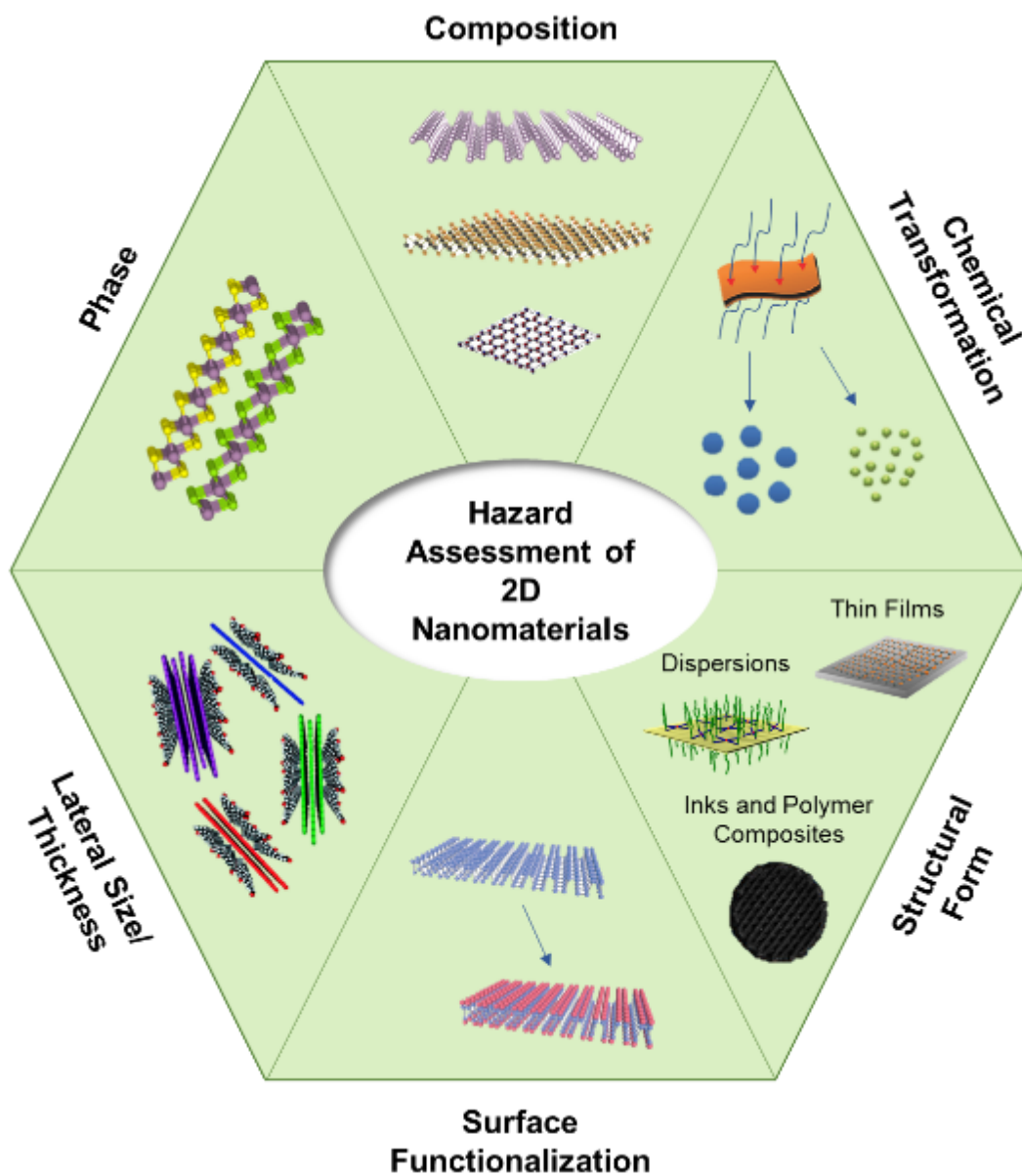


**Figure 1.3:** Physicochemical properties of 2D nanomaterials that affect their toxicity. Complete characterization of these properties is needed to accurately assess the hazard of the specific nanomaterials. Figure adapted from references<sup>103,120,127–132</sup>.

### 1.3.2 Composition

Chemical composition is one of the most important considerations for determining the biological interactions and fate of 2D materials *in vivo*. The surface chemistry and the dissolution of the material will be determined by its chemical composition, which will in turn affect the cellular interactions, uptake, and biodistribution.<sup>133,134</sup> For 2D materials, several studies have assessed the cytotoxicity of TMDCs according to composition.<sup>135–138</sup> For example, Teo *et al.* investigated the toxicity of chemically exfoliated MoS<sub>2</sub>, WS<sub>2</sub>, and WSe<sub>2</sub> in human lung carcinoma epithelial cells (A549).<sup>135</sup> While low toxicity of MoS<sub>2</sub> and WS<sub>2</sub> was observed, a dose-dependent toxicity of WSe<sub>2</sub> was detected, indicating that the presence of selenium plays an important role in the toxicity of TMDCs. However, it is unclear whether this toxicity can be attributed to the nano-bio interface interactions caused by the presence of selenium at the surface of the TMDC or the toxicity related to dissolved selenium. A similar study by the same group was recently published on the cytotoxicity of vanadium ditelluride (VTe<sub>2</sub>), niobium ditelluride (NbTe<sub>2</sub>), and tantalum ditelluride (TaTe<sub>2</sub>) in the same cell line (A549), allowing for direct comparison to the cytotoxicity of MoS<sub>2</sub>, WS<sub>2</sub>, and WSe<sub>2</sub> from the previous study.<sup>137</sup> High cytotoxicity was observed after exposure to VTe<sub>2</sub>, whereas NbTe<sub>2</sub> and TaTe<sub>2</sub> showed reduced cytotoxicity. Overall, the ditellurides exhibited higher cytotoxicity than the disulfide materials, while WSe<sub>2</sub> exhibited similar cytotoxicity to the ditellurides. To further investigate the role of the chalcogen, the same group ran an identical study comparing the cytotoxicity of vanadium dichalcogenides: VS<sub>2</sub>, VSe<sub>2</sub>, and VTe<sub>2</sub>.<sup>136</sup> VS<sub>2</sub> showed the least cytotoxic effect, whereas VSe<sub>2</sub> and VTe<sub>2</sub> showed similarly higher cytotoxicity, further suggesting that the chalcogen significantly affects the toxicological response. While these initial

studies provide an initial assessment of the relative cytotoxicity of TMDCs based on composition, further studies are required to elucidate the underlying toxicity mechanisms.

### 1.3.3 Exfoliation

As layered materials are exfoliated, the fundamental properties of the material change.<sup>22,77</sup> Similarly, biological interactions with layered materials vary as a function of exfoliation state. For example, Chng *et al.* investigated the effects of exfoliation on the cytotoxicity of MoS<sub>2</sub>.<sup>139</sup> Using three different lithium sources—methyllithium, n-butyllithium, and tert-butyllithium—MoS<sub>2</sub> was chemically exfoliated, and the exfoliation yield was deduced using Raman spectroscopy. Higher exfoliation yield was achieved with tert-butyllithium and n-butyllithium, which corresponded to higher cytotoxicity. Based on this observation, the study concluded that the increase in surface area and active edge sites leads to higher toxicity in more highly exfoliated MoS<sub>2</sub>. However, limited material characterization left open the possibility that other physical properties of these MoS<sub>2</sub> samples led to the differential cytotoxicity. A more thorough investigation of the toxicity of MoS<sub>2</sub> by Wang *et al.* compared two forms of exfoliated MoS<sub>2</sub> to an aggregated form of MoS<sub>2</sub> (Figure 1.4).<sup>140</sup> The exfoliated forms of MoS<sub>2</sub> were prepared by chemical exfoliation with n-butyllithium and ultrasonication-assisted liquid phase exfoliation with the aid of the surfactant Pluronic F87. The toxicity of these materials was examined *in vitro* and in the mouse lung *in vivo*. Aggregated MoS<sub>2</sub> induced significantly increased production of pro-inflammatory cytokines, indicating a pro-inflammatory response *in vitro*, whereas the lithiated and Pluronic-dispersed MoS<sub>2</sub> showed reduced effects, which was attributed to the bioavailability and cellular uptake of these MoS<sub>2</sub> materials. *In vivo* studies revealed focal areas of inflammation in the lung after acute exposure to aggregated MoS<sub>2</sub> but no significant inflammatory response was observed for any of

the MoS<sub>2</sub> materials following sub-chronic exposure. Overall, effective exfoliation reduced the toxic response of MoS<sub>2</sub> compared to its aggregated state, suggesting that stable dispersions of exfoliated MoS<sub>2</sub> lead to higher biocompatibility. Negligible toxicity of exfoliated MoS<sub>2</sub> was also observed by Shah *et al.* in rat pheochromocytoma cells and adrenal medulla endothelial cells.<sup>141</sup> In this work, the MoS<sub>2</sub> materials were also chemically exfoliated, further supporting this synthetic pathway to biocompatible MoS<sub>2</sub>.

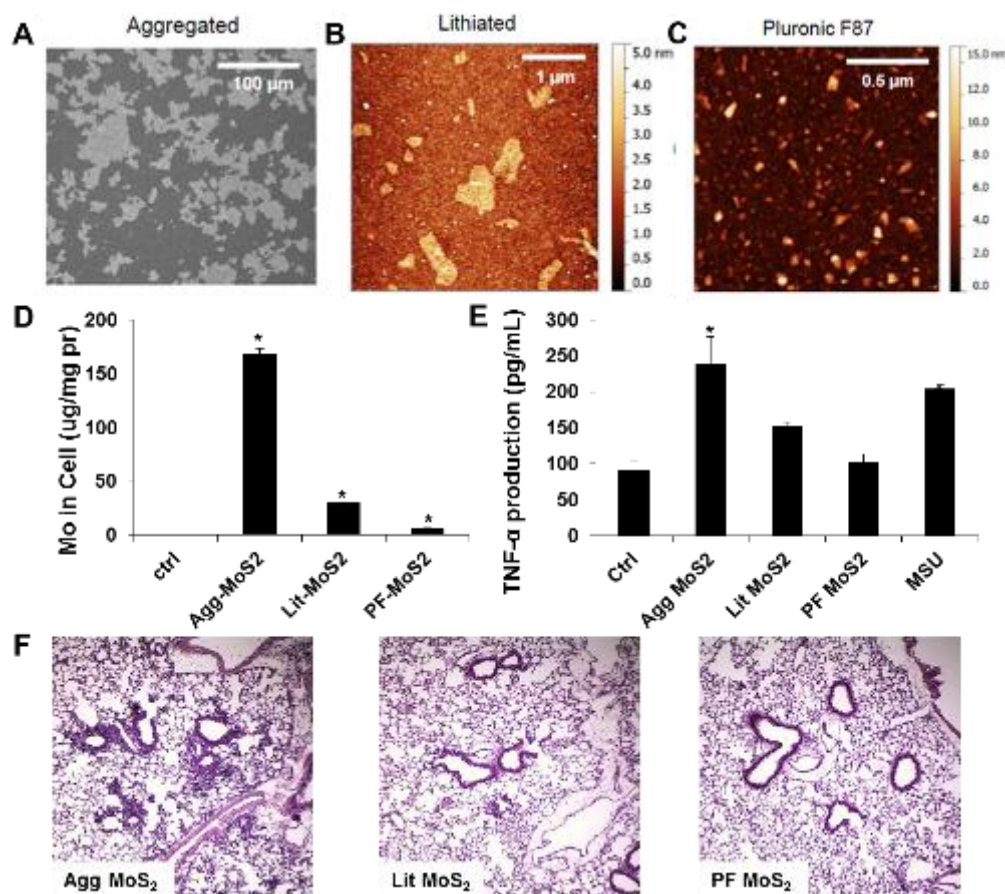


**Figure 1.4:** Effects of aqueous exfoliation methods on the pulmonary hazard potential of MoS<sub>2</sub>. (A) SEM micrograph of aggregated MoS<sub>2</sub> and AFM images of (B) chemically exfoliated MoS<sub>2</sub> using a lithiation process and (C) MoS<sub>2</sub> exfoliated by ultrasonication in the presence of Pluronic F87. (D) Cellular content of molybdenum (Mo) and (E) TNF-α production in THP-1 cells 24 hours after exposure to 50 μg mL<sup>-1</sup> of the MoS<sub>2</sub> materials. (F) Acute pulmonary effects of MoS<sub>2</sub> materials in mice after 40 hours. The H&E-stained histological images indicate that aggregated MoS<sub>2</sub> is capable of inducing inflammation in the lung while the exfoliated MoS<sub>2</sub> materials show little or no effect. Figure adapted from reference<sup>140</sup>.

The cytotoxicity of MoS<sub>2</sub> by different exfoliation and preparation methods has also been explored in a series of recent studies. For instance, a comparative study of the cytotoxicity and genotoxicity in epithelial kidney cells was performed for mechanically exfoliated MoS<sub>2</sub> *versus* MoS<sub>2</sub> that was grown by chemical vapor deposition (CVD).<sup>142</sup> Similar to exfoliated MoS<sub>2</sub> prepared by solution processing methods, both mechanically exfoliated MoS<sub>2</sub> and CVD-grown MoS<sub>2</sub> showed minimal impact on cell morphology in addition to non-significant reactive oxygen species (ROS) generation and negligible effects on cell viability. Furthermore, exfoliated MoS<sub>2</sub> did not induce measurable genetic changes. Similar results for CVD-grown MoS<sub>2</sub> were observed in both mouse embryo fibroblasts (NIH-3T3) and human adipose-derived mesenchymal stem cells (HAMSCs).<sup>143</sup> In particular, no significant loss of cell viability was observed for MoS<sub>2</sub> concentrations up to 50 µg mL<sup>-1</sup> and 300 µg mL<sup>-1</sup> in NIH-3T3 and HAMSCs, respectively. While most studies have found a high degree of biocompatibility for MoS<sub>2</sub>, a recent study by Liu *et al.* indicated that exposure to MoS<sub>2</sub> induces a loss in cell viability in HepG2 cells at concentrations as low as 30 µg mL<sup>-1</sup>.<sup>144</sup> In this case, MoS<sub>2</sub> induced a significant increase in intracellular ROS at doses greater than 2 µg mL<sup>-1</sup> in addition to membrane damage at doses greater than 4 µg mL<sup>-1</sup>. The study also found similar results for hBN. Thus, the observed toxicity was attributed to membrane damage caused by the 2D sheet-like structure of the materials. However, the study lacks proper material characterization to rule out other mechanistic possibilities.

For the case of black phosphorus, a study by Latiff *et al.* investigated the cytotoxicity of bulk BP crystals in human lung carcinoma epithelial cells (A549), which showed a dose-dependent toxicity and reduced cell viability at BP concentrations of 50 µg mL<sup>-1</sup>.<sup>145</sup> In contrast, a later study by Mu *et al.* investigated the toxicity of BP quantum dots (BPQDs) both *in vitro* in HeLa cells and

*in vivo* in mice.<sup>146</sup> At high BPQD concentrations of 200  $\mu\text{g mL}^{-1}$ , significant cytotoxicity and apoptotic effects were observed, which were attributed to oxidative stress. Weight loss in the mice after exposure indicated acute toxicity, but the mice eventually recovered, indicating that BPQDs did not induce long-term inflammatory responses or injury. Thus, the exfoliation of BP may play a role in the toxicological response, but additional studies are needed to gain mechanistic insight.

#### **1.3.4 Lateral size and thickness**

From these initial studies and the precedent set by graphene nanomaterials, it is clear that the interactions of the exfoliated form of layered 2D materials will differ fundamentally from those of their bulk counterpart. The biological response to a 2D geometry is unique, and the physical interactions of 2D materials with cells are expected to vary based on their aspect ratio and mechanical properties.<sup>147</sup> Thus, the characterization of lateral size and thickness of 2D materials is critical in order to quantify the aspect ratio and its effects on the biological response. Towards this end, Moore *et al.* investigated the role of lateral size of MoS<sub>2</sub> flakes in the cytotoxicity, cellular uptake, and inflammatory response.<sup>148</sup> Using liquid cascade centrifugation, MoS<sub>2</sub> flakes dispersed with sodium cholate of varying lateral sizes were isolated. The response of three separate MoS<sub>2</sub> samples with mean lateral sizes of 50 nm, 117 nm, and 177 nm were studied in A549, AGS, and THP-1 cell lines, chosen specifically to assess risk *via* different exposure routes. At 1  $\mu\text{g mL}^{-1}$  dose, all samples showed minimal cytotoxicity and invariant cell morphology, although an inflammatory response was observed. Assays revealed a size-dependent increase in cytokine production (IL-6, IL-10, IL-13, TNF- $\alpha$ , and IL-1 $\beta$ ) in THP-1 cells, with the smallest MoS<sub>2</sub> flake sizes inducing the largest increases in cytokine production. However, the MoS<sub>2</sub> samples were prepared under conditions that suffered from endotoxin contamination, making it difficult to

determine if the size-dependent toxicity resulted from the material itself or the increased surface area allowing for increased endotoxin levels. To elucidate the fundamental effects of lateral size on biological response, the material processing needs to be performed in a manner where other variables are held constant.

More recently, BP has also been used as a model 2D material to probe the effects of lateral size on the cytotoxic response.<sup>149,150</sup> Fu *et al.* prepared BP nanosheets by liquid phase exfoliation and then isolated three different lateral size distributions through varying centrifugation speeds.<sup>149</sup> In human hepatocyte cells (LO2), a small dose-dependent loss of viability was observed, but even at concentrations of  $50 \mu\text{g mL}^{-1}$ , cell viability still exceeded 80%. In a more mechanistic study, three different sizes of BP were prepared by aqueous liquid phase exfoliation and fractional centrifugation (Figure 1.5).<sup>150</sup> The three samples varied in both lateral size and thickness with BP-1 containing flakes of the largest lateral size and thickness and BP-3 containing flakes of the smallest lateral size and thickness. The cytotoxicity was tested in three cell lines: mouse fibroblasts (NIH-3T3), human colonic epithelial cells, and human embryonic kidney cells (293T). The cytotoxic response was found to be dependent on concentration, size, and cell type, with the 293T cells being the most sensitive and the epithelial cells being the least sensitive. Unlike  $\text{MoS}_2$ , BP flakes with the largest lateral size and thickness showed the highest levels of cytotoxicity. Additional assays showed ROS generation, but the response was not size-dependent. Further investigation into the interaction of BP with model cell membranes using a quartz crystal microbalance with dissipation monitoring revealed that the largest BP samples disrupted the integrity of the cell membrane, implicating this pathway as the most likely size-dependent toxicity

mechanism. However, the study did not account for the environmental instability of exfoliated BP, and no stability or long-term (> 24 hours) cytotoxicity data were presented.

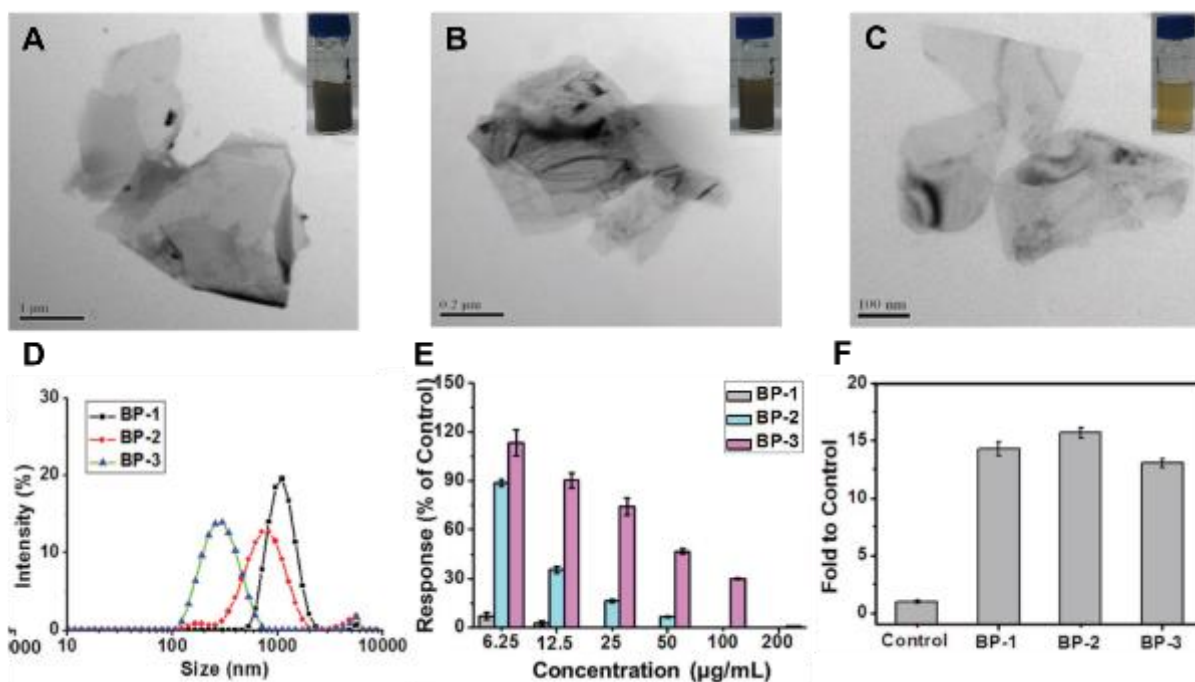


**Figure 1.5:** Effects of lateral size and thickness on the hazard potential of exfoliated black phosphorus (BP) nanomaterials. Representative TEM micrographs of flakes from three different sized BP dispersions—BP-1 (A), BP-2 (B) and BP-3 (C)—and corresponding photographs of the dispersions (insets). (D) Size measurements of the three BP dispersions in 10% FBS supplemented cell culture medium as determined by DLS. (E) Cell viability of NIH-3T3 cells after 24 hours exposure to the BP nanomaterials via RTCA. (F) Intracellular detection of reactive oxygen species in NIH-3T3 cells after exposure to  $10 \mu\text{g mL}^{-1}$  of BP nanomaterials for 4 hours. Figure adapted from reference<sup>150</sup>.

### 1.3.5 *Physical forms*

Most toxicity studies to date have focused on dispersions of 2D materials because many biological applications, such as drug delivery and imaging agents, call for such a format.<sup>74,151–155</sup> However, 2D materials are also being explored in a myriad of other applications in which the qualitatively different physical form factors are needed including thin films, three-dimensional constructs, and composites.<sup>156–161</sup> In these cases, biological interactions will fundamentally differ from those of a well-dispersed 2D material in solution. Consequently, some recent studies have begun to specifically probe the toxicity of 2D materials in solid-state formats such as thin films, foams, and composites. One such study investigated the toxicity of MoS<sub>2</sub>, WS<sub>2</sub>, and hBN coated glass slides, seeding adipose-derived human mesenchymal stem cells (hMSCs) onto these thin films and then studying the cellular response (Figure 1.6).<sup>131</sup> None of the 2D materials resulted in a significant loss in cell viability up to concentrations of 5  $\mu\text{g mL}^{-1}$ , but rather the cells showed higher cellular adhesion and enhanced proliferation compared to an uncoated glass slide. Furthermore, the presence of the 2D materials contributed to enhanced adipogenesis in the hMSCs.

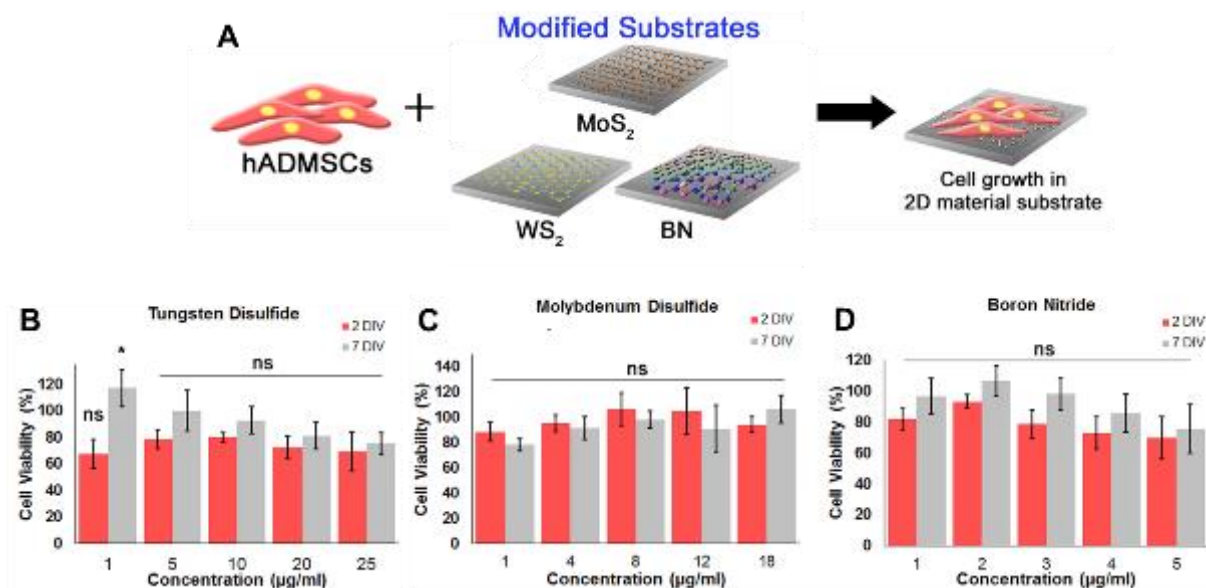


**Figure 1.6:** Cytotoxicity of 2D nanomaterial-modified glass substrates. (A) Schematic of the experimental design. Human adiopose-derived mesenchymal stem cells (hADMSCs) were seeded onto glass substrates which have been modified with a thin film of various 2D nanomaterials, including molybdenum disulfide (MoS<sub>2</sub>), tungsten disulfide (WS<sub>2</sub>) and hexagonal boron nitride (hBN). (B-D) Cell viability of modified substrates after 2 days and 7 days as determined by growth rate using a CCK-8 assay. Figure adapted from reference<sup>131</sup>.

The biocompatibility of thin films generated from printed 2D material inks was explored by McManus *et al.*<sup>162</sup> In this study, a range of 2D materials, including graphene, MoS<sub>2</sub>, WS<sub>2</sub>, and hBN, were exfoliated in water in the presence of pyrene sulfonic acid derivatives. To achieve printable viscosities of the exfoliated dispersions, Triton X-100 and propylene glycol were added to the solutions following exfoliation. Cytotoxicity of the 2D inks was then determined using an LDH assay in human lung epithelial cells (A549) and human keratinocyte cells (HaCaT). No loss

of cell viability was observed for any of the materials up to concentrations of 100  $\mu\text{g mL}^{-1}$ . Furthermore, cells seeded onto the 2D material thin films showed strong interactions with the substrates, similar to what was observed in the previous study by Suhito *et al.*<sup>131</sup> This favorable cell attachment and high biocompatibility have prompted further studies on the biological interactions of nanostructured films of 2D materials with different cell types, such as differentiation of stem cells.<sup>163</sup> Similar biocompatibility has also been reported for a number of polymer composites containing 2D materials.<sup>66,132,164,165</sup> Like 2D material thin films, these composites have shown high cell adhesion, low cytotoxicity, and accelerated cell proliferation and growth.

### **1.3.6 Surface functionalization**

Extensive studies on graphene and related carbon nanomaterials have shown that surface functionalization plays a major role in the toxicological response.<sup>166–169</sup> Analogous studies on the surface functionalization of post-carbon 2D materials have begun to be undertaken with an eye toward achieving specific biological outcomes and minimizing toxic response.<sup>129,170–172</sup> For example, Qu *et al.* showed that functionalization of BPQDs with a titanium sulfonate ligand ( $\text{TiL}_4$ ) resulted in lower cytotoxicity and reduced inflammatory response (Figure 1.7).<sup>129</sup> In this study, the cytotoxicity of bare BPQDs was compared to that of  $\text{TiL}_4$ -modified BPQDs in two different macrophage cell lines. Both BPQD samples showed minimal effect on the viability of RAW264.7 macrophage cells. On the other hand, in J774A.1 macrophage cells, bare BPQDs showed a significant loss of viability, while this effect was reduced in the case of  $\text{TiL}_4$ -modified BPQDs. The proinflammatory response of the BPQDs was also tested by measuring the cytokine ( $\text{TNF-}\alpha$ ) production in RAW264.7 cells.  $\text{TiL}_4$ -modified BPQDs showed reduced inflammatory response

compared to bare BPQDs, which correlated with the cellular uptake of the materials, namely that the intracellular level of bare BPQDs was significantly higher than that of TiL<sub>4</sub>-modified BPQDs. Further *in vivo* studies revealed that bare BPQDs showed an acute inflammatory response at 24 hour post-exposure, as evidenced by the significant increase of neutrophils in the blood and concentration of cytokines (TNF- $\alpha$ , eotaxin, IL-6, MCP-1, KC, MIP-1, MIG, VEGF) in the mice serum, whereas TiL<sub>4</sub>-modified BPQDs did not show this response. Although neither material demonstrated chronic inflammation, the differences in acute toxicity confirmed that surface functionalization of BP can be used to minimize toxicity by altering cellular uptake. Surface functionalization techniques can also be used to minimize toxicity by changing the degradation behavior of the 2D material. For example, chemically exfoliated MoS<sub>2</sub> functionalized with 2-iodoacetamide showed a higher resistance to enzymatic degradation than non-functionalized chemically exfoliated MoS<sub>2</sub>.<sup>172</sup> Upon exposure to the degradation products of both MoS<sub>2</sub> samples, both HeLa and RAW264.7 cells showed a higher loss of viability upon exposure to the degradation products of non-functionalized MoS<sub>2</sub>, thus providing evidence that the degradation products at elevated concentrations can induce a toxic response.

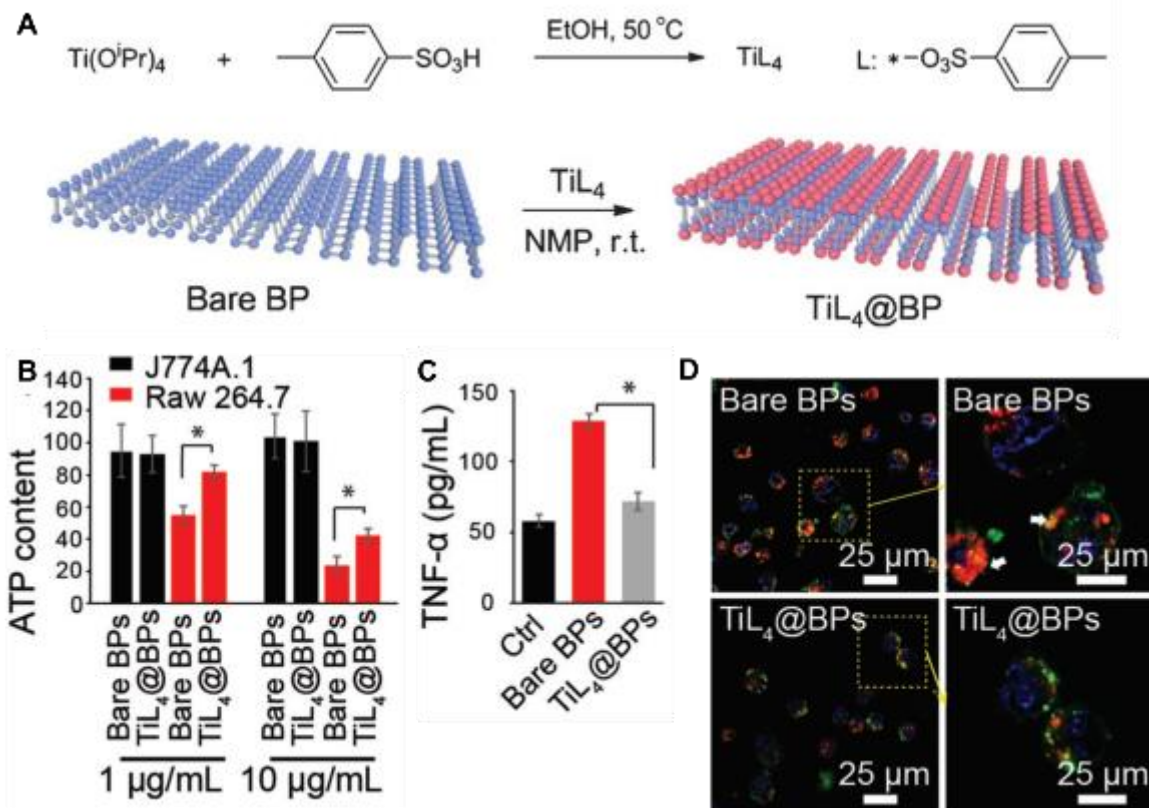


**Figure 1.7:** Effects of chemical modification on the toxicity of BP. (A) Synthesis scheme of the surface coordination of the titanium sulfonate ligand ( $\text{TiL}_4$ ) to BP to generate  $\text{TiL}_4\text{@BP}$ . (B) Cell viability of raw 264.7 and J774A.1 cells after 24 hours exposure to bare BP and  $\text{TiL}_4\text{@BP}$  as determined by an ATP assay. (C)  $\text{TNF-}\alpha$  production from raw 264.7 cells after 12 hours exposure to  $10 \mu\text{g mL}^{-1}$  of the BP materials. (D) Confocal microscopy images of J774A.1 cells stained with Magic Red to show Cathepsin B location after exposure to BP materials after 6 hours. In the control cells, cathepsin B appear as concentrated dots, localized within the lysosomes. After exposure to bare BPs, the lysosomes appear swollen, while this inflammatory effect is not observed after exposure to  $\text{TiL}_4\text{@BP}$ . Figure adapted from reference<sup>129</sup>.

### 1.3.7 Environmental stability and chemical dissolution

Although most TMDCs are considered highly stable, some studies have shown that these materials undergo environmental transformations. In particular, the dissolution of TMDCs has been shown to vary as a function of composition due to differences in the strength and reactivity of the bonds formed between metal and chalcogen atoms. By varying the metal atom but otherwise maintaining analogous TMDC structure and processing, Hao *et al.* investigated the *in vitro* cytotoxicity and *in vivo* biodistribution and toxicity of MoS<sub>2</sub>, WS<sub>2</sub>, and TiS<sub>2</sub> nanosheets (Figure 1.8).<sup>127</sup> The nanosheets were prepared using a high-temperature solution-phase synthesis method in which bulk TMDCs were ultrasonicated in *N*-methyl-2-pyrrolidone (NMP) and then redispersed in water with the aid of lipoic acid-conjugated polyethylene glycol (PEG). An MTT viability protocol revealed no cytotoxicity up to 200  $\mu\text{g mL}^{-1}$ , and further assays showed no damage to the cell membrane and no increase in ROS for this set of materials. *In vivo* biodistribution after intravenous injection into mice showed accumulation of the TMDCs mainly in the liver and spleen after 1 day, indicating that the TMDCs were most likely taken up by Kupffer cells and spleen macrophages. Despite these apparent similarities among the TMDC samples, other responses varied as a function of the metal atom such as MoS<sub>2</sub> showing the fastest metabolic rate and excretion from the mice, with significant amounts of Mo detected in the urine and feces. *In vitro* degradation of the TMDCs was further used to characterize biodistribution and metabolism. When stored in PBS, WS<sub>2</sub> showed the highest stability, due to the strong W-S covalent bond, while MoS<sub>2</sub> degraded into soluble Mo in the form of MoO<sub>4</sub><sup>2-</sup>. TiS<sub>2</sub> also oxidized, which resulted in an insoluble precipitate of TiO<sub>2</sub>. These differences in chemical reactivity also explain the *in vivo* excretion behavior where MoS<sub>2</sub> is most easily cleared from the system as it degrades to soluble MoO<sub>4</sub><sup>2-</sup>,

whereas  $\text{WS}_2$  and  $\text{TiO}_2$  persist and accumulate in organs. In a separate study, vanadium disulfide ( $\text{VS}_2$ ) nanosheets showed a similar excretion profile to  $\text{MoS}_2$ , accumulating mainly in the liver and spleen of mice, but then degrading into a soluble vanadium oxide species that was easily cleared from the body and detected in the urine and feces.<sup>173</sup>

A study by Song *et al.* found a similar dissolution and biodistribution of molybdenum oxide ( $\text{MoO}_x$ ) nanosheets, but further investigated the role of pH on the dissolution characteristics.<sup>174</sup> In this study,  $\text{MoO}_x$  nanosheets functionalized with PEG were prepared by a one-pot hydrothermal method and investigated for their capabilities as a photothermal therapeutic agent. The resulting  $\text{MoO}_x$  nanosheets, while stable in acidic pH, degrade quickly at physiological pH. This pH-dependent degradation was exploited to efficiently accumulate the  $\text{MoO}_x$  nanosheets in relatively acidic tumor cells, whereas  $\text{MoO}_x$  nanosheets elsewhere in unaffected cells were excreted quickly and efficiently to avoid long-term retention. Similar to studies on  $\text{MoS}_2$ , the  $\text{MoO}_x$  nanosheets accumulated mainly in the liver and spleen, but were eventually cleared due to dissolution into soluble molybdate anions.

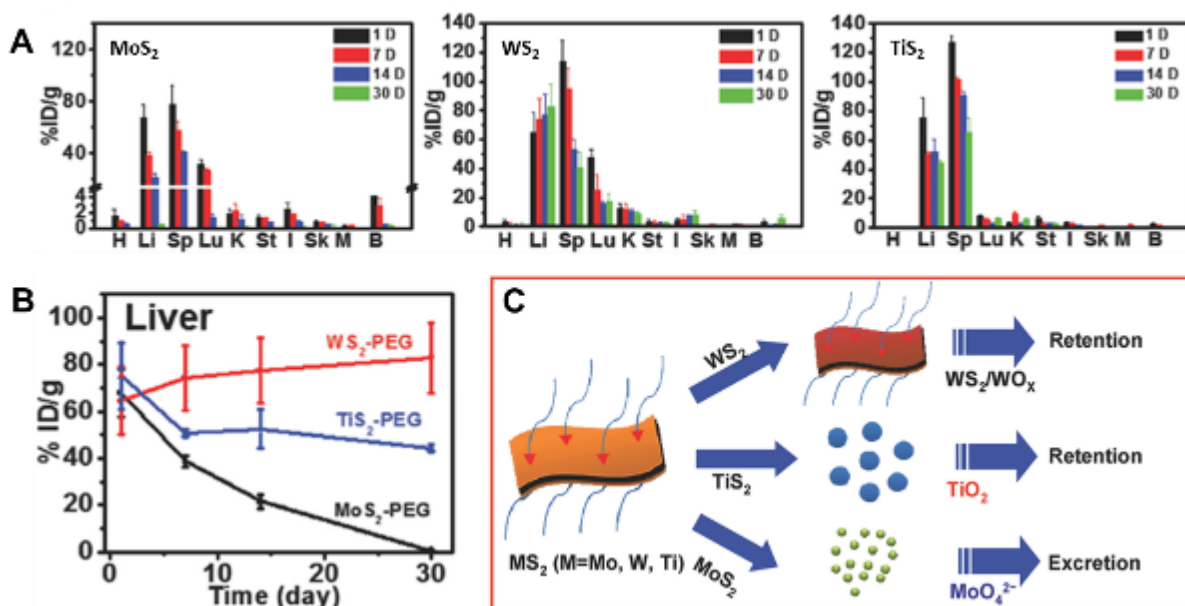


**Figure 1.8:** Biodistribution and fate of PEGylated TMDCs. (A) In vivo biodistribution of PEGylated MoS<sub>2</sub>, WS<sub>2</sub> and TiS<sub>2</sub> in major organs of mice after intravenous injection for up to 30 days. All materials accumulated mainly in the liver and spleen but after 30 days MoS<sub>2</sub> was cleared from the system while WS<sub>2</sub> and TiS<sub>2</sub> persisted. (B) Clearance of the PEGylated TMDCs from the liver over 30 days. (C) Schematic illustrating the chemical transformation the PEGylated TMDCs. MoS<sub>2</sub> dissolves and forms soluble MoO<sub>4</sub><sup>2-</sup> which is excreted. TiS<sub>2</sub> oxidizes to form TiO<sub>2</sub>, which is insoluble in aqueous solution and the aggregates are retained. WS<sub>2</sub> undergoes some oxidation but its chemical stability leads to its retention in the organs. Figure adapted from reference<sup>127</sup>.

### 1.3.8 Crystal structure

In addition to the composition, the crystal structure of the material can also play a role in dissolution and biological fate. For example, MoS<sub>2</sub> has two common polytypes: trigonal prismatic (2H) and octahedral (1T). Naturally occurring bulk MoS<sub>2</sub> has a 2H structure, which is maintained following ultrasonication-based exfoliation in solution.<sup>120</sup> However, lithiation-based chemical exfoliation of MoS<sub>2</sub> results in a phase change of the material to 1T.<sup>25</sup> The chemical dissolution pathways of these two polytypes of MoS<sub>2</sub> in biological and environmental media was investigated by Wang *et al.* (Figure 1.9).<sup>175</sup> 1T-MoS<sub>2</sub> (or ce-MoS<sub>2</sub>) was prepared by chemical exfoliation using n-butyllithium, whereas 2H-MoS<sub>2</sub> (or ue-MoS<sub>2</sub>) was prepared using ultrasonication in an aqueous solution containing sodium cholate. Rapid oxidation and degradation of the ce-MoS<sub>2</sub> was observed, while the ue-MoS<sub>2</sub> showed a significantly lower rate of degradation. This preferential degradation of ce-MoS<sub>2</sub> indicates that ce-MoS<sub>2</sub> samples will contain a mixture of soluble ions (e.g., MoO<sub>4</sub><sup>2-</sup>) and nanosheets during exposure and cellular uptake. This could impact the biological interactions and final biodistribution of the material. In the same study, chemically exfoliated MoSe<sub>2</sub> was also investigated and showed a similar oxidative dissolution to ce-MoS<sub>2</sub>. However, unlike ce-MoS<sub>2</sub>, the chalcogen product in this case will be insoluble, having different implications for its biological interactions and fate. Additionally, the bulk form of MoS<sub>2</sub> did not show significant dissolution, indicating that the dissolution of MoS<sub>2</sub> is accelerated as its thickness approaches the 2D limit.

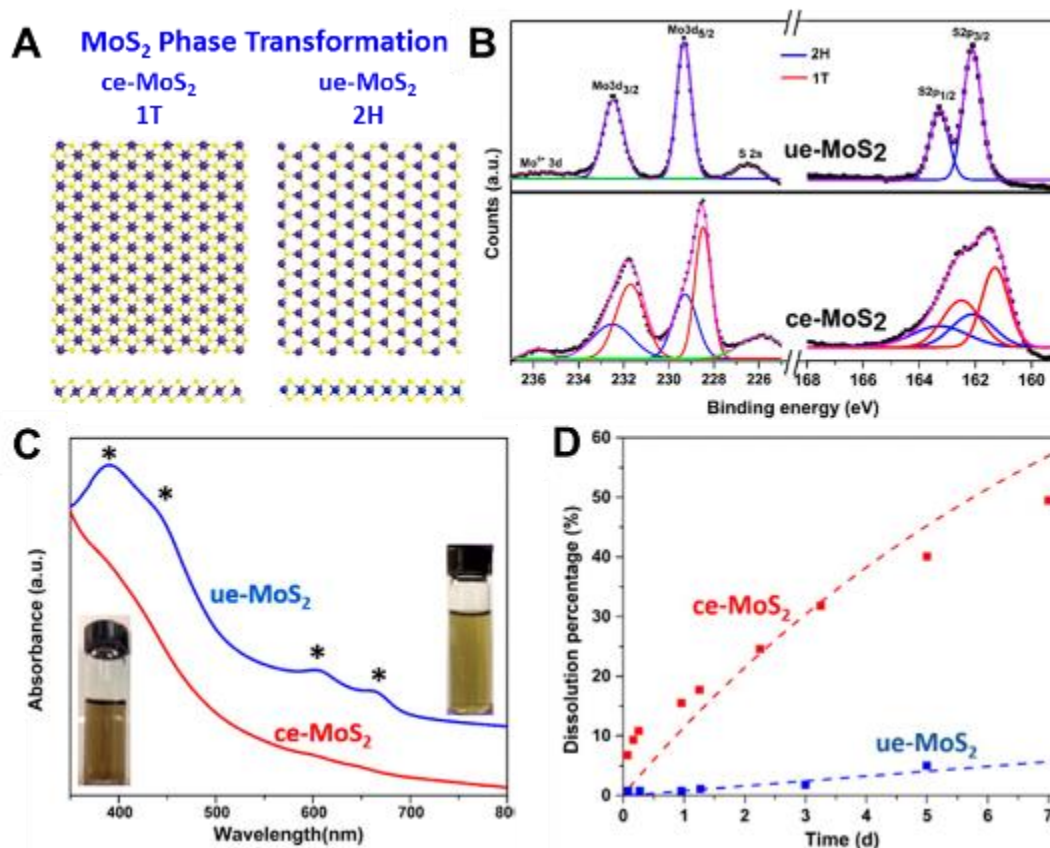


**Figure 1.9:** Stability and dissolution of 1T and 2H phases of MoS<sub>2</sub>. (A) Illustration of the 1T and 2H phases of MoS<sub>2</sub>. Chemical exfoliation of MoS<sub>2</sub> (ce-MoS<sub>2</sub>) results in a phase change to the 1T phase while ultrasonication-assisted exfoliation (ue-MoS<sub>2</sub>) maintains the 2H phase. (B) XPS spectra and fitting of the Mo 3d and S 2p peaks of ce-MoS<sub>2</sub> and ue-MoS<sub>2</sub>. ue-MoS<sub>2</sub> is in the 2H phase while ce-MoS<sub>2</sub> contains both 1T and 2H phase materials. (C) UV-Vis spectra and pictures of ue-MoS<sub>2</sub> and ce-MoS<sub>2</sub>. ue-MoS<sub>2</sub> demonstrates the exciton peaks intrinsic to the 2H phase of the material. (D) Dissolution of ce-MoS<sub>2</sub> and ue-MoS<sub>2</sub> in HEPES buffer (pH 7), showing a significantly faster rate of dissolution for the ce-MoS<sub>2</sub>. Figure adapted from reference<sup>175</sup>.

The environmental stability of 2D materials has clear implications for toxicity and fate, and thus needs to be considered when assessing hazard potential. Additionally, a greater understanding of the material properties and environmental factors that influence stability and dissolution of 2D materials provides opportunities for engineering biomedical constructs with desirable degradation properties. This concept of designing biodegradable 2D materials for biomedical applications has grown in recent years due to the ambient instability of black phosphorus in the presence of water and oxygen.<sup>87,92,176</sup> While many BP constructs have been proposed for biological imaging, drug delivery, sensing, and theranostics, limited research has been devoted to the understanding the degradation of BP and the resulting byproducts, which will be imperative to safely utilizing this 2D material in biomedical contexts.

#### **1.4 Introduction to 3D printing**

3D printing is a method that has recently been gaining significant momentum in the research community.<sup>177–183</sup> 3D printing, or additive manufacturing (AM), is a bottom-up manufacturing technique which creates a 3D object by using layer-by-layer technologies. Currently, it is used most frequently for rapid prototyping because it allows for fast and efficient iterations of different designs.<sup>184</sup> In particular, the high degree of customization in 3D printing has led to interest in the biomedical research community.<sup>185–188</sup> 3D printing offers an opportunity to fabricate customizable constructs, but the field is currently limited by material compatibility. The development of inks using materials that have interesting optical, electronic and physical properties would significantly push this field of additive manufacturing forward by allowing the fabrication of new and functional constructs.

### ***1.4.1 Additive manufacturing methods***

AM can be generally classified into two categories: energy-based or deposition-based. Energy-based methods require a source of energy, such as heat or light, to effectively solidify the material. One example would be the use of a laser to achieve photopolymerization of a material. Many of the earlier technologies were energy-based, including selective laser sintering (SLS) and stereolithography (SLA).<sup>189,190</sup> These energy-based methods are restricted to materials that can be selectively sintered, in the case of SLS, or are photo-crosslinkable, in the case of SLA. In addition, most energy-based methods require excess raw material, and are not compatible with multi-material printing.<sup>190</sup> These material limitations, in addition to the more complicated instrument design requiring an energy source, have resulted in a shift in focus to more deposition-based methods.

Deposition-based AM methods are motivated much more by the material than by the printing technology itself. The basis of deposition-based AM is quite simple; a material is extruded through a nozzle and deposited in a layer-by-layer fashion.<sup>178</sup> The earliest of the deposition-based methods is fused deposition modeling (FDM).<sup>190</sup> This method involves heating the raw material past its glass transition temperature to extrude onto a substrate, and upon cooling, solidifies to form the 3D object. Another method is direct extrusion whereby the material itself must be shear thinning and upon extrusion the material must be self-supporting, limiting material choice. A more universal deposition-based AM method is direct ink writing (DIW).<sup>178,191,192</sup> This method employs materials in liquid form which can be extruded at ambient temperatures. The liquid then solidifies after extrusion to form a self-supporting structure. This can happen through a number of different

mechanisms depending on the material. The transition can be triggered by a thermal, chemical, or optical mechanism or can simply precipitate to form a solid structure.

Although a plethora of AM technologies exist, advances in the field of 3D printing are still limited by the lack of material compatibility as well as the necessary optimization needed for each AM technology and each new material.<sup>178,193</sup> DIW offers the best path forward because it has the potential to be compatible with a wide range of materials and the instrumentation involved is relatively simple (mechanical motion in three dimensions).

#### ***1.4.2 Biological applications of 3D printing***

3D printing is especially promising in the realm of biotechnology in applications such as tissue engineering and regenerative medicine due to the customizability of the technique.<sup>185</sup> The advances in scanning imaging allow for implants that are designed specifically for individual patients. Many 3D printed mechanical implants have already been designed and successfully implemented, such as customizable implants for knee replacements,<sup>194</sup> and cranial and maxillofacial defects.<sup>195</sup> In addition, 3D printed scaffolds, generally hydrogels, have been explored for tissue engineering applications.<sup>196–200</sup> However, similar to the 3D printing field in general, printable materials are the limiting factor in driving this field forward.

The success of the AM field depends very strongly on the development of methods to 3D print functional materials. For example, Mannoor *et al.* demonstrated the ability to 3D print a bionic ear. This “ear” integrates a conducting polymer containing silver nanoparticles, printed in the shape of a coil, into a cell-seeded hydrogel matrix in the shape of human ear using AM. The result was that cartilage tissue could be grown around this coil which acted as an antenna and could receive electromagnetic signals and act as a cyborg ear.<sup>201</sup> This study integrated structural, biological and

electronic materials using AM technology and showcased the potential impact of nanoscale building blocks on the fields of 3D printing and tissue engineering.

Although most 3D printing is currently limited by material compatibility, it has the potential to create complex mechanisms and functional objects with the realization of 3D-printable functional inks. In order to create these functional structures, different materials with various physicochemical properties need to be adapted to 3D printing. Kong *et al.* demonstrated this multi-material approach by 3D printing quantum dot-based light-emitting diodes (QD-LEDs). This fabrication was a significant achievement in the field of 3D printing because it demonstrates the ability to 3D print several diverse materials into a single functional structure. The QD-LEDs represented a proof-of-concept of the versatility of 3D printing, illustrating that it can be used for a wide range of materials, such as semiconducting inorganic nanoparticles, organic polymers, and liquid metals. This result establishes that electronics can be fully fabricated in freeform using 3D printing techniques. In addition, this indicates that electronics have the potential to be directly integrated into 3D printed constructs and provide further functionality to these existing technologies<sup>202</sup>. The demonstration of 3D printed QD-LEDs was a significant step forward for the field of 3D printing. However, one of the key challenges for future work is to incorporate more classes of nanoscale functional materials as building blocks for 3D printed devices.

## **CHAPTER 2:**

### **HAZARD ASSESSMENT AND ANTIBACTERIAL APPLICATIONS OF GRAPHENE OXIDE NANOMATERIALS**

This chapter is based, in part, on the research described in the following publications:

Li, R.; Guiney, L. M.; Chang, C. H.; Mansukhani, N. D.; Ji, X.; Wang, X.; Liao, Y-P.; Jiang, W.; Sun, B.; Hersam, M. C.; Nel, A. E.; Xia, T. "The Surface Oxidation of Graphene Oxide Determines Membrane Damage, Lipid Peroxidation, and Cytotoxicity in Macrophages in a Pulmonary Toxicity Model," *ACS Nano*, 2018; 12(2): 1390-1402.

Chen, X.; Jiang, W.; Ahmed, A.; Guiney, L. M.; Wang, X.; Jiang, J.; Lu, J.; Liu, X.; Xu, I.; Chang, C. H.; Sun, B.; Ji, Y.; Hersam, M. C.; Nel, A. E.; Xia, T. "Oxidative State and Lateral Size of Graphene Oxide Determine Differential Cell Death Mechanisms and Pro-inflammatory Responses in Three Liver Cell Types," in preparation

Li, R.; Mansukhani, N. D.; Guiney, L. M.; Ji, X.; Zhao, Y.; Chang, C. H.; French, C. T.; Miller, J. F.; Hersam, M. C.; Nel, A. E.; Xia, T. "Identification and Optimization of Carbon Radicals on Hydrated Graphene Oxide for Ubiquitous Antibacterial Coatings," *ACS Nano* 2016; 10(12): 10966-10980.

**\*Contribution made by L. M. Guiney in all papers: production and characterization of nanomaterials with refined physicochemical properties.**

## 2.1 Background

Chemically modified graphene has been widely studied for various applications, such as polymer composites, energy-related materials, and catalysis.<sup>203,204</sup> Of particular interest is graphene oxide (GO), an oxygenated form of graphene decorated with abundant functional groups. GO is widely used due to its wide availability, facile synthesis, and outstanding electronic, optical, and chemical properties.<sup>4,5,205</sup> A major use for this material is in biomedical applications for drug delivery, biosensors, and tissue engineering due to its aqueous dispersibility, 2D planar structure, large surface area, and surface functionalities.<sup>206</sup> In addition, GO has broad-based antibacterial effects that require detailed structure–activity relationships (SARs) to be established.<sup>207–209</sup>

As-prepared GO can have different oxidation levels and a variety of surface functional groups such as epoxy (-COC-), hydroxyl (-OH), and carboxyl (-COOH) groups as well as carbon radicals ( $\bullet$ C) and these groups may present on the honeycombed planar structure at different densities and combinations.<sup>210,211</sup> The isolated electrons in the  $p$  orbital of the carbon are usually conjugated by  $\pi$  bonding, resulting in the formation of carbon radicals at discrete sites in the plane of the GO surface.<sup>210</sup> Although some attempts have been made to explore these physicochemical properties in terms of the toxicity and bactericidal effects of GO, the results of the importance of the oxidation level,<sup>211,212</sup> lateral flake size,<sup>213</sup> and catalytic capability<sup>214</sup> have been inconclusive and even contradictory between studies. One reason is the overall complexity of the surface functional groups, which are interlinked, so that the change in one group will also affect other groups, often in a non-predictable fashion. To overcome this challenge requires a new approach to change the surface functionalities in a more systematic fashion that will enable elucidation of the key functional group(s) that is/are responsible for GO toxicity or antibacterial activity. For instance, it

has been shown that solvothermal reduction of GO in NMP could be used to quantitatively adjust oxidation levels,<sup>13</sup> while an alkalized aqueous solvent can be used for a hydrolysis approach to open epoxy rings and thereby quantitatively adjust hydroxyl density on the GO surface.<sup>215</sup> While it is also possible that the level of carbon radicals could be modulated by the reduction and hydration processes, this aspect has not been studied for GO. These advances prompted us to hypothesize that quantitative adjustment of GO surface functionalities could be used to explore the structure-activity relationships of these functionalities, including carbon radicals, to the mammalian toxicity and antibacterial effects of GO.

Among the reported effects of GO in mammalian cells is the delineation of induction of cell death.<sup>15</sup> For instance, studies have shown that GO could induce dose-dependent cell death in normal lung fibroblasts (HLF), macrophages (THP-1 and J744A), epithelial cells (BEAS-2B), and lung cancer cells (A549).<sup>15</sup> However, the data are inconsistent and even contradictory with respect to how physicochemical properties like the lateral flake size, surface coating (surfactants), and oxidation states contribute to toxicological effects in mammalian systems.<sup>15</sup> Since GO nanosheets have also been reported to induce inflammation and fibrogenic effects in the lung,<sup>168</sup> we hypothesized that the oxidation status and surface reactivity of the material play a key role in these adverse outcomes, and that this organ system could be useful to delineate the structure-activity relationships related to deliberate variation of the surface properties. Thus, the pulmonary toxicity of GO nanomaterials both *in vitro* and *in vivo* is investigated.

To further investigate these structure-activity relationships of GO, other organ systems were also explored, including the liver. The majority of GO biomedical applications involve using GO as a drug carrier due to its large surface area, high loading efficiency, and the ability to easily tailor

the surface functional groups.<sup>216</sup> For systemic delivery of the nanocarriers, the primary target organ is the liver.<sup>217</sup> The liver, which is the largest solid organ and gland in the body, has many vital functions, such as the production of bile to remove waste and break down fats, synthesis of certain proteins for blood plasma, and regulation of the mononuclear phagocyte system.<sup>218</sup> Additionally, the liver acts as a biological filtration system that sequesters 30-99% of administered nanoparticles from the bloodstream.<sup>219</sup> The predominant cells in the liver are hepatocytes: epithelial cells which perform important roles in metabolic, endocrine, and secretory functions.<sup>220</sup> To facilitate the exchange of a wide variety of substances between the blood and hepatocytes, the hepatocytes are directly exposed to the blood by being in close contact with the liver blood sinusoids that carry blood from the edges of the lobule to the central vein. The sinusoids are lined by two cell types: macrophage cells called Kupffer cells, which phagocytose dead red blood cell debris and other particulate substances; and sinusoid lining cells, which are endothelial cells that play a prominent role in maintaining liver homeostasis and driving liver regeneration.<sup>221</sup> Previous studies have shown that GO materials translocate to the bloodstream following inhalation and ingestion, and then accumulate in organs including the liver.<sup>222-225</sup> Accumulation in the liver will increase the potential of liver toxicity. Indeed, many studies have shown that GO materials may exert various degrees of toxicity with different administration routes, including acute and chronic inflammation in the liver tissues or cell models.<sup>166,226</sup> However, the detailed mechanism of liver toxicity induced by GO, including the roles of different cell types, is still not clear.

Additionally, GO is found to have antibacterial effects on a broad spectrum of bacteria.<sup>207</sup> Although the 2D structure and surface chemistry of GO have been suggested to play a major role in the bacterial killing effects by membrane disruption or oxidative stress,<sup>209,213,214</sup> a structure-

activity relationship connecting specific surface functionalities to antibacterial effects has not been established for GO. Currently, there are two major schools of thought on the mechanism of GO-induced bactericidal effects. One is that GO induces direct physical contact with and destructive extraction of lipid molecules from the bacterial membrane as a result of contact with its sharp edges.<sup>208,209,213,214</sup> While this hypothesis is mostly based on computerized simulation, there is a paucity of experimental evidence to directly demonstrate exact details and the mechanism of cutting or piercing the bacterial surface. Thus, research is clearly needed on this front. Another mechanism that has been put forward with more supportive experimental data is catalytic damage to bacteria by the generation of reactive oxygen species and charge transfer, leading to oxidative stress.<sup>208,214,227</sup> While in this scenario, it is assumed that GO surface functional groups play a critical role in mediating the catalytic damage, the complex chemistry of the GO surface functional groups makes it difficult to determine the exact structure-activity relationships that lead to antibacterial effects.

## **2.2 Results and discussion**

### ***2.2.1 Varying the physicochemical properties of graphene oxide***

Oxidation levels can be modified through the use of reduction processes based on solvothermal or chemical methods for the production of reduced graphene oxide (rGO), which is chemically similar to graphene, albeit not identical. During reduction, the variety and evolution of oxygenated species on the GO surface can be tracked by methods such as Raman spectroscopy, X-ray photoelectron spectroscopy (XPS), and electron paramagnetic resonance (EPR).<sup>228,229</sup> It is also possible to use hydration chemistry for opening epoxy rings through hydrolysis, with the ability to

change the density of surface hydroxyl groups. This can be achieved by heating GO in an alkaline environment.

Reduction and hydration methods were used to modify the surface functional groups and to establish a GO material library to study the structure-activity relationships involved in mammalian and bacterial toxicity. Pristine GO was prepared by the Hummers' method and was used as the base material for preparing the library. The total level of oxidized groups on GO surface was reduced by solvothermal reduction in NMP, while heating in alkaline water could be used to increase the hydroxyl density through hydrolysis of the epoxy surface groups (Figure 2.1). Through control of the reaction conditions (time or temperature), it was possible to prepare a series of GO samples with quantifiable differences in oxidation state and surface functional groups. From these materials, we selected two reduced GO (rGO-1 and rGO-2) and two hydrated GO (hGO-1 and hGO-2) nanomaterials for a comparative study *vs.* pristine GO. XPS was used to determine the levels of oxidized functional groups on the GO surface. Figure 2.2 shows the C1s XPS spectra of the rGO-2, GO and hGO-2 sheets with C-C bonds at 284.4 eV, C-OH bonds at 285.9 eV, C-O-C bonds at 286.6 eV and C=O at 287.8 eV, which were also detected in other reports.<sup>230,231</sup> Simulation analysis of the XPS peaks allowed us to calculate the atomic % of carboxylic acid (-COOH), epoxy (-COC-), and hydroxyl (-OH) groups on the GO surface. This calculation showed that the NMP reduction could significantly reduce the peak intensities of the total oxygen content as well as the % of each oxidized group on the material surface. In contrast, GO hydration significantly decreased the intensity of the C-O-C peak to 5.6%, while the C-OH peak increased from 4.5% to 16.4% for hGO-2. These changes likely result from the reaction between the epoxy groups and nucleophiles in aqueous solution, leading to the generation of -OH

groups. The total oxygen levels remained stable during hydration, likely as a result of the fact that opening of the epoxy rings will not change the oxygen levels.

The isolated electrons in the  $p$  orbital of the carbon atom are usually conjugated to the GO backbone by  $\pi$  bonding, which can result in the formation of carbon radicals.<sup>210</sup> Thus, we also characterized the carbon radical ( $\bullet\text{C}$ ) density on the GO surface through an EPR method. Interestingly, this demonstrated that in addition to the changes in oxygen levels and hydroxyl groups as a result of reduction and hydration chemistry, there is a dramatic change in the density of carbon radicals. As shown in Figure 2.3, all GO samples showed a single resonance peak of  $\pi$ -conjugated  $\bullet\text{C}$  with  $g = 2.0091$ . hGO samples showed significantly higher EPR peaks than pristine GO (with hGO-2 being the highest), while rGO samples showed lower radical density than GO. rGO-2 exhibited the weakest EPR signal. These changes suggest that hydrolysis of  $-\text{COC}-$  groups is accompanied by the generation of carbon radicals ( $\bullet\text{C}$ ), which can stably exist on the planar GO surface as  $\pi$ -conjugated  $\bullet\text{C}$ .<sup>210</sup> These results demonstrate the utility of reduction and hydration chemistry to quantitatively change the surface functionalities of GO sheets.

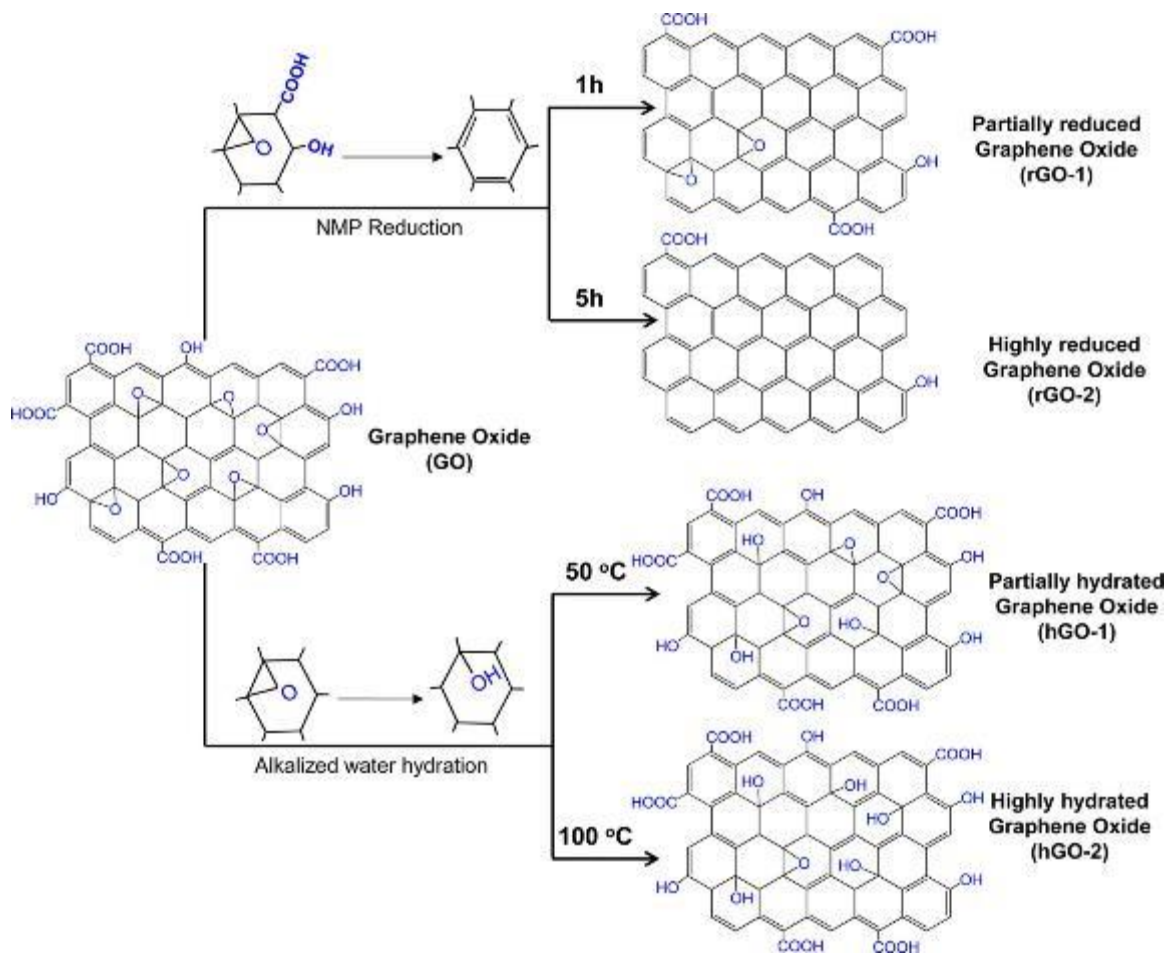


**Figure 2.1:** Schematic of GO nanomaterial library synthesis. GO was synthesized by a modified Hummers' method. rGO-1 and rGO-2 were synthesized by solvothermal reduction of GO in NMP at 150 °C for 1 or 5 h, respectively. To prepare hGO-1 and hGO-2, GO was hydrated in aqueous alkalized solution at 50 °C or 100 °C for 24 h. Reaction of the epoxy groups with nucleophiles leads to the opening of the epoxy rings and the generation of hydroxyl groups (as well as carbon radicals as shown in Figure 2.3).

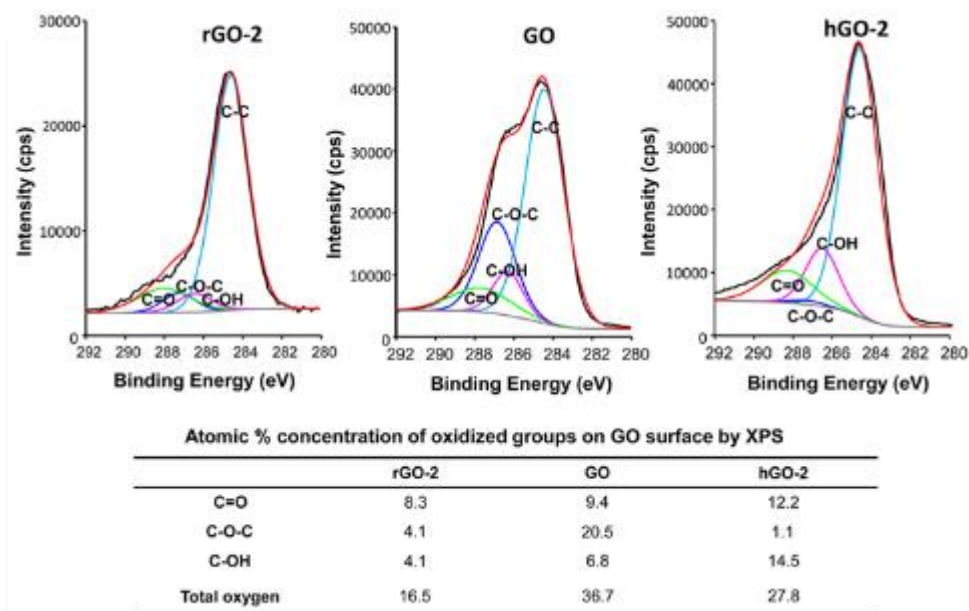


**Figure 2.2:** XPS spectra and quantification of oxygen-containing groups on the GO surface.

XPS was performed by the stepwise (50 meV) acquisition of high resolution spectra of the C 1s region.

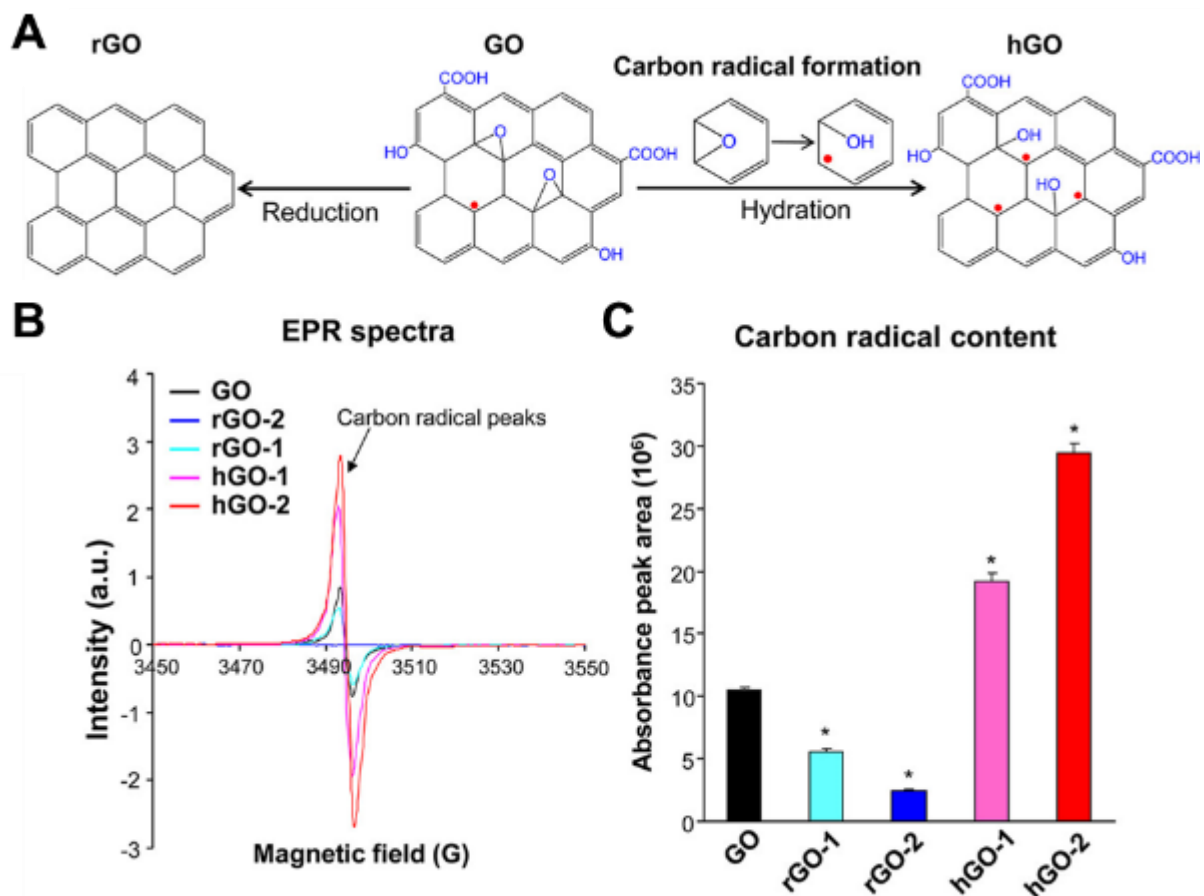


**Figure 2.3:** Detection of carbon radicals on GO surface by EPR. (A) Schematic illustrating the formation of carbon radicals on the GO surface as a result of the hydration process. (B) EPR spectra of all GO nanomaterials. (C) Carbon radical content of all GO nanomaterials as determined by EPR. EPR was used to assess the carbon radical density on GO surface by testing 5 mg of each of the dried GO samples by an X-band Bruker ELEXYS 580 spectrometer with  $g$  value of 2.0091.

We also thoroughly characterized other physicochemical properties of the GO library materials, including primary size, shape, hydrodynamic size and surface charge in aqueous solution. Raman spectra demonstrated that rGO, GO and hGO samples preserved their graphene structure, with maintenance of the signature G and D bands (Figure 2.4). This suggests that there are no major structural changes during the catalytic modification of the GO surface. Atomic force microscopy (AFM) showed that all the GO materials were irregularly shaped nanosheets with a lateral size distribution of ~50-300 nm (Figure 2.5), confirming that no significant changes in flake size or morphology occur during the reduction or hydration processes.

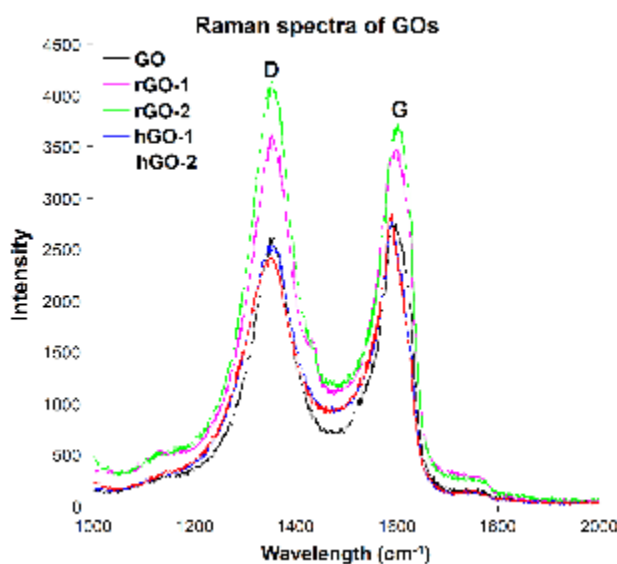


**Figure 2.4:** Raman spectroscopy of GO nanomaterials. Signature D and G bands of GO were detected using a 785 nm near-infrared diode and a 50x objective lens. Spectra are an average of 2 scans with 10 second exposure in the 500-2000 cm<sup>-1</sup> range.

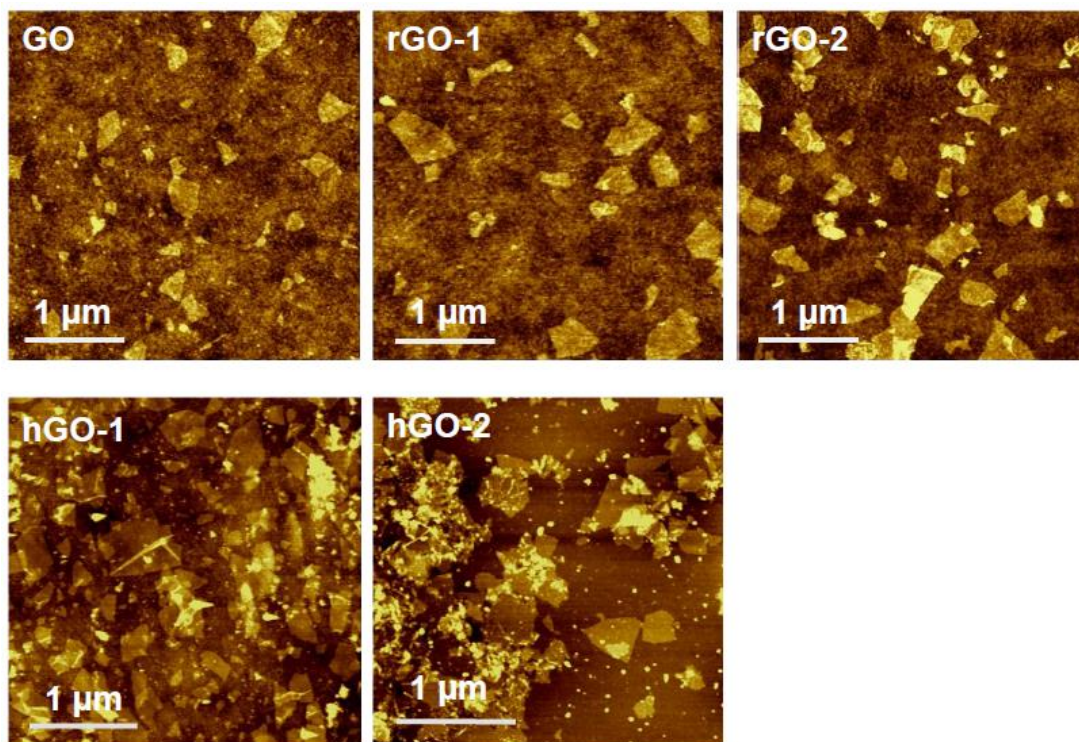


**Figure 2.5:** AFM images of GO nanomaterials. AFM images were obtained by placing a drop of the GO solution (10  $\mu\text{g/mL}$ ) on silicon wafers that were pretreated with a 2.5 mM APTES aqueous solution. After washing with water and drying with  $\text{N}_2$ , AFM images were obtained using a nAsylum Research Cypher ES AFM.

### 2.2.2 Pulmonary toxicity of graphene oxide nanomaterials

The library of pristine, rGO and hGO nanosheets described in the previous section were prepared to delineate the effects of the surface functional groups in pulmonary epithelial cells and macrophages, as well as the murine lung. The *in vitro* experimentation was followed by oropharyngeal instillation into the murine lung, focusing on mechanistic injury responses that may explain how adverse effects at the cellular level relate to an adverse outcome at the organ level. We identified the critical role of surface functional groups, including carbon radicals, in impacting GO biocompatibility in the lung. This includes adverse effects on the cellular membrane, cytotoxicity, and cellular uptake, leading to pro-inflammatory effects in the lung.

Cellular responses to GO are dependent on physical interactions with the plasma membrane, following which there is the possibility of cellular uptake and the potential to interact with subcellular structures.<sup>15</sup> Previous studies have demonstrated that the lateral GO flake size may determine cellular interactions to the extent that a large lateral size may restrict the ability to be taken up by cells.<sup>232</sup> In accordance with this view, smaller GO flakes were more readily taken up into the cell without significant interaction with the plasma membrane. The study did not take into consideration the impact of surface functionality and the oxidation status of GO. To clarify this point, THP-1 cells were incubated with pristine, reduced and hydrated GO samples for 16 h, before TEM analysis (Figure 2.6). The low electron density of GO only allows visualization of the suspended GO when vertically positioned as nanosheets horizontally aligned with the grid lack enough contrast to be visible. Despite this limitation, it was possible to demonstrate that GO or hGO-2 nanosheets insert or attach to the surface membrane of THP-1 cells (Figure 2.6). This interaction with the mammalian cell lipid bilayer is likely premised on the amphiphilic nature of

these materials, which display a hydrophobic planar structure with hydrophilic edges.<sup>233</sup> In contrast, rGO-2 has a reduced number of hydrophilic edge groups, is more hydrophobic in nature and is principally internalized by phagocytic uptake in THP-1 cells.

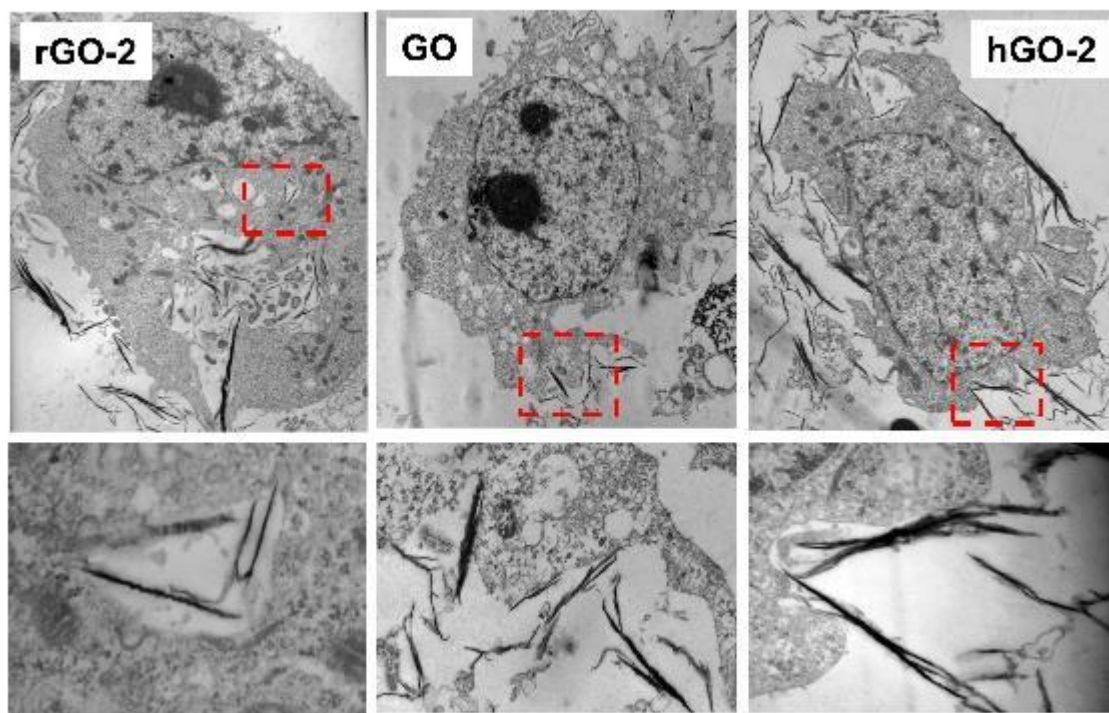


**Figure 2.6:** Visualizing the interactions of GO with THP-1 cells by TEM. After exposure to rGO-2, GO or hGO-2 for 16 h, the cells were washed, fixed and stained for TEM viewing.

We were interested to see if this accumulation of the GO and hGO at the surface membrane leads to lipid peroxidation. Lipid peroxidation was studied by using the BODIPY® 581/591 C11 reagent to visualize the green shift (~510 nm) in fluorescence activity (from red at ~590 nm) in the presence of lipid peroxides. The data was quantitatively expressed by conducting flow cytometry and calculating the percentage of cells exhibiting increased fluorescence intensity at 510 nm

(Figure 2.7). Cumene hydroperoxide (CH) was used as a positive control reagent. The relative abundance of lipid peroxidation in THP-1 was 13, 37 and 5% of cells in the population in response to pristine GO, hGO-2 and rGO-2, respectively. While pristine GO showed an increase in lipid peroxidation, hGO-2 had a pronounced effect, while the effect of rGO-2 was limited. Lipid peroxidation can lead to a failure in membrane integrity which can lead to cell death.

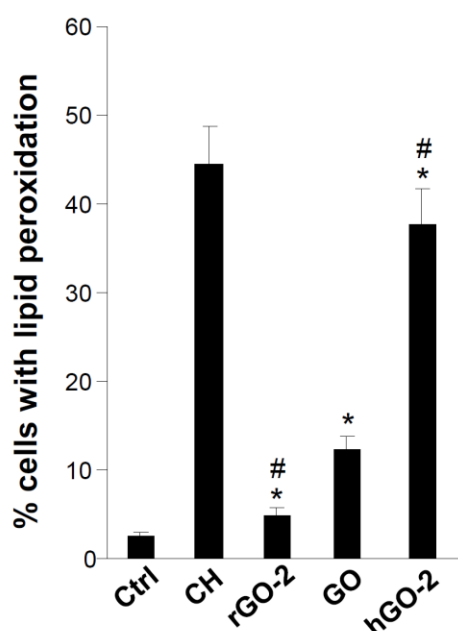


**Figure 2.7:** Assessment of the lipid peroxidation by GO nanosheets. To assess lipid peroxidation, THP-1 cells were treated with 100  $\mu\text{g/mL}$  GO for 16 h or 10  $\mu\text{M}$  cumene hydroperoxide (positive control) for 1 h. Cells were stained with 10  $\mu\text{M}$  Image-iT® Lipid Peroxidation Sensor Lipid Peroxidation Sensor according to the manufacturer's instructions. Flow cytometry analysis was carried out in a FACS Vantage SE flow cytometer.

Because lipid peroxidation can trigger cell death, we evaluated the cytotoxic potential of GO nanosheets in THP-1 and BEAS-2B cells. After 48 h exposure, most GO samples show significant cytotoxicity in THP-1 and BEAS-2B cells in the ranking order: hGO-2 > hGO-1 > GO > rGO-1 > rGO-2 (Figure 2.8). Interestingly, BEAS-2B cells were more sensitive to the cytotoxic effects of hGO than THP-1 cells. The cytotoxicity ranking of the various types of GO correlates well with the carbon radical density, yielding correlation coefficients of 0.95 in BEAS-2B cells and 0.98 in THP-1 cells (Figure 2.9). These data confirm the importance of carbon radicals on GO in promoting toxicity in mammalian cells.

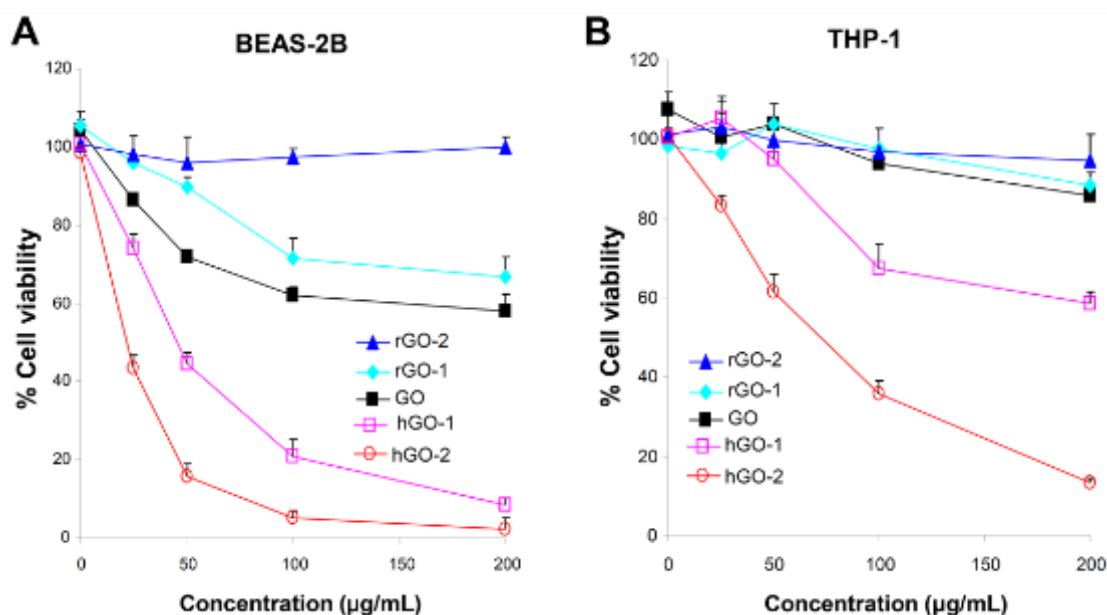


**Figure 2.8:** Cell viability assessment in (A) BEAS-2B and (B) THP-1 cells by the MTS assay.

For cellular viability assessment, a MTS assay was used to assess the impact of 0-200 µg/mL of each GO suspension in THP-1 or BEAS-2B cells over 48h.

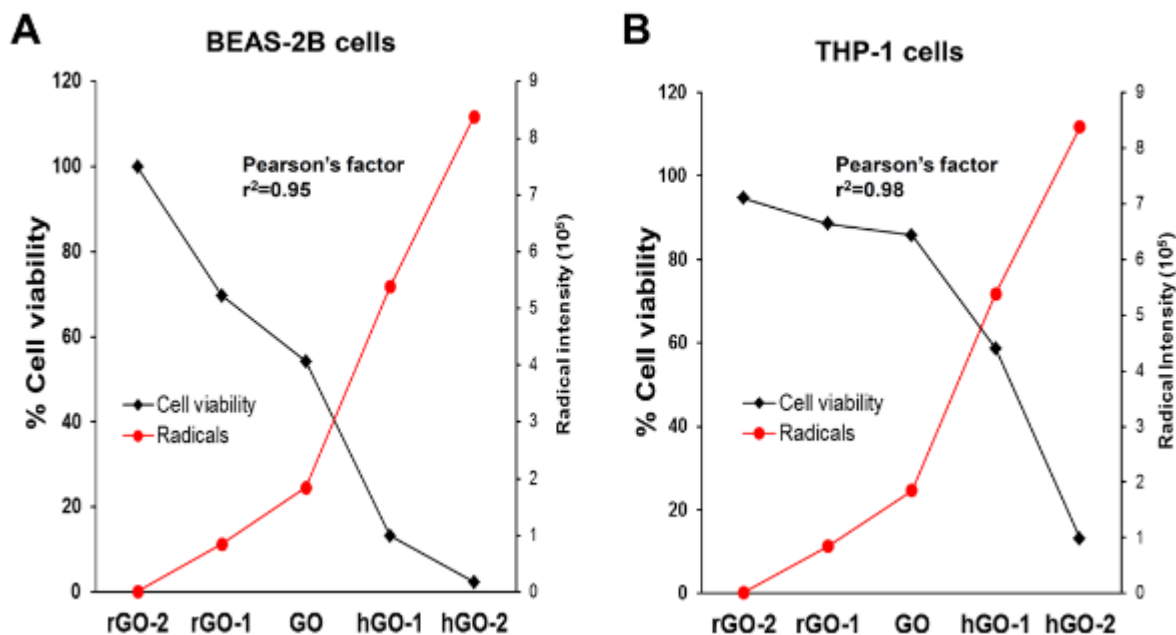


**Figure 2.9:** Calculation of the correlation coefficient of the cytotoxicity results versus carbon radical measurement for (A) BEAS-2B and (B) THP-1 cells.

To see if the *in vitro* hazard profiling is predictive of *in vivo* toxicological outcome, we used an oropharyngeal aspiration approach, according to which mice were exposed to 2 mg/kg hGO-2, GO, and rGO-2. This dose was selected based on prior dose-response studies, where a dose of 2 mg/kg for graphene and GO falls on the linear part of the dose response curve.<sup>168</sup> Following exposure for 40 h, animals were sacrificed and bronchoalveolar lavage fluid (BALF) obtained to examine the effects of GO on cells and cytokines. We demonstrated the presence of lipid peroxidation in alveolar macrophages, by using an Image-iT<sup>®</sup> lipid peroxidation kit for confocal viewing. This demonstrated that the percent of cells undergoing lipid peroxidation (green fluorescence) amounted to 69% and 55% in animals exposed to GO and hGO-2, respectively

(Figure 2.10). Quartz was used as a positive control and resulted in lipid peroxidation in 50% of the cells. In contrast, the percent lipid peroxidation was 11% in the BALF cells of rGO-2 exposed animals. These data show that the impact of the GO nanomaterials on pulmonary alveolar macrophages duplicate the results seen in tissue culture cells.

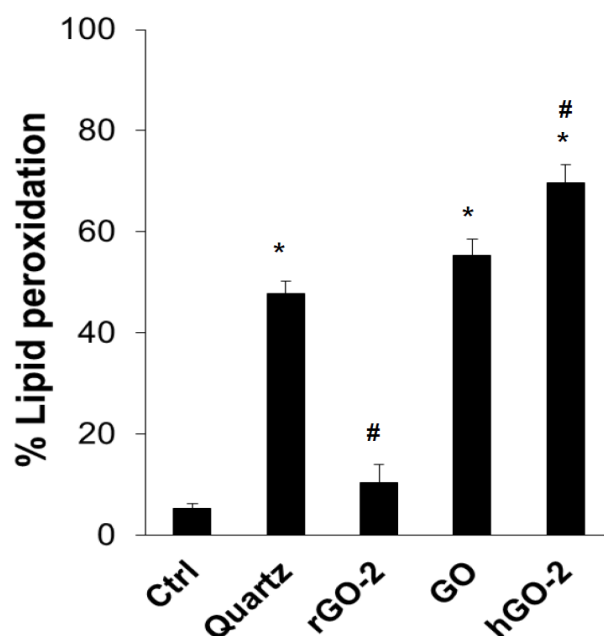


**Figure 2.10:** Lipid peroxidation of primary macrophages in the BALF after GO exposure by oropharyngeal aspiration. Animal exposure to rGO-2, GO and hGO-2 nanosheets was performed by using oropharyngeal aspiration of 2 mg/kg of each of the samples. Animals were sacrificed after 40 h to collect primary alveolar macrophages. Flow cytometry analysis was used to quantify the percentage of cells undergoing lipid peroxidation.

The level of oxidative modification of the GO surface as well as the presence of carbon radicals determine the *in vitro* and *in vivo* hazard potential, as reflected by lipid peroxidation of the surface membrane, membrane damage, and cytotoxicity in small airways of the lung. This indicates that the structure-activity relationships related to the oxidation status and expression of surface OH, COOH, COC groups and carbon radicals needs to be included with physicochemical properties, such as edge size and colloidal behavior, which depends on the relative degree of hydrophobicity of the planar surface and charged edges.<sup>234,235</sup> Collectively, these properties determine the hazard potential of GO, which can dynamically differ from material to material.<sup>14,15</sup> This complexity may also explain the apparent discrepancies in the data on GO toxicity, which could vary as a result of the experimental approach and different exposure routes.<sup>14,15,168</sup> While some *in vitro* and *in vivo* studies clearly show that GO pose no particular risks and can be of beneficial biological use,<sup>236–239</sup> others have indicated that GO nanosheets can be hazardous.<sup>168</sup>

In summary, the hazard potential in pulmonary cell types and the lung was determined through the use of a GO library with systematically varied surface functionalities. We demonstrated that pristine GO and hydrated GO samples, which express the highest •C densities, exhibit the highest pro-oxidative effects *in vitro* and *in vivo*, as evidenced by the tracking of lipid peroxidation and cell death, compared to reduced GO. The *in vitro* results were confirmed in mice exposed to GO by oropharyngeal aspiration. GO and hGO-2 induce significantly higher lipid peroxidation in macrophage membranes and death of the cells than rGO. Collectively, these data demonstrate that the *in vitro* and *in vivo* hazard potential of GO is determined, in part, by the surface functionalization, in particular, the density of •C on the material surfaces. This study is of

considerable importance in understanding the hazard potential of GO in mammalian tissues, and provides structure-activity relationships that can be used for safer designed materials.

### ***2.2.3 Toxicity of graphene oxide nanomaterials in liver cells***

The toxicity of GO in liver cells was comprehensively investigated using a similar library of materials. We prepared two sizes of GO and rGO: small GO (GO-S) and small rGO (rGO-S) had an average lateral diameter of ~110 nm; and large GO (GO-L) and large rGO (rGO-L) had an average lateral diameter of ~510 nm. This range of sizes of GO could be mainly accumulating and retained in the liver as demonstrated by a previous study in mice.<sup>240</sup> Three representative liver cell types were selected, including hepatocytes (Hepatocytes 1-6 cell line, termed as Hepa 1-6), liver sinusoid endothelial cells (LSEC) and macrophages (Kupffer 5 cell line, termed as Kup5). We examined the cytotoxicity, cellular uptake, cell membrane interaction, and lysosomal interaction of the GO materials in the three liver cell types, and the mechanisms of cell death and pro-inflammatory effects were further explored. Our results show that the GO materials induced differential cell death and pro-inflammatory responses in three cell types that could be correlated to the physicochemical properties of GO. These results are important to understand the mechanism of GO-induced liver toxicity and provide valuable information for safer design of GO materials for potential biomedical applications.

The two groups of GO and rGO with varying average lateral sizes were prepared and characterized. The morphology of GO and rGO was observed using AFM, and showed that all the materials were comprised of nanosheets with irregular shapes (Figure 2.11). The lateral sizes of the materials were evaluated according to the size distribution analysis by AFM. The average size of GO-S was similar to rGO-S, with an average lateral size of 115 nm for GO-S and 161 nm for

rGO-S. The average lateral sizes of GO-L and rGO-L were 510 nm and 501 nm, respectively. The surface functional groups of GO and rGO were examined by X-ray photoelectron spectroscopy (XPS), and characteristic peaks were observed at 284, 286, 288 and 290 eV representing C-C/C-H, C-O, C=O and O=C-O groups, respectively (Figure 2.11). The total O/C ratio of GO and rGO was consequently analyzed as well as the atomic proportion of each functional group (Table 2.1). The analysis showed that the O/C ratio of rGO samples was significantly decreased compared to their GO counterparts, indicating that the chemical reduction process reduced the oxygen content on the rGO surface. In addition, since the cellular experiments were carried out using GO or rGO suspensions in aqueous solutions, we determined the hydrodynamic size distribution of GO and rGO in Kup5, LSEC, and Hepa 1-6 cell culture medium (Table 2.2). GO-S and rGO-S showed a similar size distribution from 260 nm to 380 nm regardless of the different components of the three media, while GO-L and rGO-L showed a larger size distribution from 450 nm to 770 nm. Furthermore, all the samples exhibited a negative  $\zeta$ -potential value from -12 mV to -15 mV in all media. These characterization data demonstrate that the GO and rGO samples with small or large lateral sizes have comparable physicochemical properties except for the differences in oxygen content resulting from the reduction process.

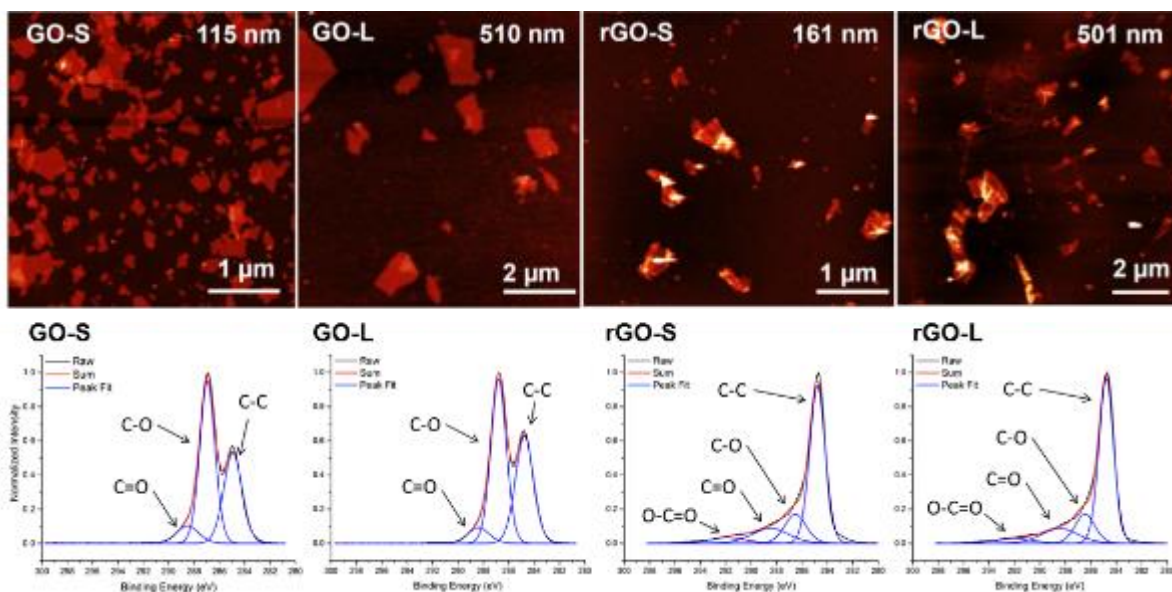


**Figure 2.11:** AFM images of GO nanomaterial library (top) and corresponding XPS spectra of the C 1s region.

**Table 2.1:** XPS summary showing relative amounts of functional groups on GO nanomaterials.

Sample	O:C	%CC/CH	%C-O	%C=O	%O-C=O
GO	1.0 : $2.2 \pm 0.1$	$48.5 \pm 2.2$	$44.7 \pm 1.8$	$6.8 \pm 1.1$	-
rGO-1h	1.0 : $2.1 \pm 0.1$	$53.8 \pm 1.1$	$39.7 \pm 0.8$	$6.5 \pm 0.4$	-
rGO-2h	1.0 : $6.7 \pm 0.1$	$63.0 \pm 2.0$	$16.7 \pm 0.9$	$14.9 \pm 1.2$	$5.4 \pm 0.1$
rGO-5h	1.0 : $7.7 \pm 0.1$	$64.1 \pm 0.7$	$15.5 \pm 0.7$	$15.2 \pm 0.7$	$5.1 \pm 0.2$

**Table 2.2:** Hydrodynamic sizes and zeta potential of GO and r-GO after suspension in cell media.

Hydrodynamic Size (nm)	GO		rGO	
	GO-S	GO-L	rGO-S	rGO-L
Kup5 Medium	258.9 ± 6.6	448.4 ± 19.2	383.7 ± 52.5	685.1 ± 37
LSEC Medium	256.4 ± 7.2	556.8 ± 6.3	352.4 ± 7.3	557.9 ± 16
Hepa-1 Medium	278.5 ± 5	448.6 ± 8.1	370 ± 12.3	765.6 ± 20.5
Zeta Potential (mV)	GO		rGO	
	GO-S	GO-L	rGO-S	rGO-L
Kup5 Medium	-13.8 ± 1.6	-11.9 ± 2.6	-12.9 ± 2.5	-12.7 ± 1
LSEC Medium	-14.7 ± 2.3	-14.4 ± 1.2	-14.9 ± 2	-14.7 ± 3.6
Hepa-1 Medium	-14.4 ± 2.6	-14.6 ± 4.2	-14.3 ± 2.9	-13.7 ± 1.6

To determine the cytotoxicity of GO and rGO in liver cells, two complementary assays with different modes of detection (absorbance and fluorescence) were employed: ATP and CellTox Green. Zinc oxide nanoparticles (ZnO,  $D=22.6 \pm 5.1$  nm) were used as a positive control in each cytotoxicity assay. As shown in Figure 2.12, the three liver cell types showed significant differences in cytotoxicity when exposed to GO and rGO for 24 h. In Kup5 cells, GO and rGO showed a dose-dependent ( $0$  to  $50 \mu\text{g mL}^{-1}$ ) increase in cell death (CellTox Green) and decrease in cell viability (ATP). The differing effects in cell viability after GO and rGO treatment was observed at the dose of  $50 \mu\text{g mL}^{-1}$ , and the ranking of toxicity was GO-L ( $91.3 \pm 4.8\%$  cell death), GO-S ( $73.2 \pm 6.5\%$  cell death), rGO-L ( $66.0 \pm 4.3\%$  cell death) and rGO-S ( $55.7 \pm 1.9\%$  cell death). This result suggests that GO induced a stronger cytotoxic response in Kup5 cells compared to that of rGO, and that larger lateral sizes, for both GO and rGO, led to a stronger cytotoxic response compared to their smaller counterparts. Compared to Kup5, GO induced minimal cytotoxicity in LSEC regardless of size. However, rGO induced high levels of cytotoxicity in LSEC, and the cytotoxicity levels are similar for rGO of different lateral sizes with rGO-S ( $72.6 \pm 5.9\%$  cell death)

and rGO-L ( $69.4 \pm 3.4\%$  cell death) at  $50 \mu\text{g mL}^{-1}$ . For Hepa 1-6 cells, negligible cell death was detected after treatment with GO or rGO at all doses, and there were no differences between two lateral sizes of GO or rGO. This indicates that both GO and rGO do not cause cell death in Hepa 1-6 cells.

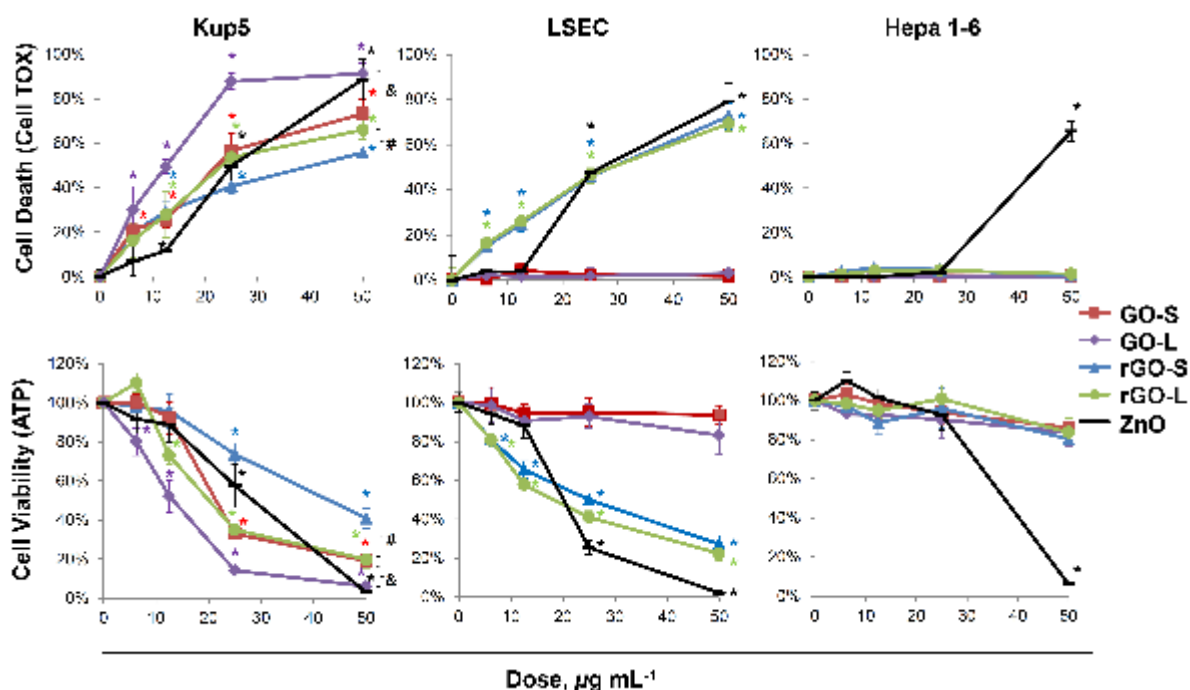


**Figure 2.12:** Cytotoxicity of GO and rGO in liver cells. CellTox Green (top) and ATP (bottom) assays were used to determine cell death and cell viability, respectively, in Kup5, LSEC and Hepa 1-6 cells. Zinc oxide nanoparticles were used as a positive control in both assays.

Using flow cytometry with fluorescein isothiocyanate (FITC)-conjugated Annexin V and propidium iodide (PI) staining, we assessed the cell death mechanisms—apoptosis or necrosis—induced by GO and rGO 16 h after dosing. Necrotic cell death is defined as the PI positive ( $\text{PI}^+$ )

population, while apoptotic cell death is defined as the Annexin V positive (Annexin V<sup>+</sup>) population. ZnO nanoparticles were used as positive controls for apoptotic cell death as previously described.<sup>241</sup> PI<sup>+</sup> population dramatically increased in Kup5 cells treated with GO-S (48.2% of PI<sup>+</sup>) and GO-L (51.0% of PI<sup>+</sup>), indicating that GO mainly induced necrosis in the Kup5 cell line (Figure 2.13A). In contrast, necrotic cell death was absent in LSEC cells after treatment with GO-S or GO-L (Figure 2.13B). However, apoptotic cell death was observed in both Kup5 and LSEC cells treated with rGO, with percentages of 45.0%, 44.0%, 32.3% and 31.4% for rGO-S and rGO-L in Kup5, and rGO-S and rGO-L in LSEC, respectively. To further examine whether rGO materials induced apoptosis in Kup5 and LSEC cells, we quantified the amount of caspase-3/-7, which is activated in apoptotic cells (Figure 2.13C, D). We found that caspase-3/-7 was significantly activated in both Kup5 (4.3-fold increase for rGO-S and 4.9-fold increase for rGO-L compared to cell control) and LSEC (2.8-fold increase for rGO-S and 2.6-fold increase for rGO-L compared to cell control), suggesting that rGO materials trigger apoptosis in both Kup5 and LSEC cells. Overall, GO triggered necrotic cell death in Kup5 cells, while rGO triggered apoptotic cell death in both Kup5 and LSEC cells.

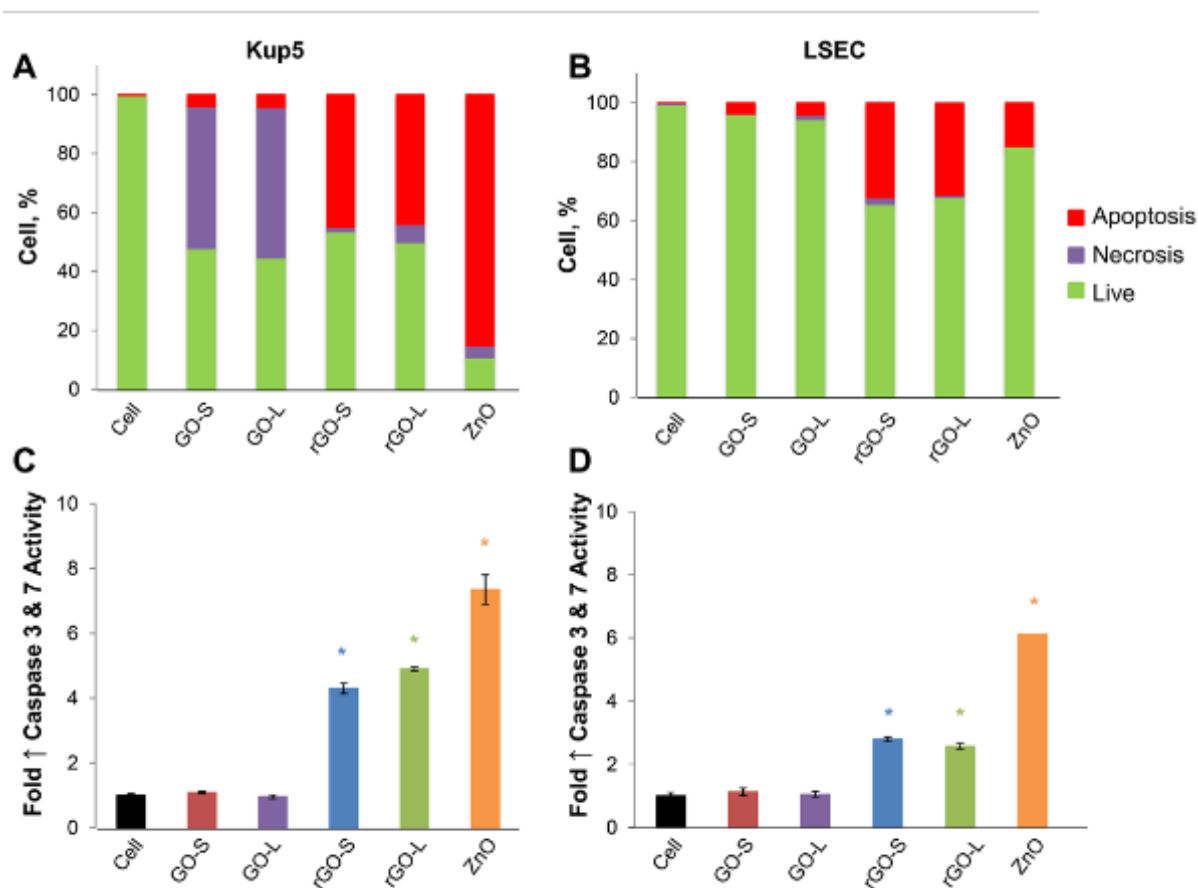


**Figure 2.13:** Cell death mechanisms of GO and rGO in liver cells. Flow cytometry with fluorescein isothiocyanate (FITC)-conjugated Annexin V and propidium iodide (PI) staining was used to determine the cell death mechanism—apoptosis or necrosis—induced by GO and rGO after 16 h in (A) Kup5 and (B) LSEC cells. Caspase-3/-7 activity in (C) Kup5 and (D) LSEC cells.

The cytotoxicity of GO materials is dependent on the GO-cell interactions, including membrane adsorption, cellular uptake, subcellular localization and processing. To demonstrate how the GO and rGO interacted with the cell membrane and the degree of cellular uptake, the GO/rGO were labeled with a fluorescent dye and the cellular uptake was quantified by side scattering flow cytometry (Figure 2.14). rGO-S and rGO-L were associated with  $19.9 \pm 1.3$  % and  $31.1 \pm 3.5$  % of Kup5 cells, respectively. However, GO-S and GO-L showed minimal cellular association in the Kup5 cell line suggesting that the cell death mechanism of GO in Kup5 cells is primarily due to the membrane attachment with GO leading to membrane damage. Meanwhile, both GO and rGO were taken up in LSEC cells, with a cell association percentage of  $25.6 \pm 0.9$  % for GO-S,  $34.6 \pm 1.5$  % for GO-L,  $27.6 \pm 3.0$  % for rGO-S, and  $28.9 \pm 0.2$  % for rGO-L, respectively. In contrast, Hepa 1-6 cells showed a lower uptake percentage, with less than  $11.5 \pm 2.1$  %, for all of the materials.

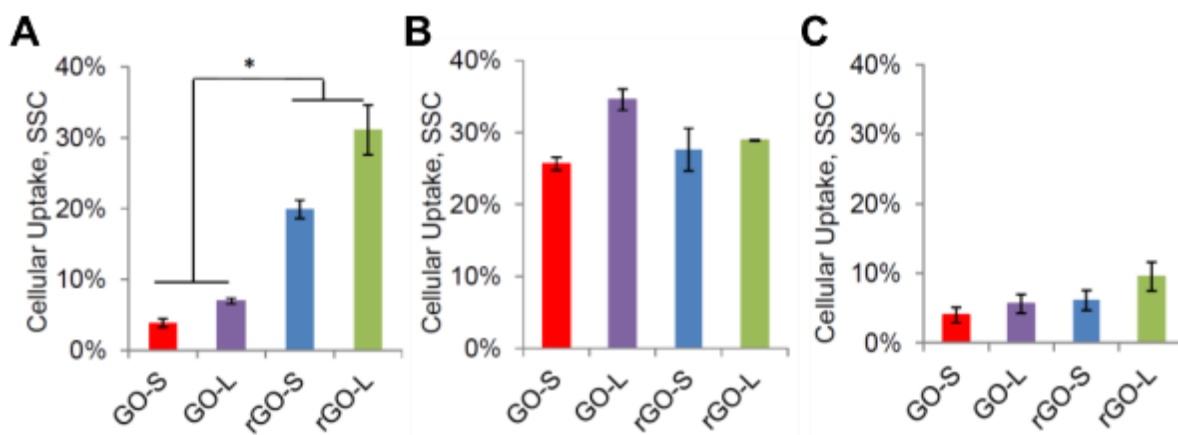


**Figure 2.14:** Cellular uptake of GO and rGO in (A) Kup5, (B) LSEC, and (C) Hepa 1-6 cells as measured by side scatter flow cytometry using GO/rGO labeled with FITC conjugated to BSA.

It is noted that GO and rGO show higher uptake by LSEC compared to Hepa 1-6. Previous studies found that LSEC expressed considerable amounts of scavenger receptor B1 (SR-B1, an essential mediator of lipid transfer and cell uptake) while in hepatocytes SR-B1 expression was low. We posit that the differential cellular uptake observed between LSEC and Hepa 1-6 may have resulted from the SR-B1 mediated selective uptake. To support this claim, a blockade of SR-B1 signaling with a selective inhibitor, block lipid transport-1 (BLT-1), was applied in LSEC and Hepa 1-6 cells before treatment with GO and rGO (Figure 2.15). The results showed that the cellular uptake of the materials by LSEC fell dramatically to less than 5%, and the effects are less for Hepa 1-6 cells due to the already very low (<10%) cellular uptake levels. This suggests that SR-B1 is the major cell surface scavenger that mediates cell uptake of GO or rGO by LSEC, which at least partially explains the differential cellular uptake capability between LSEC and Hepa 1-6.

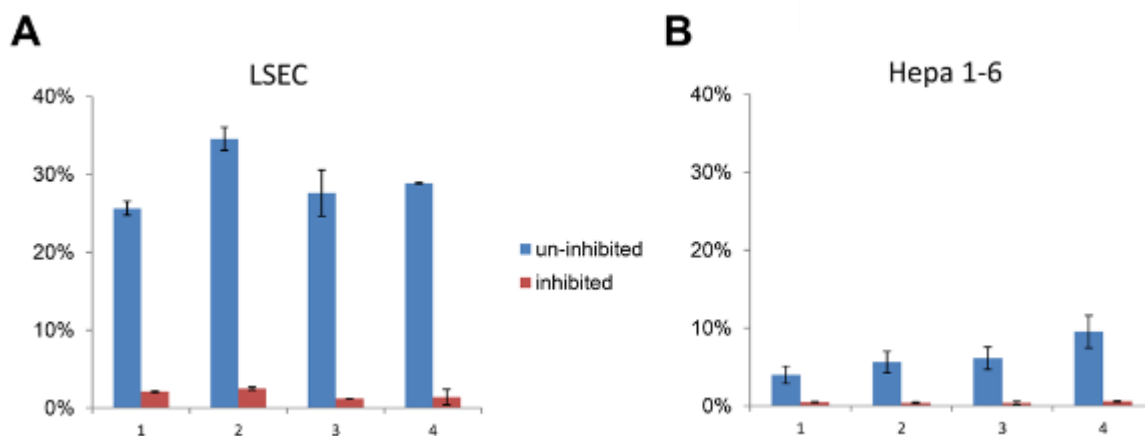


**Figure 2.15:** Effects of SR-B1 signaling on cellular uptake of GO and rGO in (A) LSEC and (B) Hepa 1-6 cells. Cellular uptake of GO and rGO was measured with and without treatment of BLT-1, a selective inhibitor for SR-B1.

Recent studies demonstrated that GO materials could induce membrane lipid peroxidation and subsequent membrane damage in cells.<sup>209,211,242</sup> Hence, we examined the cell membrane lipid peroxidation in the three liver cell types under exposure to GO and rGO using an Image-iT kit (Figure 2.16). The BODIPY 581/591 C11 reagent undergoes a shift in peak fluorescence emission from ~590 nm (wavelength, red) to ~510 nm (wavelength, green) during the peroxidation process, as demonstrated by using cumene hydroperoxide (CH) as a positive control. It is observed that GO induced prominent lipid peroxidation in GO treated cells compared to the cell control in Kup5 cells, while GO showed negligible pro-oxidative effects in LSEC and Hepa 1-6 cells. These results were quantified using flow cytometry, which showed that GO-S and GO-L induced lipid peroxidation in  $8.1 \pm 2.6 \%$  and  $16.9 \pm 3.2 \%$  of Kup5 cells, while the lipid peroxidation levels for LSEC and Hepa 1-6 cells were negligible compared to the control. The differential cell membrane lipid peroxidation among different cell types treated with GO may be associated with functional differences of liver macrophages, endothelial cells, and hepatocytes which warrants further investigation.<sup>243</sup> In contrast, rGO showed minimal effects on lipid peroxidation in Kup5, LSEC and Hepa 1-6 cells. In agreement with our previous findings, these results suggest that the lipid peroxidation induced by GO in Kup5 cells is likely due to carbon radicals on the GO surface that could generate reactive oxygen species (ROS) that react with membrane lipids.<sup>211</sup>

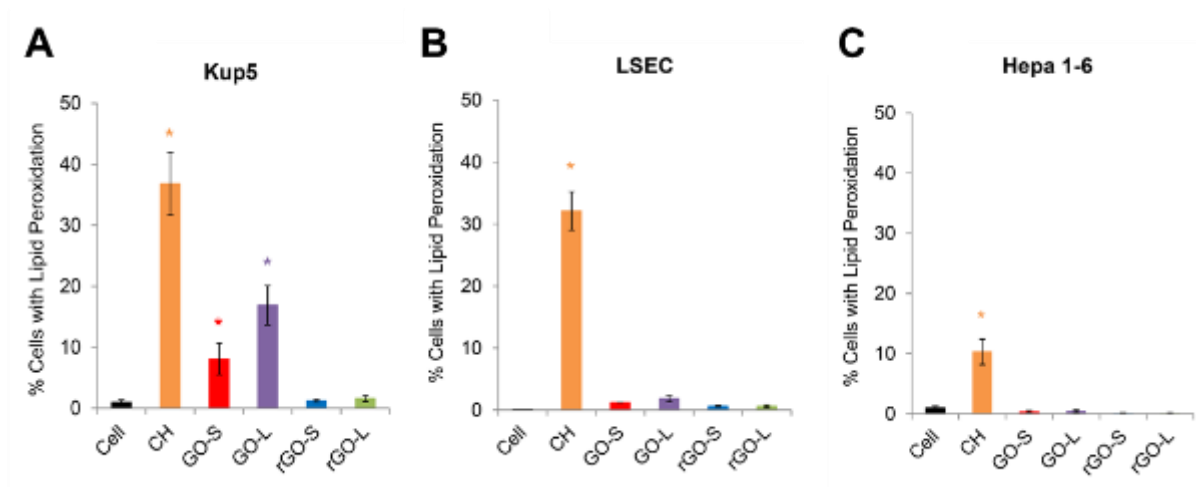


**Figure 2.16:** Lipid peroxidation induced by GO and rGO in (A) Kup5, (B) LSEC, and (C) Hepa 1-6 cells using the BODIPY 581/591 C11 reagent and an Image-iT kit.

In addition to cell death, previous studies demonstrated that GO-based materials could induce pro-inflammatory cytokine production, including IL-1 $\beta$  and TNF- $\alpha$ .<sup>168,232</sup> IL-1 $\beta$  production involves triggering of the NLRP3 inflammasome activation resulting from lysosomal damage and consequent release of cathepsin B.<sup>244</sup> Hence, we used a fluorescent cathepsin B substrate, Magic Red, to visualize the lysosomal damage and observed cathepsin B release after cellular uptake of GO or rGO in Kup5 and LSEC (Figure 2.17A). Monosodium urate (MSU) crystals were used as a positive control to demonstrate the change from a punctate Magic Red staining pattern seen in intact lysosomes in control cells to a diffuse staining pattern in the cytosol after lysosomal damage. The punctate Magic red staining was observed in Kup5 cells after treatment with GO-S or GO-L, indicating that GO did not induce lysosomal damage. The result is reasonable considering that GO was not internalized into Kup5 cells but instead interacted with the cell membrane. In contrast,

rGO-S and rGO-L resulted in extensive lysosomal damage, as demonstrated by the diffuse staining pattern of Magic Red in the cytosol. Similar to Kup5 cells, rGO induced significant lysosomal damage in LSEC, while GO had no effect on the lysosomes.

We then assessed the IL-1 $\beta$  levels in the three liver cell types after exposure to GO and rGO (Figure 2.17). Consistent with the confocal images of cathepsin B release, the assessment of IL-1 $\beta$  levels revealed that rGO induced significant increases above the non-treated control of Kup5 and LSEC, while GO showed minimal or negligible effect. Meanwhile, it was observed that rGO-L (at the dose of 50  $\mu\text{g mL}^{-1}$ ) induced higher IL-1 $\beta$  ( $470 \pm 17 \text{ pg mL}^{-1}$ ) compared to rGO-S ( $371 \pm 15 \text{ pg mL}^{-1}$ ) in Kup5. However, the effect of lateral size was not observed in IL-1 $\beta$  secretion in LSEC. This is in agreement with the cytotoxicity result that a size effect was only observed in Kup5 cells where larger sized materials induced higher cell death. We also examined the IL-1 $\beta$  secretion in Hepa-1 cells, and there are no significant IL-1 $\beta$  production after treatment with GO and rGO.

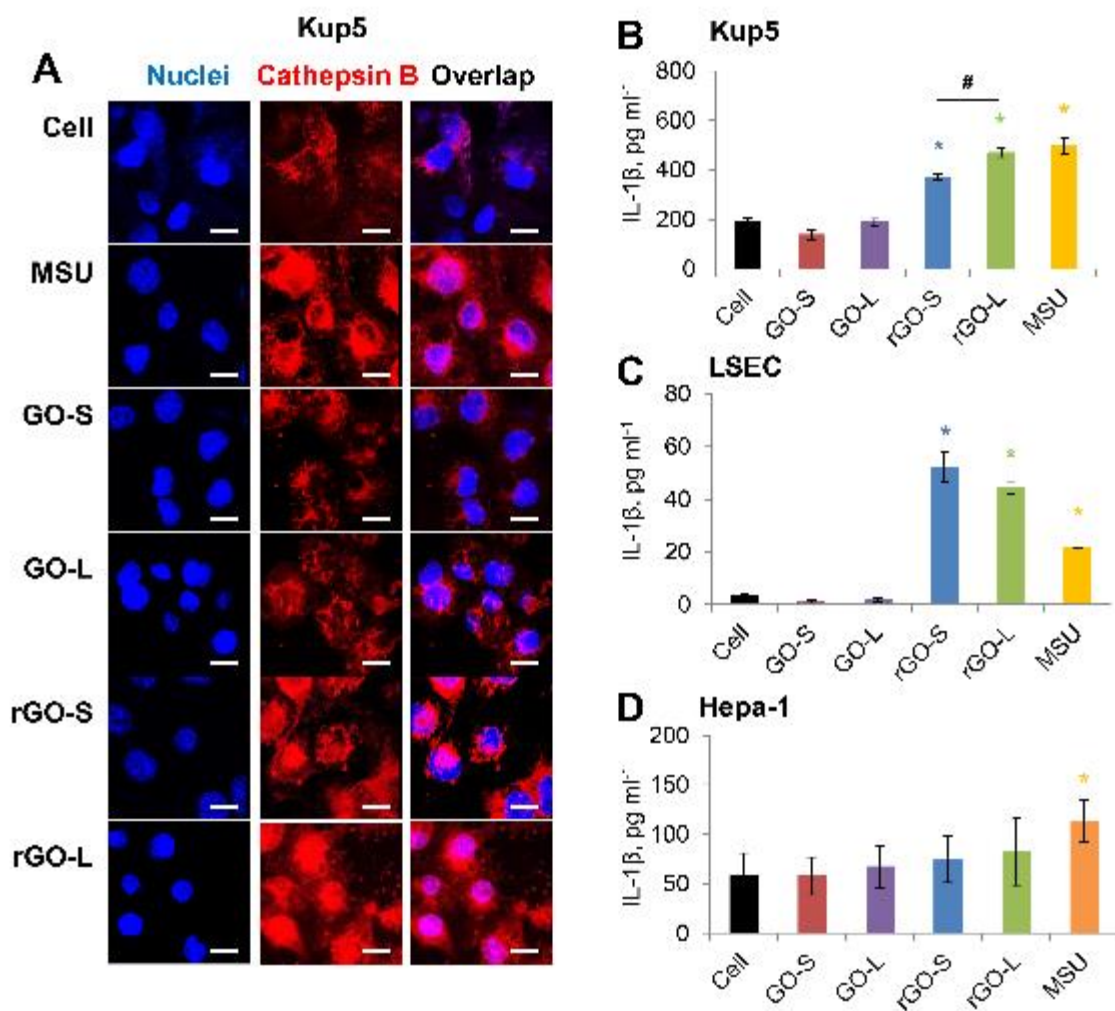


**Figure 2.17:** Pro-inflammatory effects of GO and rGO in liver cells. (A) Lysosomal damage in Kup5 cells as demonstrated by the release of Cathepsin B (red) after cellular uptake. Monosodium urate (MSU) was used as a positive control. Significant increases in the IL-1 $\beta$  production in (B) Kup5, (C) LSEC, and (D) Hepa 1-6 cells are indicative of a pro-inflammatory response.

Looking at the aggregation of GO and rGO under simulated lysosomal conditions that utilize an acidic phagolysosomal simulant fluid (PSF), which exhibits a pH of 4.5, the hydrodynamic size of rGO increased dramatically up to a few micrometers in PSF, while the hydrodynamic size of GO only slightly increased to about 1  $\mu\text{m}$ , which indicates that GO is relatively stable compared to rGO in PSF (Table 2.3). The data suggest that the poor stability of rGO in lysosomes results in large aggregates that could have more interactions with the lysosomal membrane and cause lysosomal damage given that the average size of a lysosome is from 0.1  $\mu\text{m}$  to 1.2  $\mu\text{m}$ .<sup>245</sup>

**Table 2.3:** Hydrodynamic sizes of GO and r-GO after suspension in PSF for 6h.

	GO		rGO	
	GO-S	GO-L	rGO-S	rGO-L
GO Size (nm)	829.8 $\pm$ 80.9 (0.378)	1040.9 $\pm$ 142.5 (0.322)	12215.2 $\pm$ 896.4 (0.472)	16214.4 $\pm$ 8099.8 (0.476)

In addition to IL-1 $\beta$ , we examined another major pro-inflammatory cytokine, TNF- $\alpha$ , which is frequently involved in acute inflammatory events in the liver system upon exposure to nanoparticles.<sup>246</sup> The production of TNF- $\alpha$  was dramatically increased in the Kup5 cell line after treatment with GO, with the secretion up to 860  $\pm$  90 pg mL<sup>-1</sup> for GO-S and 4000  $\pm$  510 pg mL<sup>-1</sup> for GO-L at the dose of 50  $\mu\text{g mL}^{-1}$  (Figure 2.18). However, TNF- $\alpha$  production was not induced in Kup5 cells treated with rGO, and also not detected in LSEC and Hepa 1-6 cells after treatment with GO or rGO. Previous studies have demonstrated that the TNF- $\alpha$  production in macrophages is stimulated through activation of toll-like receptors (TLR), and GO-induced macrophagic cell death occurs by activating TLR-4-dependent necrosis.<sup>247</sup> To investigate whether the GO-induced necrotic process requires interaction with TLR4, a specific TLR4 inhibitor CLI-095 was used

before treatment with GO. The induction of TNF- $\alpha$  was remarkably reduced (2.2-fold decrease for GO-S and 2.4-fold decrease for GO-L, compared to control cells) by pre-treatment with the TLR4 inhibitor. Also, it is known that nuclear factor-kappa B (NF- $\kappa$ B) is involved in the production of inflammatory cytokines (such as IL-1 and TNF- $\alpha$ ) through TLR4 receptors.<sup>248,249</sup> Thus, we blocked the NF- $\kappa$ B signaling pathway by celastrol, a quinone methide triterpenoid. The induction of TNF- $\alpha$  was largely prevented (2.6-fold decrease for GO-S and 4.4-fold decrease for GO-L, compared to control cells). Taken together, the pro-inflammatory cytokine, TNF- $\alpha$ , production was induced by GO in the Kup5 cell line through the TLR-4 and NF- $\kappa$ B pathway.

We found that GO materials showed significant differences in cytotoxic and pro-inflammatory effects among these three liver cell types. The differences in these toxicological effects are due to their distinct interactions with the cell membrane, cellular uptake, and the resulting lysosomal damage and pro-inflammatory cytokine production (Figure 2.19). In addition, the toxicological effects could be linked to oxidation states and lateral sizes of GO materials.

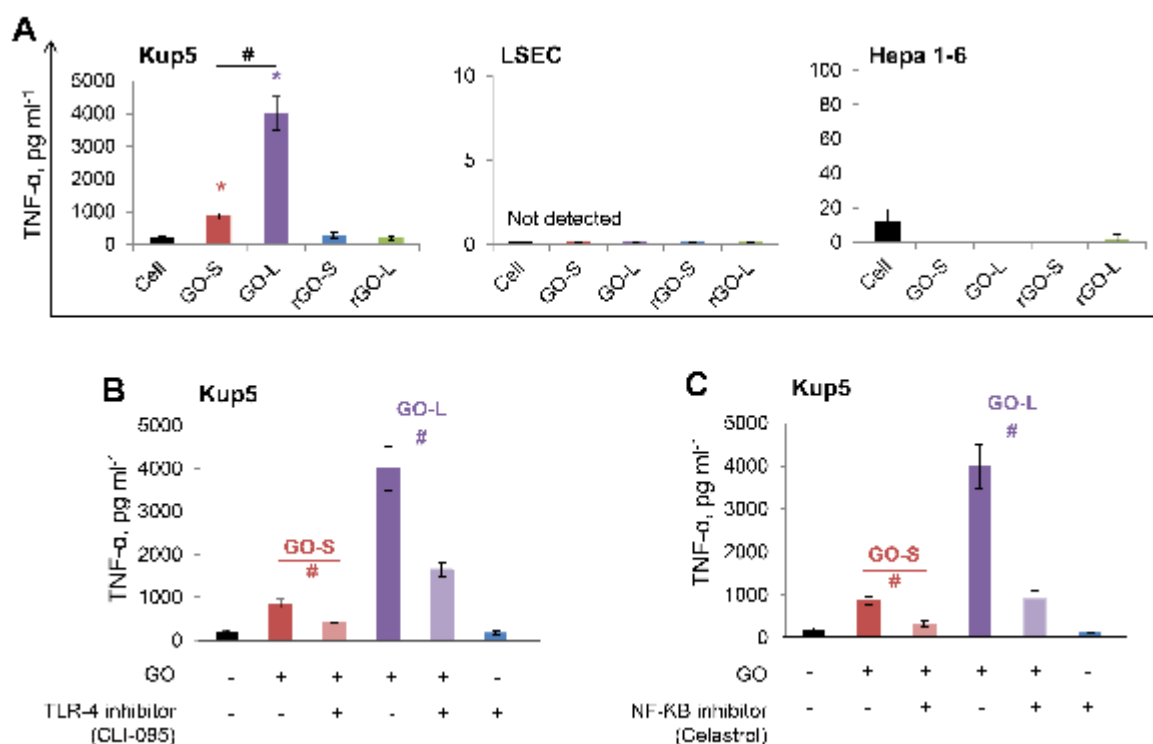


**Figure 2.18:** (A) TNF- $\alpha$  production induced by GO and rGO in Kup5, LSEC, and Hepa 1-6 cells. Treatment with the (B) TLR-4 or (C) NF- $\kappa$ B inhibitor illustrates that the pro-inflammatory response of GO is dependent on TLR-4 activation through the NF- $\kappa$ B signaling pathway in Kup5 cells.

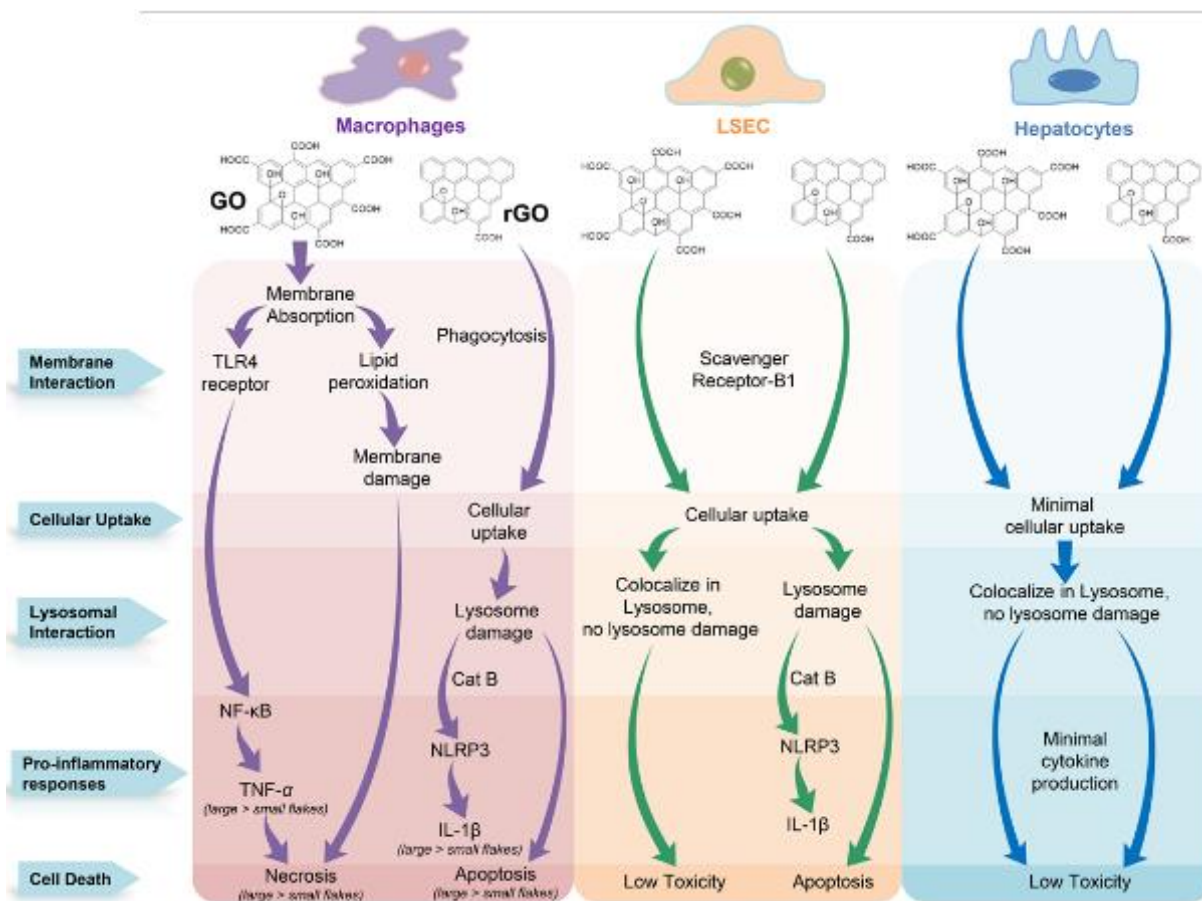


**Figure 2.19:** Cytotoxic effects of GO and rGO nanomaterials are due to distinct membrane interactions, cellular uptake, and cellular localization and processing, which are dictated by the physicochemical properties of the nanomaterials, including oxidation and lateral size.

#### 2.2.4 Antibacterial effects of graphene oxide nanomaterials

Using the reduction and hydration methods, we successfully synthesized a library of GO with different surface functionalities as described in section 2.2.1 and tested for antibacterial effects, using antibiotic resistant bacteria as a model. To study the killing effects of pristine GO in bacteria, we selected wildtype and antibiotic resistant (AR) *E. coli* (Gram negative). The AR strains were included in light of the public health relevance of drug-resistant bacteria. Moreover, no previous studies have determined if GO can overcome antibiotic resistance. The strain of *E. coli* that was chosen is resistant to 24 different types of antibiotics, including ampicillin. We found that hGO sheets have significantly enhanced antibacterial effects on the AR *E. coli* compared to pristine GO, with hGO-2 achieving almost 100% killing at 500  $\mu\text{g/mL}$  (Figure 2.20A). In contrast, rGO-1 and rGO-2 showed decreased bactericidal effects compared to the pristine material. Comparison of the antibacterial efficiency with the physicochemical characteristics of the library materials (including oxidized chemical content, carbon radical density, sheet size and zeta potential), demonstrated the strongest correlation ( $r=0.99$ ) to carbon radical density (Figure 2.20B). However, as expected, the correlation coefficient to the hydroxyl content was also strong ( $r=0.94$ ) in light of the intimate relationship with the carbon radical content. These results demonstrate the important role of carbon radicals in GO-induced antibacterial effects in antibiotic resistant bacterial strains. Similar to mammalian cells discussed in section 2.2.2, the bactericidal effects of GO are dependent on interactions with the bacterial membrane, where surface reactive groups such as the carbon radicals could lead to membrane damage and cell death as a result of lipid peroxidation (Figure 2.22).

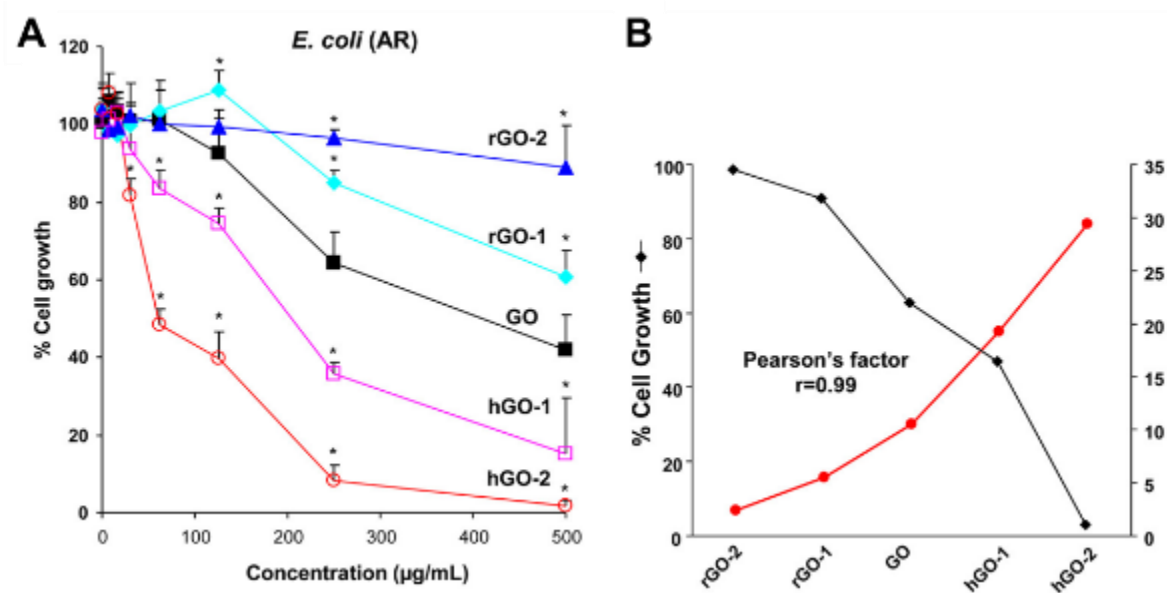


**Figure 2.20:** Bactericidal effects of the GO library. (A) Bacterial killing effects of GO samples in AR *E. coli*. To determine the bacterial killing by GO samples, AR *E. coli* were exposed to 8–500 µg/mL rGO-2, rGO-1, GO, hGO-1, and hGO-2 at 37 °C for 24 h; \* $p < 0.05$  compared to GO. (B) Calculation of the correlation coefficient between •C density and bacteria killing. Pearson’s analysis was used to evaluate the correlation between the rate of cell growth and the absorbance peak area of •C on the GO surface.

Because GO is often incorporated into composites (*e.g.*, bandages and biofilms) for antibacterial activity, we were interested to see whether immobilization of hGO to material surfaces could attain significant bactericidal effects. Our proof-of-concept testing was covalent attachment of hGO-2 to the surface of a silicone catheter, which has relevance from the perspective of bacterial contamination of indwelling clinically used devices.<sup>250</sup> A method was developed to prepare the substrate surface for coating, namely, surface amination by (3-aminopropyl)triethoxysilane (APTES), followed by conjugation of the amine groups with hGO-2 (Figure 2.21A). These coatings showed extraordinary durability and could stably attach to the catheter surface, even after sonication and washing procedures. A series of silicone catheters were coated with hGO-2 for 1, 3, 5, and 10 cycles (denoted as 1C, 3C, 5C, and 10C). Each layer of coating resulted in progressive darkening of the catheter surface. The antibacterial effects of the coated catheter surfaces were tested in a  $\beta$ -galactosidase assay, which reflects progressive bacterial membrane leakage (Figure 2.21B). We also performed a quantitative evaluation of the bactericidal effects of the 10C hGO-2-coated catheter surface. As shown in Figure 2.21C, after 1, 3, and 6 h of incubation, the bacteria settling on the catheter surface were collected, serially diluted, and introduced into LB agar plates to assess the number of colony forming units (CFU). The coated catheters showed a time-dependent reduction of CFU, compared to the uncoated catheters. A dramatic decrease of CFU could be seen after 1 h of exposure to a hGO-2 film, amounting to 2.2 log reduction after 6 h exposure. All considered, the above results show that hGO-2 coating of catheter surfaces can be used to kill AR *E. coli*.

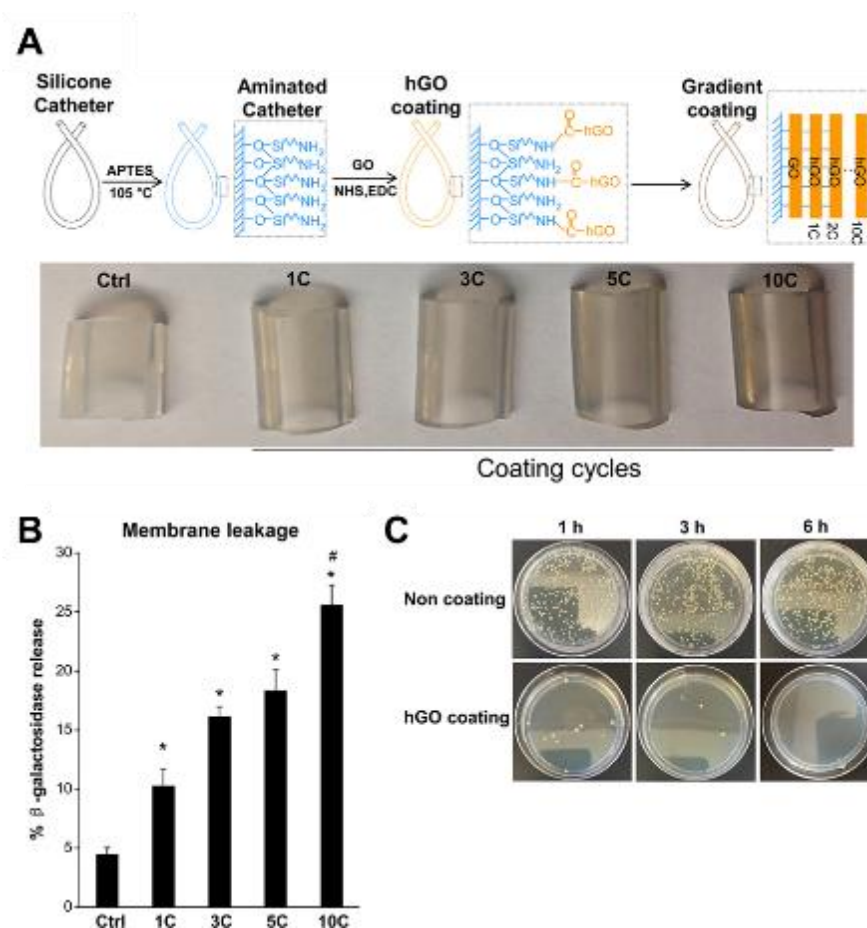


**Figure 2.21:** Inhibition of AR bacterial growth by hGO-2 covalently attached to the surface of a silicone catheter. (A) Schematic to describe hGO-2 coating of catheters as well as product images. (B)  $\beta$ -Galactosidase release from bacteria grown on coated catheters. The  $\beta$ -galactosidase release from embedded bacteria on catheter surfaces was determined after 2 h incubation. (C) Assessing the growth of bacteria retrieved from the coated catheter surfaces. After bacteria settled on catheter surfaces, they were incubated for 1, 3, and 6 h. The images show the growing colonies from uncoated or hGO-2-coated surfaces at each time point at same dilutions.

Through detailed characterization and toxicity testing, we identified the GO surface carbon radical as the functional group most proximately associated with the antibacterial activity of this material. The hydration method could be used to modulate the carbon radical density, which led to the realization that the hydrated GO (hGO) material that expressed the highest radical density levels also exerted the most effective bacteria killing effects. To explore the potential applications of hGO, we coated both glass and silicon catheter surfaces with hGO in a proof-of-principle study. Immobilized hGO provided highly effective bactericidal effects in antibiotic resistant *E. coli* commensurate with the coating density. These results demonstrate the important role of carbon radicals and potential use of GO on medical devices for combating multidrug resistant bacteria.

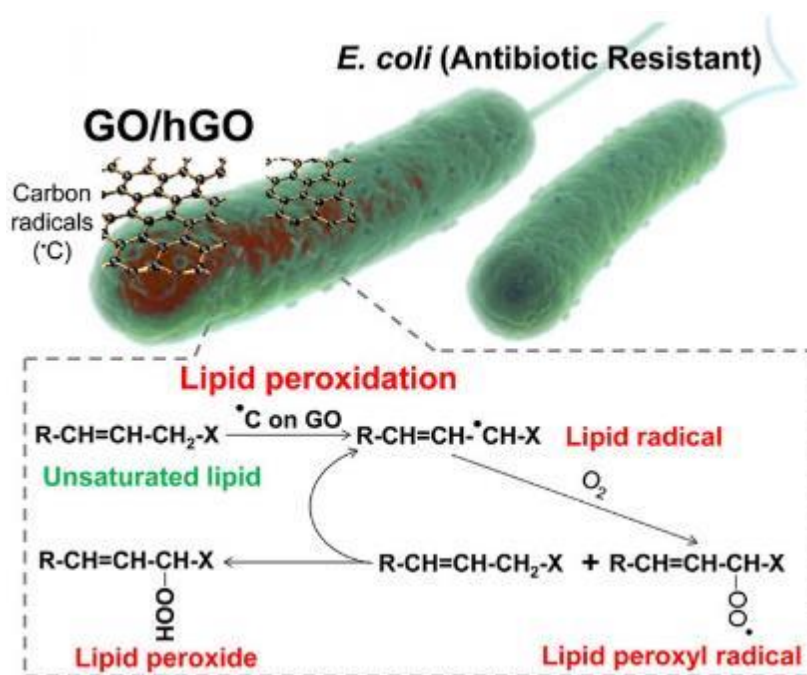


**Figure 2.22:** Schematic image to explain the bactericidal effect of GO including membrane association and lipid peroxidation.

## 2.3 Experimental methods

### 2.3.1 Preparation of graphene oxide nanomaterial library

GO was prepared using a modified Hummers' method as described previously.<sup>167</sup> Briefly, graphite flakes (Asbury Mills 3061 grade) were oxidized and then filtered and centrifuged to remove any residual contaminants. The oxidized graphite was then re-dispersed in DI water (for GO samples) or NMP (for rGO samples) and ultrasonicated using a Fisher Scientific Model 500 Sonic Dismembrator for 1 hour at 50% power (~55 Watts) in an ice bath. The GO was then centrifuged using a Beckman Coulter J26-XPI at 5000 rpm for 10 minutes (~4,620g). The top 80% of the supernatant was retained as the final GO sample and for further processing for the reduced graphene oxide samples. The concentration of the GO solution was determined by optical absorbance at 330 nm.

GO samples of varying lateral size were prepared by altering the above ultrasonication parameters. For small GO (GO-S), oxidized graphite was ultrasonicated for 2 hours at 50% power in an ice bath. For large GO (GO-L), oxidized graphite was bath sonicated for 30 minutes. Centrifugation and reduction parameters remained constant.

To prepare reduced GO (rGO) GO was dispersed in NMP (ACS reagent grade 328634, Sigma-Aldrich) by ultrasonication for 1 hour at 50% power (~55W) as described before.<sup>251</sup> The solution was heated to 150°C with constant stirring in a silicone oil bath for 1 hour (rGO-1) or 5 hours (rGO-2).

To prepare hydrated GO (hGO), 10 mL GO aqueous suspension (5 mg/mL) was diluted into 90 mL deionized water and mixed with 80 mg NaOH (0.02 M), using a sonication probe (Sonics & Materials, USA) at 32 W for 10 min. The GO mixture was transferred into a round flask and

refluxed at 50 or 100 °C in an oil bath with constant magnetic stirring for 24 h. 1 M HCl solutions were used to neutralize the reaction. The mixture was then centrifuged at 50, 000 rpm for 30 min to collect the hydrated GO pellets. After washing with deionized water three times, the hydrated GO samples were dispersed in water and stored at 4 °C.

### **2.3.2 Physicochemical characterization of GO library**

To obtain AFM images, silicon wafers were pretreated by 2.5 mM APTES aqueous solution for 30 min to functionalize the surface with a monolayer. The wafers were rinsed with DI water and dried under N<sub>2</sub>. A drop of 10 µg/mL GO solution was placed on the wafer, followed by washing twice with DI water (~5 s) and drying under N<sub>2</sub>. Next, the GO AFM sample underwent heat treatment for 30 min at 250 °C. AFM images were obtained by an Asylum Research Cypher ES AFM. Images were taken at random locations in the sample and showed little variation. All images were obtained with the same tip and scanning conditions.

Zeta-potential and hydrodynamic size measurements of the GO suspensions were performed using a ZetaSizer Nano-ZS instrument (Malvern Instruments, Worcestershire WR, UK).

X-ray photoelectron spectroscopy (AXIS Ultra DLD, Kratos, UK) has been used to investigate the chemical state and calculate the atomic concentration of oxidized groups on GO surface with monochromatic Al K $\alpha$  at 15 kV and 10 mA. For sample preparation, a suspension of GO samples was dropped on the silicon substrate and dried at room temperature. The data analysis and curve fitting were performed with the CasaXPS program (Casa Software Ltd., UK).

The EPR measurements were obtained with an X-band Bruker ELEXYS 580 spectrometer. Five milligrams of GO nanosheets were dried by vacuum and allowed to settle to the bottom of the 2 mm i.d. quartz EPR tubes prior to data collection. The field was calibrated using a standard

sample with a known  $g$ -factor (2,2-diphenyl-1-picrylhydrazyl). The EPR spectra were detected at room temperature with the frequency at 9.785845 GHz, center field at 3480 G, attenuator at 13.0 dB, and  $g$  value at 2.0029.

### 2.3.3 *Determination of pulmonary toxicity*

BEAS-2B and THP-1 cells were obtained from ATCC (Manassas, VA), and were cultured in BEGM or complete RPMI 1640 (supplemented with 10 % fetal bovine serum), respectively, at 5 % CO<sub>2</sub> and 37°C. Before exposure to GO samples, BEAS-2B cells were seeded at a density of  $1 \times 10^4$ /well in 96-well plates (Corning, NY, USA) overnight at 37°C. All the GO solutions were freshly prepared in BEGM containing 0.2% BSA or in complete RPMI 1640. These suspensions were dispersed by sonication (Sonics & Materials, USA) at 32 W for 10 s at the desired final concentration, before addition to the cells. Aliquots of  $3 \times 10^4$  THP-1 cells were seeded overnight in 0.1 mL complete RPMI medium into 96-well plates (Corning, NY, USA), receiving 1 µg/mL phorbol 12-myristate acetate (PMA), while BEAS-2B cells were suspended in BEGM media at a density at  $1 \times 10^4$  cells per well. After exposure to 0-200 µg/mL of each of the GO suspensions for 24 or 48 h, the cell culture medium was removed, followed by the addition of 120 µL culture medium containing 10% MTS stock solution for 1-2 hour at 37 °C in a humidified 5% CO<sub>2</sub> incubator.<sup>252</sup> The supernatants were transferred to a new 96-multiwell plate and centrifuged at 2000g for 10 min in NI Eppendorf 5430 to spin down the cell debris and nanoparticles. 100 µL of the supernatant was removed from each well and transferred into a new 96-well plate. The absorbance of formed formazan was read at 490 nm on a SpectraMax M5 microplate spectrophotometer.

To detect the cellular uptake of GO using TEM, after exposure to 100  $\mu\text{g/mL}$  rGO-2, GO or hGO-2 for 16 h, the cells were washed and fixed with 2% glutaraldehyde in PBS. Following post-fixation in 1% osmium tetroxide in PBS for 1 h, the cells were dehydrated in a graded series of ethanol, and then treated with propylene oxide before embedding in Epon. Approximately 50-70 nm thick sections were cut on a Reichert-Jung Ultracut E ultramicrotome and picked up on Formvar-coated copper grids. The sections were stained with uranyl acetate and Reynolds lead citrate and examined on a JEOL transmission electron microscope at 80 kV in the UCLA BRI Electron Microscopy Core, as previously reported.

THP-1 cells were treated with 100  $\mu\text{g/mL}$  of each of the GO samples for 16 h or 10  $\mu\text{M}$  cumene hydroperoxide (positive control) for 1 h. Alveolar macrophages were obtained from the BALF of mice exposed to 5 mg/kg quartz or 2 mg/kg rGO-2, GO or hGO-2 for 40 h, and allowed to adhere to the bottom of 8-well chambers. After washing, the cells were incubated with 10  $\mu\text{M}$  Image-iT® Lipid Peroxidation Sensor and Hoechst 33342 in culture media for 30 min. The stained cells were washed three times in PBS and used for flow cytometry analysis on a FACS Vantage SE flow cytometer from BD (Franklin Lakes, NJ), using FlowJo® Software (Ashland, OR) to calculate the ratio of the emission fluorescence intensities at 590 nm to 510 nm.

#### ***2.3.4 Determination of cytotoxicity in liver cells***

Mouse liver macrophagic cell line, Kupffer 5 (Kup5, obtained from RIKEN BioResource Center, Japan), was maintained in completed Dulbecco's Modified Eagle's Medium (DMEM containing 10% fetal bovine serum, 10  $\mu\text{g mL}^{-1}$  bovine insulin, 100 units  $\text{mL}^{-1}$  penicillin, 100  $\text{g mL}^{-1}$  streptomycin, and 250  $\mu\text{M}$  1-Thioglycerol) at 37 °C in a 5%  $\text{CO}_2$  humidified atmosphere and subcultured prior to confluence using TrypLE™ Express (Thermo Fisher, US). Human liver

sinusoidal endothelial cell (LSEC, obtained from ATCC, US) line was maintained in completed Eagle's Minimum Essential Medium (EMEM containing 10% fetal bovine serum, 100 units mL<sup>-1</sup> penicillin and 100 g mL<sup>-1</sup> streptomycin) at 37 °C in a 5% CO<sub>2</sub> humidified atmosphere and subcultured prior to confluence using trypsin-EDTA solution with a concentration of 0.25% (w/v) Trypsin - 0.53 mM EDTA. Mouse liver hepatocytes (Hepa 1-6, obtained from ATCC, US) were maintained in completed Dulbecco's Modified Eagle's Medium (DMEM containing 10% fetal bovine serum, 100 units/mL penicillin and 100 g/mL streptomycin) at 37 °C in a 5% CO<sub>2</sub> humidified atmosphere and subcultured prior to confluence using trypsin-EDTA solution with a concentration of 0.25% (w/v) Trypsin - 0.53 mM EDTA.

$2 \times 10^4$  cells (Kup5, LSEC and Hepa 1-6) in 100  $\mu$ L cell medium were seeded in each well of a 96-well clear bottom black plate (for cell death study) and a clear bottom white plate (for cell viability study) and allowed to attach overnight. Then, cells were pre-treated with 100  $\mu$ L of cell medium containing 0.5  $\mu$ g mL<sup>-1</sup> LPS for 4 h (No LPS treatment to Hepa 1-6 cells) before exposure to GO/rGO materials (concentration from 6.25, 12.5, 25, 50  $\mu$ g mL<sup>-1</sup>) for 24 h. Cell death was determined by the CellTox Green Cytotoxicity assay according to the manufacturer's instructions (Promega Corporation, USA). Cell viability determined by cellular ATP content was accessed by the ATPlite Firststep assay (PerkinElmer, USA) according to the manufacturer's instructions. The fluorescence intensity (cell death study) and optical absorbance (cell viability study) were read on a SpectraMax M5 microplate spectrophotometer.

To determine cell death mechanisms,  $1 \times 10^6$  cells (Kup5, LSEC and Hepa 1-6) were treated with GO or rGO with a concentration of 50  $\mu$ g mL<sup>-1</sup> and incubated for 16 h at 37 °C, 5% CO<sub>2</sub>. Cells were detached using a cell lifter (Fisher Scientific, US) and then harvested by centrifugation

at 200 g for 5 mins. Cells were stained by resuspension in the binding buffer containing  $50 \mu\text{g mL}^{-1}$  Annexin V-FITC and  $50 \mu\text{g mL}^{-1}$  PI (Abcam, Annexin V-FITC apoptosis detection kit). After 15 min incubation on ice in the dark, cells were analyzed for cell death using flow cytometry (BD FACS HTLSRII). The fluorescence from Annexin V was measured through FITC channel and PI was measured through PE channel. Forward scatter (FSC) and side scatter (SSC) properties were used to acquire a total of at least 10,000 cells and to gate out the cell debris. Apoptotic cells were identified as Annexin V positive and necrosis cells were identified as PI positive using FCS Express 6 software.

For the determination of cell membrane lipid peroxidation,  $4 \times 10^4$  Cells were seeded into an 8-well chamber and incubated overnight and then treated with  $25 \mu\text{g mL}^{-1}$  GO or rGO for 6h. Cells treated with  $20 \mu\text{M}$  cumene hydroperoxide (CH) for 1.5 h were used as a positive control. After treatment, cells were washed three times with DPBS and then stained with  $10 \mu\text{M}$  Image-iT (Fisher Scientific, US) lipid peroxidation sensor for 30 min and  $10 \mu\text{g mL}^{-1}$  Hoechst 33342 for 20 min. The chamber was directly visualized under a confocal microscope (Leica TCS SP5, Germany) in the CNSI Advanced Light Microscopy/Spectroscopy Shared Facility. The lipid peroxidation of cells was determined by the reduction and oxidation of the image iT sensor at excitation/emission wavelengths of 581/591 nm (Texas Red) and 488/510 nm (FITC), respectively. Meanwhile, the percentage of cells with lipid peroxidation was quantified by flow cytometry (BD FACS Vantage SE) with a FITC channel.

For the assessment of lysosomal damage and cathepsin B release,  $4 \times 10^4$  cells (Kup5, LSEC and Hepa 1-6) in  $200 \mu\text{L}$  of medium were seeded into each well of an 8-well chamber (Thermo Fisher Scientific, Rochester, USA) and allowed to attach overnight. Then, cells were treated with

200  $\mu\text{L}$  of complete cell medium containing 0.5  $\mu\text{g mL}^{-1}$  LPS for 4 h (No LPS treatment was performed to Hepa 1-6). After LPS treatment, 200  $\mu\text{L}$  of GO/rGO with a concentration of 50  $\mu\text{g mL}^{-1}$  were added to cells and incubated for 6 h. After fixation in 4% PFA for 30 min in PBS at 25 °C, cells were washed three times with PBS and stained with Magic Red (ImmunoChemistry Technologies, US) at 26 nM for 2 h. Following further washes with PBS, the cell nuclei were stained for 30 min with 10  $\mu\text{g mL}^{-1}$  Hoechst 33342. The chamber was visualized under a confocal microscope with 60 $\times$  objective (Leica Confocal SP5, Germany). Cells without GO or rGO treatment were used as a negative control. Cells treated with 50  $\mu\text{g mL}^{-1}$  monosodium urate (MSU) crystals were used as a positive control demonstrating that the punctate Magic Red staining seen in intact lysosomes (control cells) changes to diffuse cytosolic fluorescence after damage to the lysosome.

For assessment of pro-inflammatory cytokines,  $2 \times 10^4$  cells (Kup5, LSEC or Hepa 1-6 cells) in 100  $\mu\text{L}$  cell medium were seeded in each well of a 96-well plate and allowed to attach overnight. Then, cells were pre-treated with 100  $\mu\text{L}$  of cell medium containing 0.5  $\mu\text{g/mL}$  LPS (No LPS treatment was performed to Hepa 1-6 cells) before exposure to GO/rGO materials (concentration from 6.25, 12.5, 25, 50  $\mu\text{g mL}^{-1}$ ). After 24 h incubation, the supernatant was collected for the assessment of IL-1 $\beta$  (BD Biosciences, USA) and TNF- $\alpha$  (BD Biosciences, USA) according to manufacturer's instruction. Further, to investigate the TLR4 signaling effect on the secretion of TNF- $\alpha$ , a selective TLR4 signaling inhibitor, CLI-095 (InvivoGen, US), was used with a concentration of 1  $\mu\text{M}$  to pretreat Kup5 cells overnight prior to GO (50  $\mu\text{g mL}^{-1}$ ) exposure. After 24 h incubation, the supernatant was collected for the assessment of TNF- $\alpha$ . Similarly, to inhibit the NK- $\kappa\text{B}$  activity, a selective NK- $\kappa\text{B}$  inhibitor, Celastrol (Sigma, US), was used with a

concentration of 5  $\mu\text{M}$  to pretreat Kup5 cells overnight prior to GO (50  $\mu\text{g mL}^{-1}$ ) treatment. After 24 h incubation, the supernatant was collected for the assessment of TNF- $\alpha$ .

### 2.3.5 Determination of bactericidal effects

Five bacterial strains were used in this study: a wide-type *E. coli* strain (ATCC 25922), an AR *E. coli* strain (ATCC BAA-2452), a silver-resistant *E. coli* strain (kindly donated by Dr. Susanne S  tterlin from the Department of Clinical Microbiology, Uppsala University, Sweden), a sensitive *L. crispatus* strain (ATCC 53545), and an AR *L. crispatus* strain (ATCC 55221). Bacterial growth was carried out in LB broth (Lennox, Sigma-Aldrich, USA) for *E. coli* and Lactobacilli MRS broth for *L. crispatus* (BD, Franklin Lakes, NJ, USA), respectively. To assess the bactericidal efficiency of the GO nanosheets, a growth inhibition curve was constructed. In detail, a 5 mg/mL stock solution of each material was dispersed in LB and Lactobacilli MRS media at 500  $\mu\text{g/mL}$ . The resulting mixture was sonicated using a sonication probe (Sonics & Materials, USA) at 32 W for 15 s. The GO suspensions were diluted stepwise with the culture media to obtain a series of gradients (7.8, 15.6, 31.3, 62.5, 125, 250, and 500  $\mu\text{g/mL}$ ), of which 50  $\mu\text{L}$  of material suspension was pipetted into 384-well polystyrene microplates. Nine replicate measurements were performed for each concentration. Using a separate plate, 50  $\mu\text{L}$  of a log-phase bacterial culture (OD<sub>600</sub> between 0.5 and 0.7) was pipetted into a 384-well plate before a plastic 384 pin replicator (Genetix Molecular Devices, USA) was used to inoculate bacteria from the plate to the plate containing the serial dilution of GO samples. Sterility and blank controls (bacterial media with no inoculation) were also included for each concentration (three replicates). After 24 h incubation at 37  $^{\circ}\text{C}$ , a SpectraMax M5 microplate reader was used to monitor OD<sub>600</sub>.

Inhibition of bacterial growth on hGO-2-coated substrates was determined by a modified protocol.<sup>253</sup> AR *E. coli* in log phase were collected by centrifugation at 15 000 rpm for 5 min, washed twice with PBS, and diluted in fresh LB medium at 0.7 o.d. Bacteria were exposed to hGO-2 films by immersing the coated or catheters (5 × 5 mm) in bacteria suspensions for 5 min. The substrates were air-dried for 30 min to allow the attachment of bacteria to the surface. The bacteria settling on catheter surfaces were then placed in a Petri dish with fresh broth and incubated at 37 °C for 1, 3, or 6 h. The growing bacteria were collected to perform 10-fold serial dilutions in 1 mL of PBS. Aliquots (0.1 mL) of each dilution were introduced to LB agar plates for 24 h incubation.

## 2.4 Summary

Herein, a GO library with different surface functionalities was used to determine the hazard potential of GO nanomaterials. In the investigation of the pulmonary toxicity of GO, we demonstrated that pristine GO and hydrated GO samples, which express the highest carbon radical densities, exhibit the highest pro-oxidative effects *in vitro* and *in vivo*. This toxicity pathway involves plasma membrane adsorption, lipid peroxidation, membrane damage, and cell death. These *in vitro* toxicological pathways are also responsible for acute inflammation in the murine lung following local exposure. hGO-2, representative of a material with high carbon radical density, induced significantly more lipid peroxidation and membrane damage in tissue culture cells than rGO. These results also accurately predict similar effects in primary alveolar macrophages, along with inducing acute pro-inflammatory responses in the lung. Pristine GO showed moderate effects, while rGO-2 induced low levels of lung inflammation.

A similar study based on the same library of GO nanomaterials elucidated the critical role of oxidation state and lateral size of GO materials in the determination of cell death mechanisms and pro-inflammatory responses in three major liver cell types. We demonstrate that GO induces necrotic cell death *via* cell membrane damage and triggers the pro-inflammatory cytokine TNF- $\alpha$  secretion in Kupffer cells, while little cytotoxicity and pro-inflammatory responses were detected in LSEC and hepatocytes. rGO induces apoptotic cell death *via* cell lysosome damage after uptake by Kupffer cells and LSEC, and triggers the pro-inflammatory cytokine IL-1 $\beta$  secretion, with negligible effects in hepatocytes. These data provide valuable information concerning GO-induced liver toxicity, which again will inform efforts to realize safer design strategies for GO in biomedical applications.

Finally, we delineated the GO surface groups that are responsible for bactericidal effects and explored the potential use of GO coatings on the surface of a medical device that may be contaminated by antibiotic resistant bacteria. We found that the carbon radical density on the GO surface plays a major role in the antibacterial effects of these materials. The efficacy of bacterial killing can be enhanced by a novel hydration process of the GO surface that opens its epoxy rings to generate more  $\bullet$ C groups on the surface. A high  $\bullet$ C density enhances the oxidative potential of hGO, which allows these sheets to induce lipid peroxidation of the bacterial membrane with significantly higher bactericidal effects in antibiotic-resistant bacterial strains. In contrast, surface reduction decreases  $\bullet$ C density and antibacterial killing by GO. Coating of hGO on silicone surfaces allows effective killing of antibiotic-resistant *E. coli* and may be useful for preventing biofilm formation on catheter surfaces.

### CHAPTER 3:

## ENVIRONMENTAL STABILITY AND APPLICATIONS OF 2D NANOMATERIALS

This chapter is based, in part, on the research described in the following publications:

Chowdhury, I.; Mansukhani, N. D.; Guiney, L. M.; Hersam, M. C.; Bouchard, D. "Aggregation and Stability of Reduced Graphene Oxide: Complex Roles of Divalent Cations, pH, and Natural Organic Matter," *Environ. Sci. Technol.* 2015; 49(18): 10886-10893.

Shams, M.; Guiney, L. M.; Ramesh, M.; Hersam, M. C.; Chowdhury, I. "Influence of Functional Groups on the Degradation of Graphene Nanomaterials," *Environ. Sci. Technol.*, under review

Alam, I.; Guiney, L. M.; Hersam, M. C.; Chowdhury, I. "Antifouling Properties of Two Dimensional Molybdenum Disulfide and Graphene Oxide Nanomaterials," *Environ. Sci. Nano*, under review

Alam, I.; Guiney, L. M.; Hersam, M. C.; Chowdhury, I. "Fouling Mitigation from Graphene Oxide and Molybdenum Disulfide Polypyrrole Functionalized Surfaces," in preparation

**\*Contribution made by L. M. Guiney in all papers: production and characterization of nanomaterials with refined physicochemical properties.**

### 3.1 Background

Graphene-based nanomaterials, including pristine graphene, graphene oxide (GO) and reduced graphene oxide (rGO), have attracted significant attention due to their exceptional properties<sup>3,5,254</sup> that have potential electronic, energy, medical, and environmental applications.<sup>255–258</sup> GO is an oxidized version of graphene which can be easily produced from graphite in a scalable process. Due to the presence of oxygen-containing functional groups on the surface of GO, it is easily dispersed in water without the need for surfactants. However, the disruption of the graphene lattice renders GO electronically insulating, unlike graphene which is highly conductive. A variety of scalable processes can be used to drive the reduction of GO to rGO, restoring some of the superlative electronic properties of graphene. rGO is one of the most common forms of graphene-based nanomaterials widely used in electronics, energy storage devices and biomedical applications thanks to the scalable production of GO.<sup>5,259</sup> With many promising applications, rGO will eventually enter the environment which necessitates a thorough understanding of its environmental fate.

Most graphene-based materials in the environment will appear in reduced form. GO is considered a metastable material which undergoes spontaneous reduction.<sup>260,261</sup> UV irradiation,<sup>262</sup> natural reductants, bacteria,<sup>263</sup> and biota can accelerate this reduction in the environment. Recent studies show that GO is reduced to rGO by sunlight exposure<sup>264,265</sup> and by bacterial degradation.<sup>263</sup> Most recent work on environmental implications of graphene-based nanomaterials have primarily focused on GO<sup>266–269</sup> and found that aggregation of GO<sup>267</sup> follows colloidal theory including Derjaguin-Landau-Verwey-Overbeek (DLVO) theory<sup>270</sup> and the Schulze-Hardy rule.<sup>271</sup> Presence of natural organic matter (NOM) noticeably increases the stability of GO due to steric repulsion.

Furthermore, long-term stability studies show that GO is highly stable in natural surface water.<sup>267</sup> Studies on GO transport through porous media<sup>269,272,273</sup> found that GO is highly mobile in saturated porous media and that any retention is reversible. Increased ionic strength (IS) results in greater GO retention primarily due to straining. These observed transport trends can be explained by DLVO theory.

Photodegradation is one major pathway for the transformation of nanomaterials in the environment. To further understand the long-term environmental impact of graphene nanomaterials, it is important to study sunlight mediated photolysis and degradation. Recent studies have shown that GO can be highly stable against aggregation in a natural aquatic environment, indicating that GO will persist in water where sunlight mediated photo-transformation can occur.<sup>267,268</sup> This transformation can have an impact on the fate and transport of these materials. Transformation by sunlight photolysis is one of the primary routes by which carbonaceous materials such as fullerenes transform into CO<sub>2</sub> and other oxygen containing functionalities.<sup>265,274–276</sup> A recent study<sup>277</sup> showed that GO readily photo-reacts under simulated sunlight and photo-disproportionates to CO<sub>2</sub>-reduced materials similar to rGO as well as more fragmented low molecular-weight species. Furthermore, GO photoreactivity involves the simultaneous formation of oxidative and reductive transient species. To date, studies have investigated only the photodegradation of GO. The influence of functional groups on the degradation process of graphene nanomaterials is still unknown. These knowledge gaps have motivated this study to determine the influence of functional groups on the direct photolysis of graphene nanomaterials. We hypothesize that the degradation of the graphene flakes starts at the defect sites on the basal planes, caused by the presence of the epoxy and hydroxyl functional

groups. Thus, we anticipate that the presence, identity, and quantity of these functional groups will influence the degradation process of the materials.<sup>278,279</sup> Furthermore, we hypothesize that rGO will be more resistant to degradation due to the presence of fewer functional groups and increased hydrophobicity.

Since most graphene-based nanomaterials in the environment are expected to be in reduced form, understanding fate and transport of rGO is essential. Through the creation of a highly characterized GO nanomaterial library, we systematically investigated the role of surface oxidation state on the fate of GO and long-term stability of rGO in natural and engineered aquatic environments. pH, ion valence and NOM were determined to play significantly complex roles with GO and rGO species. Furthermore, the photodegradation of GO nanomaterials was investigated as a function of surface oxidation. While GO degrades rapidly upon sunlight irradiation, rGO degrades at a significantly slower rate as a result of both the level of oxygen-containing functional groups and the dispersion stability of the nanomaterials. The transportation and transformation of nanomaterials are key factors to consider when determining their environmental risk.<sup>280</sup> This work provides important insight into the role of functional groups in the stability and degradation of graphene nanomaterials, and thus contributes to the design of sustainable applications of these materials.

Based on the interactions of GO with foulants (e.g., NOM and *E. coli*) in aquatic environments observed in our investigation of their environmental stability, the use of 2D nanomaterials—specifically GO and molybdenum disulfide (MoS<sub>2</sub>)—in water membrane technologies was explored. Membrane-based water treatment processes have become the prominent choice for producing potable water due to their potential to solve the global fresh water challenge.<sup>281</sup>

Modification of membrane surfaces for improved permeability, salt rejection, and recovery is one of the research priorities in this field. However, the advancement of membrane technology is severely hampered by the long-standing problem of fouling, which is caused by the accumulation of foreign substances on membrane surfaces or inside the membrane pores.<sup>282,283</sup> Fouling has been found to deteriorate membrane performance causing low water permeability, poor product water quality, high energy consumption, and short membrane life. Biofouling, colloidal fouling, organic fouling, and scaling remain the most significant problems for efficient application of nanofiltration and reverse osmosis.<sup>284,285</sup> Recently, many synthetic polymers such as polysulfone (PSF) and polyethersulfone (PES) have been used to prepare membrane surfaces due to their desirable thermal and mechanical properties, and chemical stability.<sup>286</sup> Although these modified membranes show slightly improved antifouling properties, they still suffer from low water permeability and favorable electrostatic interactions between the membrane surface and diverse foulants.<sup>287</sup> Thus, the concept of making composite membranes with hybrid materials such as mesoporous silica, TiO<sub>2</sub>, ZnO, and oxidized multi-walled carbon nanotubes (CNTs) have been explored for better efficiency during water filtration, but improvements thus far have been minimal due to the additives that are required.<sup>288</sup>

Graphene-family nanomaterials, such as graphene oxide (GO), demonstrate both antibacterial and anti-corrosive properties, which can be exploited in membrane coatings.<sup>235</sup> Several studies have demonstrated the strong antimicrobial properties of GO against a wide variety of microorganisms including gram-positive and gram-negative bacterial pathogens, phyto-pathogens, and biofilm-forming microorganisms.<sup>207,212,289–291</sup> Additionally, GO is hydrophilic which could result in higher water permeation, making the membrane less susceptible to fouling during

filtration.<sup>288,292,293</sup> In addition to GO, molybdenum disulfide ( $\text{MoS}_2$ ) is explored as a candidate for antifouling surfaces due to its analogous structure and size when prepared using a lithiation exfoliation process. Unlike GO,  $\text{MoS}_2$  has a very smooth surface without reactive oxygen-containing functional groups and thus could provide an unfavorable surface for foulant attachment. Despite significant research that has focused on  $\text{MoS}_2$  as a material for water filtration applications, its use as an antifouling material has not been extensively explored. In order to effectively integrate  $\text{MoS}_2$  into filtration membranes, it is important to understand both the antibacterial properties as well as the antifouling mechanisms.

Furthermore, removal of foulants increases cost and produces additional waste as a result of chemical cleaning.<sup>294</sup> Chemical cleaning efficiency depends on a wide range of parameters such as ionic strength and pH of the cleaning solutions, pressure, temperature, and cleaning duration.<sup>295</sup> Therefore, modification of the commercially available membranes to prevent initial fouling is a new field of research. Previously, voltage application was successfully used to delay the attachment of bacteria and remove the biofilm effectively.<sup>296–298</sup> However, in water treatment plants there are also many organic foulants present along with bacteria. These foulants, collectively called extracellular polymeric substances (EPS), are found in metabolic products of bacteria and are difficult to remove from membrane surfaces.<sup>299,300</sup> Thus, the attachment and release of model foulants on GO and  $\text{MoS}_2$  functionalized surfaces was also investigated as a function of applied voltage.

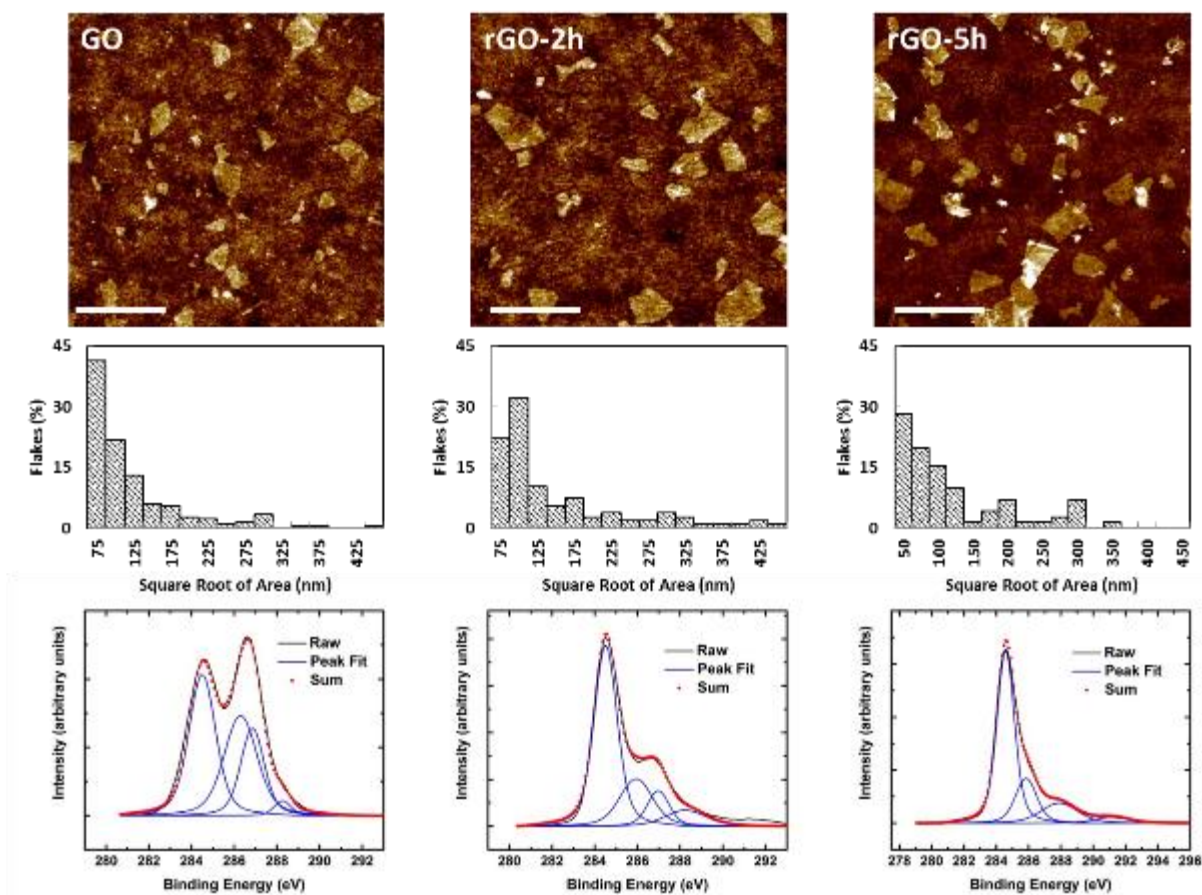
## 3.2 Results and discussion

### 3.2.1 Aqueous stability of graphene oxide nanomaterials

In this study, GO and three differently-reduced GO—partially reduced GO (rGO-1h), intermediate reduced GO (rGO-2h), and fully reduced GO (rGO-5h)—were used. GO was synthesized using a modified Hummers method described previously.<sup>167,267</sup> In this study, rGO was reduced by a solvothermal process. Chemically reduced GO, rather than rGO reduced via environmental processes, was used to obtain similarly sized rGO sheets with varying oxidation states so that the fundamental role of surface oxidations on the fate of rGO could be investigated. The reduction was achieved by heating a purified GO suspension in NMP to 150°C with constant stirring in a silicone oil bath. The heat reflux was performed for 1, 2, or 5 hours to achieve varying levels of reduction. After solvothermal reduction, the rGO was separated from the NMP using vacuum filtration with 0.1µm alumina filters (Millipore), rinsed heavily with DI water, and re-dispersed in DI water at an approximate concentration of 1 mg/mL. Concentrations of GO and rGO were determined by measuring mass following vacuum filtration. For AFM and FTIR characterization, the original dispersions in NMP were analyzed.

AFM images (Figure 3.1) show that average vertical and lateral size of the flakes remained similar from GO to rGO-5h, indicating the reduction process did not significantly change physical dimensions of the graphene flakes. XPS and FTIR were utilized to determine surface functionalities of the GO nanomaterials. XPS results confirm the reduction of oxygen-containing functional groups as the GO was reduced to rGO-5h (Figure 3.1). The relative amounts of functional groups on GO and rGO, as determined from XPS spectra, is summarized in Table 3.1. Progressing from unreduced GO to rGO-5h, the relative presence of carbon increases from 40%

to 64% while the presence of various functional groups correspondingly decreases. We note that the percent of carboxyl functional groups increases as the reduction process proceeds due to the higher thermal stability of carboxyl functional groups relative to carbonyl and epoxy functional groups. The overall oxygen-to-carbon ratio also decreases as GO is reduced. These results are qualitatively corroborated by FTIR (Figure 3.2).

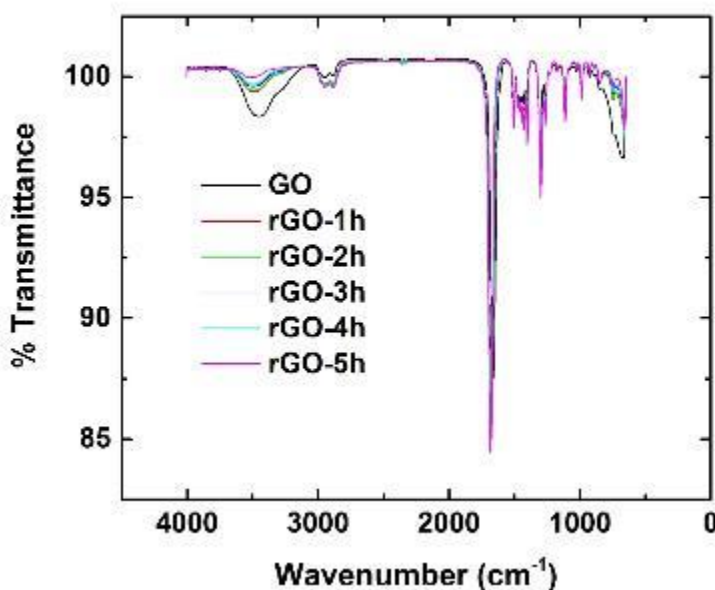


**Figure 3.1:** AFM and XPS characterization of GO nanomaterials. Each column shows the characterization data of one of three GO and rGO samples: GO, rGO-2h, and rGO-5h, respectively, from left to right. A representative AFM image (top row) and the flake size histograms of each (middle row) show that physical dimensions of the GO remain comparable despite the reduction process. Representative XPS spectra of each sample are shown in the bottom row, highlighting the stark drop in carbon-oxygen peaks and rise in the carbon-carbon peak as GO is reduced.

**Table 3.1:** XPS summary showing relative amounts of functional groups on GO

nanomaterials.

Sample	O:C	%CC/CH	%C-O	%C=O	%O-C=O
GO	1.0 : 2.2	40.3	29.9	25.8	4.0
rGO-1h	1.0 : 2.8	52.9	22.4	17.7	7.0
rGO-2h	1.0 : 3.1	53.8	23.3	14.6	8.3
rGO-5h	1.0 : 4.0	63.9	13.2	10.6	12.2

**Figure 3.2:** FT-IR spectra of GO nanomaterials.

Electrokinetic and hydrodynamic properties of rGO were determined over a range of solution chemistries including different salt types (NaCl, CaCl<sub>2</sub>), varying ionic strength (IS), and NOM concentrations. In DI water, the electrophoretic mobility (EPM) increased as GO was successively reduced (Figure 3.3A). Interestingly, EPM increased initially from GO to rGO-1h, but then remained similar from rGO-1h to rGO-5h, indicating that further reduction of GO does not

influence surface potential of rGO although the hydrodynamic size of graphene changed noticeably.  $D_h$  of rGO increased from 373 nm to 1049 nm as GO was reduced fully to rGO-5h (Figure 3.3B). Even though EPM remained quite similar from rGO-1h to rGO-5h, increased  $D_h$  with rGO indicates that surface functional groups are playing major roles in aggregation. XPS results show that functional groups of GO decrease as GO is reduced to rGO-5h which leads to higher hydrophobicity of the materials and increased aggregation.

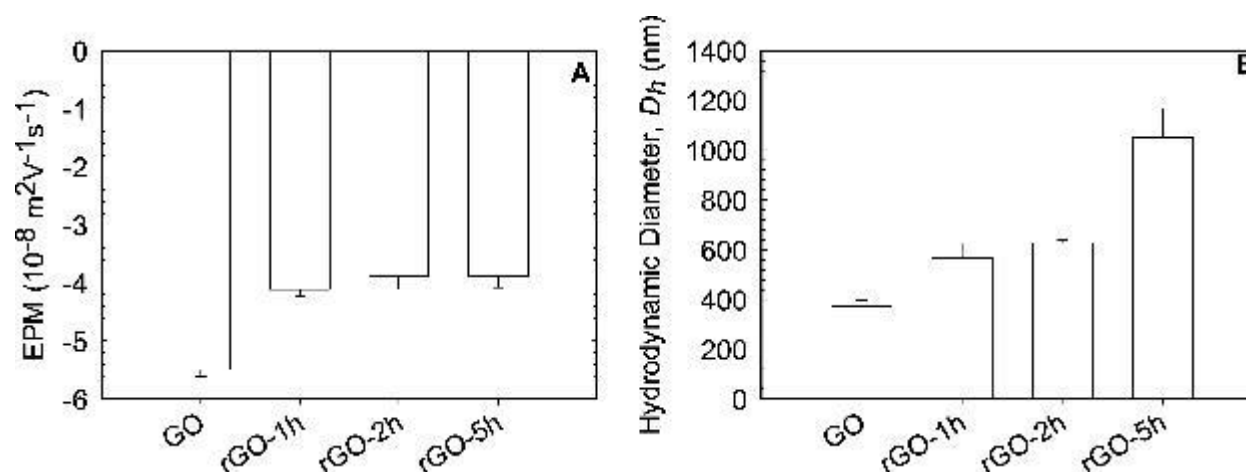


**Figure 3.3:** (A) Electrophoretic mobilities (EPM) and (B) hydrodynamic diameter ( $D_h$ ) of GO nanomaterials in DI water. Error bars are one standard deviation of at least three samples.

In the presence of 10 mM NaCl, the EPM of GO decreased as the pH increased from 4 to 10 (Figure 3.4A) due to the deprotonation of surface functional groups of GO with increased pH.<sup>267,268</sup> However, the hydrodynamic diameter ( $D_h$ ) of GO was relatively unchanged ( $\sim 500$  nm) throughout the pH range (Figure 3.4B), which has been observed previously.<sup>261,262</sup> In the presence of 10 mM NaCl with 0.1 mM  $\text{CaCl}_2$ , the EPM of GO increased as pH increased from 4 to 10, in contrast to what was observed in the presence of NaCl alone.  $D_h$  of GO increased from  $\sim 460$  nm to  $\sim 1350$  nm

as pH increased from 4 to 10 in the presence of 0.1 mM  $\text{CaCl}_2$  and 10 mM NaCl. This trend indicates that a small amount of background  $\text{CaCl}_2$  (0.1 mM) can significantly affect the physicochemical properties of GO as a function of pH. Since  $\text{CaCl}_2$  concentrations in natural aquatic environments often exceed 0.1 mM, the presence of  $\text{Ca}^{2+}$  ions will play a major role in GO stability, an effect that may be due to the binding capacity of  $\text{Ca}^{2+}$  ions to functional groups of GO.<sup>301,302</sup> Higher pH causes increased deprotonation of the GO surface functional groups, resulting in higher binding of  $\text{Ca}^{2+}$  ions with GO functional groups and increased surface charge of GO. Increased EPM also results in greater  $D_h$  due to charge screening. In the presence of 10 mM NaCl with 0.1 mM  $\text{MgCl}_2$  background, EPM of GO decreased slightly as pH increased from 4 to 10. However, this decrease in EPM is not as significant ( $p > 0.05$ ) as that observed in the presence of 10 mM NaCl alone, indicating  $\text{Mg}^{2+}$  ions are also binding with GO surface functional groups, but not as strongly as  $\text{Ca}^{2+}$  ions. GO  $D_h$  values remained similar across the pH range in the presence of background 0.1 mM  $\text{MgCl}_2$ .

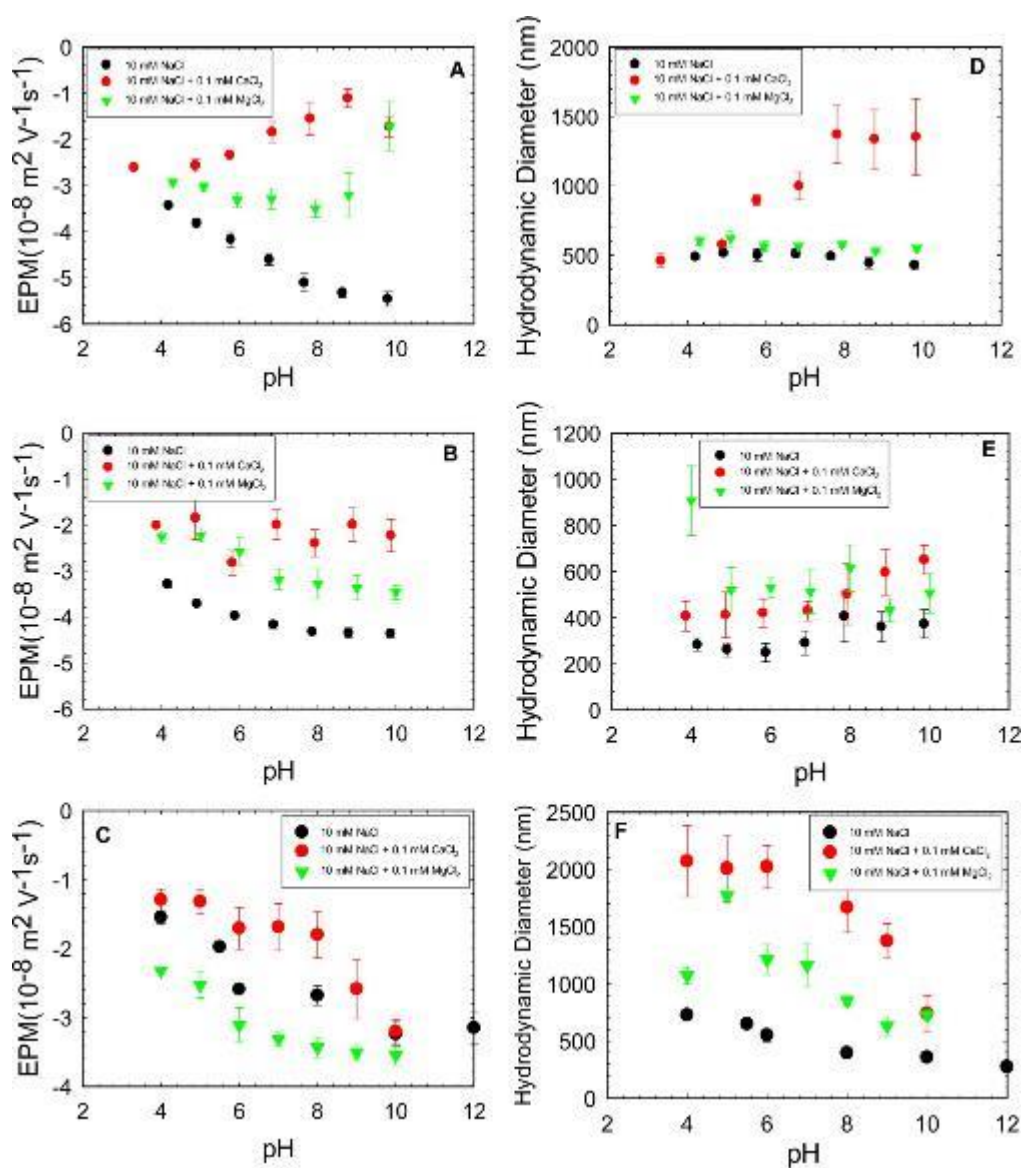


**Figure 3.4:** Electrophoretic mobilities and hydrodynamic diameter of GO nanomaterials as a function of pH in the presence of NaCl, without (black) and with background  $\text{CaCl}_2$  (red) and  $\text{MgCl}_2$  (green). EPM of (A) GO, (B) rGO-1h, (C) rGO-2h; hydrodynamic diameter of (D) GO, (E) rGO-1h, (F) rGO-2h. Error bars are one standard deviation of at least three samples.

In the presence of 10 mM NaCl only, EPM of rGO-1h decreased as pH increased from 4 to 10 (Figure 3.4B). The decrease for rGO-1h as a function of pH is not as significant as that observed for GO because rGO-1h contains fewer surface functional groups (Table 3.1), and deprotonation of surface functional groups with increased pH is lower for rGO-1h.  $D_h$  of rGO-1h was also relatively insensitive to pH changes in the presence of 10 mM NaCl. The EPM of rGO-1h remained almost constant from pH 4 to 10 in the presence of 10 mM NaCl with 0.1 mM  $\text{CaCl}_2$ , and was significantly higher than in NaCl alone, indicating that binding of  $\text{Ca}^{2+}$  ions with surface functional groups of rGO-1h influences the electrokinetic properties of rGO-1h. Increase of EPM due to the binding of  $\text{Ca}^{2+}$  ions with rGO-1h is not as significant as that observed for GO because rGO-1h has fewer surface functional groups. Similarly, the  $D_h$  of rGO-1h increased slightly (~400 nm to ~600 nm) from pH 4 to 10 in the presence of 0.1 mM  $\text{CaCl}_2$  (Figure 3.4E), but this increase in  $D_h$  is not as significant as that observed for GO. In the presence of 10 mM NaCl with 0.1 mM  $\text{MgCl}_2$ , EPM of rGO-1h decreased as pH increased from 4 to 10. In the presence of 0.1 mM  $\text{MgCl}_2$ ,  $D_h$  of rGO-1h remained fairly constant (~500 nm) throughout the pH range investigated in this study.

In the presence of 10 mM NaCl only, both the EPM and  $D_h$  of rGO-2h decreased as pH increased from 4 to 10 (Figure 3.4C, F). In the presence of 10 mM NaCl with 0.1 mM  $\text{CaCl}_2$ , EPM of rGO-2h decreased as pH increased from 4 to 10, in contrast to the trend observed for GO in the presence of 0.1 mM  $\text{CaCl}_2$ . Since rGO-2h contains a very low number of surface functional groups (Table 3.1), the binding capacity of  $\text{Ca}^{2+}$  ions is minimal. Thus, increased pH does not result in further binding of  $\text{Ca}^{2+}$  ions with rGO-2h, and an increase in EPM as a function of pH was not observed.  $D_h$  of rGO-2h decreased from ~2070 nm to ~740 nm as a function of pH, also in

contrast to the trend observed for GO. Similar trends were observed for rGO-2h in the presence of 10 mM NaCl with 0.1 mM  $\text{MgCl}_2$ .

Long-term stability of the GO nanomaterials in natural and artificial waters is summarized in Figure 3.5. In Call's Creek water, GO remains highly stable over a month-long study, which is likely due to the low IS (conductivity 26  $\mu\text{S}/\text{cm}$ ) and presence of NOM ( $2.8 \pm 0.57$  mg/L). Moreover, Call's Creek primarily contains monovalent ions ( $\text{Na}^+$ ,  $\text{K}^+$ ) and a negligible amount of divalent ions ( $\text{Mg}^{2+}$ ,  $\text{Ca}^{2+}$ ). Additionally, all rGO samples were less stable than GO in Call's Creek water which is consistent with the aggregation study. The suspended concentration of fully-reduced GO (rGO-5h) decreases below 25% within one day, and below 10% within five days. After one day, about 60% of both rGO-1h and rGO-2h were suspended in Call's Creek water, and after almost one month, ~15% of rGO-1h, ~15% rGO-2h and ~8% rGO-5h remain suspended which indicates reduced GO may not be completely removed from the water column in natural surface waters.

Long-term stability of the GO nanomaterials in synthetic surface water in the absence of NOM is shown in Figure 3.5B. After one day, GO and all types of rGO concentrations decrease to less than 10% of the initial concentration which indicates that graphene-based materials are not stable in surface water in the absence of NOM. The addition of 5  $\text{mg L}^{-1}$  SRHA to the synthetic surface water increased stability of all graphene-based materials investigated in this study (Figure 3.5C); after one day, 80% GO, 53% rGO-1h and 45% rGO-2h remained suspended in synthetic surface water in the presence of SRHA, but <5% of fully-reduced rGO-5h. After seven days, almost all GO settled out of the suspension, while both rGO-1h and rGO-2h remained suspended. Even after nearly a month, 36% rGO-1h and 7% rGO-2h remained suspended, while GO had completely

settled out. Two opposing processes govern interactions of SRHA with GO and rGO. First, SRHA can bind with GO which provides steric repulsion and increases stability. Secondly, SRHA can facilitate binding with GO functional groups in the presence of divalent ( $\text{Ca}^{2+}$ ,  $\text{Mg}^{2+}$ ) cations, which can increase aggregation of GO flakes and reduce stability. Thus, GO settled out in synthetic surface water in the presence of SRHA. In contrast, binding with divalent cations in the presence of SRHA is much lower for rGO, which has fewer surface functional groups than GO. rGO-1h and rGO-2h therefore remained stable in synthetic surface water in the presence of SRHA due to steric repulsion. Completely reduced GO (rGO-5h) was not stable due to a lack of functional groups.

Long term-stability of GO nanomaterials in synthetic ground water is shown in Figure 3.5D. Within one day, the concentrations of all samples decreased to below 10% in synthetic ground water in the absence of SRHA. The addition of 1 mg/L SRHA did not significantly increase stability of GO and rGO in synthetic groundwater, indicating rGO will settle out from groundwater in the environment due to higher concentrations of divalent cations ( $\text{Ca}^{2+}$ ,  $\text{Mg}^{2+}$ ) than in synthetic surface water.

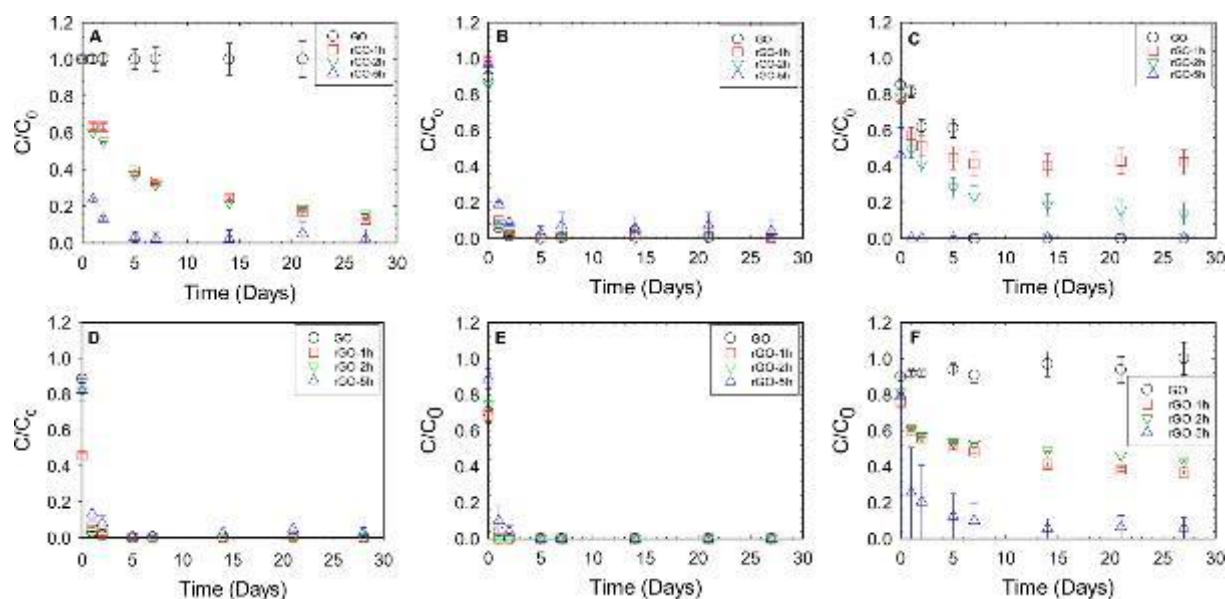


**Figure 3.5:** Long-term stability of GO nanomaterials in natural and artificial water. Normalized rGO concentrations in the presence of (A) Call's Creek; (B) synthetic surface water; (C) synthetic surface water with 5 mg/L SRHA; (D) synthetic groundwater; (E) Oconee effluent wastewater; and (F) synthetic wastewater.

Among all water samples investigated here, effluent wastewater collected from North Oconee Water Reclamation Facility was the most effective in reducing GO and rGO aqueous stability (Figure 3.5F). Within one day, almost all GO and rGO had settled out from the suspension due to high wastewater IS (conductivity 881  $\mu\text{S}/\text{cm}$ ), although a substantial amount of organic matter was present (6.5 mg/L TOC). Moreover, the effluent wastewater may have had residual coagulant (primarily alum), which would cause rapid rGO aggregation. In synthetic wastewater (as per OECD guideline), the suspended concentration of GO remained quite similar throughout the month-long stability study, indicating GO will be highly stable in this wastewater (Figure 3.5F).

Fully-reduced rGO-5h started to settle out very quickly and after a month, only 12% of rGO-5h remained suspended. Both rGO-1h and rGO-2h followed similar trends and after a month, about 36% rGO-1h and 42% rGO-2h remained suspended.

Overall, pH, divalent cations and NOM can play complex roles in the aquatic stability and fate of rGO and GO. These results show that stability of GO in water decreases with successive reduction of functional groups, with pH having the greatest influence on rGO stability. Stability is also dependent on ion valence and the concentration of surface functional groups. While pH did not noticeably affect stability of GO in the presence of 10 mM NaCl, adding 0.1 mM  $\text{CaCl}_2$  reduced the stability of GO with increased pH, due to adsorption of  $\text{Ca}^{2+}$  ions on the surface functional groups of GO which reduces the surface charge of GO. As the concentration of rGO functional groups decreased, so did the influence of  $\text{Ca}^{2+}$  ions on rGO stability. Long-term studies show that a significant amount of rGO-1h and rGO-2h remain stable in Call's Creek surface water, while effluent wastewater readily destabilizes rGO.

### ***3.2.2 Photodegradation of graphene oxide nanomaterials***

The transportation and transformation of nanomaterials are key factors to consider when determining their environmental risk.<sup>280</sup> This next study provides important insight into the role of functional groups on the stability and degradation of graphene nanomaterials and will contribute to the design of more sustainable applications of these materials. Graphene oxide nanomaterials were prepared as described in the previous section. To vary the functional group composition, two samples of reduced GO—partially reduced graphene oxide (rGO-2h) and fully reduced graphene oxide (rGO-5h)—were prepared by a solvothermal reduction process. The GO nanomaterials were exposed to simulated sunlight at 25 °C for one week and the physical and chemical changes of the

nanomaterials were characterized to determine the role of surface oxidation on the photodegradation of GO nanomaterials.

Upon irradiation, GO shows obvious physical changes within the first 24 hours. A significant decrease in average flake size in this first 24 hours can be seen in the AFM image analysis (Figure 3.6). This size reduction is attributed to the degradation of graphene oxide flakes during irradiation. Conversely, rGO-5h does not show any significant change in the average lateral size of the flakes. A Zetasizer Nano ZS was also used to analyze the change in particle size. From the hydrodynamic diameter values, a rapid decrease in size of the GO is observed, compared to rGO-2h and rGO-5h (Figure 3.7A), implying that the rGO samples degrade at a significantly slower rate.

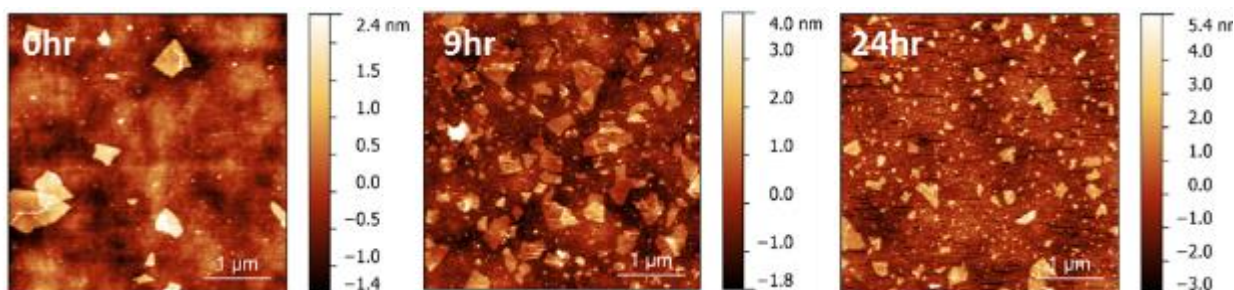


**Figure 3.6:** AFM images of GO showing degradation of particles before and after irradiation.

Degradation of GO and rGO particles was further analyzed by total organic carbon (TOC) measurements (Figure 3.7B). GO samples showed a TOC reduction of 32.1% after 3 days of irradiation. It should be noted that the majority of this TOC reduction occurred in the first 6 hours (27.65%) but then slowed considerably over the next 162 hours, indicating that GO undergoes rapid photodegradation upon the initial 6 hours of exposure to sunlight. Among all samples, the slowest rate of TOC reduction was observed for rGO-5h. These results indicate delayed degradation of rGO samples.

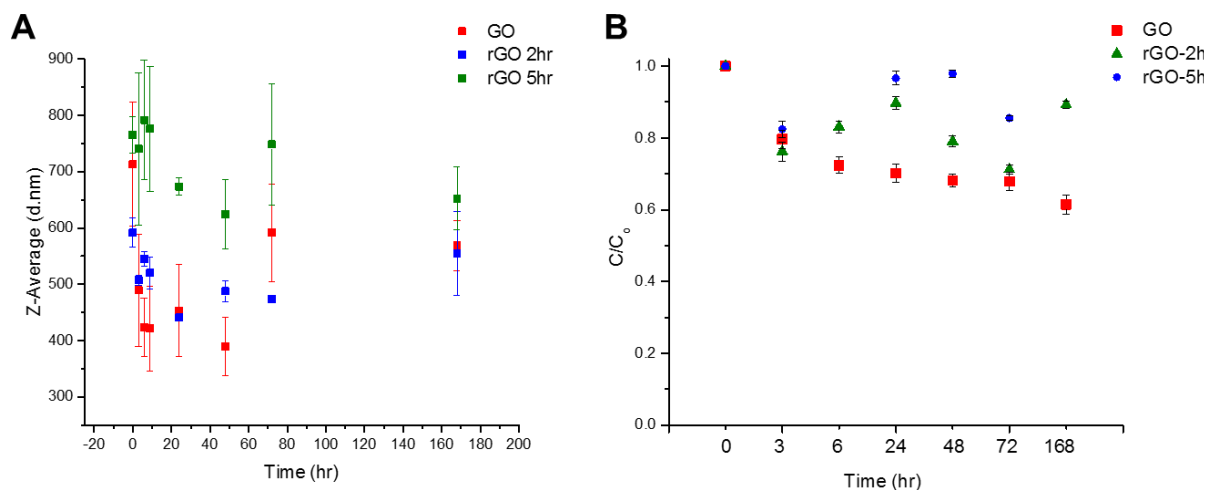


**Figure 3.7:** (A) Hydrodynamic diameter and (B) total organic carbon analysis of GO, rGO-2h and rGO-5h as a function of irradiation time.

Additionally, upon irradiation, the GO samples darkened due to sunlight exposure, which can be clearly seen in the photos of the GO dispersions (Figure 3.8), again indicating the degradation of GO. Previously, this color change has been suggested as partial restoration of the conjugated carbon ring network due to removal of oxygen-containing functional groups. This same phenomenon has been observed during the chemical reduction of GO sheets.<sup>303,304</sup> Removal of these functional groups due to sunlight exposure in turn increases the hydrophobicity of the particles and thus induces aggregation in aqueous environments. This aggregation is noticeable in the images of the rGO dispersions and may lead to slower degradation of these particles due to limited absorption of light of these particles.

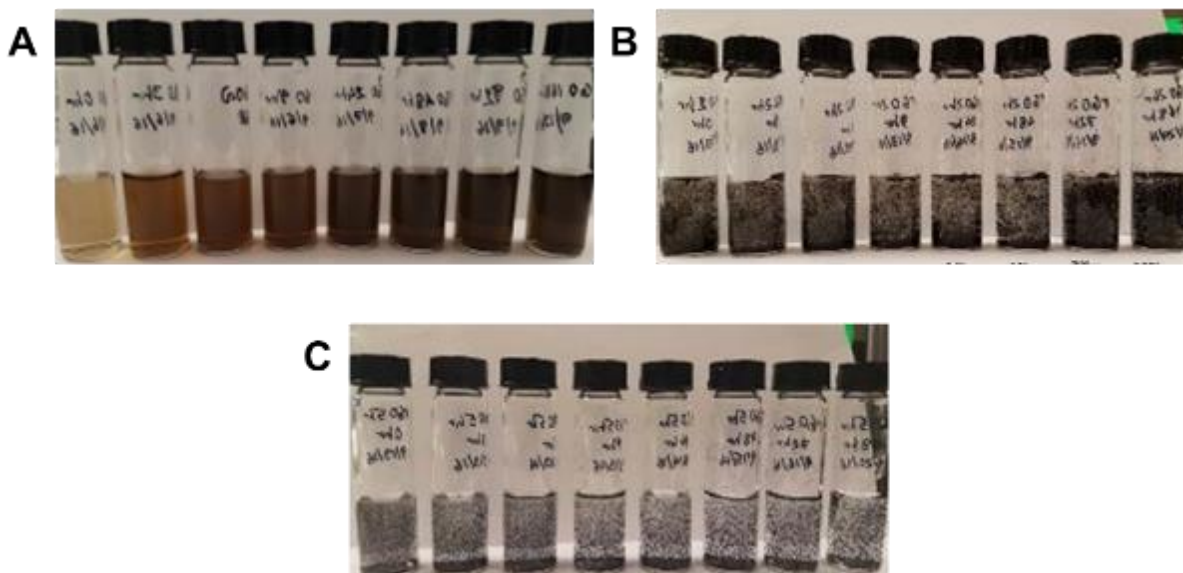


**Figure 3.8:** Images of (A) GO, (B) rGO-2h, and (C) rGO-5h dispersions as a function of time after irradiation, from left ( $t = 0$  hours) to right ( $t = 168$  hours).

Changes in the oxygen-containing functional groups and delayed degradation was also verified by XPS. Figure 3.9 and Table 3.2 summarize the chemical degradation of the GO nanomaterials. The spectra exhibit three major peaks corresponding to C-C at 284.8 eV, epoxy and hydroxyl functional groups (C-O) at 286.9 eV, and carbonyl groups (C=O) at 289 eV. During the solvothermal process, the epoxy and hydroxyl groups on the basal plane of the GO are driven off, evident by the decrease in the C-O peak and the overall decrease of oxygen in rGO-2h and rGO-5h. Furthermore, the emergence of the peak at 292 eV, due to the  $\pi \rightarrow \pi^*$  transition, is indicative of the restoration of the graphene lattice. After 72 hours of irradiation, no significant compositional changes in the rGO materials are observed. GO, on the other hand, undergoes a noticeable chemical reduction where the amount of hydroxyl (C-OH) and epoxy

(C-O-C) groups decreases significantly from 39.7 at.% to 13.9 at.% upon irradiation for 72 hours. These hydroxyl and epoxy functional groups are located mainly on the basal plane of graphene oxide and it is hypothesized that these functional groups will react first in the presence of sunlight as they are single bonded groups. Functional groups on the edges, such as carboxylic acid, are much more stable and not likely to react initially.

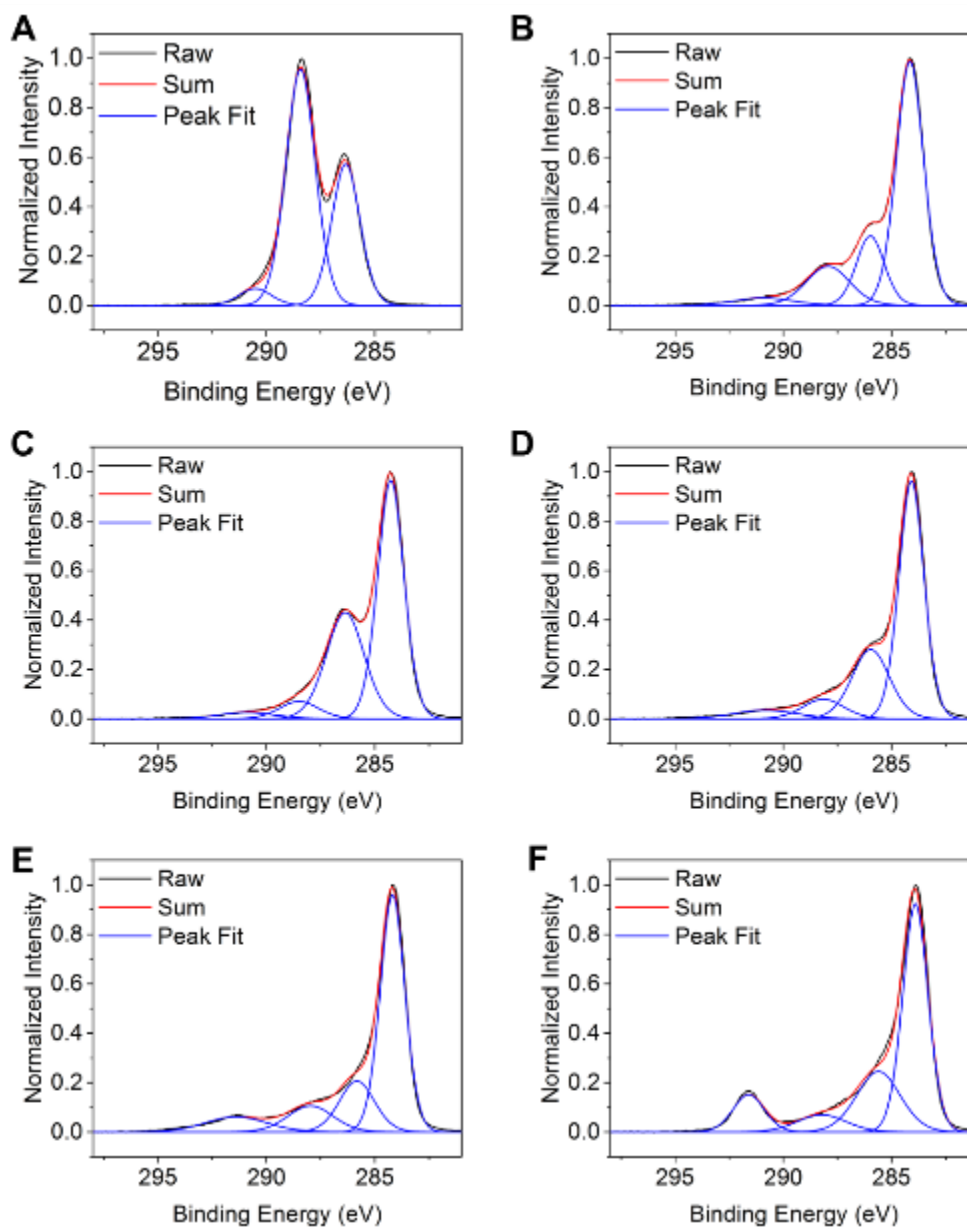


**Figure 3.9:** Chemical degradation of GO nanomaterials. XPS spectra of initial dispersions of (A) GO, (C) rGO-2h, and (E) rGO-5h prior to irradiation and (B) GO, (D) rGO-2h, and (F) rGO-5h after 72 hours of irradiation.

**Table 3.2:** XPS summary showing atomic % (at.%) of oxygen and carbon associated with different functional groups on GO nanomaterials after 72 hours irradiation.

	GO		rGO-2h		rGO-5h	
	0 hr	72 hr	0 hr	72 hr	0 hr	72 hr
<b>C-C</b>	24.4 ± 1.6	47.4 ± 0.1	43.6 ± 0.5	49.2 ± 0.2	51.6 ± 0.6	47.4 ± 0.1
<b>C-O</b>	39.7 ± 0.9	13.9 ± 0.1	27.2 ± 1.1	22.7 ± 1.7	15.9 ± 0.7	21.6 ± 0.3
<b>C=O</b>	3.1 ± 0.2	12.1 ± 0.1	5.2 ± 0.7	5.6 ± 1.5	10.5 ± 1.5	7.2 ± 0.4
<b><math>\pi \rightarrow \pi^*</math></b>	-	3.3 ± 0.1	2.4 ± 0.1	4.4 ± 0.1	8.3 ± 0.1	9.7 ± 0.1
<b>Oxygen</b>	32.8 ± 0.4	23.4 ± 0.1	21.6 ± 0.1	18.0 ± 0.1	13.7 ± 0.1	14.1 ± 0.1

This composition data is further supported by the optical absorbance spectra of the GO nanomaterials. The initial GO dispersion shows absorption peaks at 230 nm, related to the  $\pi$ - $\pi^*$  transitions of the aromatic C–C bonds, and a shoulder at 300 nm, corresponding to the n- $\pi^*$  transitions of the C=O bonds (Figure 3.10A). Conversely, the initial rGO-2h and rGO-5h dispersions show a single absorption peak at 270 nm, indicating the restoration of the  $\pi$ -conjugated network of graphene. Furthermore, the disappearance of the shoulder at 300 nm suggests the loss of oxygen-containing groups (Figure 3.10B, C). Changes in the oxygen-containing functional groups as a result of the photodegradation were also verified by UV-Vis optical absorbance spectroscopy. The presence of oxygen-containing functional groups on the surface disrupt the conjugated system of graphene, causing a shift in the absorbance peaks. In the case of GO, the absorbance increased over time, indicating a photochemical change likely caused by the formation of light-absorbing photoproducts. Sunlight exposure also resulted in a shift in the peak position from 230 nm to 270 nm, indicating the restoration of the  $\pi$ -conjugation network of graphene. The disappearance of the shoulder at 300 nm suggests the removal of oxygen groups consistent with the XPS results. Conversely, no significant changes of UV-Vis spectra are observed in the rGO materials.

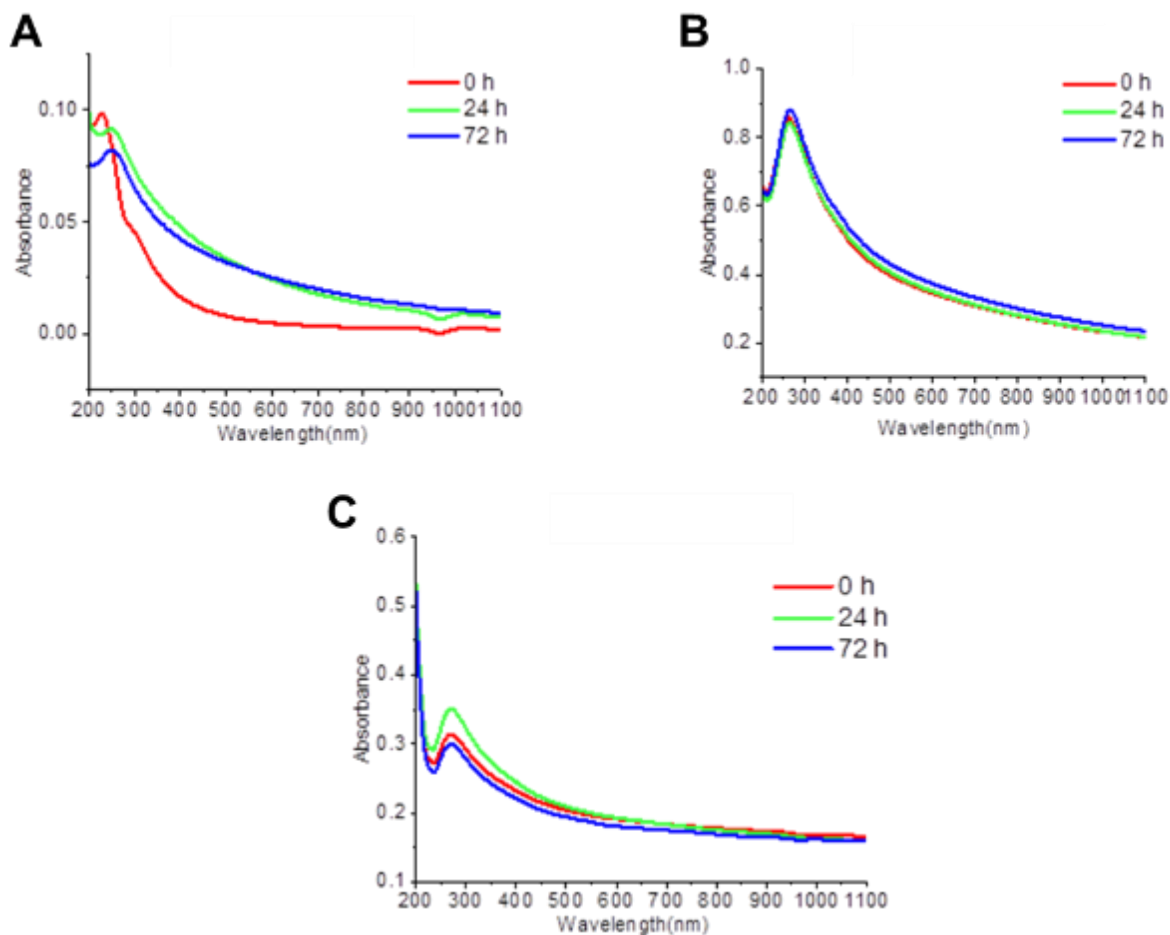


**Figure 3.10:** Optical absorbance spectra of irradiated (a) GO, (b) rGO-2h (c) rGO-5h samples.

The shift in the major peak from 230 nm to 270 nm in GO implies the restoration of graphene lattice and disappearance of the peak at 300 nm indicates the removal of oxygen containing functional groups in GO. No significant changes are observed in the optical absorbance spectra for the rGO materials after irradiation.

The proposed mechanism for the photodegradation of GO and rGO under direct sunlight is illustrated in Figure 3.11. In direct photolysis, functional groups of graphene nanomaterials act as chromophores. Hydroxyl and epoxy functional groups, located mainly on the basal plane of GO, are hypothesized to react first in the presence of sunlight as they are single bonded groups. Other functional groups on the edges are double bonded groups, which require more energy to break than single bonds, and are thus less likely to react initially.

The hydroxyl and epoxy functional groups (C-OH and C-O), which are strong electron donating groups, absorb photons that excite electrons from the ground state to the excited state, producing many excited electrons and holes. Eventually, these electrons and holes disrupt the chemical bonds of the functional groups, initiating the breaking of the covalent bonds and contributing to the physical breakdown of the GO material.

rGO has significantly fewer oxygen-containing functional groups than GO. Specifically, the amount of hydroxyl and epoxy functional groups is significantly lower. This reduction in electron donating functional groups in rGO will reduce the breaking of covalent bonds in rGO. Hence, rGO is more resistant to degradation than GO under direct photolysis, as we have shown in our photodegradation studies. Furthermore, rGO particles aggregate due to the increased hydrophobicity of these materials, which can reduce the opportunity for photodegradation.

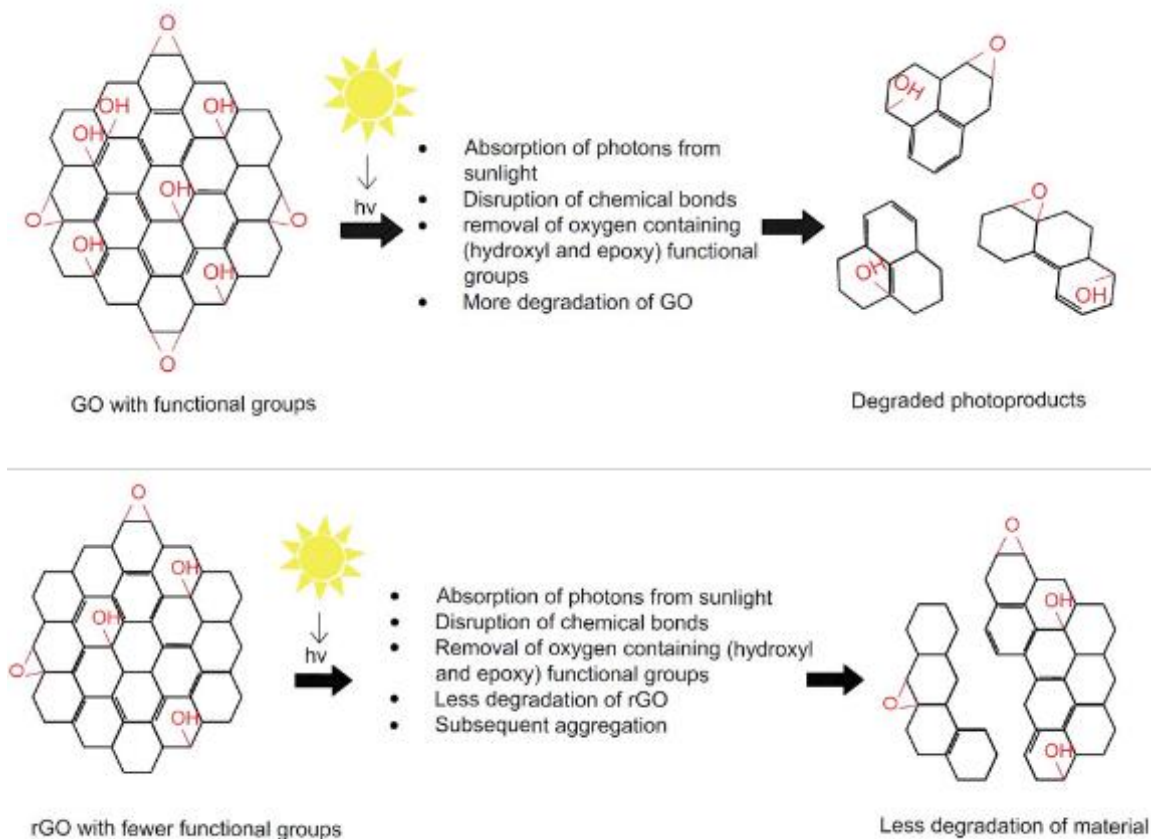


**Figure 3.11:** Proposed mechanisms for the photodegradation of GO nanomaterials as a function of surface oxidation. Oxygen-containing functional groups on the basal plane of GO (top) such as hydroxyl and epoxy groups will react first after exposure to sunlight, initiating the degradation of the GO and creating holes in the graphene lattice, which further accelerates the GO breaking apart into smaller and smaller flakes. rGO (bottom) contains significantly fewer oxygen-containing functional groups on the basal plane resulting in less hole formation and higher overall stability.

Overall, these results suggest that sunlight exposure causes degradation of both graphene oxide and reduced graphene oxide nanomaterials. Oxygen-containing functional groups on the basal plane, such as epoxy and hydroxyl groups, are the most likely photoreactive sites that contribute to the breakdown of GO nanomaterials. The presence of fewer oxygen-containing functional groups on the surface of rGO materials leads to higher hydrophobicity of the materials and delayed degradation.

### ***3.2.3 Antifouling properties of graphene oxide and molybdenum disulfide functionalized membranes***

In this work, a quartz crystal microbalance with dissipation monitoring (QCM-D) was used to study the interactions of GO and MoS<sub>2</sub> with NOM and *E. coli* (K-12). NOM is mainly composed of humic substances and polysaccharides and is very common in the aquatic environment.<sup>305</sup> *E. coli* is also common in natural water and one of the most commonly used bacteria strains for fouling studies.<sup>235,306,307</sup> Interaction of these foulants with MoS<sub>2</sub> and GO will thus give a clear indication of the antifouling properties of the materials. The impact of ion presence and valency on the fouling properties in natural surface water is also investigated.

The average hydrodynamic diameters of 10 mg/L GO (pH 4.51) and 50 mg/L MoS<sub>2</sub> (pH 4.32) were 385.3 nm and 153.5 nm, respectively. Zeta potentials of GO and MoS<sub>2</sub> were -41.33 mV and -40.34 mV, respectively. The high polydispersity index (PDI) of the materials suggests the presence of a range of differently sized particles, which is further confirmed by AFM image analysis. The highly negative zeta potential of MoS<sub>2</sub> and GO indicate that they are moderately stable in water. Additionally, this suggests that MoS<sub>2</sub> and GO functionalized surfaces could effectively repel foulants due to the negative surface charge of most foulants.<sup>308</sup> Representative AFM images of GO

and MoS<sub>2</sub> on silicon dioxide (SiO<sub>2</sub>) are shown in Figure 3.12. The roughness of the GO and MoS<sub>2</sub> on PLL coated gold sensors were  $2.5 \pm 0.3$  nm and  $2.4 \pm 0.3$  nm, respectively. The surface roughness of a bare PLL surface was found to be  $5.1 \pm 1.2$  nm. From these measurements it is clear that the deposition of the 2D materials reduced the roughness of the polymer surface by half.

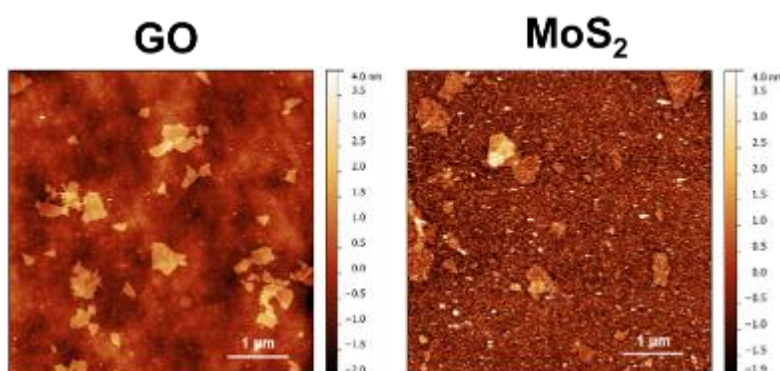


**Figure 3.12:** AFM images of GO and MoS<sub>2</sub> on SiO<sub>2</sub>. The flakes are mainly monolayer or bilayer with a range of lateral sizes.

Gold sensors were coated with the nanomaterial of interest using the same procedure from previous studies.<sup>267,301</sup> Briefly, the gold sensor surface was rinsed with Milli-Q water for 50-60 min to achieve a stable baseline reading. The QCM-D system was equilibrated with HEPES buffer in 100 mM NaCl solution for 30 min at a flow rate of 0.1 mL/min. Poly-L-lysine hydrobromide (PLL) in HEPES buffer solution was introduced at 0.1 mL/min. The PLL layer was rinsed with HEPES for 20 min to remove the unadsorbed PLL. Finally, 1 mM NaCl solution (background electrolyte) was used to remove the buffer at a flow rate of 0.1 mL/min for 30 min. 10 mg/L GO or 50 mg/L MoS<sub>2</sub> was deposited on the PLL coated surface by flowing at a rate of 0.1 mL/min for at least 30 min. MoS<sub>2</sub> showed slow deposition on PLL and thus a higher concentration of MoS<sub>2</sub>

was employed to achieve a fully coated sensor in a reasonable time period. The sensors were exposed to the GO and MoS<sub>2</sub> solutions until maximum frequency was achieved and the frequency shift became stable indicating maximum coverage of both materials on the PLL surface. To test the antifouling properties, NOM and *E. coli* were injected across the nanomaterial-coated surface at a flow rate of 0.1 mL/min until the QCM-D showed a stable frequency shift.

The deposition kinetics of NOM and *E. coli* were determined from the frequency shifts monitored by QCM-D from which the deposition rate and attachment efficiency can be calculated.<sup>30</sup> Shifts in frequency and dissipation were monitored at the third overtone. NOM and *E. coli* were directly deposited on PLL surfaces as a control to investigate the deposition behavior of foulants that may occur as a result of interactions of the bare polymer surface and the foulants. The maximum frequency shift caused by the deposition of NOM on both surfaces was used to determine the maximum fouling that may occur on the material surfaces during filtration. Following injection of NOM onto the nanomaterial functionalized surfaces, a slight frequency shift was observed on the GO surface (<1.5 Hz), and no frequency shift was observed on the MoS<sub>2</sub> surface, indicating that MoS<sub>2</sub> will be less prone to fouling from NOM. Due to the high zeta potential of GO and MoS<sub>2</sub> and the slight negative charge of NOM, the interaction of NOM with the material surfaces will be minimal due to electrostatic repulsion, and thus there is hardly any deposition of NOM on the material surfaces.

Although some NOM deposition is observed on GO, NOM attaches to a GO functionalized surface 70% more slowly than a bare polymer surface (Figure 3.13A). These results agree with previous studies which have shown that interactions between GO surfaces and NOM are electrostatically unfavorable<sup>309</sup> as NOM is negatively charged under environmentally relevant

conditions.<sup>310</sup> No significant deposition of NOM was observed on the MoS<sub>2</sub> surface despite a zeta potential similar to GO. The small difference in their interactions with NOM is most likely due to the presence of functional groups on GO that can interact with NOM. Previously it has been shown that GO deposits more readily on surfaces that have been coated with NOM due to the high amount of hydroxyl and carboxyl functional groups on GO that readily bind with functional groups of NOM.<sup>309</sup>

Sodium, a major monovalent ion in natural and waste water, may interact with the functional groups of organic molecules and can play a role in NOM deposition on membrane surfaces during filtration. In the presence of Na<sup>+</sup>, The initial deposition rate of NOM was 0.98 Hz/min on a GO surface and 0.64 Hz/min on an MoS<sub>2</sub> surface and the maximum shift observed was 1.65 Hz on the GO surface and 1.52 Hz on the MoS<sub>2</sub> surface. Using these deposition rates, the attachment efficiencies (Figure 3.13B) of NOM were found to be 57% and 36% on GO and MoS<sub>2</sub> surfaces, respectively, indicating that NOM deposits on MoS<sub>2</sub> 21% more slowly than on GO. Also, it indicates that NOM in the presence of Na<sup>+</sup> deposits 43% and 64% faster on a bare PLL surface than on GO and MoS<sub>2</sub> surfaces, respectively. The slower deposition rate of NOM on MoS<sub>2</sub> makes it a more advantageous material choice than GO for antifouling properties. The increase in the overall deposition of NOM in this case is mainly due to reduced electrostatic repulsion and the effect of charge neutralization caused by the presence of Na<sup>+</sup> ions. The presence of Na<sup>+</sup> clearly plays a strong role in the deposition of NOM as indicated by the resulting higher frequency shifts and higher attachment efficiencies to the GO and MoS<sub>2</sub> surfaces.

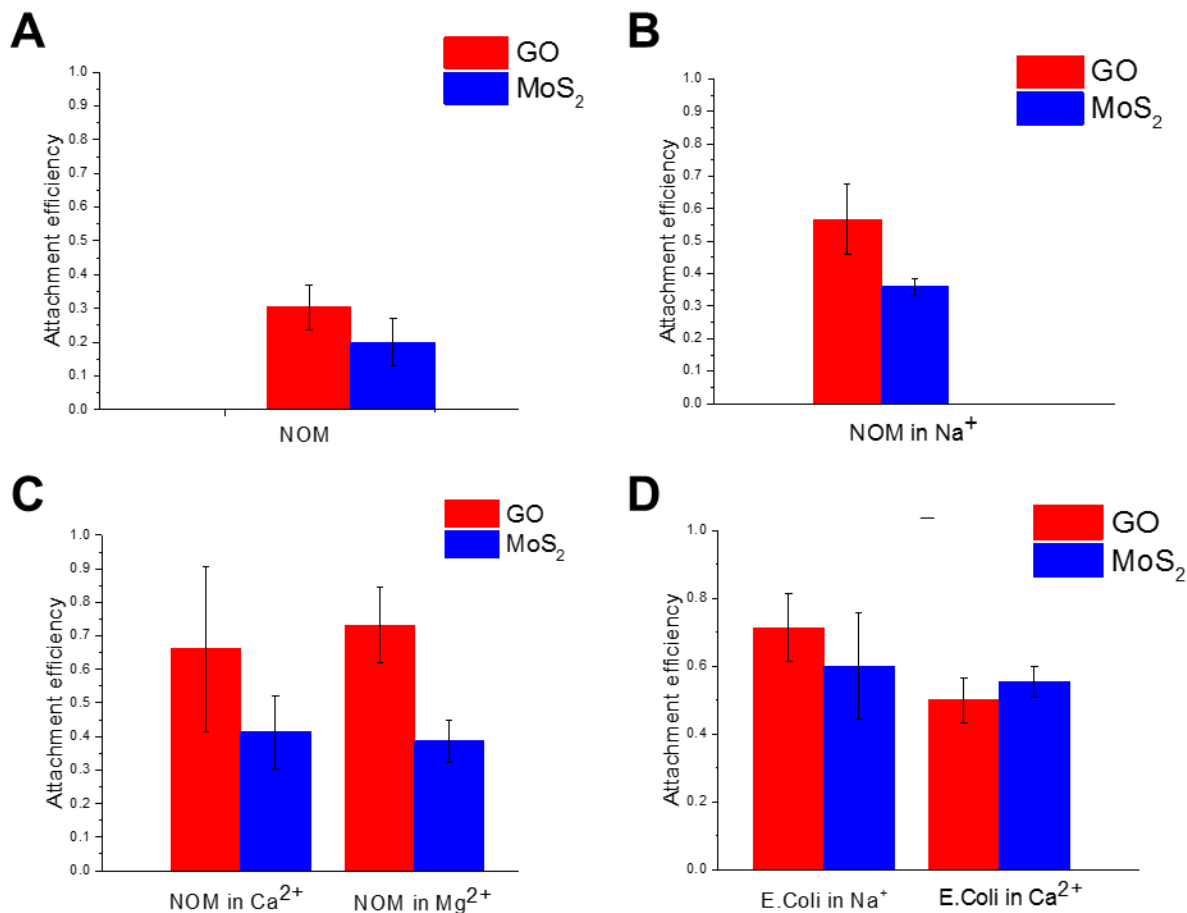


**Figure 3.13:** Attachment efficiency of NOM on GO and MoS<sub>2</sub> functionalized surfaces in (A) the absence of salts and in the presence of (B) monovalent cations and (C) divalent cations. (D) Attachment efficiency of *E. coli* in the presence of monovalent and divalent cations.

Next, the interactions of GO and MoS<sub>2</sub> with NOM in the presence of divalent cations was investigated. The maximum shifts observed for NOM in Ca<sup>2+</sup> were 5.97 Hz and 5.37 Hz on GO and MoS<sub>2</sub>, respectively, and in Mg<sup>2+</sup> the maximum frequency shifts were 4.60 Hz and 3.81 Hz on GO and MoS<sub>2</sub>, respectively. From these values of maximum frequency shift, it is clear that the

deposition of NOM on both material surfaces in the presence of divalent cations is higher than in the presence of monovalent ions. The attachment efficiencies of NOM in the presence of  $\text{Ca}^{2+}$  were 66% and 41% on GO and  $\text{MoS}_2$  surfaces, respectively, suggesting NOM in the presence of  $\text{Ca}^{2+}$  deposits more slowly on  $\text{MoS}_2$  than GO (Figure 3.13C). The initial deposition rate of NOM in  $\text{Ca}^{2+}$  on GO was 1.18 Hz/min while the rate on  $\text{MoS}_2$  was 0.74 Hz/min. On the other hand, the initial deposition rate of NOM in  $\text{Mg}^{2+}$  on GO was 1.31 Hz/min while the rate on  $\text{MoS}_2$  was 0.69 Hz/min. The attachment efficiencies of NOM in  $\text{Mg}^{2+}$  were 73% and 39% on GO and  $\text{MoS}_2$  surfaces, respectively, indicating the superior antifouling properties of  $\text{MoS}_2$  over GO. However, increased values of both maximum frequency shifts and attachment efficiencies suggest that electrostatic repulsion between the NOM and the GO or  $\text{MoS}_2$  surface is reduced in the presence of  $\text{Ca}^{2+}$  or  $\text{Mg}^{2+}$ . This decrease in the energy barrier between NOM and the surface allows the NOM to come into close contact with the material surfaces in the presence of divalent ions. This higher deposition of NOM can also be attributed to salt bridging caused by the divalent ions. This bridging effect is well documented in the literature.<sup>311,312</sup> Chen and Elimelech observed a slightly higher interaction of fullerenes and Suwannee River humic acid (SRHA) on bare silica in the presence of  $\text{CaCl}_2$  due to SRHA macromolecules undergoing complex formation with  $\text{Ca}^{2+}$  that reduces electrostatic and steric effects.<sup>308</sup> Chowdhury et al. found a similar bridging effect of divalent cations during the interaction of GO and Suwannee River fulvic acid (SRFA) using QCM-D.<sup>309</sup> Chowdhury et al. also reported the decrease of surface charge of GO in presence of NOM and divalent cations that caused GO aggregation in solution. It is clear from this study that the antifouling ability of both GO and  $\text{MoS}_2$  decreases significantly when NOM is present with divalent cations in solution.

Finally, the deposition of *E. coli* was investigated in the presence of monovalent and divalent cations (Figure 3.13D). After 30 minutes of *E. coli* injection in  $\text{Na}^+$  and  $\text{Ca}^{2+}$ , a maximum frequency shift of 7.39 Hz and 9.42 Hz was observed on GO surfaces, while the shift was 5.59 Hz and 5.08 Hz on  $\text{MoS}_2$  surfaces, respectively, indicating that overall deposition of *E. coli* was significantly lower on  $\text{MoS}_2$  than GO. Both of the 2D material functionalized surfaces showed reduced deposition of *E. coli* compared to the bare PLL surface where the maximum frequency shift was 16.23 Hz on average after 30 min of *E. coli* exposure. The attachment efficiencies of *E. coli* in the presence of  $\text{Na}^+$  were 71% and 62% on GO and  $\text{MoS}_2$  surfaces, respectively, and in the presence of  $\text{Ca}^{2+}$  were 50% and 55% on GO and  $\text{MoS}_2$  surfaces, respectively. The initial deposition rate of the *E. coli* suspension ( $\approx 10^6$ - $10^7$  cells/mL) in 10 mM  $\text{Na}^+$  and 0.5 mM  $\text{Ca}^{2+}$  on GO were 0.26 Hz/min and 0.18 Hz/min, respectively, while the deposition rate of *E. coli* in  $\text{Na}^+$  and  $\text{Ca}^{2+}$  on  $\text{MoS}_2$  were 0.22 Hz/min and 0.20 Hz/min, respectively. Low attachment efficiency for both cases compared to the bare PLL surface indicates an improvement of the antifouling properties due to the presence of the 2D materials on the surface. The initial deposition rate of *E. coli* on the bare PLL surface was 0.36 Hz/min on average, which is higher than both of the functionalized surfaces. However, the attachment efficiencies reported in this study may be underestimated. Poitras and Tufenkji reported that QCM-D underestimates the mass adsorbed on the crystal surface for “soft mass” such as bacterial cells.<sup>313</sup> They reported that along with frequency shift, the dissipation shift also changed significantly during *E. coli* deposition. Values reported here are higher than previously found,<sup>313</sup> which may be due to different *E. coli* strains. However, it is important to report that the increase in dissipation shift during the *E. coli* deposition was much higher than the NOM deposition, which indicates that the *E. coli* creates a softer layer than NOM on these surfaces.

*E. coli*, which are gram-negative bacteria, have an outer covering of lipopolysaccharides that impart a strongly negative charge to the surface of the gram negative bacterial cells.<sup>314</sup> Due to electrostatic repulsion, *E. coli* showed less attachment to both MoS<sub>2</sub> and GO. Any attachment of *E. coli* to the material surfaces that did occur might be due to extracellular polymeric substances (EPSs). EPSs are natural polymers of high molecular weight that are secreted by microorganisms into the environment.<sup>315</sup> EPSs constitute 50% to 90% of a biofilm's total organic matter and are responsible for bacterial attachment to a surface.<sup>316–318</sup> Previously, it has been observed that stationary phase cells cultivated in LB media have less negative charge than the exponential phase cells and tend to aggregate more,<sup>319</sup> which may also contribute to the cell attachment on the material surfaces. In another study, it was reported that *E. coli* MG1655 aggregate more in the stationary phase due to high protein content on free EPS. In the stationary phase, bacterial cells usually secrete maximum EPSs that help them to adhere to the surface.<sup>320</sup>

Overall, MoS<sub>2</sub> showed superior antifouling properties compared to GO. In most cases, the deposition of foulants was more reversible on MoS<sub>2</sub> than GO due to the presence of functional groups on GO that bind more easily with the foulants. Unlike NOM, interactions of *E. coli* with material surfaces in the presence of monovalent and divalent cations did not vary based on valency.

### 3.2.4 Foulant removal from graphene oxide and molybdenum disulfide functionalized membranes

Next, we investigated the use of these types of GO- and MoS<sub>2</sub>-modified surfaces for their potential application in reducing the fouling and improving the self-cleaning ability of water filtration membranes. Specifically, the application of external voltage to the surface is explored as an alternative to standard chemical cleaning procedures to remove foulants from the membrane surface. In this study, gold sensors were first coated with polypyrrole (PPy), a conducting polymer, instead of the PLL used in the previous study. This PPy surface was then functionalized with GO or MoS<sub>2</sub> using the same method as described in the previous section. The attachment and release of a model foulant, bovine serum albumin (BSA), on GO and MoS<sub>2</sub> functionalized surfaces is investigated with and without an applied voltage (Figure 3.14).

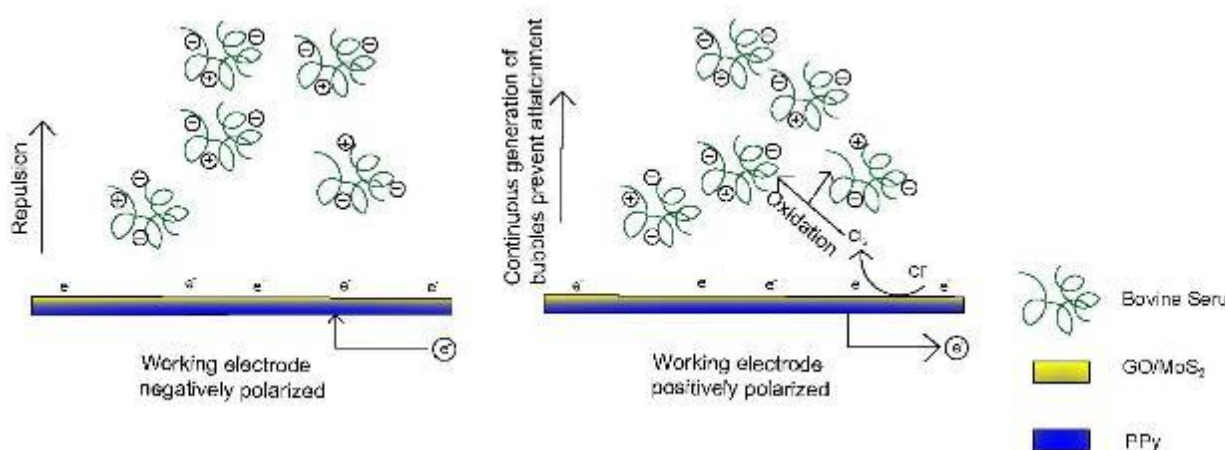


**Figure 3.14:** Schematic illustrating the proposed antifouling and self-cleaning mechanisms of GO- and MoS<sub>2</sub>-functionalized surfaces upon application of an external voltage.

To understand the fouling behavior of BSA, the model foulant was deposited on a bare PPy surface, a GO-PPy surface and a MoS<sub>2</sub>-PPy surface without the application of any voltage. BSA deposited more on the bare PPy surface than on GO-PPy and MoS<sub>2</sub>-PPy surfaces with a maximum frequency shift of  $44.27 \pm 10$  Hz. BSA deposited on GO-PPy and MoS<sub>2</sub>-PPy surfaces with frequency shifts of  $33.55 \pm 5.02$  Hz and  $26.73 \pm 4.21$  Hz, respectively. Figure 3.15 shows that BSA attached to GO-PPy and MoS<sub>2</sub>-PPy surfaces 45% and 47% more slowly than the bare PPy surface, respectively.

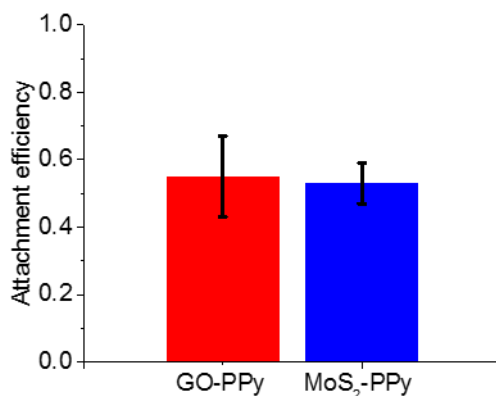


**Figure 3.15:** Attachment efficiency of BSA on GO and MoS<sub>2</sub> functionalized surfaces.

Electrochemical control was then used to explore whether applying a potential difference can delay the attachment or accelerate the release the foulants. Figure 3.16 shows the deposition behavior of BSA on bare PPy, GO-PPy and MoS<sub>2</sub>-PPy surfaces under  $-0.5/+0.5$  V<sub>Ag/AgCl</sub>. Comparing these maximum frequency shifts with the no voltage condition, the application of negative external voltage ( $-0.5$  V<sub>Ag/AgCl</sub>) delays the attachment of BSA on bare PPy and MoS<sub>2</sub>-PPy surfaces. Frequency shifts during BSA attachment decreased to  $9.2 \pm 1.1$  Hz and  $6.28 \pm 0.26$  Hz

on PPy and MoS<sub>2</sub>-PPy surfaces, respectively, under -0.5 V<sub>Ag/AgCl</sub> (Figure 3.16A). Under negative bias, BSA attaches to the GO-PPy surface 36% more slowly and to the MoS<sub>2</sub>-PPy surface 91% more slowly than to the bare-PPy surface (Figure 3.16B). The negative bias creates a repulsive electrostatic force between BSA and the surfaces. Small attachment of BSA on PPy and MoS<sub>2</sub>-PPy surfaces under negative potential is most likely due to the positively charged amine groups on its structure, as these will interact favorably with the negatively charged surface. In contrast, Figure 3.16A also shows that the attachment of BSA does not change under a positive bias. The only difference between the control and the positive bias condition was found in the attachment efficiency of BSA. The BSA deposition rate during +0.5 V<sub>Ag/AgCl</sub> application decreased by ~50% for all of the surfaces compared to the control condition (Figures 3.16B).

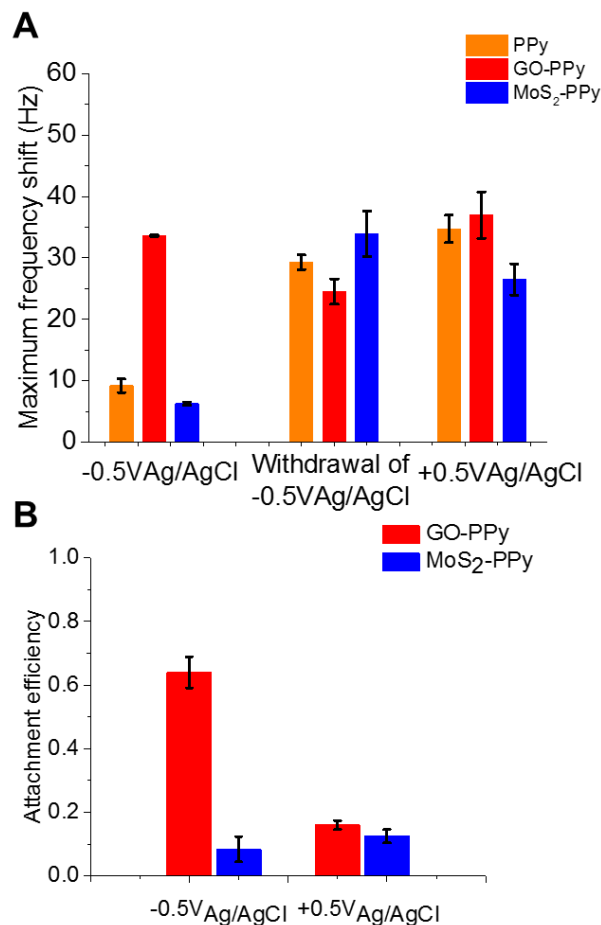


**Figure 3.16:** (A) Deposition behavior of BSA under positive and negative potential. Reduced deposition of the BSA is observed upon application of  $-0.5 V_{Ag/AgCl}$  on PPy and MoS<sub>2</sub>-PPy surfaces. Deposition is reported in terms of the EQCM-D frequency shift. (B) Attachment efficiency of the BSA molecules on GO-PPy and MoS<sub>2</sub>-PPy surfaces under positive and negative potential. Higher attachment efficiency of BSA on the PPy-GO surface indicates faster deposition during negative bias application. However, efficiencies of  $<1$  suggest that both the modified surfaces perform better than the bare polymer surface under negative potential.

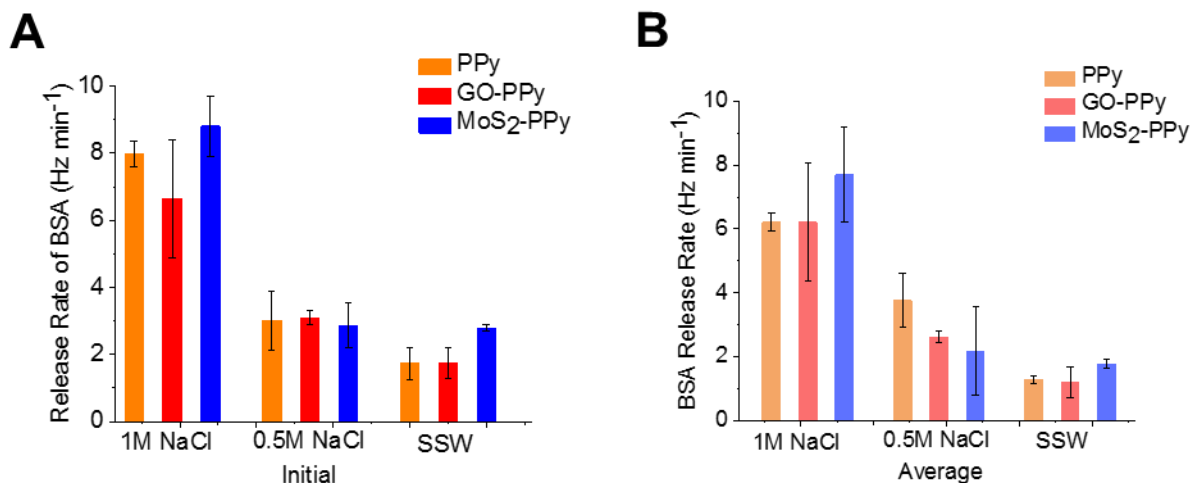


**Figure 3.17:** (A) Initial and (B) average release rates of BSA under different concentrations of NaCl and SSW electrolysis treatment under  $+0.74V_{Ag/AgCl}$ .

As BSA showed some deposition on all surfaces, the release of BSA from the surfaces was further investigated using an external specific voltage. Graded solutions of 0.01 M, 0.1 M, 0.5 M and 1 M NaCl were used to release the deposited BSA from PPy, GO-PPy and MoS<sub>2</sub>-PPy surfaces. After deposition of BSA on the surfaces, the NaCl solutions were passed through the EQCM-D cells without the application of voltage, but no release was detected as there was no change in the frequency shift. Upon application of  $+0.74V_{Ag/AgCl}$  bias, 0.01M and 0.1M NaCl solutions still resulted in no release for 20 min. With the  $+0.74V_{Ag/AgCl}$  bias, 1 M NaCl showed the highest rate of BSA release from all surfaces as shown in Figure 3.17. The BSA removal rate was highest from the MoS<sub>2</sub>-PPy surface with a rate of 8.8 Hz min<sup>-1</sup> initially and 7.7 Hz min<sup>-1</sup> on average. From the PPy and GO-PPy surfaces, the average release rate was almost the same (6.215 Hz min<sup>-1</sup> and 6.205 Hz min<sup>-1</sup>, respectively). The release rate varied with time, with the highest release occurring in

first 5 minutes. Initially, current generated during chronoamperometry (under constant voltage) was high which indicates a more rigorous electrochemical reaction occurs in first 5 min. The addition of GO and MoS<sub>2</sub> onto the surface did not hamper the release performance. In the case of MoS<sub>2</sub>-PPy the release rate was slightly higher than from the PPy surface. Slower release rates were observed for all surfaces for release experiments with 0.5 M NaCl at +0.74 V<sub>Ag/AgCl</sub>. Under these conditions, average release rates of BSA from PPy, GO-PPy and MoS<sub>2</sub>-PPy surfaces were 3.76 Hz min<sup>-1</sup>, 2.61 Hz min<sup>-1</sup> and 2.16 Hz min<sup>-1</sup>, respectively. These release rates are 2-3 times lower than those with 1 M NaCl electrolysis treatment. From these data, it is clear that the concentration of chloride ions affects the degradation and release of the BSA layer. No measurable release of the BSA layer during 0.01 M and 0.1 M NaCl electrolysis treatments also indicates that there was insufficient free chlorine generation to release the BSA. Moreover, with the decrease in NaCl concentration, the overall conductivity of the solution decreases, which may also affect the BSA release rate. Higher conductivity results in easier and faster electron transport, resulting in a more efficient oxidation reaction at the surface.

In the presence of SSW with a +0.74 V<sub>Ag/AgCl</sub> bias, the release rate of BSA decreased significantly from the PPy, GO-PPy, and MoS<sub>2</sub>-PPy surfaces when compared to the 1 M NaCl electrolysis treatment results (Figure 3.17). However, the BSA release rates decreased with time indicating that the presence of divalent cations and other ions in the SSW can hamper the release performance. The average release rates during SSW electrolysis from PPy, GO-PPy, and MoS<sub>2</sub>-PPy surfaces were 1.28 Hz min<sup>-1</sup>, 1.19 Hz min<sup>-1</sup>, and 1.77 Hz min<sup>-1</sup>, respectively. Precipitation of salts during the electrolysis treatment is a likely reason for the decreased BSA release rate. It has

been hypothesized that precipitated solids can affect the electrochemical reactions by limiting the direct contact of free chlorine to the deposited BSA layer on the surface.

In brief, our results show that it was possible to delay the attachment of the BSA foulant on GO-PPy and MoS<sub>2</sub>-PPy surfaces significantly upon the application of  $-0.5V_{\text{Ag/AgCl}}$ , likely due to the electrostatic repulsion created by the external negative voltage on the surface. During the release study, it was found that it is possible to release the deposited BSA from all of the surfaces by NaCl electrolysis by applying a voltage of  $+0.74V_{\text{Ag/AgCl}}$ . Continuous generation of free chlorine (Cl<sub>2</sub>) accelerates the degradation of the deposited BSA, resulting in release of the foulant from the surface.

### 3.3 Experimental methods

#### 3.3.1 *Preparation of graphene oxide nanomaterial library*

GO was synthesized using a modified Hummers' method as described previously.<sup>167,267</sup> Natural graphite flakes (Asbury Mills, 3061 grade) were oxidized by exposure to concentrated sulfuric acid and other oxidizing agents. The slurry was then filtered, rinsed, and centrifuged to remove residual contaminants and unexfoliated graphite. The pellet was then re-dispersed in NMP and ultrasonicated for 1 hour at 50% power (~55 Watts) in a Fisher Scientific Model 500 Sonic Dismembrator. Following ultrasonication, the GO was centrifuged in a Beckman Coulter JS-7.5 rotor with a Beckman Coulter J26-XPI at 5000rpm (~4,620g) for 10 minutes. The top 80% of the supernatant was retained for further processing.

Chemically reduced GO were prepared by heating a purified GO suspension in NMP to 150°C with constant stirring in a silicone oil bath. The heat reflux was performed for 1, 2, or 5 hours to achieve varying levels of reduction. After solvothermal reduction, the rGO was separated from the

NMP using vacuum filtration with 0.1  $\mu\text{m}$  alumina filters (Millipore), rinsed heavily with DI water, and re-dispersed in DI water at an approximate concentration of 1 mg/mL.

### **3.3.2 *Physicochemical characterization of GO library***

For AFM imaging, silicon wafers were cleaned and dried, and then functionalized with a monolayer of (3-aminopropyl) triethoxysilane (APTES) by soaking the wafers in a 2.5 mM solution of APTES in isopropyl alcohol (IPA) for 30 minutes. Following the APTES treatment, the wafers were rinsed with IPA and dried with a nitrogen gun. The GO solutions were bath sonicated for 5 minutes before being drop-casted onto the APTES functionalized wafers. The GO was allowed to sit for 10 minutes on the wafer before being rinsed with water and dried with a nitrogen gun. The samples were then annealed at 250°C on a hotplate before imaging with a Cypher Asylum ES AFM.

FTIR measurements were performed directly on the GO and rGO in solution in NMP using attenuated total reflection (ATR) mode on a Thermo Nicolet Nexus 870 spectrometer. For XPS, approximately 5 mg of GO or rGO in DI water were deposited on a 0.1  $\mu\text{m}$  mixed cellulose ester filter (Millipore) using vacuum filtration. The film was allowed to settle for 15 minutes, rinsed with 30 mL DI water, and allowed to dry in air. XPS measurements were performed promptly using a Thermo Scientific ESCALAB 250Xi. XPS spectra were then corrected for background and fitted for peaks manually.

### **3.3.3 *Environmental stability of GO nanomaterials***

Electrokinetic and hydrodynamic properties of rGO were determined over a range of solution chemistries including different salt types (NaCl,  $\text{CaCl}_2$ ), varying IS, and NOM concentrations. Suwannee River Humic Acid Standard II (SRHA) (International Humic Substances Society, MN)

was used as standard NOM, and an SRHA stock solution was prepared with accepted procedures.<sup>308,321</sup> rGO hydrodynamic diameter ( $D_h$ ), electrophoretic mobility (EPM), and zeta potential were measured with a ZetaSizer Nano ZS (Malvern Instrument, Worcestershire, U.K.), following well-established techniques. Influence of pH on the physicochemical properties of rGO was investigated over a pH range from 4 to 10 in the presence of NaCl, CaCl<sub>2</sub> and MgCl<sub>2</sub>. This titration experiment was conducted using an autotitrator (MPT-2, Malvern Instrument, Worcestershire, U.K.); NaOH and HCl were the titrants for controlling pH.

Change of rGO  $D_h$  as a function of IS, ion valence, and presence of organic matter was measured by time-resolved dynamic light scattering (TR-DLS).<sup>322</sup> An rGO concentration of 10 mg/L provided a strong DLS signal and was therefore used in all aggregation studies. Both NaCl and CaCl<sub>2</sub> were background electrolytes. Long-term stability of GO and rGO was investigated in synthetic and natural waters to relate well-controlled simple solution chemistries to more complex, environmentally relevant conditions; eight types of water were used. 6 mL of 10 mg/L rGO suspended in the treatment water were placed in a 20-mL borosilicate glass bottle (Fisher Scientific, PA) and continuously shaken at 100 rpm; rGO concentration and  $D_h$  were monitored for 28 days. Concentration was determined using a UV-vis plate reader (Enspire Multimode Reader 2300, PerkinElmer Inc, MA) at 230 nm wavelength, and  $D_h$  was determined by a DynaPro Plate Reader II (Wyatt Technology, CA).

### **3.3.4 Photodegradation of GO nanomaterials**

Zeta potential, hydrodynamic diameter and polydispersity index of the particles were measured using a Zetasizer Nano ZS (Malvern Instruments, Inc.). A 1 cm light path quartz cuvette was used

for size measurements and a folded capillary cell DTS1070 was used for zeta potential measurements. Solutions were bath sonicated for 5 minutes prior to measuring.

Total organic carbon (TOC) was measured using a Shimadzu TOC-Vcsh total organic carbon analyzer utilizing the NDIR method (combustion at 720°C due to the attached total nitrogen measurement unit). Sample solutions were diluted and transferred to 40mL vials. The volume of injected solution was 80  $\mu$ L, with three injections for each sample. After analyzing 10 samples, a wash was done.

### ***3.3.5 Antifouling properties of GO and MoS<sub>2</sub> functionalized surfaces***

GO dispersions were prepared as described in section 3.3.1. Chemical exfoliation using lithium intercalation was used to produce MoS<sub>2</sub> nanosheets, as described in a previous study.<sup>140</sup> Briefly, lithium intercalation was achieved by combining bulk MoS<sub>2</sub> powder and butyllithium in a low vapor and oxygen condition. The lithiated MoS<sub>2</sub> was rinsed extensively with hexane, filtered, and exfoliated by the addition of deionized water. The resulting dispersion was centrifuged to remove any unexfoliated material. The supernatant was further dialyzed against DI water for 7 days to remove residual lithium and hexane.

Suwannee River humic acid (Standard II, International Humic Substances Society) was used to prepare the NOM suspension at a concentration of 10 mg/L. *Escherichia coli* (*E. coli*, MG1655, K-12) was supplied by the *E. coli* Genetic Resource Center of Yale University. GO or MoS<sub>2</sub> surfaces on gold crystals for QCM-D measurements were prepared by modifying the gold sensors with cationic Poly-L-lysine hydrobromide (PLL, molecular weight 70 000–150 000 Da by viscosity, P-1274, Sigma Aldrich, St. Louis, MO). PLL was dissolved in HEPES buffer (pH 7.4) made from 10 mM *N*-(2-hydroxyethyl) piperazine-*N*-2-ethanesulfonic acid (Sigma), 100 mM

NaCl, and deionized water, and was stored at 4 °C. The final concentration of the stock PLL solution was 0.1 g L<sup>-1</sup>. The gold substrate cells were exposed to the PLL stock solution for 15-20 min to create a homogeneous layer. Calcium chloride (CaCl<sub>2</sub>·2H<sub>2</sub>O, CAS 10035048), sodium chloride (NaCl, CAS 7647-14-5), and magnesium chloride (MgCl<sub>2</sub>·6H<sub>2</sub>O, CAS: 7791-18-6) were used to prepare salt solutions. 10 mM NaCl and 0.5 mM CaCl<sub>2</sub>/MgCl<sub>2</sub> were used for the experiment. 10 mg/L GO and 50 mg/L MoS<sub>2</sub> were prepared from the stock sample solutions.

### 3.4 Summary

Since a significant fraction of graphene-based nanomaterials may be transformed to rGO via sunlight and microorganisms, it is necessary to understand the fate of rGO. We show that colloidal stability of rGO in the aquatic environment varies as a function of pH, ionic strength, ion valence, and presence of NOM. pH can play a significant role in the stability of rGO. Although GO remains highly stable from pH 4 to 10, stability of rGO increases significantly with increased pH, indicating that pH variation in the natural environment plays an important role in the stability of rGO. We also show that Ca<sup>2+</sup> ions can affect stability of GO and rGO, in particular decreasing stability at high pH. While GO remains highly stable at pH 7 in 10 mM NaCl, adding only 0.1 mM CaCl<sub>2</sub> destabilizes it immediately. Since most natural and engineered aquatic systems contain a small amount of CaCl<sub>2</sub>, pH and Ca<sup>2+</sup> ions can have a major effect on stability of GO and rGO in the environment. The long-term stability study shows a significant amount of partially-reduced GO remains suspended in Call's Creek water, indicating rGO may not be removed completely from surface waters. Adding NOM can increase the stability of rGO more than that of GO, particularly

in the presence of  $\text{Ca}^{2+}$  ions, indicating that NOM and divalent ions play major roles in the stability of rGO.

Furthermore, our studies indicate that sunlight induced photolysis can degrade graphene oxide and reduced graphene oxide in the environment. The oxygen-containing functional groups, mainly those present on the basal plane, play a strong role in the photodegradation of the GO and rGO sample. This degradation will have an obvious impact on the fate on these emerging materials in the environment. Based on the findings of this research, it can be assumed that graphene oxide nanomaterials will undergo degradation in natural surface water due to sunlight exposure. However, graphene oxide nanomaterials with higher levels of oxidation will experience higher rates of photodegradation while reduced forms of graphene oxide will show a higher resistance to this degradation, due to fewer defects and functional groups on the surface as well as increased aggregation in aqueous environments.

Due to their unfavorable interactions with NOM and other foulants present in aquatic systems, GO and an analogous TMDC ( $\text{MoS}_2$ ) offer opportunities to engineer novel membranes for water filtration applications. In our fundamental study of these interactions, we found that  $\text{Ca}^{2+}$  and  $\text{Mg}^{2+}$  play a significant role in bridging with NOM molecules and GO and  $\text{MoS}_2$  functionalized surfaces. The presence of  $\text{Ca}^{2+}$  and  $\text{Mg}^{2+}$  along with NOM in natural water results in the deposition of a layer of NOM that may impede high water flux and thus the efficiency of the membrane. Monovalent ions have less effect on the accumulation of foulants on the material surfaces. Additionally, *E. coli* showed deposition on both GO and  $\text{MoS}_2$  surfaces. Comparing the attachment efficiencies and frequency shifts in every case, it was found that  $\text{MoS}_2$  shows more potential for antifouling applications than GO. Functional groups on GO can interact with the monovalent and

divalent cations as well as with foulants, causing accumulation and deposition on the material surface. Electrostatic interactions and bridging effects can be altered by changing the solution chemistry, providing a possible approach for cleaning and regeneration of the material surface.

One such approach involved the application of an external potential in order to delay the attachment or reverse the deposition of foulants on the surface. We observed that the application of a small external potential ( $\pm 0.5V_{Ag/AgCl}$ ) plays a significant role in delaying the attachment of BSA onto MoS<sub>2</sub>-PPy and bare PPy surfaces. Even without any applied voltage, the MoS<sub>2</sub>-PPy surface performs better than a control PPy surface and a functionalized GO-PPy surface in terms of attachment efficiency and overall BSA deposition mainly due to the high energy barrier between MoS<sub>2</sub> and the foulant. However, due to the complex structure and hydrophobic nature of BSA, there is still a significant amount of attachment. Even though this same high energy barrier exists in the case for GO-PPy surface, the functional groups of GO create favorable interactions for BSA deposition. By applying negative voltage, it was possible to decrease BSA attachment by 50-70%, due to the increased electrostatic repulsion, increased mobility of foulants, and the generation of biocides on the MoS<sub>2</sub>-PPy and PPy surfaces. Due to the non-conductive nature of GO, the BSA attachment delay was not as significant, but an improvement was still observed. This application of external voltage provides a method to make foulant cleaning easier and faster, especially with the highly effective MoS<sub>2</sub>-PPy surface used in this study. The presence of chloride ions in the water has been found to be equally beneficial on all of the surfaces by generating biocides such as free chlorine under positive potential. Free chlorine generation was independent of the PPy/MoS<sub>2</sub>/GO surface properties and highly dependent on the concentration of NaCl in water. Regeneration of the membrane surface by applying an external voltage provides an alternative

option to full replacement of fouled membranes. This type of technology will also greatly benefit the marine industry for removal of foulants from ship hulls in seawater where there is an abundance of chloride ions. Moreover, cleaning the membrane surfaces physically by applying voltage rather than chemical cleaning presents several practical advantages in terms of cost and time.

**CHAPTER 4:**  
**AQUEOUS STABILITY OF EXFOLIATED BLACK PHOSPHORUS**

This chapter is based, in part, on the research described in the following publication:

Guiney, L. M.; Ramesh, M.; Kang, J.; Sponenburg, R. A.; MacRenaris, K.; Hersam, M. C.  
“Stability of solution-processed black phosphorus in aqueous and biological media,” in preparation

## 4.1 Background

Black phosphorus (BP), a layered allotrope of phosphorus, has recently been explored for its potential applications in electronics and optoelectronics.<sup>72,73,79,323,324</sup> The bandgap of BP varies as a function of thickness from 0.3 eV to ~2 eV, allowing broadband absorption from the visible to the mid-infrared region, which is highly desirable for optoelectronics.<sup>76–78</sup> Furthermore, the semiconducting nature and high carrier mobility of BP enable its use in high-performance electronic devices such as field-effect transistors.<sup>113,118,325–327</sup> However, the chemical reactivity of BP has limited its deployment in many technologies since device performance degrades in many common environments such as ambient conditions.<sup>328,329</sup> As a result, a number of schemes have been developed to passivate the surface of BP in an effort to mitigate deleterious degradation pathways. For example, the encapsulation of BP with thin films of aluminum oxide prevents exposure to water and oxygen and thus minimizes BP oxidation.<sup>330</sup> Covalent chemical functionalization of the BP surface has also been shown to slow the degradation of BP in ambient conditions.<sup>331</sup> Although these passivation schemes enable the use of BP in ambient conditions, a fundamental understanding of the chemical reactivity of BP in other environments has the potential to broaden its range of potential applications.

Although BP is the most stable allotrope of phosphorus, in the few-layer limit, the kinetics of degradation are accelerated, resulting in rapid degradation in ambient conditions.<sup>332</sup> Even though light, oxygen, and water have been identified as the main factors that drive the chemical degradation of BP, the specific roles of these factors and their relative importance in the degradation mechanism are still being debated.<sup>80–85,333,334</sup> While this environmental instability is considered to be a drawback for many electronic and optoelectronic applications, this same

degradation provides opportunities for biomedical applications. In particular, the biodegradation of BP *in vivo* has the potential to eliminate the challenges associated with alternative nanomaterial constructs that tend to persist, aggregate, or bioaccumulate, thus causing toxicity issues over time.

As a result of this potential for biodegradability, recent research has focused on exploiting BP for biological applications including drug delivery, imaging, sensing, and theranostics.<sup>75,103,129,150,335,336</sup> For example, the high surface area of exfoliated BP nanosheets allows for high levels of functionalization that are desirable for drug delivery vehicles.<sup>86–88</sup> As an ultrathin semiconductor, BP nanosheets also offer potential for transistor-based biosensors.<sup>90</sup> With intrinsic thickness-dependent photoluminescence, BP nanosheets can further be employed as biomedical fluorescence agents.<sup>91</sup> In addition, due to efficient optical absorption in the infrared biological transparency window, BP nanosheets possess a high photothermal conversion rate, offering potential as a biodegradable photothermal therapy agent.<sup>92–94,149</sup> Combining these attributes, BP nanosheets can also achieve more functional synergistic theranostic applications.<sup>74,95,337</sup>

Despite this broad and diverse potential in biomedical applications, BP research in the biological field remains in its infancy since fundamental interactions with biological media have not been fully explored. In this regard, scalable solution-based production methods such as liquid phase exfoliation (LPE) of bulk BP crystals are critical to produce sufficient quantities of exfoliated BP nanosheets for thorough spectroscopic characterization in aqueous environments.<sup>103,118</sup> In this manner, early work has studied the degradation products and kinetics of BP nanosheets in water,<sup>338</sup> although the broader range of aqueous environments encountered in biomedical applications have not been thoroughly investigated. To address this knowledge gap,

here we study the role of biologically relevant environmental factors such as solution composition, temperature, dissolved oxygen, ionic strength, and pH on the aqueous stability of BP nanosheets. By quantifying the degradation kinetics and products of BP under this broad range of conditions, this work aims to establish the suitability of BP nanosheets for a diverse set of biomedical applications.

## 4.2 Results and discussion

### 4.2.1 *Aqueous liquid phase exfoliation of black phosphorus*

Using a LPE process developed previously,<sup>118</sup> BP bulk crystals were exfoliated by ultrasonication in deionized (DI)-water in which the dissolved oxygen has been removed by ultrahigh purity Ar gas bubbling. As with most solution-based exfoliation processes, this aqueous LPE method results in a polydisperse solution of BP nanosheets with average thicknesses of ~8 nm and an average lateral size of ~100 nm (Figure 4.1A). X-ray photoelectron spectroscopy (XPS) and Raman spectroscopy were used to confirm that the BP nanosheets do not experience any significant chemical degradation during the exfoliation process. In Figure 4.1B, the XPS shows the characteristic P 2p doublet at ~132 eV. Oxidized phosphorus species ( $\text{PO}_x$ ) would appear around 135 eV, but are not evident following sonication. The distinctive Raman modes of LPE BP nanosheets (i.e.,  $A_g^1$  at  $\sim 359\text{ cm}^{-1}$ ,  $B_{2g}$  at  $\sim 435\text{ cm}^{-1}$ , and  $A_g^2$  at  $\sim 462\text{ cm}^{-1}$ ) are observed in the Raman spectrum as shown in Figure 4.1C. Optical absorbance spectra of BP dispersions possess peaks at ~460 nm (Figure 4.1D). The mass extinction coefficient of the LPE BP dispersion was determined using the Beer-Lambert law at 460 nm (Figure 4.1D, inset).

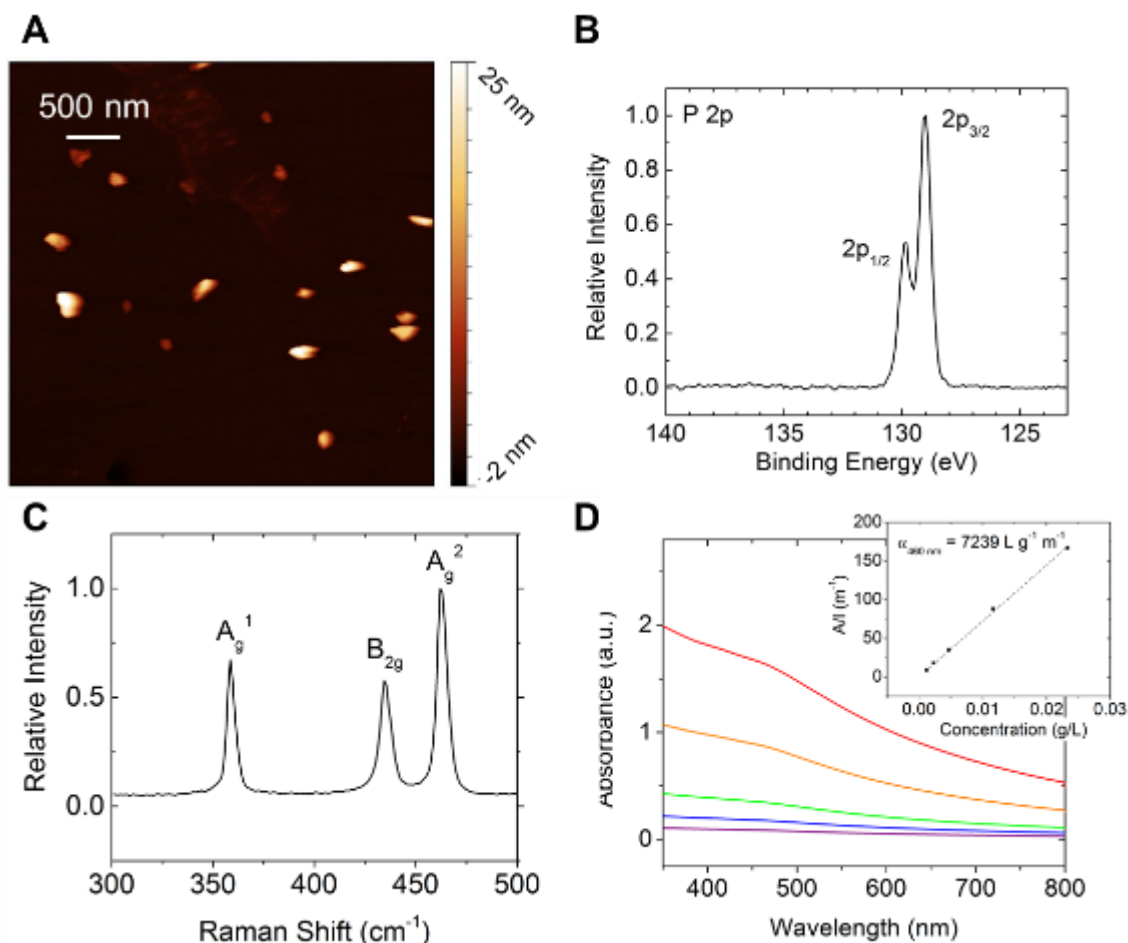


**Figure 4.1:** Characterization of BP in DI-water prepared by LPE. (A) AFM image of BP nanosheets. (B) XPS analysis of the P 2p doublet and (C) Raman spectrum for BP demonstrating no oxidation or chemical changes. (D) Optical absorbance spectra of BP nanosheets dispersed in DI-water at varying concentrations and the mass extinction coefficient of exfoliated BP in DI-water as determined by the Beer-Lambert law (inset).

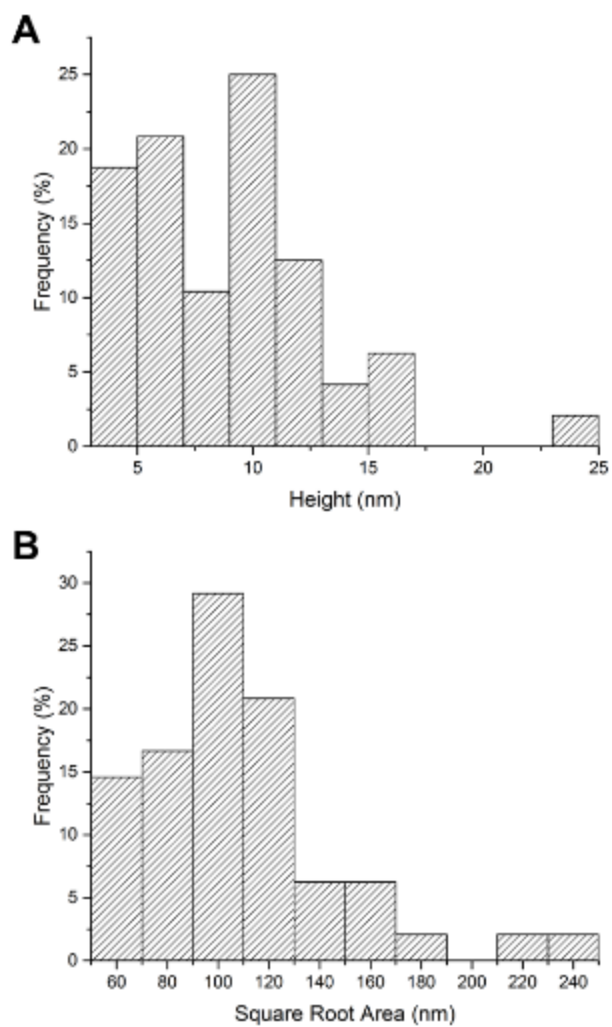


**Figure 4.2:** AFM height (A) and lateral size (B) histograms for solution-processed BP nanosheets.

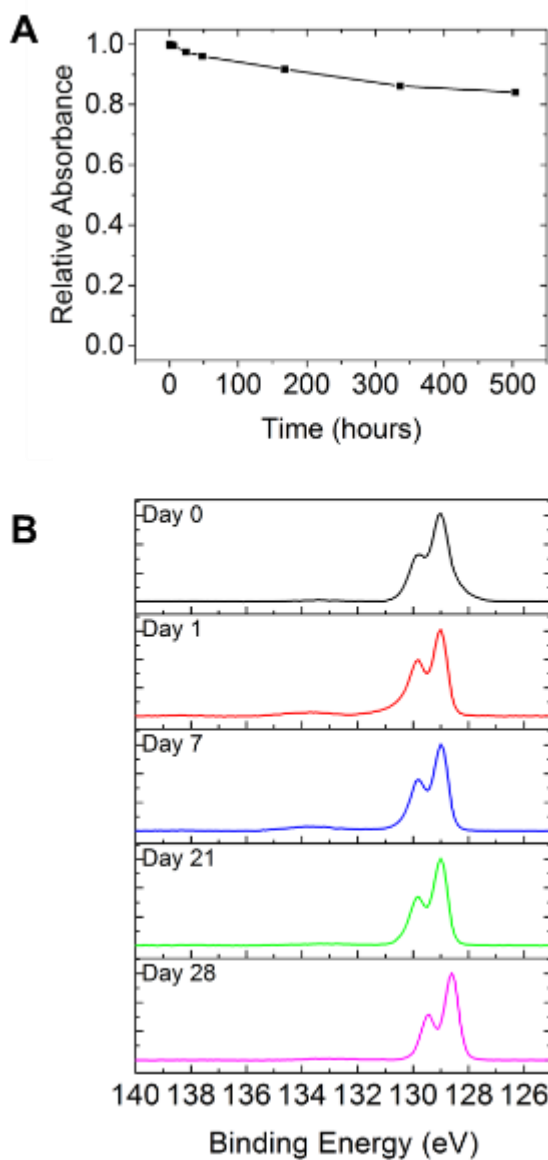


**Figure 4.3:** (A) Suspension stability and (B) chemical stability of aqueous dispersion of BP nanosheets after exposure to ambient conditions over time. Suspension stability was measured by the optical absorbance at 460 nm. Chemical stability was measured using XPS analysis.

#### 4.2.2 *Effects of surfactant selection*

Previous reports have employed amphiphilic surfactants to stabilize BP nanosheets in aqueous environments.<sup>105,118</sup> However, the LPE method employed here did not require surfactants to produce stable aqueous dispersions of BP nanosheets. Nevertheless, as a comparison for BP in DI-water alone, additional surfactant-assisted aqueous BP dispersions were prepared using 2% w v<sup>-1</sup> Pluronic F68 (F68) and 2% w v<sup>-1</sup> sodium dodecyl sulfate (SDS). SDS was chosen as a prototypical ionic surfactant since previous studies showed that SDS is effective in exfoliating and stabilizing BP in aqueous environments.<sup>118</sup> In addition, F68, a triblock copolymer consisting of a central chain of polypropylene oxide and flanked by two chains of polyethylene oxide, was selected as a prototypical nonionic surfactant due to its established biocompatibility and effectiveness in dispersing other 2D nanomaterials in aqueous media.<sup>7,57,111,120</sup> Under the same preparation conditions, the presence of F68 during exfoliation resulted in the highest exfoliation yield of 3.4%, whereas SDS showed the lowest exfoliation yield of 0.6% (Figure 4.4A, Table 4.1). Following exfoliation, the stability of these BP dispersions was monitored over time while being exposed to ambient conditions. After only 48 hours, BP dispersed in DI-water with SDS (red) showed significant degradation, while BP dispersed in DI-water (black) with F68 (blue) remained stable as monitored by optical absorbance spectroscopy (Figure 4.4B). In addition to solution stability, chemical degradation was monitored with XPS spectroscopy as shown in Figure 4.4C. For BP dispersed in DI-water and F68-water, the characteristic P 2p doublet remains intact following 7 days of solution aging in ambient conditions. On the other hand, after 7 days in SDS-water, the XPS spectrum shows a broad peak at ~135 eV, which is indicative of the formation of PO<sub>x</sub> species.

Therefore, it can be concluded that surfactant identity affects both the exfoliation yield and the overall stability of the resulting BP dispersions.

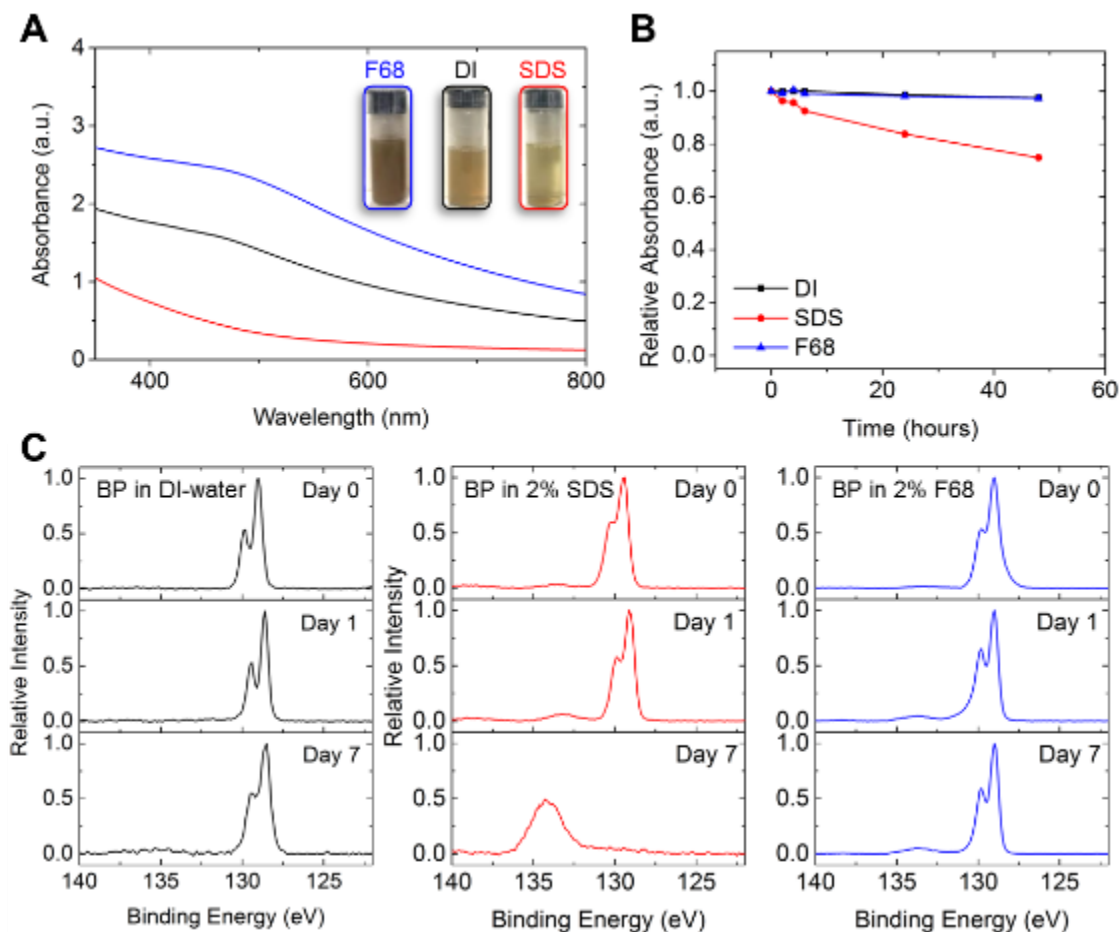


**Figure 4.4:** Dispersion and chemical stability of BP nanosheets with different surfactants. (A) Optical absorbance spectra and photographs (inset) of BP exfoliated in DI water (black), 2% w/v SDS (red) and 2% w/v Pluronic F68 (blue) using identical preparation conditions. (B) Dispersion stability of BP dispersions after exposure to air under ambient conditions. (C) XPS spectra of the P 2p region for the BP dispersions immediately after processing, 1, and 7 days.

**Table 4.1:** Exfoliation yield of BP nanosheets in different surfactants. Final BP concentration is calculated from the mass extinction coefficient shown in Figure 4.1D.

Sample	Initial BP Loading ( $\mu\text{g mL}^{-1}$ )	Dispersion Absorbance at 460 nm	Final BP Concentration ( $\mu\text{g mL}^{-1}$ )	Yield (%)
BP in DI-water	1000	1.59	21.97	2.2
BP in 2% w v <sup>-1</sup> SDS	1000	0.47	6.43	0.6
BP in 2% w v <sup>-1</sup> F68	1000	2.46	33.97	3.4

#### 4.2.3 Stability of BP in biological media

Beyond DI-water and aqueous surfactant solutions, the dispersion stability of BP nanosheets in biological media must also be considered for most biomedical applications. Towards this end, phosphate buffered saline (PBS) and Dulbecco's modified Eagle's medium (DMEM) were selected as representative media due to their widespread use in biological assays. Native (non-deoxygenated) DI-water was also used as a control to determine the role of dissolved oxygen on the stability of BP dispersions after exfoliation. The dispersion stability was monitored using optical absorbance spectroscopy and nanoparticle tracking analysis (NTA), while chemical degradation was monitored using XPS and Raman spectroscopy. As shown in Figure 4.5A, when diluted into native DI-water, the BP nanosheets show minimal degradation over a time period of 48 hours. In the same time window, only 68% of the BP nanosheets remain dispersed in DMEM. This rapid degradation is even more pronounced in PBS with only 28% of the BP nanosheets remaining dispersed after 48 hours. To confirm that the changes in the optical absorbance spectra were due to decomposition of the BP nanosheets as opposed to aggregation, NTA was used to probe the average particle size over time, which revealed no significant aggregation in any of the

samples (Figure 4.6). XPS analysis further indicates that while some oxidation of the BP nanosheets takes place in native DI-water, more significant oxidation occurs in PBS and DMEM (Figure 4.7). A similar trend in degradation rate was observed for BP dispersions stabilized with SDS and F68, which indicates that the presence of surfactants does not have a significant effect on the decomposition kinetics of BP nanosheets in biological media (Figures 4.5B, C).

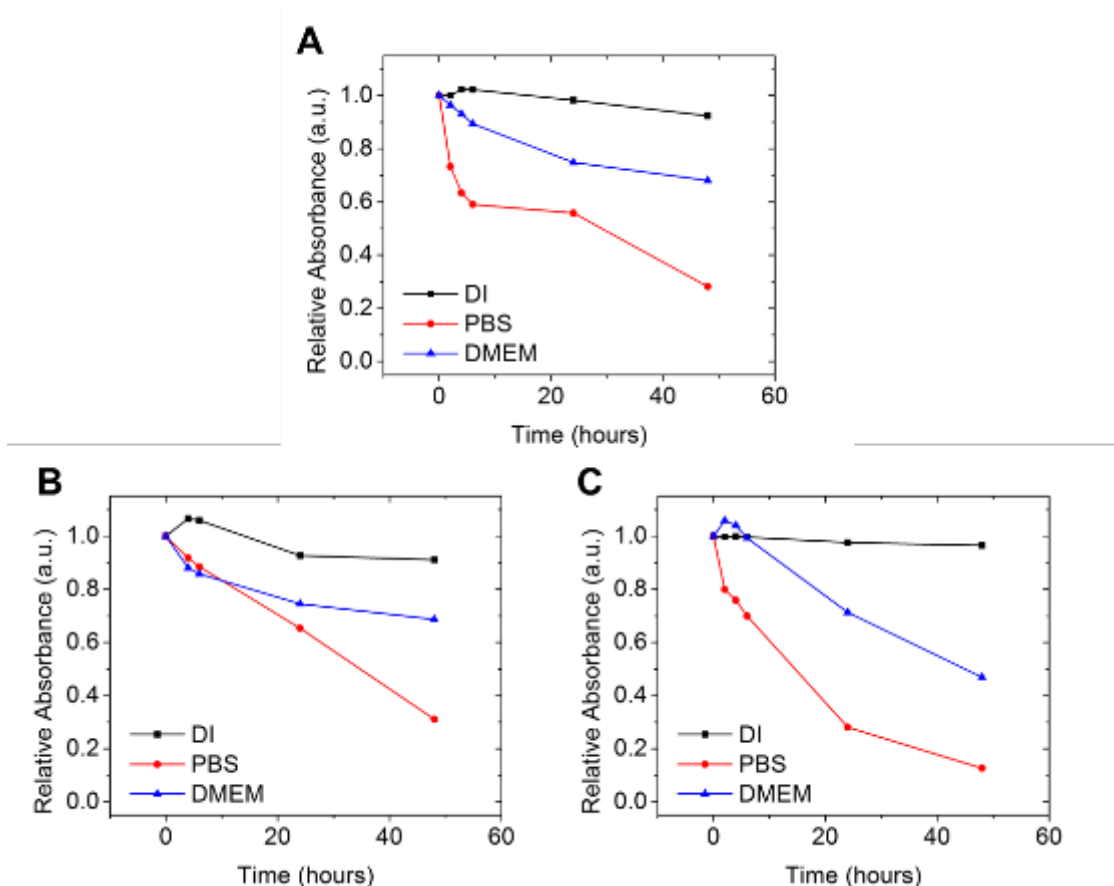


**Figure 4.5:** Stability of BP nanosheets in DI-water (A), 2% w v<sup>-1</sup> SDS-water (B), and in 2% w v<sup>-1</sup> F68-water (C) dispersions after dilution into native (oxygen-containing) DI-water, PBS, and DMEM. All measurements are normalized optical absorbance intensities at 460 nm.

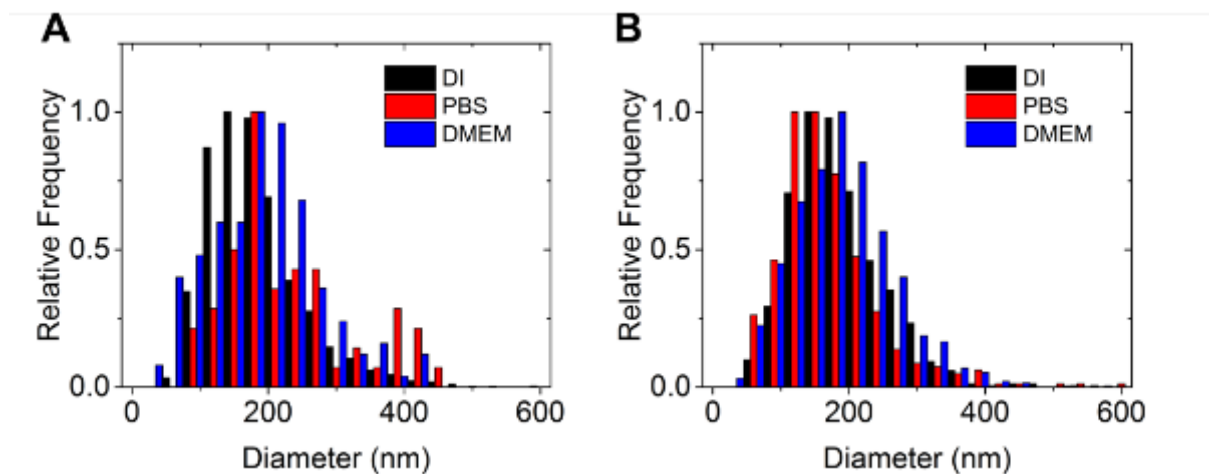


**Figure 4.6:** Size distributions of BP nanosheets after dilution into native biological media (DI-water, PBS, and DMEM) after 1 hour (A) and 48 hours (B) as measured by NTA.

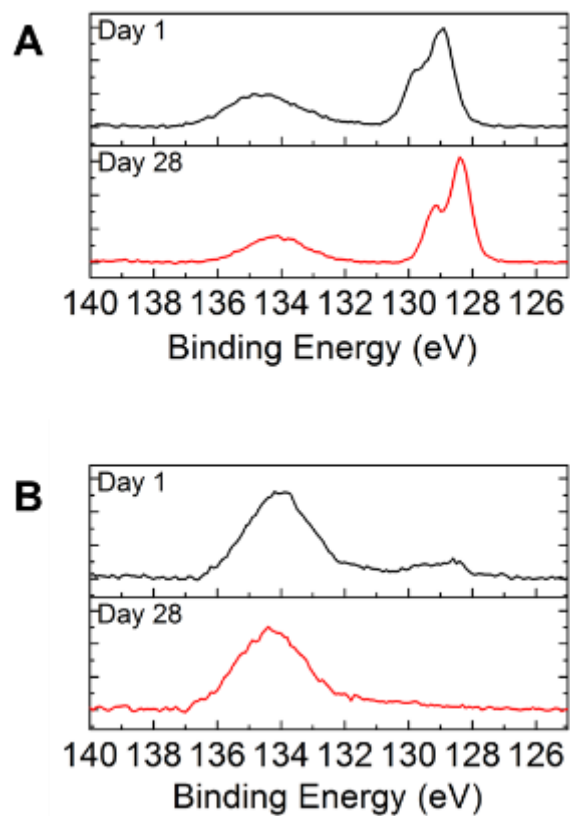


**Figure 4.7:** XPS spectra of BP nanosheets after dilution into native (oxygen-containing) DI-water (A) and native PBS (B) after 1 day and 28 days.

#### 4.2.4 Processing and environmental factors affecting stability

All of the stability studies discussed thus far were carried out in ambient conditions at room temperature. However, for many biological applications, the performance of the BP construct needs to be assessed at elevated temperatures. Accordingly, a comparative study of the stability of the BP dispersions in deoxygenated DI-water was performed at room temperature (24 °C) and at body temperature (37 °C) using optical absorbance spectroscopy (Figure 4.8A). These measurements revealed that the degradation rate of BP nanosheets in deoxygenated DI-water is highly dependent on temperature with enhanced kinetics at 37 °C compared to room temperature. Consequently, when considering BP nanosheets for biological applications such as therapeutics and imaging, the window of efficacy and stability will be reduced *in vivo* compared to *in vitro* experiments carried out under ambient conditions.

Figures 4.8B, C explore the role of other key factors in the aqueous stability of BP nanosheets. Here, the parameters of the exfoliation process were varied to determine the role of BP nanosheet size and dissolved oxygen in the dispersion stability. As mentioned previously, the LPE dispersions of BP nanosheets in DI-water contain a wide distribution of flake thicknesses and lateral sizes. In Figure 4.8B, the centrifugation parameters following sonication were varied to achieve different levels of sedimentation of the BP nanosheets. The resulting dispersions varied from thicker and larger flakes (750 rpm for 10 minutes) to thinner and smaller flakes (15,000 rpm for 10 min). As the centrifugation parameters were increased and the corresponding average flake size became smaller, the degradation rate of the BP nanosheets increased, indicating higher stability for thicker and larger flakes. Meanwhile, in Figure 4.8C, the role of deoxygenated water in the exfoliation process is illustrated. Here, separate dispersions of BP were prepared by LPE in

deoxygenated and native (non-deoxygenated) DI-water, after which the optical absorbance was monitored. The absorbance of BP nanosheets in deoxygenated DI-water shows no measurable change after 10 days, whereas the BP in native DI-water shows significant degradation, with only ~80% of the BP nanosheets remaining dispersed in solution after 10 days. Faster degradation of the BP nanosheets in native, non-deoxygenated DI-water suggests that the deoxygenated DI-water processing results in an effective passivation layer on the BP nanosheets that arrests further degradation. Thus, the use of deoxygenated DI-water to initially exfoliate the BP is critical to the long-term stability of the material in aqueous environments.

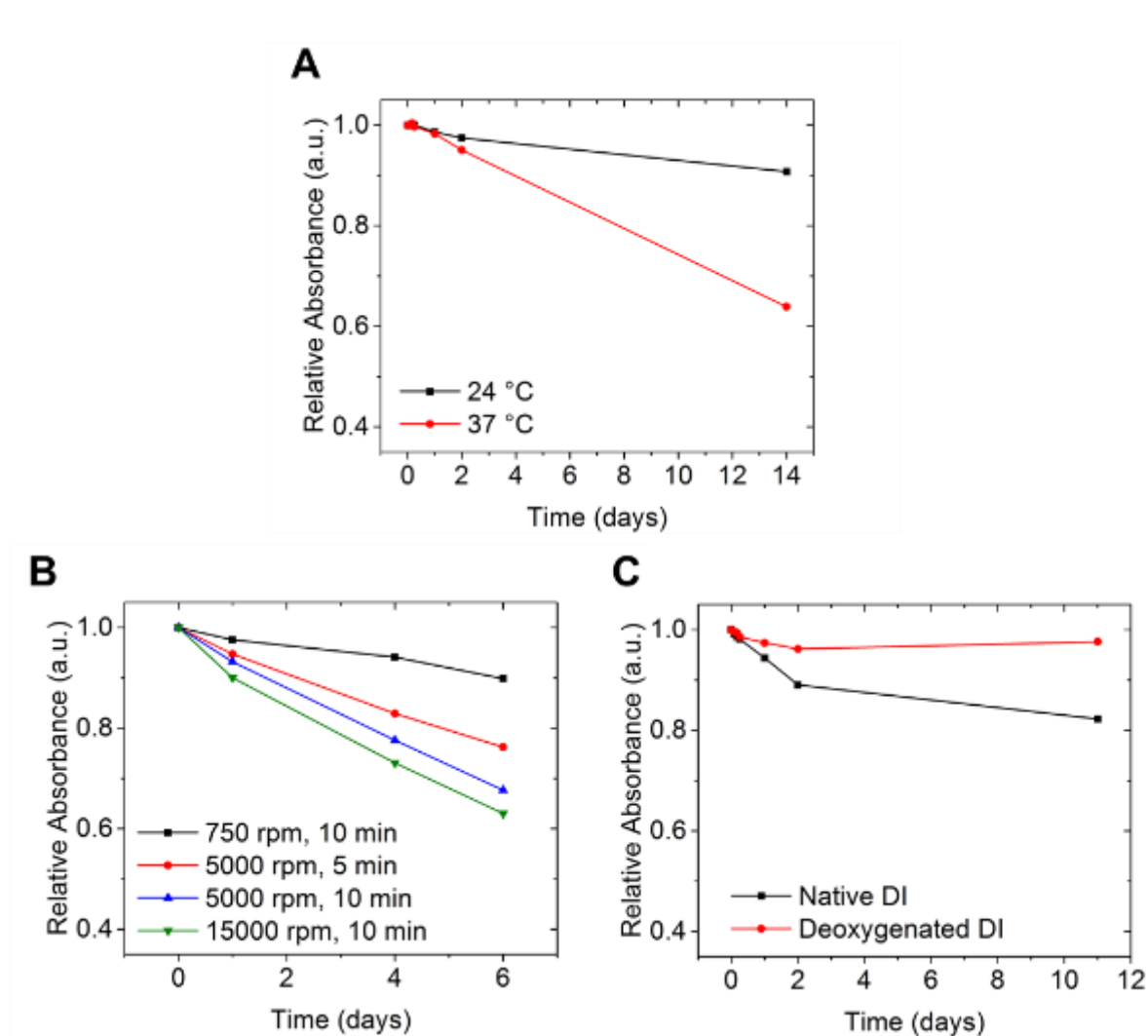


**Figure 4.8:** Factors affecting the degradation rate of aqueous dispersions of BP nanosheets. (A) Stability of BP in DI-water at room temperature (24 °C) and body temperature (37 °C). (B) Stability of BP in DI-water with different centrifugation conditions. (C) Stability of BP in native DI-water and deoxygenated DI-water. All measurements are normalized optical absorbance intensities at 460 nm.

Ionic strength and pH were also varied to determine their effects on the stability of aqueous dispersions of BP nanosheets. Two common and biologically relevant monovalent salt solutions based on potassium chloride (KCl) and sodium chloride (NaCl) were prepared at increasing concentrations. Raw BP dispersions were then added to the salt solutions, and the optical absorbance was monitored to determine the suspension stability (Figure 4.9). For both KCl and NaCl, the degradation rate of the BP nanosheets showed a strong concentration dependence. In particular, at high concentrations of KCl and NaCl, BP degrades more rapidly, indicating that the BP decomposition rate is strongly dependent on ionic strength. These results also provide a possible explanation for why BP nanosheets dispersed with SDS show lower exfoliation yields and higher degradation rates than BP nanosheets in DI-water. Specifically, as an ionic surfactant, SDS leads to the presence of Na cations in solution that may play a role in accelerating the decomposition of BP nanosheets in a manner similar to aqueous NaCl solutions. On the other hand, variations in pH within a biologically relevant window from pH 5.9 to pH 8.1 resulted in no significant differences in the BP degradation rate (Figure 4.10).

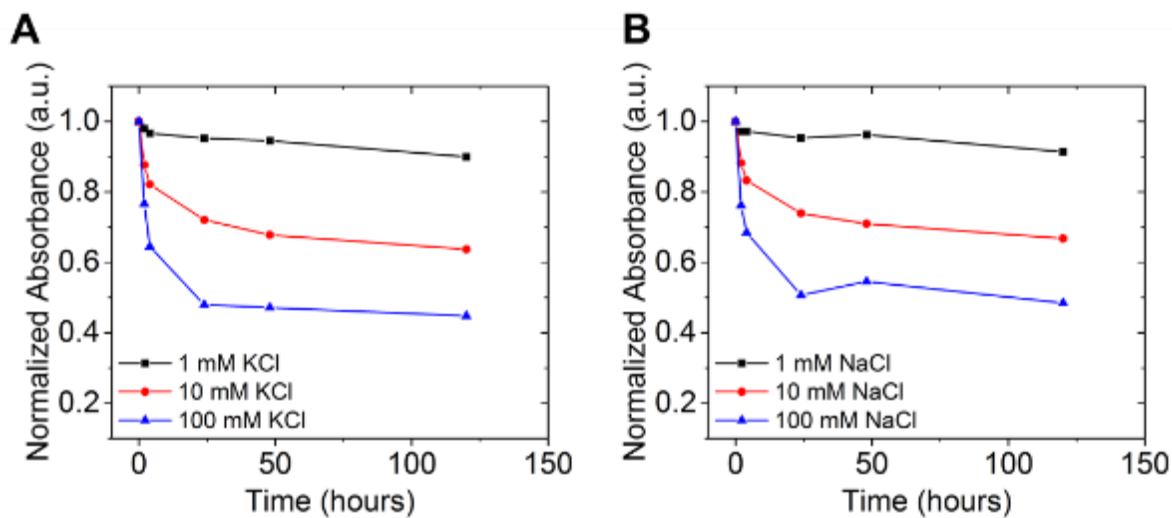


**Figure 4.9:** Degradation of BP dispersions as a function of ionic strength. Stability of BP in DI-water after dilution into native (oxygen-containing) solutions of varying concentrations of (A) KCl and (B) NaCl. Reported values are normalized optical absorbance intensities at 460 nm.

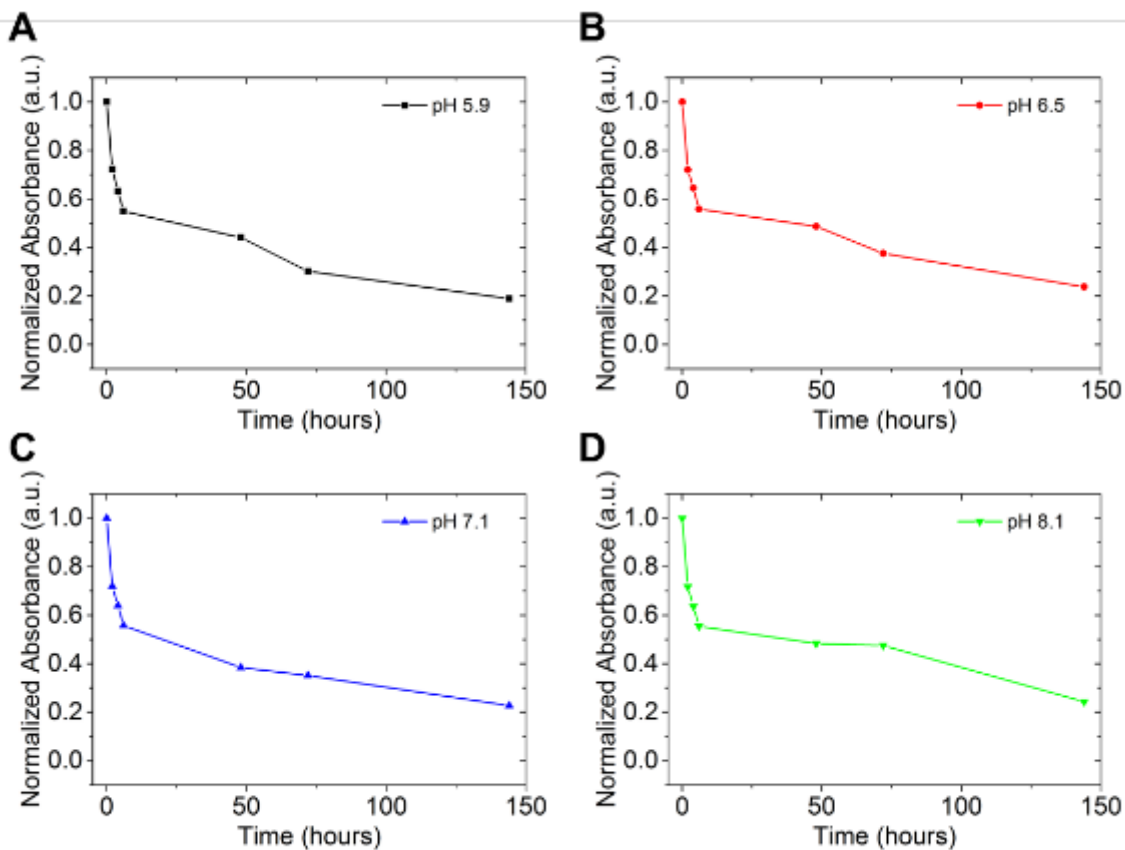


**Figure 4.10:** Stability of BP dispersion in phosphate buffers at varying pH: (A) pH 5.9, (B) pH 6.5, (C) pH 7.1, (D) pH 8.1. All measurements are normalized optical absorbance intensities at 460 nm.

#### 4.2.5 Degradation products of black phosphorus

Finally, the decomposition products of BP in aqueous media were identified and quantified, since they are likely to play a significant role in the biological fate and environmental impact of BP nanosheets. Using ion chromatography, phosphorus oxide species were separated and quantified using known standards. In particular, the BP aqueous dispersions in varying KCl concentrations from Figure 4.9A were measured using ion chromatography after 7, 30, and 60 days (Figure 4.11A). These experiments revealed four chromatography peaks that all increased with time. The four peaks were identified as different phosphorus oxide anion species: hypophosphite ( $\text{H}_2\text{PO}_2^-$ ), phosphite ( $\text{HPO}_3^{2-}$ ), phosphate ( $\text{PO}_4^{3-}$ ), and pyrophosphate ( $\text{P}_2\text{O}_7^{4-}$ ). The phosphate and phosphite anions were the most abundant degradation products. While the concentration of all species increased consistently over the two-month time period, only small increases in the amount of pyrophosphate were observed, most likely due to the hydrolysis of pyrophosphate into smaller phosphorus oxide anions in water. Similar results were observed for the BP dispersions diluted in solutions of NaCl (Figure 4.11B). Since all of the detected phosphorus oxide anions occur naturally in the human body and are involved in biological processes, it is unlikely that the decomposition of BP will result in deleterious effects *in vivo* at biological relevant concentrations.

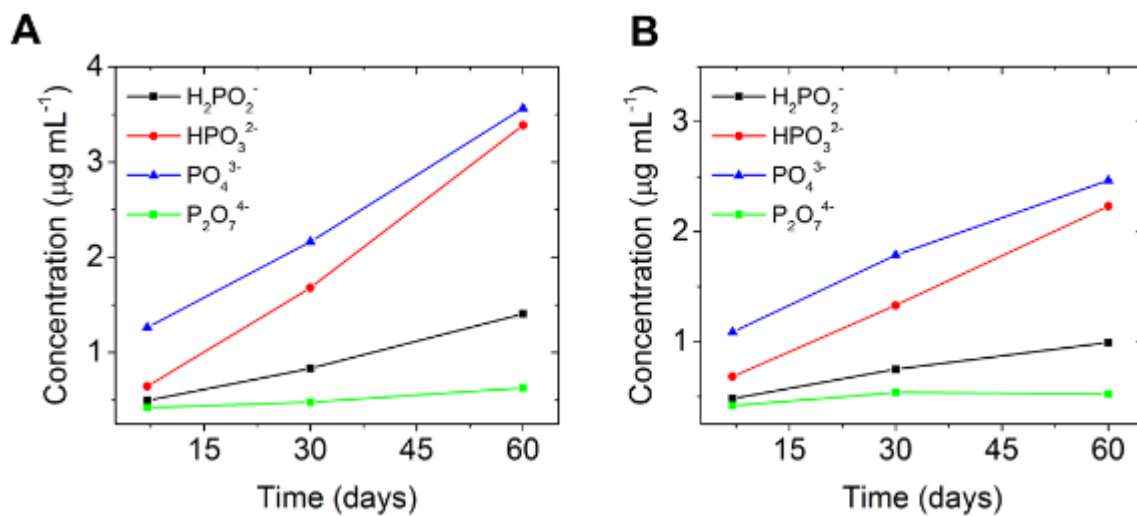


**Figure 4.11:** Degradation products of black phosphorus. Ion chromatography analysis of degradation products of BP dispersions in (A) 1 mM KCl and (B) 1 mM NaCl after 7, 30 and 60 days.

### 4.3 Experimental methods

#### 4.3.1 *Liquid phase exfoliation of BP*

Black phosphorus (BP) bulk crystal was purchased from Smart Elements and stored in a dark N<sub>2</sub> glovebox. Dissolved oxygen was removed from deionized water (DI-water, 18 M $\Omega$ ) by bubbling with ultrahigh purity (UHP) Ar gas for 30 minutes. For surfactant-assisted exfoliation, sodium dodecyl sulfate (SDS, Fisher Scientific) and Pluronic F68 (F68, Sigma Aldrich) were dissolved in DI-water at a 2% w v<sup>-1</sup> loading. The solutions were then deoxygenated similarly using UHP Ar gas for 30 minutes. In an Ar atmosphere, BP crystal was transferred into the deoxygenated solution at an approximate loading of 1 mg mL<sup>-1</sup>. The vessel was then sealed and sonicated using a probe sonicator (Fisher Scientific model 500 sonic dismembrator) for 1 hour at 65 W while being cooled on an ice bath. Following sonication, unexfoliated material was sedimented by centrifugation at 5,000 rpm for 10 minutes (Beckman Coulter Avanti J-26 XP). In an Ar atmosphere, the resulting supernatant was aliquoted into vials and sealed until further characterization. For stability studies, BP dispersions were diluted into DI-water, Dulbecco's phosphate buffered saline (PBS, 1X; without calcium, magnesium, phenol red, sodium pyruvate; Life Technologies), Dulbecco's modified Eagle's medium (DMEM, 1X, Life Technologies), salt solutions, or pH buffers at a 1:4 ratio and then stored under ambient conditions.

#### 4.3.2 *BP dispersion characterization*

Atomic force microscopy (AFM) images were collected in tapping mode using an Asylum Cypher ES. BP solutions were dropcasted onto clean SiO<sub>2</sub> substrates at 80 °C and allowed to evaporate, after which AFM measurements were immediately taken. The same samples were used to collect scanning electron microscopy (SEM) images using a Hitachi SU8030. X-ray

photoelectron spectroscopy (XPS, Thermo Fisher ESCALAB 250 Xi, Al K $\alpha$  X-ray source) and Raman spectroscopy (Horiba LabRAM HR Evolution, 532 nm excitation) samples were prepared by vacuum filtration of BP dispersions onto an anodic aluminum oxide membrane (0.02  $\mu$ m pore size, Whatman). UV-vis optical absorbance spectra were collected using an Agilent Technologies Cary 5000 spectrophotometer. Nanoparticle tracking analysis was performed using a NanoSight Nanoparticle Tracking Analysis system.

#### ***4.3.3 Determination of degradation products***

Degradation products of BP dispersion was determined using ion chromatography (IC, Dionex 5000+) with suppressed conductivity determination, modified from Dionex Application Note 71 (AN71). Method details and concentration curves are shown in Figure 4.12. Samples were filtered using 0.22  $\mu$ m PTFE syringe filters (Whatman) before measurement.

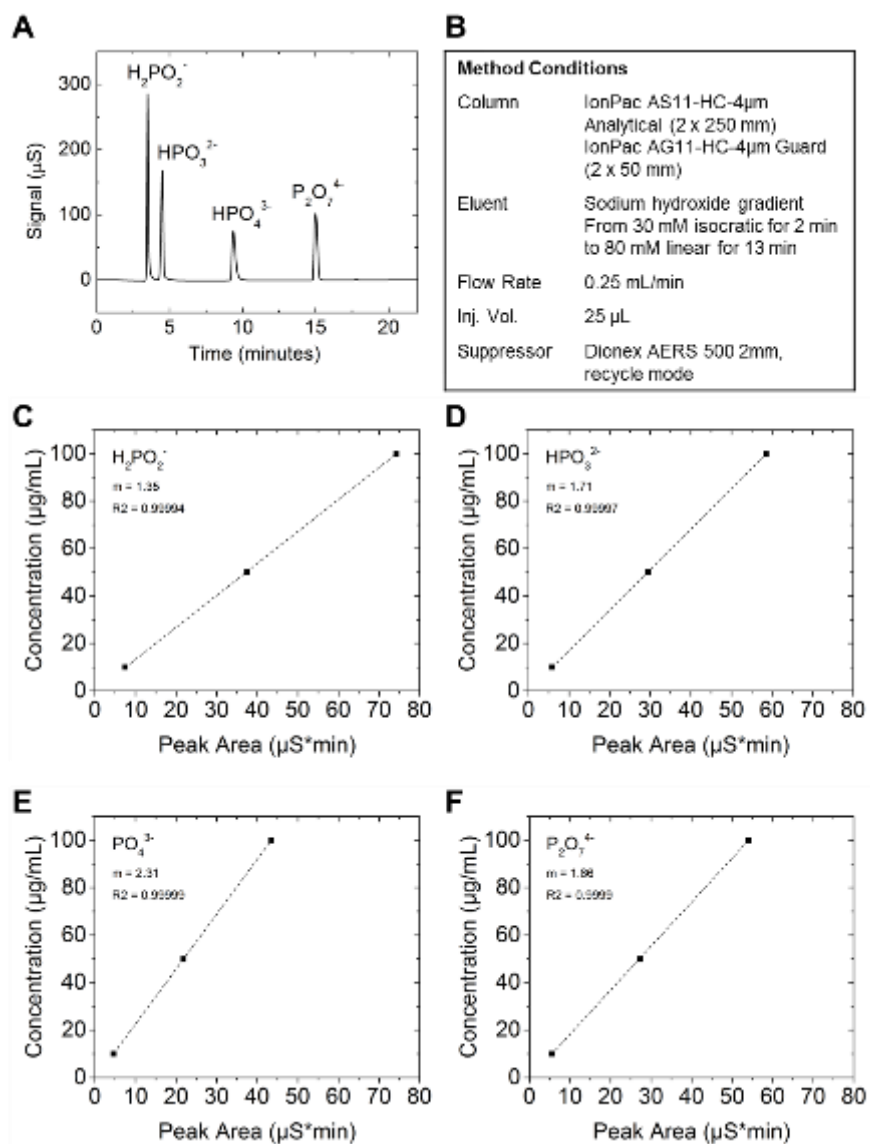


**Figure 4.12:** Ion chromatography method for the determination of phosphate species. (A) Example chromatogram for 0.05 mg mL<sup>-1</sup> standard containing hypophosphite (H<sub>2</sub>PO<sub>2</sub><sup>-</sup>), phosphite (HPO<sub>3</sub><sup>2-</sup>), phosphate (PO<sub>4</sub><sup>3-</sup>), and pyrophosphate (P<sub>2</sub>O<sub>7</sub><sup>4-</sup>) using ion chromatography. Method details (B) and concentration curves for the determination of (C) hypophosphite, (D) phosphite, (E) phosphate, and (F) pyrophosphate anions using ion chromatography.

#### 4.4 Summary

In summary, we have demonstrated that BP nanosheets can be exfoliated using a range of aqueous solution processing methods. The resulting BP nanosheet dispersions have a shelf-life of at least one month when stored under low-oxygen conditions. Furthermore, several important factors such as ionic strength, temperature, oxygenation, and flake size have been identified that influence the degradation rate of BP nanosheets in aqueous environments. In addition, the degradation products of BP nanosheets in aqueous environments were identified, all of which are likely to enable the safe use of BP nanosheets in biological applications. Overall, this work suggests that BP is a promising material for biomedical applications because it offers a unique opportunity to design biocompatible and biodegradable 2D material constructs. Furthermore, this fundamental study of the aqueous stability of BP will inform ongoing efforts to understand other biological interactions involving chemically reactive 2D materials.

## **CHAPTER 5:**

### **3D PRINTING OF LAYERED 2D MATERIALS**

This chapter is based, in part, on the research described in the following publication:

Guiney, L. M.; Mansukhani, N. D.; Jakus, A. E.; Wallace, S. G.; Shah, R. N.; Hersam, M. C. “Three-Dimensional Printing of Biocompatible, Thermally Conductive Hexagonal Boron Nitride Nanocomposites,” *Nano Lett.* 2018; under review

## 5.1 Background

With increasing electronic device density, speed, and power dissipation, thermal management has become a key consideration for integrated circuit technology.<sup>339–343</sup> Furthermore, as the field moves towards mechanically flexible electronics and roll-to-roll manufacturing techniques, additional constraints such as flexibility, stretchability, weight, and cost are placed upon thermal management materials.<sup>344–346</sup> These constraints are even more severe in the field of implantable bioelectronics where small changes in temperature can disrupt the normal functions or viability of surrounding tissues.<sup>347</sup> Consequently, a need exists for thermally conductive yet electrically insulating materials that possess high cytocompatibility and can be patterned into the complex, mechanically flexible 3D architectures that are frequently used in bioelectronic implants. Polymer materials meet most of these requirements with the exception of high thermal conductivity,<sup>342,343,348</sup> thus motivating the development of polymer nanocomposites with high thermal conductivity fillers such as hBN. Towards these ends, we introduce here a 3D printable polymer nanocomposite based on hBN that possesses high thermal conductivity, cytocompatibility, and mechanical flexibility and stretchability with significant promise for emerging applications in next-generation bioelectronics.

Three-dimensional (3D) printing is an additive manufacturing technique that offers many advantages including the ability to produce customized complex objects on demand in addition to the elimination of waste created by subtractive manufacturing techniques such as machining. The ability to rapidly design and fabricate architectures that are not otherwise possible with traditional methods has led to significant growth in the 3D printing field in both the research and industrial communities.<sup>193,349</sup> However, 3D printing is generally limited by the number and types of materials

that are compatible with this method.<sup>178</sup> The majority of 3D printing techniques are restricted to thermoplastics, photopolymers, and metals, which constrains both the mechanical and functional properties of the resulting structures. One approach for overcoming these limitations is to incorporate functional particles into polymer matrices to enhance functionality.<sup>350,351</sup> The effectiveness of this approach relies on achieving sufficiently high volume fraction of particles in the polymer matrix to modify targeted properties while still maintaining 3D printability.

Two-dimensional (2D) layered materials are superlative filler materials for polymer composites due to their high surface area, exceptional mechanical properties, and broadly tunable electrical, optical, and thermal properties.<sup>352</sup> With these attributes, 2D materials have yielded improved performance in a wide range of applications in electronic, energy, and biomedical technologies.<sup>353</sup> Several 2D materials including graphene, molybdenum disulfide, and hBN have been incorporated into polymer composites to impart mechanical strength or provide additional functionality such as electrical conductivity, thermal conductivity, or optical activity.<sup>54,158,165,354–356</sup> The ability to 3D print these functional composites has the potential to provide additional control over architecture, surface area, and manufacturability, thus further broadening their technological impact.<sup>357</sup> Indeed, recent work has shown successful 3D printing of graphene-polymer composites with high electrical conductivity that are enabling new applications in printed electronics, energy storage, and tissue engineering.<sup>161,358,359</sup> However, 3D printing of other 2D materials has not yet been achieved due to challenges in realizing 3D printable polymer composites based on non-carbon 2D materials.

Among non-carbon 2D materials, hexagonal boron nitride (hBN) is of particular interest because it is an electrically insulating yet thermally conductive analogue to graphene. The structure

of hBN consists of hexagonally bonded alternating boron and nitrogen atoms in planar 2D layers, which are stacked together by a combination of van der Waals forces and electrostatic interactions.<sup>360,361</sup> Although it is electrically insulating, hBN is still highly thermally conductive, with a theoretical thermal conductivity as high as  $300 \text{ W K}^{-1} \text{ m}^{-1}$  along the basal plane.<sup>362,363</sup> Additionally, hBN is lightweight, abundant, and readily commercially available, making it a prime candidate for thermal management applications. Consequently, previous work has incorporated hBN into polymer composites in order to enhance thermal conductivity. Using this strategy, thermal conductivities ranging from  $\sim 0.5\text{-}3 \text{ W K}^{-1} \text{ m}^{-1}$  have been demonstrated.<sup>364,365</sup> Additional processing such as stretching, magnetic alignment, oriented shearing, and chemical treatments have further enhanced the thermal conductivity of these composites.<sup>55,56,366,367</sup> The resulting hBN-polymer composites have shown significant promise for flexible electronic devices.<sup>368,369</sup> However, the hBN-polymer composites to date have shown a tradeoff between thermal and mechanical properties, especially in the high hBN loading limit. Furthermore, previously reported hBN-polymer composites have been primarily prepared using casting procedures that require post-processing steps to manipulate the 3D shape of the final structure.

Recently, Gao *et al.* demonstrated that hBN can be incorporated into a 3D printable poly(vinyl alcohol) (PVA) composite to improve thermal conductivity and thus be used in textiles for personal cooling. Although the authors claim that the material is 3D printed, they only demonstrate the extrusion of single fibers, and do not show that the material is self-supporting or that it can be printed in multiple layers, which is a key challenge for material development in 3D printing. Furthermore, the demonstrated thermal conductivity of these printed fibers remains relatively low ( $< 0.1 \text{ W K}^{-1} \text{ m}^{-1}$ ), even after additional hot-drawing of the fiber to align the hBN nanosheets.<sup>370</sup>

## 5.2 Results and discussion

### 5.2.1 3D printable ink formulation

We present here a 3D printable hBN-polymer ink that builds off a highly versatile formulation that has been previously utilized to 3D print a wide range of particle systems such as graphene and carbon nanotubes,<sup>161</sup> bioceramics,<sup>371</sup> lunar and martian materials,<sup>372</sup> and metals and alloys.<sup>164</sup> The 3D printable hBN inks contain only two solid components: hBN and poly(lactic-*co*-glycolic acid) (PLGA). PLGA is an elastomer that acts as a biocompatible polymer binder for the functional hBN particles. The PLGA and hBN particles are dissolved and dispersed, respectively, within a tri-solvent system: dibutyl phthalate (DBP) is used as a plasticizer; ethylene glycol monobutyl ether (EGBE) is used as a surfactant to disperse the hBN particles; and dichloromethane (DCM) is a high volatility solvent that dissolves the PLGA and provides the mechanism for solidification during the printing process. Due to its high vapor pressure, in addition to the high surface area that is created upon extrusion, the DCM evaporates rapidly resulting in a solid construct. During this 3D printing process, the PLGA precipitates and condenses around the hBN particles (Figure 5.1 and Figure 5.3), resulting in a well-defined printed strut that is self-supporting (Figure 5.2). The printed struts are uniform in size and span gaps of several millimeters without noticeable sagging or deformation, allowing for the creation of complex geometries with well-controlled porosity. In addition, the 3D printability of the hBN-polymer ink enables the realization of structures that are not possible with conventional polymer processing methods (Figure 5.2A).

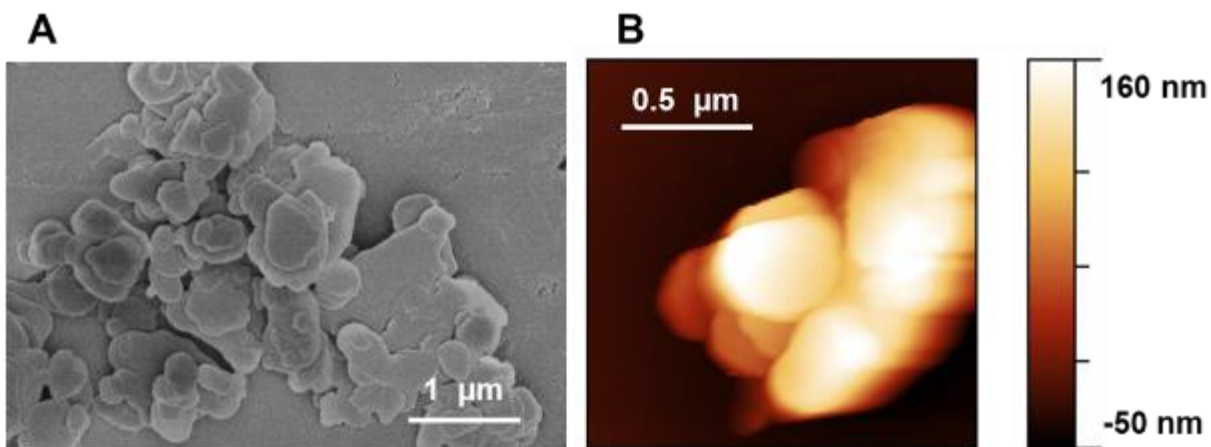


**Figure 5.1:** (a) Scanning electron microscopy (SEM) and (b) atomic force microscopy (AFM) images of the hBN powder, showing the characteristic particle lateral size (0.1–2  $\mu\text{m}$ ) and thickness (10–100 nm).

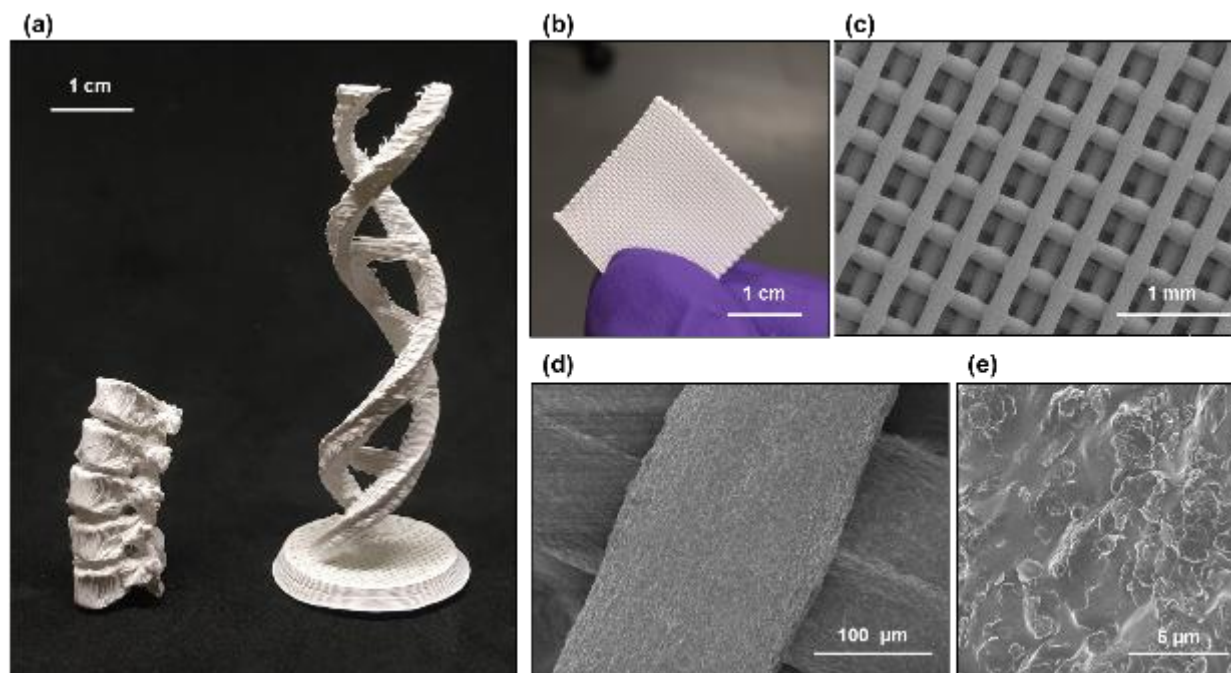


**Figure 5.2:** 3D printed hBN nanocomposite structures. (a) Photograph of complex structures including a small lumbar spine replica (left) and a double helix (right) that were 3D printed using a 60% vol. hBN nanocomposite ink. (b) Photograph and (c-e) scanning electron micrographs of a 3D printed 40% vol. hBN scaffold. The 3D printed strands are highly uniform and can be printed consistently over relatively large areas and heights. The printed strands can span gaps as seen in the grid inner structure in both the photograph and scanning electron micrographs as well as in the bridge structures of the double helix. The surface morphology is relatively smooth since the PLGA polymer uniformly coats and disperses the hBN flakes within the polymer matrix.

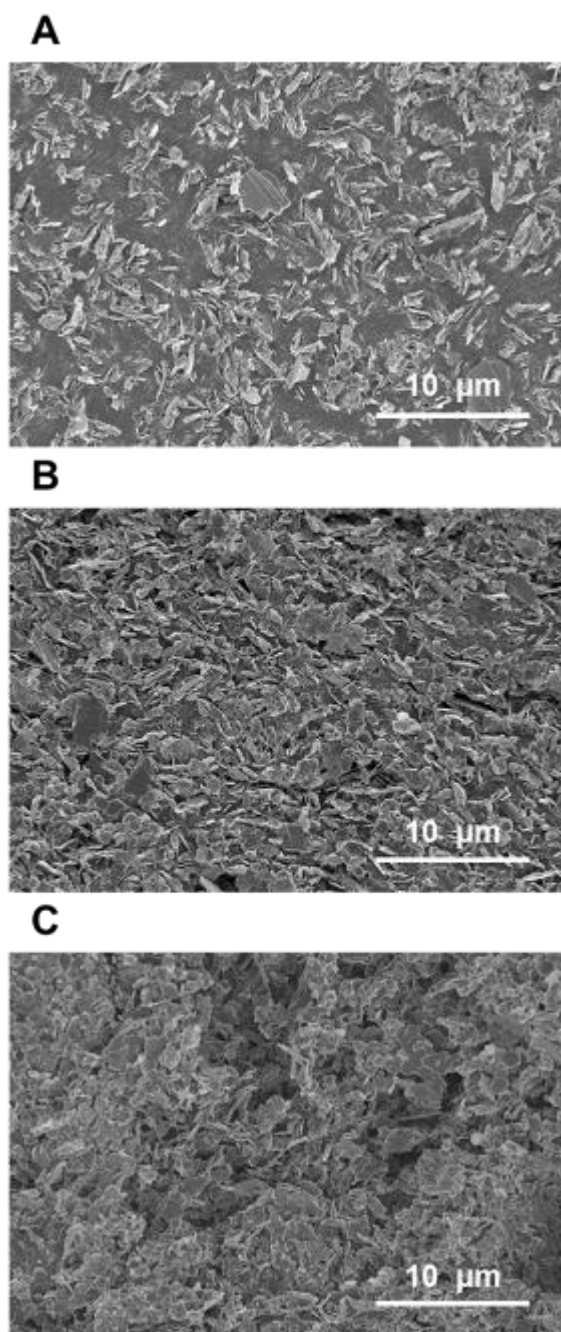


**Figure 5.3:** Cross-sectional SEM images of the 3D printed hBN nanocomposites as a function of hBN loading: (a) 20% vol.; (b) 40% vol.; (c) 60% vol.

### **5.2.2 Mechanical properties of 3D printed hBN**

The 3D printed hBN constructs are highly robust mechanically, allowing for direct handling immediately following printing. In addition, the hBN scaffolds are flexible and can be cut, folded, or rolled while still maintaining their mechanical integrity (Figure 5.4A), which allows for the possibility of additional manipulation of the constructs after printing in order to achieve an even wider range of sizes and geometries. For a quantitative assessment of the mechanical properties, tensile testing was performed for a range of hBN loadings, which are reported as a volume fraction of the solid components (Figure 5.4B-E). The tensile strength of the 3D printed constructs decreases significantly as the amount of hBN increases due to the decreasing amount of polymer present, which bears the majority of the tensile load.<sup>371</sup> The amount of plasticizer added to the ink formulation is directly proportional to the amount of hBN to help improve fluidity and prevent clogging during the printing process, and is still present in the resulting 3D printed constructs (Figure 5.5, Table 5.1). Consequently, the elastic modulus shows a similar trend, where the 3D printed constructs become less stiff with higher hBN content due to the increasing amount of plasticizer.

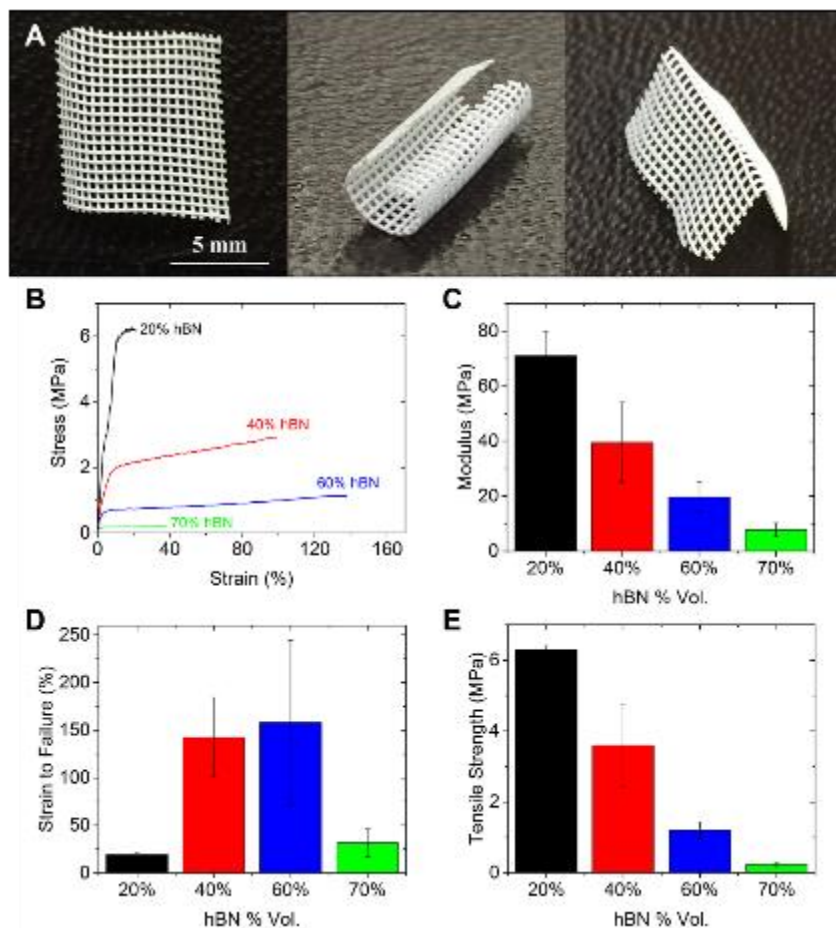


**Figure 5.4:** Mechanical properties of 3D printed hBN. (A) Images of a single 3D printed 40% vol. hBN gridded sheet that has been cut, rolled and folded but still maintains its mechanical integrity. (B) Stress-strain curves for 3D printed samples with varying hBN content resulting from tensile testing. Corresponding modulus (C), strain to failure (D), and tensile strength (E) values ( $n \geq 3$ ) for the stress-strain curves shown in (B). Tensile strength and modulus are significantly different ( $p < 0.05$ ) for each composition. Strain to failure of 40% vol. and 60% vol. samples are significantly higher ( $p < 0.05$ ) than the strain to failure for 20% vol. and 70% vol. samples. Error bars represent one standard deviation.

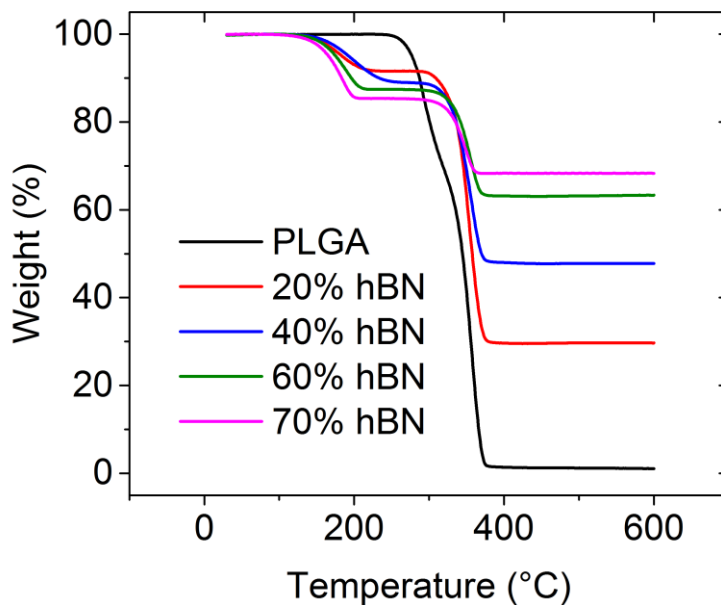


**Figure 5.5:** Thermogravimetric analysis (TGA) scans of 3D printed hBN with varying hBN:PLGA composition ratios. PLGA curve is the raw PLGA polymer pellets used in the ink formulations (no solvents). Samples were heated from 30°C to 600°C at a heating rate of 5°C/minute in a nitrogen environment.

**Table 5.1:** Compositions of 3D printed hBN based on the TGA scans shown in Figure 5.5.

The volume percent reported in the last two columns of the table takes into account only the solid components of the 3D printed hBN (i.e., hBN and PLGA).

Sample Name	Weight % solvents	Weight % hBN	Weight % PLGA	Volume % hBN	Volume % PLGA
<b>20% vol. hBN</b>	8.4	29.7	61.9	20.8	79.2
<b>40% vol. hBN</b>	10.8	47.8	41.5	38.7	61.3
<b>60% vol. hBN</b>	12.6	63.2	24.3	58.8	41.2
<b>70% vol. hBN</b>	14.7	68.3	17.0	68.7	31.3

The elongation to failure of the 3D printed constructs initially increases with increasing hBN content, and then sharply declines when the hBN loading is increased from 60% to 70%. The initial increase in ductility is likely due to the presence of increasing amounts of plasticizer, which tracks proportionally with the hBN content, and the crystal structure of the polymer, which was found to vary as a function of hBN content (Figure 5.6). In particular, when more polymer is present in the ink, the DCM evaporates more slowly during the printing process, resulting in a more crystalline polymer structure and thus a stiffer, more brittle material. On the other hand, for high fractions of hBN and correspondingly low fractions of polymer, the solvent evaporation occurs more quickly, leading to a more porous scaffold with a more amorphous polymer structure that facilitates increased elongation. The presence of high levels of plasticizer may also inhibit the ordering of the polymer chains at high hBN loadings, which would further decrease polymer crystallinity. It should be noted that eventually a limit is reached where there is an insufficient amount of polymer to adequately coat the hBN particles, resulting in a soft, brittle material, as observed for the case of 70% vol. hBN. Overall, by controlling the composition and trisolvant ink formulation, a wide range of mechanical properties can be achieved for 3D printed hBN constructs to meet the needs of specific applications.

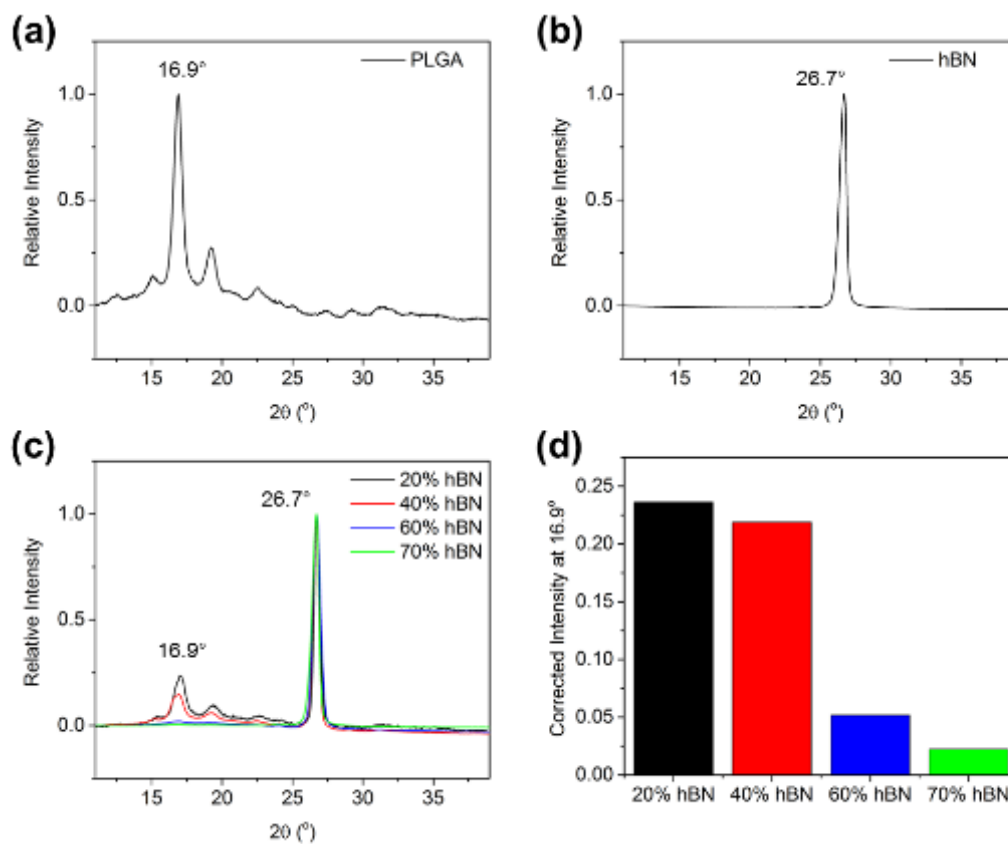


**Figure 5.6:** Powder X-ray diffraction (PXRD) scans of (a) raw PLGA, (b) raw hBN powder, and (c) 3D printed hBN with varying hBN:PLGA composition ratios to determine the relative crystallinity of the PLGA polymer matrix. The relative crystallinity of the 3D printed structures was determined by normalizing the PXRD spectra to the primary hBN peak at  $26.7^\circ$  and then measuring the intensity of the primary PLGA peak at  $16.9^\circ$ . This intensity was then corrected for the amount of PLGA present in the hBN composite with the corrected intensity values provided in (d), which shows the highest relative crystallinity in the 20% vol. hBN and the lowest relative crystallinity in the 70% vol. hBN.

### 5.2.3 Thermal conductivity of 3D printed hBN

One such application is the use of 3D printable hBN as a thermal interface material. Due to the high thermal conductivity of the hBN filler, the overall thermal conductivity of the polymer composite is expected to be enhanced with the addition of hBN. The thermal conductivity of the 3D printed constructs was calculated using Equation 1, where  $k$  is the thermal conductivity,  $\alpha$  is the measured thermal diffusivity,  $\rho$  is the measured density, and  $c_p$  is the measured specific heat capacity:

$$k = \alpha \rho c_p \quad (1)$$

The resulting thermal conductivities are shown in Figure 5.7A. The thermal conductivity of the 3D printed materials initially increases with increasing hBN content as expected. However, above a threshold, the thermal conductivity of the constructs begins to decrease despite the high hBN loading. This reduction in the thermal conductivity correlates with a significant change in the microstructure of the 3D printed constructs at high hBN loadings, which is apparent from cross-sectional scanning electron microscopy of the constructs (Figure 5.3). Specifically, due to the rapid evaporation of DCM for high loading hBN inks, the porosity of the printed structure increases (Figure 5.7B). This increased porosity likely leads to the observed decrease in thermal conductivity since the pores not only disrupt the percolation of the hBN particles, but also act as a thermal insulator within the polymer matrix. Nevertheless, at the optimal loading of 40% vol. hBN, the thermal conductivity reaches  $2.1 \text{ W K}^{-1} \text{ m}^{-1}$ , which is suitable for many thermal management applications.

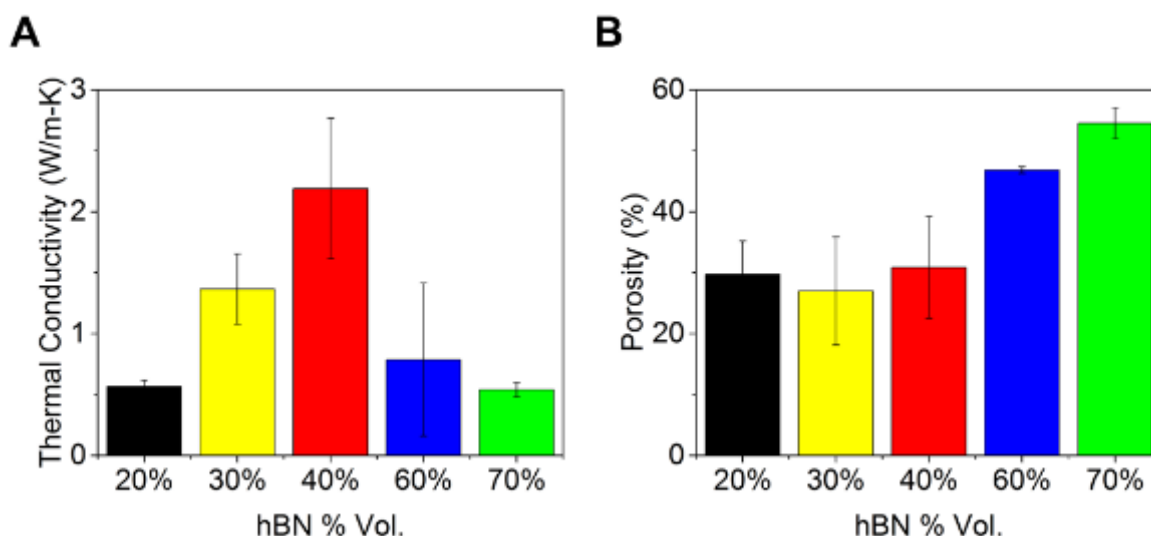


**Figure 5.7:** Thermal conductivity (A) and porosity (B) of 3D printed constructs ( $n = 3$ ) at varying hBN content. Thermal conductivity for 20%, 30% and 40% vol. hBN are significantly different from each other ( $p < 0.05$ ), while there is no significant difference between 20%, 60% and 70% vol. hBN samples. Porosity is significantly higher ( $p < 0.05$ ) in 60% and 70% vol. hBN constructs, while the porosity does not vary significantly between the 20%, 30% and 40% vol. hBN constructs. Thermal conductivity increases as a function of hBN content until a significant increase in the porosity of the scaffolds causes a disruption in the thermally conductive network. Porosity was determined by comparison of the theoretical density to the experimentally measured density of the constructs. Error bars represent one standard deviation.

#### 5.2.4 Cytocompatibility of 3D printed hBN

For biomedical applications, hBN also potentially offers advantages as a polymer composite filler due to its established biocompatibility *in vitro*.<sup>66,373,374</sup> By using a biocompatible polymer matrix in this 3D printable hBN formulation, it is anticipated that the material can be integrated into implantable devices. To confirm cytocompatibility, constructs of varying hBN content (20%, 40%, and 60% vol.) were 3D printed into sheets 6 layers thick and then cut into 5 mm cylinder scaffolds and rinsed with ethanol to remove residual solvents. Passage 2 female bone-marrow-derived human mesenchymal stem cells (hMSCs) were purchased and extended to passage 5 before seeding onto the hBN scaffolds. The growth and proliferation of the hMSCs on the scaffolds in Dulbecco's modified Eagle's medium (DMEM) was evaluated at multiple time points over 4 weeks using a live/dead stain and confocal imaging (Figure 5.8A). This growth was further quantified using a double-stranded DNA (dsDNA) quantification assay (Figure 5.8C). The cellular attachment and morphology of the cells were further characterized using scanning electron microscopy (Figure 5.8B). At day 1, we already observe a favorable interaction of the cells with the 40% vol. hBN scaffold, as the cells attach and spread out on the surface of the scaffold. Over the course of 4 weeks, high viability, growth, and proliferation of the hMSCs are also observed qualitatively through live/dead staining on scaffolds containing 20% vol. and 60% vol. hBN (Figure 5.9). The healthy growth of the cells results in the formation of extracellular matrix and the ability of the cells to span gaps and pores within the scaffold. Previously, Jakus *et al.* have demonstrated that hMSCs seeded onto a 3D printed PLGA scaffold containing no filler showed limited viability and growth over a 14 day period.<sup>161</sup> In the same study, the addition of graphene to the ink system significantly enhanced the viability and growth of hMSCs similar to the high

cytocompatibility observed with hMSCs on these 3D printed hBN nanocomposite scaffolds. While further biocompatibility tests are required before this 3D printable hBN nanocomposite could be used for *in vivo* applications, the high cytocompatibility of these 3D printable hBN constructs offers a distinct advantage for thermal applications specifically in bioelectronics.

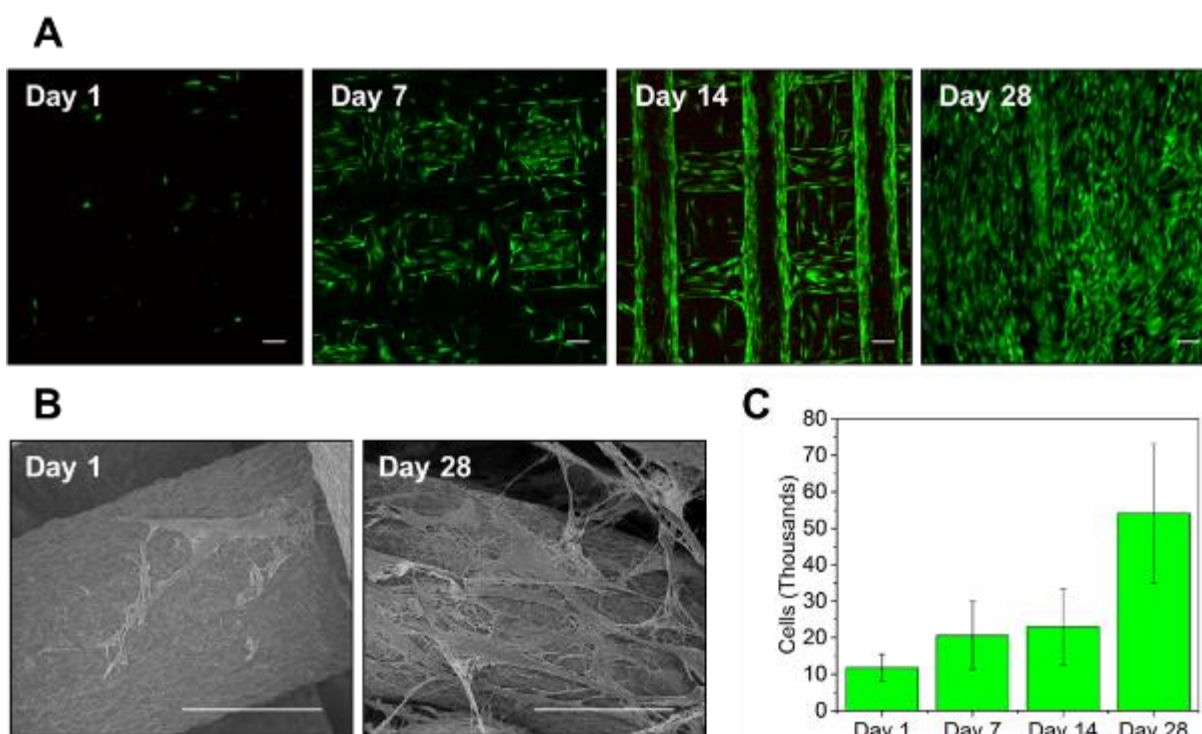


**Figure 5.8:** Cytocompatibility of 3D printed hBN. (A) Top down view reconstructions from scanning laser confocal microscopy of live (green) and dead (red) stained human mesenchymal stem cells (hMSCs) on a 40% vol. hBN scaffold 1, 7, 14 and 28 days after seeding. (B) SEM micrographs of hMSCs seeded onto a 40% vol. hBN scaffold 1 day and 28 days after seeding. (C) DNA quantification of hMSCs seeded onto 40% vol. hBN scaffolds (n=3) over 28 days. Error bars represent one standard deviation. Scale bars for all images are 100  $\mu$ m.

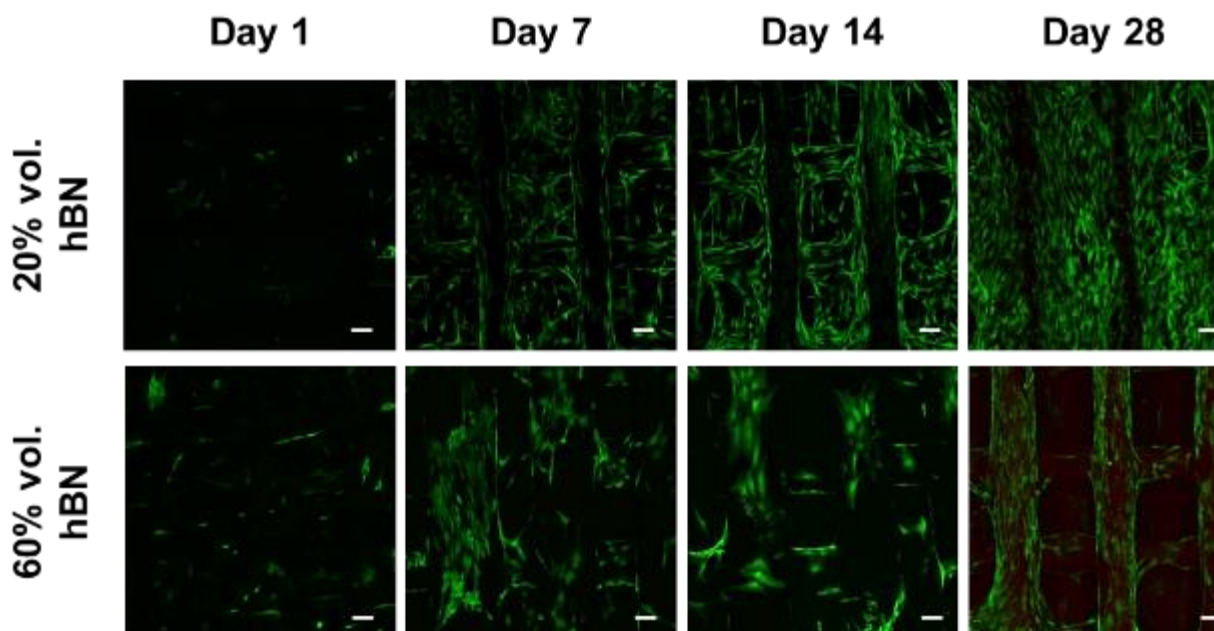


**Figure 5.9:** Live/dead confocal fluorescence imaging of 20% vol. hBN and 60% vol. hBN scaffolds after seeding with hMSCs. Live cells appear green, and dead cells appear red. Almost no dead cells were observed on the scaffolds, but it is hypothesized that dead cells tend to fall off the scaffold and thus are not observed attached to the scaffolds in these top-down reconstructions. The cells showed consistent growth and proliferation over the 28 day period. Scale bars for all images are 100  $\mu\text{m}$ .

### 5.3 Experimental methods

#### 5.3.1 Ink preparation and printing

Poly(lactic-co-glycolic acid) (82:18) copolymer (Evonik), hexagonal boron nitride powder (MilliporeSigma), dichloromethane (MilliporeSigma), ethylene glycol butyl ether (MilliporeSigma), and dibutyl phthalate (MilliporeSigma) were all used as received. To prepare

the inks, PLGA was dissolved in DCM and then added to a mixture of hBN, EGBE, and DBP. Five different volume ratios of solid components were prepared and characterized ranging from 20% vol. hBN to 70% vol. hBN. Due to the high volume fraction of particles in these inks, the amount of EGBE and DBP added to the ink formulations was proportional to the amount of hBN present in order to keep the hBN particles well dispersed and prevent clogging of the nozzle. DCM was added in excess and then allowed to evaporate under ambient conditions until a viscosity of  $\sim 30 \text{ Pa s}$  was achieved. All samples were printed using a 3D BioPlotter (EnvisionTEC GmbH). Depending on the composition and the tip diameter, the printing speed was varied in the range  $5\text{--}20 \text{ mm s}^{-1}$  and the printing pressure was varied in the range  $0.5\text{--}3.0 \text{ bar}$ .

### **5.3.2 Mechanical characterization**

Tensile testing was performed to determine the mechanical properties of the 3D printed scaffolds. Solid tensile bars with a gauge length of 20 mm and cross-sectional area of  $3 \text{ mm}^2$  were printed using a  $250 \text{ }\mu\text{m}$  tip. Tensile tests (LF Plus mechanical tester, Lloyd Instruments) were performed at an extension rate of  $2 \text{ mm/min}$ .

### **5.3.3 Thermal characterization**

The thermal diffusivity was measured using laser flash analysis (Netzch LFA 457) following a Cowan with pulse correction model and a linear baseline. Solid films of material were 3D printed and then heated under vacuum for one hour at  $50 \text{ }^\circ\text{C}$  to remove the remaining solvent preceding measurement. The measurements were performed at  $65 \text{ }^\circ\text{C}$  under vacuum using a graphite coating as per Netzch recommendations to mitigate the translucent nature of the polymer. The measurements were performed with the laser pulse perpendicular to the printed filament as the experiments showed a lack of anisotropic thermal conductivity. The density was determined by

measuring the mass and geometric volume of the printed samples. The specific heat capacity of each sample was determined using differential scanning calorimetry (DSC822e Differential Scanning Calorimeter, Mettler Toledo) using the well-established sapphire method.<sup>375</sup> In this method, the mass-corrected DSC signal of a sample across the temperature range of 60 °C to 70 °C was compared to that of a sapphire standard undergoing the same temperate profile.

#### **5.3.4 *In vitro* cytocompatibility**

For in vitro cytocompatibility studies, 2 cm x 2 cm boxes of 6 layers with an internal structure of 90° offset grids with a 0.5 mm distance between the center of the strands were printed using a 250 µm tip. 5 mm cylinders were punched out using a biopsy punch and then rinsed with ethanol and sterile PBS before seeding with hMSCs. Compatibility with hMSCs was established using a method described previously.<sup>161</sup> Briefly, passage 2 hMSCs were purchased from Lonza, extended to passage 5, and then seeded onto the hBN scaffolds (~25,000 cells per scaffold) in Dulbecco's modified Eagle's medium (DMEM). Viability was established using a live/dead stain (Invitrogen) and imaged using a Nikon C2+ Laser Scanning Confocal Microscope. Following live/dead imaging, the scaffolds were fixed for scanning electron microscopy (SEM) imaging using an aqueous solution of 3% sucrose and 2% gluteraldehyde for 15 minutes. The scaffolds were then dehydrated using a series of increasing ethanol concentrations followed by critical point drying (Samdri 795 Critical Point Dryer) and then coated with 15 nm of osmium before SEM imaging (Hitachi SU8030). The quantification of cells was determined using Quanti-iT Picogreen dsDNA Assay Kit (Invitrogen) at 1, 7, 14, and 28 days after lysing the cells by gentle bath sonication of the scaffolds (in 0.02% Triton X100 detergent). The fluorescence was measured at an excitation of 485 nm and emission of 535 nm using a Cytation 3 Plate Reader.

## 5.4 Summary

In conclusion, by incorporating hBN into a 3D printable polymer composite at high volume content, we have demonstrated a lightweight material with high thermal conductivity, controllable mechanical properties, and tailorable architecture. These hBN-polymer composites can be 3D printed with feature resolutions down to 100  $\mu\text{m}$ , resulting in constructs that are robust mechanically and amenable to subsequent handling. Both the mechanical and thermal properties of the 3D printed constructs are affected by the underlying composite microstructure, which can be controlled by modifying the relative amounts of the trisolvent system in the ink formulation as well as the solid component ratio. The highly flexible and stretchable qualities of these hBN-polymer composites in addition to their cytocompatibility further make them leading candidates for thermal management applications in emerging bioelectronic technologies. Overall, the ability to 3D print these hBN-polymer composites at room temperature with no additional post-printing processing will facilitate their widespread use in rapid prototyping for a range of additive manufacturing applications.

**CHAPTER 6:**  
**FUTURE OUTLOOK**

There are many opportunities for the continuation of the work presented in this thesis. The growing use of 2D nanomaterials in electronics, optoelectronics, energy capture and storage, and biomedical applications requires a greater understanding the health and environmental implications of exposure to these nanomaterials.<sup>123–126</sup> Further studies are required to fully understand the role of various physicochemical properties, such as composition, exfoliation, flake size and thickness, surface functionalization, physical forms and chemical dissolution, in the interactions at the nano-bio interface. Moving forward, in order to integrate ongoing toxicity studies of 2D nanomaterials into a complete material hazard assessment, comprehensive material characterization is needed. Furthermore, understanding how the material properties and behavior change in biological media will be important to accurately assess the nano-bio interface. Dispersion stability, particle size and dissolution rate are important factors that could change dramatically in biologically relevant media due to changes in pH or the presence of salts and proteins, fundamentally changing how the material will interact with or be taken up by cells.<sup>376</sup>

In addition to thorough material characterization, thoughtful design of toxicity studies is required for 2D materials. When investigating *in vitro* cytotoxicity of these materials, the cell line selection will play a large role in the measured toxicological response, especially since certain cell lines have already shown different sensitivities to 2D material exposure.<sup>129,150</sup> Thus, it is important to resist the temptation to generalize cytotoxicity results for different cell lines based on any single study. In addition, when selecting cell lines, the potential exposure routes of a particular 2D material should be considered. To date, cytotoxicity of emerging 2D materials has focused mainly on biomedical exposure due to the obvious implications for biomedical technologies.<sup>147,377,378</sup> However, because 2D materials are being explored for a wide range of applications and industries,

occupational and environmental exposure also merit investigation. Understanding the effects of all potential exposure routes will provide the most comprehensive picture of the hazard potential associated with 2D materials.

Due to their relatively infrequent study thus far in the field of toxicology, cytotoxicity has been the most widely used metric for gauging the biocompatibility of emerging 2D materials. This empirically reported cytotoxicity provides some insight, but a deeper mechanistic understanding is generally required to assess the hazard potential. In particular, structure-activity relationships need further study for 2D materials interacting with biological systems. Furthermore, quantification of the specific physicochemical properties that elicit deleterious biological responses would allow for the design of safer 2D materials.

The lack of thorough material characterization, consistent design of *in vitro* assays, and mechanistic understanding of the cytotoxic response has led to contradictory reports of the biocompatibility of many 2D materials. Additionally, the cytotoxicity of the 2D materials in most cases is reported as a simple quantification of cell viability, without details of the characterization of cell growth or cell morphology that would enable better comparison across studies. To provide a more comprehensive understanding of the toxicity mechanisms of 2D materials, we thus recommend an interdisciplinary approach that relates the physicochemical properties of the materials to specific biological endpoints (Figure 6.1). Nanomaterial libraries should also be used to systematically vary the physicochemical properties of the 2D material of interest. Ideally, thoroughly characterized and monodisperse populations of 2D materials should be used to isolate the effects of specific characteristics (e.g., lateral size, thickness, surface functionalization, and electronic structure) on biological outcomes. Using *in vitro* high throughput screening (HTS)

assays, cellular interactions can be elucidated by quantifying the biodistribution, inflammation, fibrosis, and metabolic functions as a result of exposure to 2D materials. These results can then be validated by limited, carefully designed *in vivo* assays. In addition to the acute exposure testing, the long-term biodistribution and effects need to be investigated. From the initial toxicity studies of TMDCs, it is clear that some of these materials persist in organs and tissues, and thus bioaccumulation of 2D materials may present long-term repercussions.<sup>127</sup>

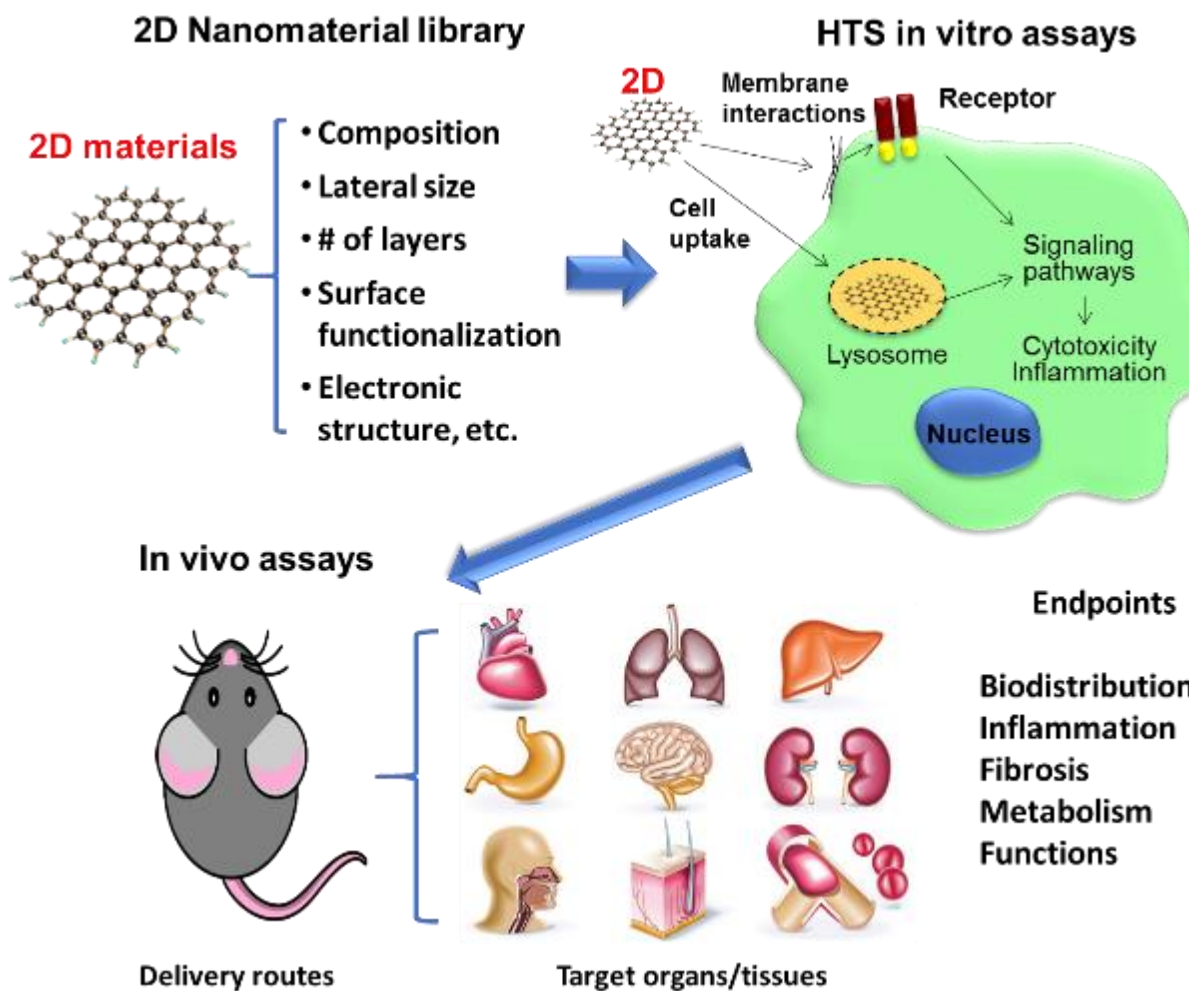


**Figure 6.1:** A proposed approach for the hazard assessment of 2D nanomaterials. A library of 2D nanomaterials where the physicochemical properties are systematically varied and extensively characterized can be used to relate specific properties to an injurious biological outcome. *In vitro* high throughput screening (HTS) assays can be used to quantify a response for specific biological endpoints. From these assays, carefully selected *in vivo* assays can be used to validate the *in vitro* results and confirm the hazard potential of the 2D nanomaterial.

The field of 2D material research is still accelerating, with continual discovery of additional 2D materials and phenomena associated with their unique structures and compositions.<sup>379–381</sup> With a constantly expanding library of 2D materials, the ability to predict toxicological outcomes is of critical importance. Recent 2D materials of interest, such as black phosphorus, indium selenide, and germanium sulfide, demonstrate high environmental instability.<sup>332,382,383</sup> In these cases, a firm understanding of the dissolution behavior in addition to the temporal evolution of material properties is paramount for both their biomedical application as well as understanding the health and environmental risks of these materials. While some studies have begun to probe the toxicological effects of structural parameters such as lateral size, thickness, and surface functionalization, the effects of the electronic structure of 2D materials remain largely unexplored. In the case of MoS<sub>2</sub>, it has been observed that the crystal structure and resulting change in electronic properties results in a change in the dissolution behavior of the material,<sup>175</sup> thus motivating further studies along these lines.<sup>384</sup> Overall, a comprehensive assessment of the hazard potential of 2D materials requires an interdisciplinary approach to elucidate the relationship between the physicochemical properties of the materials and the resulting biological outcomes. In this manner, predictive toxicological models can be developed that will ultimately enable the development of mitigation schemes that will accelerate the safe use of 2D materials in widely used technological applications.

Following from Chapter 4, additional opportunities to expand the application of our 3D printable 2D material ink formulation exist. While this initial study showed promising thermal conductivity and cytocompatibility, further optimization of the ink formulation and printing parameters could result in significantly improved performance. Specifically, the selection of the

hBN flakes with larger lateral sizes and a higher aspect ratio could induce shear alignment of flakes during the extrusion process, resulting in aligned hBN flakes in the direction of printing, enhancing the overall thermal conductivity of the construct. Furthermore, this ink formulation has been shown to be compatible with both graphene and hBN, indicating that there are further opportunities for the incorporation of other 2D materials, which would expand the class of 3D printable materials to include new electronic, optical and mechanical properties. Successful integration of this palette of functional materials could enable the development of fully printable devices and constructs.

## REFERENCES

- (1) Novoselov, K.; Geim, A.; Morozov, S. Electric Field Effect in Atomically Thin Carbon Films. *Science* **2004**, *306*, 666–669.
- (2) Geim, A. K.; Novoselov, K. S. The Rise of Graphene. *Nat. Mater.* **2007**, *6*, 183–191.
- (3) Geim, A. K. Graphene: Status and Prospects. *Science* **2009**, *324*, 1530–1535.
- (4) Chen, D.; Feng, H.; Li, J. Graphene Oxide: Preparation, Functionalization, and Electrochemical Applications. *Chem. Rev.* **2012**, *112*, 6027–6053.
- (5) Compton, O. C.; Nguyen, S. T. Graphene Oxide, Highly Reduced Graphene Oxide, and Graphene: Versatile Building Blocks for Carbon-Based Materials. *Small* **2010**, *6*, 711–723.
- (6) Ciesielski, A.; Samorì, P. Graphene via Sonication Assisted Liquid-Phase Exfoliation. *Chem. Soc. Rev.* **2014**, *43*, 381–398.
- (7) Seo, J. T.; Green, A. A.; Antaris, A. L.; Hersam, M. C. High-Concentration Aqueous Dispersions of Graphene Using Nonionic, Biocompatible Block Copolymers. *J. Phys. Chem. Lett.* **2011**, *2*, 1004–1008.
- (8) Akhavan, O.; Ghaderi, E.; Shirazian, S. A.; Rahighi, R. Rolled Graphene Oxide Foams as Three-Dimensional Scaffolds for Growth of Neural Fibers Using Electrical Stimulation of Stem Cells. *Carbon N. Y.* **2016**, *97*, 71–77.
- (9) Li, R.; Mansukhani, N. D.; Guiney, L. M.; Ji, Z.; Zhao, Y.; Chang, C. H.; French, C. T.; Miller, J. F.; Hersam, M. C.; Nel, A. E.; *et al.* Identification and Optimization of Carbon Radicals on Hydrated Graphene Oxide for Ubiquitous Antibacterial Coatings. *ACS Nano* **2016**, *10*, 10966–10980.
- (10) Zheng, X. T.; Ananthanarayanan, A.; Luo, K. Q.; Chen, P. Glowing Graphene Quantum Dots and Carbon Dots: Properties, Syntheses, and Biological Applications. *Small* **2015**, *11*, 1620–1636.
- (11) Chen, Y.; Tan, C.; Zhang, H.; Wang, L. Two-Dimensional Graphene Analogues for Biomedical Applications. *Chem. Soc. Rev.* **2015**, *44*, 2681–2701.
- (12) Zhu, Y.; Murali, S.; Cai, W.; Li, X.; Suk, J. W.; Potts, J. R.; Ruoff, R. S. Graphene and Graphene Oxide: Synthesis, Properties, and Applications. *Adv. Mater.* **2010**, *22*, 3906–3924.
- (13) Dubin, S.; Gilje, S.; Wang, K.; Tung, V. C.; Cha, K.; Hall, A. S.; Farrar, J.; Varshneya, R.; Yang, Y.; Kaner, R. B. A One-Step, Solvothermal Reduction Method for Producing

- Reduced Graphene Oxide Dispersions in Organic Solvents. *ACS Nano* **2010**, *4*, 3845–3852.
- (14) Sydlik, S. A.; Jhunjhunwala, S.; Webber, M. J.; Anderson, D. G.; Langer, R. The in vivo Compatibility of Graphene Oxide with Differing Oxidation States. *ACS Nano* **2015**, *9*, 3866–3874.
  - (15) Zhang, B.; Wei, P.; Zhou, Z.; Wei, T. Interactions of Graphene with Mammalian Cells: Molecular Mechanisms and Biomedical Insights. *Adv. Drug Deliv. Rev.* **2016**, *105*, 145–162.
  - (16) Chhowalla, M.; Shin, H. S.; Eda, G.; Li, L.-J.; Loh, K. P.; Zhang, H. The Chemistry of Two-Dimensional Layered Transition Metal Dichalcogenide Nanosheets. *Nat. Chem.* **2013**, *5*, 263–275.
  - (17) Wang, Q. H.; Kalantar-Zadeh, K.; Kis, A.; Coleman, J. N.; Strano, M. S. Electronics and Optoelectronics of Two-Dimensional Transition Metal Dichalcogenides. *Nat. Nanotechnol.* **2012**, *7*, 699–712.
  - (18) Manzeli, S.; Ovchinnikov, D.; Pasquier, D.; Yazyev, O. V.; Kis, A. 2D Transition Metal Dichalcogenides. *Nat. Rev. Mater.* **2017**, *2*, 17033.
  - (19) Lv, R.; Robinson, J. A.; Schaak, R. E.; Sun, D.; Sun, Y.; Mallouk, T. E.; Terrones, M. Transition Metal Dichalcogenides and Beyond: Synthesis, Properties, and Applications of Single- and Few-Layer Nanosheets. *Acc. Chem. Res.* **2015**, *48*, 56–64.
  - (20) Sorkin, V.; Pan, H.; Shi, H.; Quek, S. Y.; Zhang, Y. W. Nanoscale Transition Metal Dichalcogenides: Structures, Properties, and Applications. *Crit. Rev. Solid State Mater. Sci.* **2014**, *39*, 319–367.
  - (21) Koski, K. J.; Cui, Y. The New Skinny in Two-Dimensional Nanomaterials. *ACS Nano* **2013**, *7*, 3739–3743.
  - (22) Butler, S.; Hollen, S.; Cao, L.; Cui, Y. Progress, Challenges, and Opportunities in Two-Dimensional Materials Beyond Graphene. *ACS Nano* **2013**, *7*, 2898–2926.
  - (23) Eknapakul, T.; King, P. D. C.; Asakawa, M.; Buaphet, P.; Takagi, H.; Shen, K. M.; Baumberger, F.; Sasagawa, T.; Jungthawan, S.; Meevasana, W. Electronic Structure of a Quasi-Freestanding MoS<sub>2</sub> Monolayer. *Nano Lett.* **2014**, *14*, 1312–1316.
  - (24) Kuc, A.; Zibouche, N.; Heine, T. Influence of Quantum Confinement on the Electronic Structure of the Transition Metal Sulfide TS<sub>2</sub>. *Phys. Rev. B* **2011**, *83*, 245213.
  - (25) Eda, G.; Yamaguchi, H.; Voiry, D.; Fujita, T.; Chen, M.; Chhowalla, M. Photoluminescence from Chemically Exfoliated MoS<sub>2</sub>. *Nano Lett.* **2011**, *11*, 5111–5116.

- (26) Splendiani, A.; Sun, L.; Zhang, Y.; Li, T.; Kim, J.; Chim, C.-Y.; Galli, G.; Wang, F. Emerging Photoluminescence in Monolayer MoS<sub>2</sub>. *Nano Lett.* **2010**, *10*, 1271–1275.
- (27) Radisavljevic, B.; Radenovic, A.; Brivio, J.; Giacometti, V.; Kis, A. Single-Layer MoS<sub>2</sub> Transistors. *Nat. Nanotechnol.* **2011**, *6*, 147–150.
- (28) Yin, W.; Yan, L.; Yu, J.; Tian, G.; Zhou, L.; Zheng, X.; Zhang, X.; Yong, Y.; Li, J.; Gu, Z.; *et al.* High-Throughput Synthesis of Single-Layer MoS<sub>2</sub> Nanosheets as a Near-Infrared Photothermal-Trigged Drug Delivery for Effective Cancer Therapy. *ACS Nano* **2014**, *8*, 6922–6933.
- (29) Li, B. L.; Setyawati, M. I.; Chen, L.; Xie, J.; Ariga, K.; Lim, C. T.; Garaj, S.; Leong, D. T. Directing Assembly and Disassembly of 2D MoS<sub>2</sub> Nanosheets with DNA for Drug Delivery. *ACS Appl. Mater. Interfaces* **2017**, *9*, 15286–15296.
- (30) Pumera, M.; Loo, A. H. Layered Transition-Metal Dichalcogenides (MoS<sub>2</sub> and WS<sub>2</sub>) for Sensing and Biosensing. *TrAC Trends Anal. Chem.* **2014**, *61*, 49–53.
- (31) Lee, J.; Dak, P.; Lee, Y.; Park, H.; Choi, W.; Alam, M. A.; Kim, S. Two-Dimensional Layered MoS<sub>2</sub> Biosensors Enable Highly Sensitive Detection of Biomolecules. *Sci. Rep.* **2014**, *4*, 7352.
- (32) Wang, L.; Wang, Y.; Wong, J. I.; Palacios, T.; Kong, J.; Yang, H. Y. Functionalized MoS<sub>2</sub> Nanosheet-Based Field-Effect Biosensor for Label-Free Sensitive Detection of Cancer Marker Proteins in Solution. *Small* **2014**, *10*, 1101–1105.
- (33) Sarkar, D.; Liu, W.; Xie, X.; Anselmo, A. MoS<sub>2</sub> Field-Effect Transistor for Next-Generation Label-Free Biosensors. *ACS Nano* **2014**, *8*, 3992–4003.
- (34) Gan, X.; Zhao, H.; Quan, X. Two-Dimensional MoS<sub>2</sub>: A Promising Building Block for Biosensors. *Biosens. Bioelectron.* **2017**, *89*, 56–71.
- (35) Li, Z.; Wong, S. L. Functionalization of 2D Transition Metal Dichalcogenides for Biomedical Applications. *Mater. Sci. Eng. C* **2016**, *70*, 1095–1106.
- (36) Mo, L.; Li, J.; Liu, Q.; Qiu, L.; Tan, W. Nucleic Acid-Functionalized Transition Metal Nanosheets for Biosensing Applications. *Biosens. Bioelectron.* **2017**, *89*, 201–211.
- (37) Ou, J. Z.; Chrimes, A. F.; Wang, Y.; Tang, S.; Strano, M. S.; Kalantar-zadeh, K. Ion-Driven Photoluminescence Modulation of Quasi-Two-Dimensional MoS<sub>2</sub> Nanoflakes for Applications in Biological Systems. *Nano Lett.* **2014**, *14*, 857–863.
- (38) Kong, R.-M.; Ding, L.; Wang, Z.; You, J.; Qu, F. A Novel Aptamer-Functionalized MoS<sub>2</sub> Nanosheet Fluorescent Biosensor for Sensitive Detection of Prostate Specific Antigen. *Anal. Bioanal. Chem.* **2015**, *407*, 369–377.

- (39) Wang, N.; Wei, F.; Qi, Y.; Li, H.; Lu, X. Synthesis of Strongly Fluorescent Molybdenum Disulfide Nanosheets for Cell-Targeted Labeling. *ACS Appl. Mater. Interfaces* **2014**, *6*, 19888–19894.
- (40) Bai, X.; Wang, J.; Mu, X.; Yang, J.; Liu, H.; Xu, F.; Jing, Y.; Liu, L.; Xue, X.; Dai, H.; *et al.* Ultrasmall WS<sub>2</sub> Quantum Dots with Visible Fluorescence for Protection of Cells and Animal Models from Radiation-Induced Damages. *ACS Biomater. Sci. Eng.* **2017**, *3*, 460–470.
- (41) Chen, L.; Feng, Y.; Zhou, X.; Zhang, Q.; Nie, W.; Wang, W.; Zhang, Y.; He, C. One-Pot Synthesis of MoS<sub>2</sub> Nanoflakes with Desirable Degradability for Photothermal Cancer Therapy. *ACS Appl. Mater. Interfaces* **2017**, *9*, 17347–17358.
- (42) Deng, R.; Yi, H.; Fan, F.; Fu, L.; Zeng, Y.; Wang, Y.; Li, Y.; Liu, Y.; Ji, S.; Su, Y. Facile Exfoliation of MoS<sub>2</sub> Nanosheets by Protein as a Photothermal-Triggered Drug Delivery System for Synergistic Tumor Therapy. *RSC Adv.* **2016**, *6*, 77083–77092.
- (43) Qian, X.; Shen, S.; Liu, T.; Cheng, L.; Liu, Z. Two-Dimensional TiS<sub>2</sub> Nanosheets for in vivo Photoacoustic Imaging and Photothermal Cancer Therapy. *Nanoscale* **2015**, *7*, 6380–6387.
- (44) Ren, Q.; Li, B.; Peng, Z.; He, G.; Zhang, W.; Guan, G.; Huang, X.; Xiao, Z.; Liao, L.; Pan, Y.; *et al.* SnS Nanosheets for Efficient Photothermal Therapy. *New J. Chem.* **2016**, *40*, 4464–4467.
- (45) Shen, S.; Chao, Y.; Dong, Z.; Wang, G.; Yi, X.; Song, G.; Yang, K.; Liu, Z.; Cheng, L. Bottom-Up Preparation of Uniform Ultrathin Rhenium Disulfide Nanosheets for Image-Guided Photothermal Radiotherapy. *Adv. Funct. Mater.* **2017**, *27*, 1700250.
- (46) Liu, T.; Chao, Y.; Gao, M.; Liang, C.; Chen, Q.; Song, G.; Cheng, L.; Liu, Z. Ultra-Small MoS<sub>2</sub> Nanodots with Rapid Body Clearance for Photothermal Cancer Therapy. *Nano Res.* **2016**, *9*, 3003–3017.
- (47) Li, Z.; Shao, J.; Luo, Q.; Yu, X. F.; Xie, H.; Fu, H.; Tang, S.; Wang, H.; Han, G.; Chu, P. K. Cell-Borne 2D Nanomaterials for Efficient Cancer Targeting and Photothermal Therapy. *Biomaterials* **2017**, *133*, 37–48.
- (48) Zhong, C.; Zhao, X.; Wang, L.; Li, Y.; Zhao, Y. Facile Synthesis of Biocompatible MoSe<sub>2</sub> Nanoparticles for Efficient Targeted Photothermal Therapy of Human Lung Cancer. *RSC Adv.* **2017**, *7*, 7382–7391.
- (49) Peng, M. Y.; Zheng, D. W.; Wang, S. B.; Cheng, S. X.; Zhang, X. Z. Multifunctional Nanosystem for Synergistic Tumor Therapy Delivered by Two-Dimensional MoS<sub>2</sub>. *ACS Appl. Mater. Interfaces* **2017**, *9*, 13965–13975.

- (50) Wang, S.; Zhao, J.; Yang, H.; Wu, C.; Hu, F.; Chang, H.; Li, G.; Ma, D.; Zou, D.; Huang, M. Bottom-up Synthesis of WS<sub>2</sub> Nanosheets with Synchronous Surface Modification for Imaging Guided Tumor Regression. *Acta Biomater.* **2017**, *58*, 442–454.
- (51) Watanabe, K.; Taniguchi, T.; Kanda, H. Direct-Bandgap Properties and Evidence for Ultraviolet Lasing of Hexagonal Boron Nitride Single Crystal. *Nat. Mater.* **2004**, *3*, 404–409.
- (52) Golberg, D.; Bando, Y.; Huang, Y.; Terao, T.; Mitome, M.; Tang, C.; Zhi, C. Boron Nitride Nanotubes and Nanosheets. *ACS Nano* **2010**, *4*, 2979–2993.
- (53) Song, L.; Ci, L.; Lu, H.; Sorokin, P. B.; Jin, C.; Ni, J.; Kvashnin, A. G.; Kvashnin, D. G.; Lou, J.; Yakobson, B. I.; *et al.* Large Scale Growth and Characterization of Atomic Hexagonal Boron Nitride Layers. *Nano Lett.* **2010**, *10*, 3209–3215.
- (54) Loeblein, M.; Tsang, S. H.; Pawlik, M.; Phua, E. J. R.; Yong, H.; Zhang, X. W.; Gan, C. L.; Teo, E. H. T. High-Density 3D-Boron Nitride and 3D-Graphene for High-Performance Nano-Thermal Interface Material. *ACS Nano* **2017**, *11*, 2033–2044.
- (55) Kuang, Z.; Chen, Y.; Lu, Y.; Liu, L.; Hu, S.; Wen, S.; Mao, Y.; Zhang, L. Fabrication of Highly Oriented Hexagonal Boron Nitride Nanosheet/Elastomer Nanocomposites with High Thermal Conductivity. *Small* **2015**, *11*, 1655–1659.
- (56) Song, W. L.; Wang, P.; Cao, L.; Anderson, A.; Meziani, M. J.; Farr, A. J.; Sun, Y. P. Polymer/Boron Nitride Nanocomposite Materials for Superior Thermal Transport Performance. *Angew. Chemie - Int. Ed.* **2012**, *51*, 6498–6501.
- (57) Zhu, J.; Kang, J.; Kang, J.; Jariwala, D.; Wood, J. D.; Seo, J. W. T.; Chen, K. S.; Marks, T. J.; Hersam, M. C. Solution-Processed Dielectrics Based on Thickness-Sorted Two-Dimensional Hexagonal Boron Nitride Nanosheets. *Nano Lett.* **2015**, *15*, 7029–7036.
- (58) Fang, H.; Bai, S. L.; Wong, C. P. Thermal, Mechanical and Dielectric Properties of Flexible BN Foam and BN Nanosheets Reinforced Polymer Composites for Electronic Packaging Application. *Compos. Part A Appl. Sci. Manuf.* **2017**, *100*, 71–80.
- (59) Ciofani, G.; Danti, S.; Genchi, G. G.; Mazzolai, B.; Mattoli, V. Boron Nitride Nanotubes: Biocompatibility and Potential Spill-Over in Nanomedicine. *Small* **2013**, *9*, 1672–1685.
- (60) Ciofani, G.; Raffa, V.; Mencias, A.; Cuschieri, A. Cytocompatibility, Interactions, and Uptake of Polyethyleneimine-Coated Boron Nitride Nanotubes by Living Cells: Confirmation of Their Potential for Biomedical Applications. *Biotechnol. Bioeng.* **2008**, *101*, 850–858.
- (61) Chen, X.; Wu, P.; Rousseas, M.; Okawa, D.; Gartner, Z.; Zettl, A.; Bertozzi, C. R. Boron Nitride Nanotubes Are Noncytotoxic and Can Be Functionalized for Interaction with

- Proteins and Cells. *J. Am. Chem. Soc.* **2009**, *131*, 890–891.
- (62) Mallineni, S. S. K.; Shannahan, J.; Raghavendra, A. J.; Rao, A. M.; Brown, J. M.; Podila, R. Biomolecular Interactions and Biological Responses of Emerging Two-Dimensional Materials and Aromatic Amino Acid Complexes. *ACS Appl. Mater. Interfaces* **2016**, *8*, 16604–16611.
  - (63) Lin, L.; Xu, Y.; Zhang, S.; Ross, I. M.; Ong, A. C. M.; Allwood, D. A. Fabrication and Luminescence of Monolayered Boron Nitride Quantum Dots. *Small* **2014**, *10*, 60–65.
  - (64) Weng, Q.; Wang, B.; Wang, X.; Hanagata, N.; Li, X.; Liu, D.; Wang, X.; Jiang, X.; Bando, Y.; Golberg, D. Highly Water-Soluble, Porous, and Biocompatible Boron Nitrides for Anticancer Drug Delivery. *ACS Nano* **2014**, *8*, 6123–6130.
  - (65) Rajabi, A. H.; Jaffe, M.; Arinzeh, T. L. Piezoelectric Materials for Tissue Regeneration: A Review. *Acta Biomater.* **2015**, *24*, 12–23.
  - (66) Farshid, B.; Lalwani, G.; Shir Mohammadi, M.; Simonsen, J.; Sitharaman, B. Boron Nitride Nanotubes and Nanoplatelets as Reinforcing Agents of Polymeric Matrices for Bone Tissue Engineering. *J. Biomed. Mater. Res. - Part B Appl. Biomater.* **2017**, *105*, 406–419.
  - (67) Shuai, C.; Han, Z.; Feng, P.; Gao, C.; Xiao, T.; Peng, S. Akermanite Scaffolds Reinforced with Boron Nitride Nanosheets in Bone Tissue Engineering. *J. Mater. Sci. Mater. Med.* **2015**, *26*, 188.
  - (68) Lu, T.; Wang, L.; Jiang, Y.; Liu, Q.; Huang, C. Hexagonal Boron Nitride Nanoplates as Emerging Biological Nanovectors and Their Potential Applications in Biomedicine. *J. Mater. Chem. B* **2016**, *4*, 6103–6110.
  - (69) Kumar, V.; Nikhil, K.; Roy, P.; Lahiri, D.; Lahiri, I. Emergence of Fluorescence in Boron Nitride Nanoflakes and Its Application in Bioimaging. *RSC Adv.* **2016**, *6*, 48025–48032.
  - (70) Mannix, A. J.; Kiraly, B.; Hersam, M. C.; Guisinger, N. P. Synthesis and Chemistry of Elemental 2D Materials. *Nat. Rev. Chem.* **2017**, *1*, '0014.
  - (71) Bridgman, P. W. Two New Modifications of Phosphorus. *J. Am. Chem. Soc.* **1914**, *36*, 1344–1363.
  - (72) Xia, F.; Wang, H.; Jia, Y. Rediscovering Black Phosphorus as an Anisotropic Layered Material for Optoelectronics and Electronics. *Nat. Commun.* **2014**, *5*, 4458.
  - (73) Ling, X.; Wang, H.; Huang, S.; Xia, F.; Dresselhaus, M. S. The Renaissance of Black Phosphorus. *Proc. Natl. Acad. Sci.* **2015**, *112*, 4523–4530.
  - (74) Qian, X.; Gu, Z.; Chen, Y. Two-Dimensional Black Phosphorus Nanosheets for

- Theranostic Nanomedicine. *Mater. Horiz.* **2017**, *4*, 800–816.
- (75) Lee, H. U.; Park, S. Y.; Lee, S. C.; Choi, S.; Seo, S.; Kim, H.; Won, J.; Choi, K.; Kang, K. S.; Park, H. G.; *et al.* Black Phosphorus (BP) Nanodots for Potential Biomedical Applications. *Small* **2016**, *12*, 214–219.
  - (76) Buscema, M.; Groenendijk, D. J.; Blanter, S. I.; Steele, G. A.; Van Der Zant, H. S. J.; Castellanos-Gomez, A. Fast and Broadband Photoresponse of Few-Layer Black Phosphorus Field-Effect Transistors. *Nano Lett.* **2014**, *14*, 3347–3352.
  - (77) Li, L.; Kim, J.; Jin, C.; Ye, G. J.; Qiu, D. Y.; Da Jornada, F. H.; Shi, Z.; Chen, L.; Zhang, Z.; Yang, F.; *et al.* Direct Observation of the Layer-Dependent Electronic Structure in Phosphorene. *Nat. Nanotechnol.* **2017**, *12*, 21–25.
  - (78) Tran, V.; Soklaski, R.; Liang, Y.; Yang, L. Layer-Controlled Band Gap and Anisotropic Excitons in Few-Layer Black Phosphorus. *Phys. Rev. B* **2014**, *89*, 235319.
  - (79) Eswaraiah, V.; Zeng, Q.; Long, Y.; Liu, Z. Black Phosphorus Nanosheets: Synthesis, Characterization and Applications. *Small* **2016**, *12*, 3480–3502.
  - (80) Brent, J. R.; Ganguli, A. K.; Kumar, V.; Lewis, D. J.; McNaughten, P. D.; O'Brien, P.; Sabherwal, P.; Tedstone, A. A. On the Stability of Surfactant-Stabilised Few-Layer Black Phosphorus in Aqueous Media. *RSC Adv.* **2016**, *6*, 86955–86958.
  - (81) Favron, A.; Gaufres, E.; Fossard, F.; Phaneuf-Laheureux, A. L.; Tang, N. Y. W.; Lévesque, P. L.; Loiseau, A.; Leonelli, R.; Francoeur, S.; Martel, R. Photooxidation and Quantum Confinement Effects in Exfoliated Black Phosphorus. *Nat. Mater.* **2015**, *14*, 826–832.
  - (82) Hu, Z.; Li, Q.; Lei, B.; Zhou, Q.; Xiang, D.; Lyu, Z.; Hu, F.; Wang, J.; Ren, Y.; Guo, R.; *et al.* Water-Catalyzed Oxidation of Few-Layer Black Phosphorous in a Dark Environment. *Angew. Chemie - Int. Ed.* **2017**, *56*, 9131–9135.
  - (83) Zhou, Q.; Chen, Q.; Tong, Y.; Wang, J. Light-Induced Ambient Degradation of Few-Layer Black Phosphorus: Mechanism and Protection. *Angew. Chemie - Int. Ed.* **2016**, *55*, 11437–11441.
  - (84) Abellan, G.; Wild, S.; Lloret, V.; Scheuschner, N.; Gillen, R.; Mundloch, U.; Maultzsch, J.; Varela, M.; Hauke, F.; Hirsch, A. Fundamental Insights into the Degradation and Stabilization of Thin Layer Black Phosphorus. *J. Am. Chem. Soc.* **2017**, *139*, 10432–10440.
  - (85) Huang, Y.; Qiao, J.; He, K.; Bliznakov, S.; Sutter, E.; Chen, X.; Luo, D.; Meng, F.; Su, D.; Decker, J.; *et al.* Interaction of Black Phosphorus with Oxygen and Water. *Chem. Mater.* **2016**, *28*, 8330–8339.

- (86) Yin, F.; Hu, K.; Chen, S.; Wang, D.; Zhang, J.; Xie, M.; Yang, D.; Qiu, M.; Zhang, H.; Li, Z. Black Phosphorus Quantum Dot Based Novel SiRNA Delivery Systems in Human Pluripotent Teratoma PA-1 Cells. *J. Mater. Chem. B* **2017**, *5*, 5433–5440.
- (87) Tao, W.; Zhu, X.; Yu, X.; Zeng, X.; Xiao, Q.; Zhang, X.; Ji, X.; Wang, X.; Shi, J.; Zhang, H.; *et al.* Black Phosphorus Nanosheets as a Robust Delivery Platform for Cancer Theranostics. *Adv. Mater.* **2017**, *29*, 1603276.
- (88) Chen, W.; Ouyang, J.; Liu, H.; Chen, M.; Zeng, K.; Sheng, J.; Liu, Z.; Han, Y.; Wang, L.; Li, J.; *et al.* Black Phosphorus Nanosheet-Based Drug Delivery System for Synergistic Photodynamic/Photothermal/Chemotherapy of Cancer. *Adv. Mater.* **2017**, *29*, 1603864.
- (89) Chen, W.; Ouyang, J.; Yi, X.; Xu, Y.; Niu, C.; Zhang, W.; Wang, L.; Sheng, J.; Deng, L.; Liu, Y.-N.; *et al.* Black Phosphorus Nanosheets as a Neuroprotective Nanomedicine for Neurodegenerative Disorder Therapy. *Adv. Mater.* **2018**, *30*, 1703458.
- (90) Chen, Y.; Ren, R.; Pu, H.; Chang, J.; Mao, S.; Chen, J. Field-Effect Transistor Biosensors with Two-Dimensional Black Phosphorus Nanosheets. *Biosens. Bioelectron.* **2017**, *89*, 505–510.
- (91) Gu, W.; Yan, Y.; Pei, X.; Zhang, C.; Ding, C.; Xian, Y. Fluorescent Black Phosphorus Quantum Dots as Label-Free Sensing Probes for Evaluation of Acetylcholinesterase Activity. *Sensors Actuators, B Chem.* **2017**, *250*, 601–607.
- (92) Shao, J.; Xie, H.; Huang, H.; Li, Z.; Sun, Z.; Xu, Y.; Xiao, Q.; Yu, X.-F.; Zhao, Y.; Zhang, H.; *et al.* Biodegradable Black Phosphorus-Based Nanospheres for in vivo Photothermal Cancer Therapy. *Nat. Commun.* **2016**, *7*, 12967.
- (93) Zhao, Y.; Tong, L.; Li, Z.; Yang, N.; Fu, H.; Wu, L.; Cui, H.; Zhou, W.; Wang, J.; Wang, H.; *et al.* Stable and Multifunctional Dye-Modified Black Phosphorus Nanosheets for Near-Infrared Imaging-Guided Photothermal Therapy. *Chem. Mater.* **2017**, *29*, 7131–7139.
- (94) Guo, T.; Wu, Y.; Lin, Y.; Xu, X.; Lian, H.; Huang, G.; Liu, J.-Z.; Wu, X.; Yang, H.-H. Black Phosphorus Quantum Dots with Renal Clearance Property for Efficient Photodynamic Therapy. *Small* **2017**, *14*, 1702815.
- (95) Lv, R.; Yang, D.; Yang, P.; Xu, J.; He, F.; Gai, S.; Li, C.; Dai, Y.; Yang, G.; Lin, J. Integration of Upconversion Nanoparticles and Ultrathin Black Phosphorus for Efficient Photodynamic Theranostics under 808 Nm Near-Infrared Light Irradiation. *Chem. Mater.* **2016**, *28*, 4724–4734.
- (96) Zhan, Y.; Liu, Z.; Najmaei, S.; Ajayan, P. M.; Lou, J. Large-Area Vapor-Phase Growth and Characterization of MoS<sub>2</sub> Atomic Layers on a SiO<sub>2</sub> Substrate. *Small* **2012**, *8*, 966–971.

- (97) Liu, H.; Si, M.; Najmaei, S.; Neal, A. T.; Du, Y.; Ajayan, P. M.; Lou, J.; Ye, P. D. Statistical Study of Deep Sub-Micron Dual-Gated Field-Effect Transistors on Monolayer CVD Molybdenum Disulfide Films. *Nano Lett.* **2013**, *13*, 2640–2646.
- (98) Lee, Y. H.; Zhang, X. Q.; Zhang, W.; Chang, M. T.; Lin, C. Te; Chang, K. Di; Yu, Y. C.; Wang, J. T. W.; Chang, C. S.; Li, L. J.; *et al.* Synthesis of Large-Area MoS<sub>2</sub> Atomic Layers with Chemical Vapor Deposition. *Adv. Mater.* **2012**, *24*, 2320–2325.
- (99) Peng, Y.; Meng, Z.; Zhong, C.; Lu, J.; Yu, W. Hydrothermal Synthesis of MoS<sub>2</sub> and Its Pressure-Related Crystallization. *J. Solid State Chem.* **2001**, *159*, 170–173.
- (100) Ramakrishna Matte, H. S. S.; Gomathi, a.; Manna, A. K.; Late, D. J.; Datta, R.; Pati, S. K.; Rao, C. N. R. MoS<sub>2</sub> and WS<sub>2</sub> Analogues of Graphene. *Angew. Chemie - Int. Ed.* **2010**, *49*, 4059–4062.
- (101) Mak, K. F.; Lee, C.; Hone, J.; Shan, J.; Heinz, T. F. Atomically Thin MoS<sub>2</sub>: A New Direct-Gap Semiconductor. *Phys. Rev. Lett.* **2010**, *105*, 136805.
- (102) Paton, K. R.; Varrla, E.; Backes, C.; Smith, R. J.; Khan, U.; O'Neill, A.; Boland, C.; Lotya, M.; Istrate, O. M.; King, P.; *et al.* Scalable Production of Large Quantities of Defect-Free Few-Layer Graphene by Shear Exfoliation in Liquids. *Nat. Mater.* **2014**, *13*, 624–630.
- (103) Kang, J.; Sangwan, V. K.; Wood, J. D.; Hersam, M. C. Solution-Based Processing of Monodisperse Two-Dimensional Nanomaterials. *Acc. Chem. Res.* **2017**, *50*, 943–951.
- (104) Coleman, J.; Lotya, M.; O'Neill, A.; Bergin, S. Two-Dimensional Nanosheets Produced by Liquid Exfoliation of Layered Materials. *Science* **2011**, *331*, 568–571.
- (105) Nicolosi, V.; Chhowalla, M.; Kanatzidis, M. G.; Strano, M. S.; Coleman, J. N. Liquid Exfoliation of Layered Materials. *Science* **2013**, *340*, 1226419.
- (106) Dines, M. B. Lithium Intercalation via N-Butyllithium of the Layered Transition Metal Dichalcogenides. *Mater. Res. Bull.* **1975**, *10*, 287–291.
- (107) Joensen, P.; Frindt, R. F.; Morrison, S. R. Single-Layer MoS<sub>2</sub>. *Mater. Res. Bull.* **1986**, *21*, 457–461.
- (108) Fan, X.; Xu, P.; Zhou, D.; Sun, Y.; Li, Y. C.; Nguyen, M. A. T.; Terrones, M.; Mallouk, T. E. Fast and Efficient Preparation of Exfoliated 2H MoS<sub>2</sub> Nanosheets by Sonication-Assisted Lithium Intercalation and Infrared Laser-Induced 1T to 2H Phase Reversion. *Nano Lett.* **2015**, *15*, 5956–5960.
- (109) Smith, R. J.; King, P. J.; Lotya, M.; Wirtz, C.; Khan, U.; De, S.; O'Neill, A.; Duesberg, G. S.; Grunlan, J. C.; Moriarty, G.; *et al.* Large-Scale Exfoliation of Inorganic Layered

- Compounds in Aqueous Surfactant Solutions. *Adv. Mater.* **2011**, *23*, 3944–3948.
- (110) May, P.; Khan, U.; Hughes, J. M.; Coleman, J. N. Role of Solubility Parameters in Understanding the Steric Stabilization of Exfoliated Two-Dimensional Nanosheets by Adsorbed Polymers. *J. Phys. Chem. C* **2012**, *116*, 11393–11400.
- (111) Kang, J.; Seo, J.-W. T.; Alducin, D.; Ponce, A.; Yacaman, M. J.; Hersam, M. C. Thickness Sorting of Two-Dimensional Transition Metal Dichalcogenides via Copolymer-Assisted Density Gradient Ultracentrifugation. *Nat. Commun.* **2014**, *5*, 5478.
- (112) Halim, U.; Zheng, C. R.; Chen, Y.; Lin, Z.; Jiang, S.; Cheng, R.; Huang, Y.; Duan, X. A Rational Design of Cosolvent Exfoliation of Layered Materials by Directly Probing Liquid-Solid Interaction. *Nat. Commun.* **2013**, *4*, 2213.
- (113) Kang, J.; Wood, J. D.; Wells, S. A.; Lee, J. H.; Liu, X.; Chen, K. S.; Hersam, M. C. Solvent Exfoliation of Electronic-Grade, Two-Dimensional Black Phosphorus. *ACS Nano* **2015**, *9*, 3596–3604.
- (114) Varrla, E.; Backes, C.; Paton, K. R.; Harvey, A.; Gholamvand, Z.; Mccauley, J.; Coleman, J. N. Large-Scale Production of Size-Controlled MoS<sub>2</sub> Nanosheets by Shear Exfoliation. *Chem. Mater.* **2015**, *27*, 1129–1139.
- (115) Yao, Y.; Lin, Z.; Li, Z.; Song, X.; Moon, K.-S.; Wong, C. Large-Scale Production of Two-Dimensional Nanosheets. *J. Mater. Chem.* **2012**, *22*, 13494–13499.
- (116) Fiori, G.; Bonaccorso, F.; Iannaccone, G.; Palacios, T.; Neumaier, D.; Seabaugh, A.; Banerjee, S. K.; Colombo, L. Electronics Based on Two-Dimensional Materials. *Nat. Nanotechnol.* **2014**, *9*, 768–779.
- (117) Guardia, L.; Paredes, J. I.; Rozada, R.; Villar-Rodil, S.; Martínez-Alonso, A.; Tascón, J. M. D. Production of Aqueous Dispersions of Inorganic Graphene Analogues by Exfoliation and Stabilization with Non-Ionic Surfactants. *RSC Adv.* **2014**, *4*, 14115–14127.
- (118) Kang, J.; Wells, S. A.; Wood, J. D.; Lee, J.; Liu, X. Stable Aqueous Dispersions of Optically and Electronically Active Phosphorene. *Proc. Natl. Acad. Sci. U. S. A.* **2016**, *113*, 11688–11693.
- (119) Siepi, M.; Morales-Narváez, E.; Domingo, N.; Monti, D. M.; Notomista, E.; Merkoçi, A. Production of Biofunctionalized MoS<sub>2</sub> Flakes with Rationally Modified Lysozyme: A Biocompatible 2D Hybrid Material. *2D Mater.* **2017**, *4*, 035007.
- (120) Mansukhani, N. D.; Guiney, L. M.; Kim, P. J.; Zhao, Y.; Alducin, D.; Ponce, A.; Larios, E.; Yacaman, M. J.; Hersam, M. C. High-Concentration Aqueous Dispersions of Nanoscale 2D Materials Using Nonionic, Biocompatible Block Copolymers. *Small* **2016**,

12, 294–300.

- (121) Ayán-Varela, M.; Pérez-Vidal, Ó.; Paredes, J. I.; Munuera, J. M.; Villar-Rodil, S.; Díaz-González, M.; Fernández-Sánchez, C.; Silva, V. S.; Cicuéndez, M.; Vila, M.; *et al.* Aqueous Exfoliation of Transition Metal Dichalcogenides Assisted by DNA/RNA Nucleotides: Catalytically Active and Biocompatible Nanosheets Stabilized by Acid-Base Interactions. *ACS Appl. Mater. Interfaces* **2017**, *9*, 2835–2845.
- (122) Paredes, J. I.; Munuera, J. M.; Villar-Rodil, S.; Guardia, L.; Ayán-Varela, M.; Pagán, A.; Aznar-Cervantes, S. D.; Cenis, J. L.; Martínez-Alonso, A.; Tascón, J. M. D. Impact of Covalent Functionalization on the Aqueous Processability, Catalytic Activity, and Biocompatibility of Chemically Exfoliated MoS<sub>2</sub> Nanosheets. *ACS Appl. Mater. Interfaces* **2016**, *8*, 27974–27986.
- (123) Riaz Ahmed, K. B.; Nagy, A. M.; Brown, R. P.; Zhang, Q.; Malghan, S. G.; Goering, P. L. Silver Nanoparticles: Significance of Physicochemical Properties and Assay Interference on the Interpretation of in vitro Cytotoxicity Studies. *Toxicol. Vitro* **2017**, *38*, 179–192.
- (124) Albanese, A.; Tang, P. S.; Chan, W. C. W. The Effect of Nanoparticle Size, Shape, and Surface Chemistry on Biological Systems. *Annu. Rev. Biomed. Eng.* **2012**, *14*, 1–16.
- (125) Sayes, C. M.; Warheit, D. B. Characterization of Nanomaterials for Toxicity Assessment. *Wiley Interdiscip. Rev. Nanomedicine Nanobiotechnology* **2009**, *1*, 660–670.
- (126) Carnovale, C.; Bryant, G.; Shukla, R.; Bansal, V. Size, Shape and Surface Chemistry of Nano-Gold Dictate Its Cellular Interactions, Uptake and Toxicity. *Prog. Mater. Sci.* **2016**, *83*, 152–190.
- (127) Hao, J.; Song, G.; Liu, T.; Yi, X.; Yang, K.; Cheng, L.; Liu, Z. In vivo Long-Term Biodistribution, Excretion, and Toxicology of PEGylated Transition-Metal Dichalcogenides MS<sub>2</sub> (M = Mo, W, Ti) Nanosheets. *Adv. Sci.* **2017**, *4*, 1600160.
- (128) Green, A. A.; Hersam, M. C. Solution Phase Production of Graphene with Controlled Thickness via Density Differentiation. *Nano Lett.* **2009**, *9*, 4031–4036.
- (129) Qu, G.; Liu, W.; Zhao, Y.; Gao, J.; Xia, T.; Shi, J.; Hu, L.; Zhou, W.; Gao, J.; Wang, H.; *et al.* Improved Biocompatibility of Black Phosphorus Nanosheets by Chemical Modification. *Angew. Chemie - Int. Ed.* **2017**, *56*, 14488–14493.
- (130) Ryder, C. R.; Wood, J. D.; Wells, S. A.; Hersam, M. C. Chemically Tailoring Semiconducting Two-Dimensional Transition Metal Dichalcogenides and Black Phosphorus. *ACS Nano* **2016**, *10*, 3900–3917.
- (131) Suhito, I. R.; Han, Y.; Kim, D.-S.; Son, H.; Kim, T.-H. Effects of Two-Dimensional Materials on Human Mesenchymal Stem Cell Behaviors. *Biochem. Biophys. Res.*

*Commun.* **2017**, *493*, 578–584.

- (132) Wang, X.; Li, T.; Ma, H.; Zhai, D.; Jiang, C.; Chang, J.; Wang, J.; Wu, C. A 3D-Printed Scaffold with MoS<sub>2</sub> Nanosheets for Tumor Therapy and Tissue Regeneration. *NPG Asia Mater.* **2017**, *9*, e376.
- (133) Nel, A.; Xia, T.; Meng, H.; Wang, X.; Lin, S.; Ji, Z.; Zhang, H. Nanomaterial Toxicity Testing in the 21st Century: Use of a Predictive Toxicological Approach and High-Throughput Screening. *Acc. Chem. Res.* **2013**, *46*, 607–621.
- (134) Zhu, M.; Nie, G.; Meng, H.; Xia, T.; Nel, A.; Zhao, Y. Physicochemical Properties Determine Nanomaterial Cellular Uptake, Transport, and Fate. *Acc. Chem. Res.* **2013**, *46*, 622–631.
- (135) Teo, W. Z.; Chng, E. L. K.; Sofer, Z.; Pumera, M. Cytotoxicity of Exfoliated Transition-Metal Dichalcogenides (MoS<sub>2</sub>, WS<sub>2</sub>, and WSe<sub>2</sub>) Is Lower than That of Graphene and Its Analogues. *Chemistry* **2014**, *20*, 9627–9632.
- (136) Latiff, N. M.; Sofer, Z.; Fisher, A. C.; Pumera, M. Cytotoxicity of Exfoliated Layered Vanadium Dichalcogenides. *Chem. - A Eur. J.* **2017**, *23*, 684–690.
- (137) Chia, H. L.; Latiff, N. M.; Sofer, Z.; Pumera, M. Cytotoxicity of Group 5 Transition Metal Ditetellurides (MTe<sub>2</sub>; M=V, Nb, Ta). *Chem. - A Eur. J.* **2018**, *24*, 206–211.
- (138) Shang, E.; Niu, J.; Li, Y.; Zhou, Y.; Crittenden, J. C. Comparative Toxicity of Cd, Mo, and W Sulphide Nanomaterials toward E. Coli under UV Irradiation. *Environ. Pollut.* **2017**, *224*, 606–614.
- (139) Chng, E. L. K.; Sofer, Z.; Pumera, M. MoS<sub>2</sub> Exhibits Stronger Toxicity with Increased Exfoliation. *Nanoscale* **2014**, *6*, 14412–14418.
- (140) Wang, X.; Mansukhani, N. D.; Guiney, L. M.; Ji, Z.; Chang, C. H.; Wang, M.; Liao, Y. P.; Song, T. Bin; Sun, B.; Li, R.; *et al.* Differences in the Toxicological Potential of 2D versus Aggregated Molybdenum Disulfide in the Lung. *Small* **2015**, *11*, 5079–5087.
- (141) Shah, P.; Narayanan, T. N.; Li, C.-Z.; Alwarappan, S. Probing the Biocompatibility of MoS<sub>2</sub> Nanosheets by Cytotoxicity Assay and Electrical Impedance Spectroscopy. *Nanotechnology* **2015**, *26*, 315102.
- (142) Appel, J. H.; Li, D. O.; Podlevsky, J. D.; Debnath, A.; Green, A. A.; Wang, Q. H.; Chae, J. Low Cytotoxicity and Genotoxicity of Two-Dimensional MoS<sub>2</sub> and WS<sub>2</sub>. *ACS Biomater. Sci. Eng.* **2016**, *2*, 361–367.
- (143) Rashkow, J. T.; Talukdar, Y.; Lalwani, G.; Sitharaman, B. Interactions of 1D- and 2D-Layered Inorganic Nanoparticles with Fibroblasts and Human Mesenchymal Stem Cells.

*Nanomedicine* **2015**, *10*, 1693–1706.

- (144) Liu, S.; Shen, Z.; Wu, B.; Yu, Y.; Hou, H.; Zhang, X.-X.; Ren, H. Cytotoxicity and Efflux Pump Inhibition Induced by Molybdenum Disulfide and Boron Nitride Nanomaterials with Sheetlike Structure. *Environ. Sci. Technol.* **2017**, *51*, 10834–10842.
- (145) Latiff, N. M.; Teo, W. Z.; Sofer, Z.; Fisher, A. C.; Pumera, M. The Cytotoxicity of Layered Black Phosphorus. *Chem. - A Eur. J.* **2015**, *21*, 13991–13995.
- (146) Mu, X.; Wang, J.-Y.; Bai, X.; Xu, F.; Liu, H.; Yang, J.; Jing, Y.; Liu, L.; Xue, X.; Dai, H.; *et al.* Black Phosphorus Quantum Dot Induced Oxidative Stress and Toxicity in Living Cells and Mice. *ACS Appl. Mater. Interfaces* **2017**, *9*, 20399–20409.
- (147) Wang, Z.; Zhu, W.; Qiu, Y.; Yi, X.; von dem Bussche, A.; Kane, A.; Gao, H.; Koski, K.; Hurt, R. Biological and Environmental Interactions of Emerging Two-Dimensional Nanomaterials. *Chem. Soc. Rev.* **2016**, *45*, 1750–1780.
- (148) Moore, C.; Movia, D.; Smith, R. J.; Hanlon, D.; Lebre, F.; Lavelle, E. C.; Byrne, H. J.; Coleman, J. N.; Volkov, Y.; McIntyre, J. Industrial Grade 2D Molybdenum Disulphide (MoS<sub>2</sub>): An in vitro Exploration of the Impact on Cellular Uptake, Cytotoxicity, and Inflammation. *2D Mater.* **2017**, *4*, 025065.
- (149) Fu, H.; Li, Z.; Xie, H.; Sun, Z.; Wang, B.; Huang, H.; Han, G.; Wang, H.; Chu, P. K.; Yu, X.-F. Different-Sized Black Phosphorus Nanosheets with Good Cytocompatibility and High Photothermal Performance. *RSC Adv.* **2017**, *7*, 14618–14624.
- (150) Zhang, X.; Zhang, Z.; Zhang, S.; Li, D.; Ma, W.; Ma, C. X.; Wu, F.; Zhao, Q.; Yan, Q.; Xing, B. Size Effect on the Cytotoxicity of Layered Black Phosphorus and Underlying Mechanisms. *Small* **2017**, *13*, 1701210.
- (151) Kalantar-zadeh, K.; Ou, J. Z.; Daeneke, T.; Strano, M. S.; Pumera, M.; Gras, S. L. Two-Dimensional Transition Metal Dichalcogenides in Biosystems. *Adv. Funct. Mater.* **2015**, *25*, 5086–5099.
- (152) Chimene, D.; Alge, D. L.; Gaharwar, A. K. Two-Dimensional Nanomaterials for Biomedical Applications: Emerging Trends and Future Prospects. *Adv. Mater.* **2015**, *27*, 7261–7284.
- (153) Li, Z.; Wong, S. L. Functionalization of 2D Transition Metal Dichalcogenides for Biomedical Applications. *Mater. Sci. Eng. C* **2017**, *70*, 1095–1106.
- (154) Yin, F.; Gu, B.; Lin, Y.; Panwar, N.; Tjin, S. C.; Qu, J.; Lau, S. P.; Yong, K.-T. Functionalized 2D Nanomaterials for Gene Delivery Applications. *Coord. Chem. Rev.* **2017**, *347*, 77–97.

- (155) Chen, H.; Liu, T.; Su, Z.; Shang, L.; Wei, G. 2D Transition Metal Dichalcogenide Nanosheets for Photo/Thermo-Based Tumor Imaging and Therapy. *Nanoscale Horizons* **2018**, DOI: 10.1039/c7nh00158d.
- (156) Finn, D. J.; Lotya, M.; Cunningham, G.; Smith, R. J.; McCloskey, D.; Donegan, J. F.; Coleman, J. N. Inkjet Deposition of Liquid-Exfoliated Graphene and MoS<sub>2</sub> Nanosheets for Printed Device Applications. *J. Mater. Chem. C* **2014**, 2, 925–932.
- (157) Hossain, R. F.; Deaguero, I. G.; Boland, T.; Kaul, A. B. Solution Dispersed 2D Graphene & MoS<sub>2</sub> for an Inkjet Printed Biocompatible Photodetector. *Proc. 25th Bienn. Lester Eastman Conf. High Perform. Devices, LEC* **2016**, 19–22.
- (158) Eksik, O.; Gao, J.; Shojaei, S. A.; Thomas, A.; Chow, P.; Bartolucci, S. F.; Lucca, D. a.; Koratkar, N. Epoxy Nanocomposites with Two-Dimensional Transition Metal Dichalcogenide Additives. *ACS Nano* **2014**, 8, 5282–5289.
- (159) Chan, K.; Wong, H.; Yeung, K.; Tjong, S. Polypropylene Biocomposites with Boron Nitride and Nanohydroxyapatite Reinforcements. *Materials (Basel)*. **2015**, 8, 992–1008.
- (160) Ternary, P.; Wan, S.; Li, Y.; Peng, J.; Hu, H.; Cheng, Q.; Jiang, L. Synergistic Toughening of Graphene Oxide - Molybdenum Disulfide - Thermoplastic Polyurethane Ternary Artificial Nacre. *ACS Nano* **2015**, 9, 708–714.
- (161) Jakus, A. E.; Secor, E. B.; Rutz, A. L.; Jordan, S. W.; Hersam, M. C.; Shah, R. N. Three-Dimensional Printing of High-Content Graphene Scaffolds for Electronic and Biomedical Applications. *ACS Nano* **2015**, 9, 4636–4648.
- (162) McManus, D.; Vranic, S.; Withers, F.; Sanchez-Romaguera, V.; Macucci, M.; Yang, H.; Sorrentino, R.; Parvez, K.; Son, S.-K.; Iannaccone, G.; *et al.* Water-Based and Biocompatible 2D Crystal Inks for All-Inkjet-Printed Heterostructures. *Nat. Nanotechnol.* **2017**, 12, 343–350.
- (163) Wang, S.; Qiu, J.; Guo, W.; Yu, X.; Nie, J.; Zhang, J.; Zhang, X.; Liu, Z.; Mou, X.; Li, L.; *et al.* A Nanostructured Molybdenum Disulfide Film for Promoting Neural Stem Cell Neuronal Differentiation: Toward a Nerve Tissue-Engineered 3D Scaffold. *Adv. Biosyst.* **2017**, 1, 1600042.
- (164) Jakus, A. E.; Taylor, S. L.; Geisendorfer, N. R.; Dunand, D. C.; Shah, R. N. Metallic Architectures from 3D-Printed Powder-Based Liquid Inks. *Adv. Funct. Mater.* **2015**, 25, 6985–6995.
- (165) Lalwani, G.; Henslee, A. M.; Farshid, B.; Lin, L.; Kasper, F. K.; Qin, Y.-X.; Mikos, A. G.; Sitharaman, B. Two-Dimensional Nanostructure- Reinforced Biodegradable Polymeric Nanocomposites for Bone Tissue Engineering. *Biomacromolecules* **2013**, 14, 900–909.

- (166) Guo, X.; Mei, N. Assessment of the Toxic Potential of Graphene Family Nanomaterials. *J. Food Drug Anal.* **2014**, *22*, 105–115.
- (167) Duch, M.; Budinger, G.; Liang, Y. Minimizing Oxidation and Stable Nanoscale Dispersion Improves the Biocompatibility of Graphene in the Lung. *Nano Lett.* **2011**, *11*, 5201–5207.
- (168) Wang, X.; Duch, M. C.; Mansukhani, N.; Ji, Z.; Liao, Y. P.; Wang, M.; Zhang, H.; Sun, B.; Chang, C. H.; Li, R.; *et al.* Use of a Pro-Fibrogenic Mechanism-Based Predictive Toxicological Approach for Tiered Testing and Decision Analysis of Carbonaceous Nanomaterials. *ACS Nano* **2015**, *9*, 3032–3043.
- (169) Seabra, A. B.; Paula, A. J.; de Lima, R.; Alves, O. L.; Duran, N. Nanotoxicity of Graphene and Graphene Oxide. *Chem. Res. Toxicol.* **2014**, *27*, 159–168.
- (170) Ji, D.; Zhang, Y.; Zang, Y.; Li, J.; Chen, G.; He, X.; Tian, H. Targeted Intracellular Production of Reactive Oxygen Species by a 2D Molybdenum Disulfide Glycosheet. *Adv. Mater.* **2016**, *28*, 9356–9363.
- (171) Dou, W. T.; Kong, Y.; He, X. P.; Chen, G. R.; Zang, Y.; Li, J.; Tian, H. GPCR Activation and Endocytosis Induced by a 2D Material Agonist. *ACS Appl. Mater. Interfaces* **2017**, *9*, 14709–14715.
- (172) Kurapati, R.; Muzi, L.; de Garibay, A. P. R.; Russier, J.; Voiry, D.; Vacchi, I. A.; Chhowalla, M.; Bianco, A. Enzymatic Biodegradability of Pristine and Functionalized Transition Metal Dichalcogenide MoS<sub>2</sub> Nanosheets. *Adv. Funct. Mater.* **2017**, *27*, 1605176.
- (173) Chen, Y.; Cheng, L.; Dong, Z.; Chao, Y.; Lei, H.; Zhao, H.; Wang, J.; Liu, Z. Degradable Vanadium Disulfide Nanostructures with Unique Optical and Magnetic Functions for Cancer Theranostics. *Angew. Chemie - Int. Ed.* **2017**, *129*, 13171–13176.
- (174) Song, G.; Hao, J.; Liang, C.; Liu, T.; Gao, M.; Cheng, L.; Hu, J.; Liu, Z. Degradable Molybdenum Oxide Nanosheets with Rapid Clearance and Efficient Tumor Homing Capabilities as a Therapeutic Nanoplatfrom. *Angew. Chemie - Int. Ed.* **2016**, *55*, 2122–2126.
- (175) Wang, Z.; Von Dem Bussche, A.; Qiu, Y.; Valentin, T. M.; Gion, K.; Kane, A. B.; Hurt, R. H. Chemical Dissolution Pathways of MoS<sub>2</sub> Nanosheets in Biological and Environmental Media. *Environ. Sci. Technol.* **2016**, *50*, 7208–7217.
- (176) Fojtů, M.; Chia, X.; Sofer, Z.; Masařík, M.; Pumera, M. Black Phosphorus Nanoparticles Potentiate the Anticancer Effect of Oxaliplatin in Ovarian Cancer Cell Line. *Adv. Funct. Mater.* **2017**, *27*, 1701955.

- (177) Choi, J.; Das, S.; Theodore, N. D.; Kim, I.; Honsberg, C.; Choi, H. W.; Alford, T. L. Advances in 2D/3D Printing of Functional Nanomaterials and Their Applications. *ECS J. Solid State Sci. Technol.* **2015**, *4*, 3001–3009.
- (178) Lewis, J. A.; Gratson, G. M. Direct Writing in Three Dimensions. *Mater. Today* **2004**, *7*, 32–39.
- (179) Li, Q.; Lewis, J. a. Nanoparticle Inks for Directed Assembly of Three-Dimensional Periodic Structures. *Adv. Mater.* **2003**, *15*, 1639–1643.
- (180) Ivanova, O.; Williams, C.; Campbell, T. Additive Manufacturing (AM) and Nanotechnology: Promises and Challenges. *Rapid Prototyp. J.* **2013**, *19*, 353–364.
- (181) Raviv, D.; Zhao, W.; Mcknelly, C.; Papadopoulou, A.; Kadambi, A.; Shi, B.; Hirsch, S.; Dikovsky, D.; Zyracki, M.; Olguin, C.; *et al.* Active Printed Materials for Complex Self-Evolving Deformations. *Sci. Rep.* **2014**, *4*, 7422.
- (182) Campbell, T. a.; Ivanova, O. S. 3D Printing of Multifunctional Nanocomposites. *Nano Today* **2013**, *8*, 119–120.
- (183) Jones, N. Three-Dimensional Printers Are Opening Up New Worlds To Research. *Nature* **2012**, *487*, 22–23.
- (184) Campbell, I.; Bourell, D.; Gibson, I. Additive Manufacturing: Rapid Prototyping Comes of Age. *Rapid Prototyp. J.* **2012**, *18*, 255–258.
- (185) Murphy, S. V; Atala, A. 3D Bioprinting of Tissues and Organs. *Nat. Biotechnol.* **2014**, *32*, 773–785.
- (186) Gross, B. C.; Erkal, J. L.; Lockwood, S. Y.; Chen, C.; Spence, D. M. Evaluation of 3D Printing and Its Potential Impact on Biotechnology and the Chemical Sciences. *Anal. Chem.* **2014**, *86*, 3240–3253.
- (187) Gou, M.; Qu, X.; Zhu, W.; Xiang, M.; Yang, J.; Zhang, K.; Wei, Y.; Chen, S. Bio-Inspired Detoxification Using 3D-Printed Hydrogel Nanocomposites. *Nat. Commun.* **2014**, *5*, 3774.
- (188) Pati, F.; Jang, J.; Ha, D.-H.; Won Kim, S.; Rhie, J.-W.; Shim, J.-H.; Kim, D.-H.; Cho, D.-W. Printing Three-Dimensional Tissue Analogues with Decellularized Extracellular Matrix Bioink. *Nat. Commun.* **2014**, *5*, 3935.
- (189) Levy, G. N.; Schindel, R.; Kruth, J. P. Rapid Manufacturing and Rapid Tooling with Layer Manufacturing (LM) Technologies, State of the Art and Future Perspectives. *CIRP Ann. - Manuf. Technol.* **2003**, *52*, 589–609.
- (190) Arafat, M. T.; Gibson, I.; Li, X. State of the Art and Future Direction of Additive

- Manufactured Scaffolds-Based Bone Tissue Engineering. *Rapid Prototyp. J.* **2013**, *20*, 13–26.
- (191) Lewis, J. A. Direct Ink Writing of 3D Functional Materials. *Adv. Funct. Mater.* **2006**, *16*, 2193–2204.
- (192) Lewis, J. A.; Smay, J. E.; Stuecker, J.; Cesarano, J. Direct Ink Writing of Three-Dimensional Ceramic Structures. *J. Am. Ceram. Soc.* **2006**, *89*, 3599–3609.
- (193) Hofmann, M. 3D Printing Gets a Boost and Opportunities with Polymer Materials. *ACS Macro Lett.* **2014**, *3*, 382–386.
- (194) He, J.; Li, D.; Lu, B.; Wang, Z.; Zhang, T. Custom Fabrication of a Composite Hemi-Knee Joint Based on Rapid Prototyping. *Rapid Prototyp. J.* **2006**, *12*, 198–205.
- (195) Klammert, U.; Gbureck, U.; Vorndran, E.; Rödiger, J.; Meyer-Marcotty, P.; Kübler, A. C. 3D Powder Printed Calcium Phosphate Implants for Reconstruction of Cranial and Maxillofacial Defects. *J. Cranio-Maxillofacial Surg.* **2010**, *38*, 565–570.
- (196) Cohen, D. L.; Malone, E.; Lipson, H.; Bonassar, L. J. Direct Freeform Fabrication of Seeded Hydrogels in Arbitrary Geometries. *Tissue Eng.* **2006**, *12*, 1325–1335.
- (197) Khalil, S.; Nam, J.; Sun, W. Multi-Nozzle Deposition for Construction of 3D Biopolymer Tissue Scaffolds. *Rapid Prototyp. J.* **2005**, *11*, 9–17.
- (198) Xu, T.; Binder, K. W.; Albanna, M. Z.; Dice, D.; Zhao, W.; Yoo, J. J.; Atala, A. Hybrid Printing of Mechanically and Biologically Improved Constructs for Cartilage Tissue Engineering Applications. *Biofabrication* **2013**, *5*, 015001.
- (199) Villar, G.; Graham, A. D.; Bayley, H. A Tissue-Like Printed Material. *Science* **2013**, *340*, 48–52.
- (200) Reiffel, A. J.; Kafka, C.; Hernandez, K. a.; Popa, S.; Perez, J. L.; Zhou, S.; Pramanik, S.; Brown, B. N.; Ryu, W. S.; Bonassar, L. J.; *et al.* High-Fidelity Tissue Engineering of Patient-Specific Auricles for Reconstruction of Pediatric Microtia and Other Auricular Deformities. *PLoS One* **2013**, *8*, e56506.
- (201) Mannoor, M. S.; Jiang, Z.; James, T.; Kong, Y. L.; Malatesta, K. a; Soboyejo, W. O.; Verma, N.; Gracias, D. H.; McAlpine, M. C. 3D Printed Bionic Ears. *Nano Lett.* **2013**, *13*, 2634–2639.
- (202) Kong, Y. L.; Tamargo, I. a; Kim, H.; Johnson, B. N.; Gupta, M. K.; Koh, T.-W.; Chin, H.-A.; Steingart, D. a; Rand, B. P.; McAlpine, M. C. 3D Printed Quantum Dot Light-Emitting Diodes. *Nano Lett.* **2014**, *14*, 7017–7023.
- (203) Georgakilas, V.; Otyepka, M.; Bourlinos, A. B.; Chandra, V.; Kim, N.; Kemp, K. C.;

- Hobza, P.; Zboril, R.; Kim, K. S. Functionalization of Graphene: Covalent and Non-Covalent Approaches, Derivatives and Applications. *Chem. Rev.* **2012**, *112*, 6156–6214.
- (204) Sun, Z.; James, D. K.; Tour, J. M. Graphene Chemistry: Synthesis and Manipulation. *J. Phys. Chem. Lett.* **2011**, *2*, 2425–2432.
- (205) Zhao, Y. Bottom-Up Construction of Highly Ordered Mesoporous Graphene Frameworks. *Sci. Bull.* **2015**, *60*, 1962–1963.
- (206) Chung, C.; Kim, Y.-K.; Shin, D.; Ryoo, S.-R.; Hong, B. H.; Min, D.-H. Biomedical Applications of Graphene and Graphene Oxide. *Acc. Chem. Res.* **2013**, *46*, 2211–2224.
- (207) Chen, J.; Peng, H.; Wang, X.; Shao, F.; Yuan, Z.; Han, H. Graphene Oxide Exhibits Broad-Spectrum Antimicrobial Activity against Bacterial Phytopathogens and Fungal Conidia by Intertwining and Membrane Perturbation. *Nanoscale* **2014**, *6*, 1879–1889.
- (208) Li, Y.; Yuan, H.; von dem Bussche, A.; Creighton, M.; Hurt, R. H.; Kane, A. B.; Gao, H. Graphene Microsheets Enter Cells through Spontaneous Membrane Penetration at Edge Asperities and Corner Sites. *Proc. Natl. Acad. Sci. U. S. A.* **2013**, *110*, 12295–12300.
- (209) Tu, Y.; Lv, M.; Xiu, P.; Huynh, T.; Zhang, M.; Castelli, M.; Liu, Z.; Huang, Q.; Fan, C.; Fang, H.; *et al.* Destructive Extraction of Phospholipids from Escherichia Coli Membranes by Graphene Nanosheets. *Nat. Nanotechnol.* **2013**, *8*, 594–601.
- (210) Yang, L.; Zhang, R.; Liu, B.; Wang, J.; Wang, S.; Han, M.; Zhang, Z.  $\Pi$ -Conjugated Carbon Radicals at Graphene Oxide to Initiate Ultrastrong Chemiluminescence. *Angew. Chemie Int. Ed.* **2014**, *53*, 10109–10113.
- (211) Liu, S.; Zeng, T. H.; Hofmann, M.; Burcombe, E.; Wei, J.; Jiang, R.; Kong, J.; Chen, Y. Antibacterial Activity of Graphite, Graphite Oxide, Graphene Oxide, and Reduced Graphene Oxide: Membrane and Oxidative Stress. *ACS Nano* **2011**, *5*, 6971–6980.
- (212) Akhavan, O.; Ghaderi, E. Toxicity of Graphene and Graphene Oxide Nanowalls Against Bacteria. *ACS Nano* **2010**, *4*, 5731–5736.
- (213) Perreault, F.; de Faria, A. F.; Nejati, S.; Elimelech, M. Antimicrobial Properties of Graphene Oxide Nanosheets: Why Size Matters. *ACS Nano* **2015**, *9*, 7226–7236.
- (214) Sun, H.; Gao, N.; Dong, K.; Ren, J.; Qu, X. Graphene Quantum Dots-Band-Aids Used for Wound Disinfection. *ACS Nano* **2014**, *8*, 6202–6210.
- (215) Pavlidis, I. V.; Patila, M.; Bornscheuer, U. T.; Gournis, D.; Stamatis, H. Graphene-Based Nanobiocatalytic Systems: Recent Advances and Future Prospects. *Trends Biotechnol.* **2014**, *32*, 312–320.
- (216) Liu, J.; Cui, L.; Losic, D. Graphene and Graphene Oxide as New Nanocarriers for Drug

- Delivery Applications. *Acta Biomater.* **2013**, *9*, 9243–9257.
- (217) Hussain, S. M.; Hess, K. L.; Gearhart, J. M.; Geiss, K. T.; Schlager, J. J. In vitro Toxicity of Nanoparticles in BRL 3A Rat Liver Cells. *Toxicol. Vit.* **2005**, *19*, 975–983.
- (218) Szabo, G.; Petrasek, J. Inflammasome Activation and Function in Liver Disease. *Nat. Rev. Gastroenterol. Hepatol.* **2015**, *12*, 387–400.
- (219) Zhang, Y.-N.; Poon, W.; Tavares, A. J.; McGilvray, I. D.; Chan, W. C. W. Nanoparticle–liver Interactions: Cellular Uptake and Hepatobiliary Elimination. *J. Control. Release* **2016**, *240*, 332–348.
- (220) Godoy, P.; Hewitt, N. J.; Albrecht, U.; Andersen, M. E.; Ansari, N.; Bhattacharya, S.; Bode, J. G.; Bolleyn, J.; Borner, C.; Böttger, J.; *et al.* Recent Advances in 2D and 3D in vitro Systems Using Primary Hepatocytes, Alternative Hepatocyte Sources and Non-Parenchymal Liver Cells and Their Use in Investigating Mechanisms of Hepatotoxicity, Cell Signaling and ADME. *Arch. Toxicol.* **2013**, *87*, 1315–1530.
- (221) Bilzer, M.; Roggel, F.; Gerbes, A. L. Role of Kupffer Cells in Host Defense and Liver Disease. *Liver Int.* **2006**, *26*, 1175–1186.
- (222) Yang, K.; Feng, L.; Hong, H.; Cai, W.; Liu, Z. Preparation and Functionalization of Graphene Nanocomposites for Biomedical Applications. *Nat. Protoc.* **2013**, *8*, 2392–2403.
- (223) Taratula, O.; Patel, M.; Schumann, C.; Naleway, M. A.; Pang, A. J.; He, H.; Taratula, O. Phthalocyanine-Loaded Graphene Nanoplatfrom for Imaging-Guided Combinatorial Phototherapy. *Int. J. Nanomedicine* **2015**, *10*, 2347–2362.
- (224) Wen, K.-P.; Chen, Y.-C.; Chuang, C.-H.; Chang, H.-Y.; Lee, C.-Y.; Tai, N.-H. Accumulation and Toxicity of Intravenously-Injected Functionalized Graphene Oxide in Mice. *J. Appl. Toxicol.* **2015**, *35*, 1211–1218.
- (225) Yang, K.; Gong, H.; Shi, X.; Wan, J.; Zhang, Y.; Liu, Z. In vivo Biodistribution and Toxicology of Functionalized Nano-Graphene Oxide in Mice after Oral and Intraperitoneal Administration. *Biomaterials* **2013**, *34*, 2787–2795.
- (226) Ou, L.; Song, B.; Liang, H.; Liu, J.; Feng, X.; Deng, B.; Sun, T.; Shao, L. Toxicity of Graphene-Family Nanoparticles: A General Review of the Origins and Mechanisms. *Part. Fibre Toxicol.* **2016**, *13*, 57.
- (227) Efremova, L. V.; Vasilchenko, A. S.; Rakov, E. G.; Deryabin, D. G. Toxicity of Graphene Shells, Graphene Oxide, and Graphene Oxide Paper Evaluated with Escherichia Coli Biotests. *Biomed Res. Int.* **2015**, *2015*, 869361.

- (228) Bagri, A.; Mattevi, C.; Acik, M.; Chabal, Y. J.; Chhowalla, M.; Shenoy, V. B. Structural Evolution during the Reduction of Chemically Derived Graphene Oxide. *Nat. Chem.* **2010**, *2*, 581–587.
- (229) Shen, Y.; Zhang, H.-B.; Zhang, H.; Ren, W.; Dasari, A.; Tang, G.-S.; Yu, Z.-Z. Structural Evolution of Functionalized Graphene Sheets during Solvothermal Reduction. *Carbon N. Y.* **2013**, *56*, 132–138.
- (230) Zhang, L.; Ji, L.; Glans, P.-A.; Zhang, Y.; Zhu, J.; Guo, J. Electronic Structure and Chemical Bonding of a Graphene Oxide–Sulfur Nanocomposite for Use in Superior Performance Lithium–Sulfur Cells. *Phys. Chem. Chem. Phys.* **2012**, *14*, 13670–13675.
- (231) An, J.-E.; Jeon, G. W.; Jeong, Y. G. Preparation and Properties of Polypropylene Nanocomposites Reinforced with Exfoliated Graphene. *Fibers Polym.* **2012**, *13*, 507–514.
- (232) Ma, J.; Liu, R.; Wang, X.; Liu, Q.; Chen, Y.; Valle, R. P.; Zuo, Y. Y.; Xia, T.; Liu, S. Crucial Role of Lateral Size for Graphene Oxide in Activating Macrophages and Stimulating Pro-Inflammatory Responses in Cells and Animals. *ACS Nano* **2015**, *9*, 10498–10515.
- (233) Kim, J.; Cote, L. J.; Kim, F.; Yuan, W.; Shull, K. R.; Huang, J. Graphene Oxide Sheets at Interfaces. *J. Am. Chem. Soc.* **2010**, *132*, 8180–8186.
- (234) Zhao, Y.; Jafvert, C. T. Environmental Photochemistry of Single Layered Graphene Oxide in Water. *Environ. Sci. Nano* **2015**, *2*, 136–142.
- (235) Hu, W.; Peng, C.; Luo, W.; Lv, M.; Li, X.; Li, D.; Huang, Q.; Fan, C. Graphene-Based Antibacterial Paper. *ACS Nano* **2010**, *4*, 4317–4323.
- (236) Nishida, E.; Miyaji, H.; Kato, A.; Takita, H.; Iwanaga, T.; Momose, T.; Ogawa, K.; Murakami, S.; Sugaya, T.; Kawanami, M. Graphene Oxide Scaffold Accelerates Cellular Proliferative Response and Alveolar Bone Healing of Tooth Extraction Socket. *Int. J. Nanomedicine* **2016**, *11*, 2265–2277.
- (237) Vera-Sánchez, M.; Aznar-Cervantes, S.; Jover, E.; García-Bernal, D.; Oñate-Sánchez, R. E.; Hernández-Romero, D.; Moraleda, J. M.; Collado-González, M.; Rodríguez-Lozano, F. J.; Cenis, J. L. Silk-Fibroin and Graphene Oxide Composites Promote Human Periodontal Ligament Stem Cell Spontaneous Differentiation into Osteo/Cementoblast-Like Cells. *Stem Cells Dev.* **2016**, *25*, 1742–1754.
- (238) Garcia-Alegria, E.; Iluit, M.; Stefanska, M.; Silva, C.; Heeg, S.; Kimber, S. J.; Kouskoff, V.; Lacaud, G.; Vijayaraghavan, A.; Batta, K. Graphene Oxide Promotes Embryonic Stem Cell Differentiation to Haematopoietic Lineage. *Sci. Rep.* **2016**, *6*, 25917.
- (239) Jasim, D. A.; Murphy, S.; Newman, L.; Mironov, A.; Prestat, E.; McCaffrey, J.; Ménard-

- Moyon, C.; Rodrigues, A. F.; Bianco, A.; Haigh, S.; *et al.* The Effects of Extensive Glomerular Filtration of Thin Graphene Oxide Sheets on Kidney Physiology. *ACS Nano* **2016**, *10*, 10753–10767.
- (240) Liu, J.-H.; Yang, S.-T.; Wang, H.; Chang, Y.; Cao, A.; Liu, Y. Effect of Size and Dose on the Biodistribution of Graphene Oxide in Mice. *Nanomedicine* **2012**, *7*, 1801–1812.
- (241) Jiang, W.; Wang, X.; Osborne, O. J.; Du, Y.; Chang, C. H.; Liao, Y. P.; Sun, B.; Jiang, J.; Ji, Z.; Li, R.; *et al.* Pro-Inflammatory and Pro-Fibrogenic Effects of Ionic and Particulate Arsenide and Indium-Containing Semiconductor Materials in the Murine Lung. *ACS Nano* **2017**, *11*, 1869–1883.
- (242) Chang, Y.; Yang, S.-T.; Liu, J.-H.; Dong, E.; Wang, Y.; Cao, A.; Liu, Y.; Wang, H. In Vitro Toxicity Evaluation of Graphene Oxide on A549 Cells. *Toxicol. Lett.* **2011**, *200*, 201–210.
- (243) Tsoi, K. M.; MacParland, S. A.; Ma, X.-Z.; Spetzler, V. N.; Echeverri, J.; Ouyang, B.; Fadel, S. M.; Sykes, E. A.; Goldaracena, N.; Kathis, J. M.; *et al.* Mechanism of Hard-Nanomaterial Clearance by the Liver. *Nat. Mater.* **2016**, *15*, 1212–1221.
- (244) Sun, B.; Wang, X.; Ji, Z.; Li, R.; Xia, T. NLRP3 Inflammasome Activation Induced by Engineered Nanomaterials. *Small* **2013**, *9*, 1595–1607.
- (245) Zhou, J.; Tan, S.-H.; Nicolas, V.; Bauvy, C.; Yang, N.-D.; Zhang, J.; Xue, Y.; Codogno, P.; Shen, H.-M. Activation of Lysosomal Function in the Course of Autophagy via MTORC1 Suppression and Autophagosome-Lysosome Fusion. *Cell Res.* **2013**, *23*, 508–523.
- (246) Elsabahy, M.; Wooley, K. L. Cytokines as Biomarkers of Nanoparticle Immunotoxicity. *Chem. Soc. Rev.* **2013**, *42*, 5552–5576.
- (247) Qu, G.; Liu, S.; Zhang, S.; Wang, L.; Wang, X.; Sun, B.; Yin, N.; Gao, X.; Xia, T.; Chen, J.-J.; *et al.* Graphene Oxide Induces Toll-like Receptor 4 (TLR4)-Dependent Necrosis in Macrophages. **2013**.
- (248) Kawai, T.; Akira, S. Signaling to NF- $\kappa$ B by Toll-like Receptors. *Trends Mol. Med.* **2007**, *13*, 460–469.
- (249) He, X.; Qian, Y.; Li, Z.; Fan, E. K.; Li, Y.; Wu, L.; Billiar, T. R.; Wilson, M. A.; Shi, X.; Fan, J. TLR4-Upregulated IL-1 $\beta$  and IL-1RI Promote Alveolar Macrophage Pyroptosis and Lung Inflammation through an Autocrine Mechanism. *Sci. Rep.* **2016**, *6*, 31663.
- (250) Kojima, S.; Nikaido, H. Permeation Rates of Penicillins Indicate That Escherichia Coli Porins Function Principally as Nonspecific Channels. *Proc. Natl. Acad. Sci.* **2013**, *110*, E2629–E2634.

- (251) Chowdhury, I.; Mansukhani, N. D.; Guiney, L. M.; Hersam, M. C.; Bouchard, D. Aggregation and Stability of Reduced Graphene Oxide: Complex Roles of Divalent Cations, PH, and Natural Organic Matter. *Environ. Sci. Technol.* **2015**, *49*, 10886–10893.
- (252) Li, R.; Ji, Z.; Chang, C. H.; Dunphy, D. R.; Cai, X.; Meng, H.; Zhang, H.; Sun, B.; Wang, X.; Dong, J.; *et al.* Surface Interactions with Compartmentalized Cellular Phosphates Explain Rare Earth Oxide Nanoparticle Hazard and Provide Opportunities for Safer Design. *ACS Nano* **2014**, *8*, 1771–1783.
- (253) Kumar, A.; Vemula, P. K.; Ajayan, P. M.; John, G. Silver-Nanoparticle-Embedded Antimicrobial Paints Based on Vegetable Oil. *Nat. Mater.* **2008**, *7*, 236–241.
- (254) Park, S.; Ruoff, R. S. Chemical Methods for the Production of Graphenes. *Nat. Nanotechnol.* **2009**, *4*, 217–224.
- (255) Yang, Y.; Asiri, A. M.; Tang, Z.; Du, D.; Lin, Y. Graphene Based Materials for Biomedical Applications. *Mater. Today* **2013**, *16*, 365–373.
- (256) Zhao, G.; Li, J.; Ren, X.; Chen, C.; Wang, X. Few-Layered Graphene Oxide Nanosheets As Superior Sorbents for Heavy Metal Ion Pollution Management. *Environ. Sci. Technol.* **2011**, *45*, 10454–10462.
- (257) Zhang, Y.; Tang, Z.-R.; Fu, X.; Xu, Y.-J. TiO<sub>2</sub>–Graphene Nanocomposites for Gas-Phase Photocatalytic Degradation of Volatile Aromatic Pollutant: Is TiO<sub>2</sub>–Graphene Truly Different from Other TiO<sub>2</sub>–Carbon Composite Materials? *ACS Nano* **2010**, *4*, 7303–7314.
- (258) Suk, M. E.; Aluru, N. R. Water Transport through Ultrathin Graphene. *J. Phys. Chem. Lett.* **2010**, *1*, 1590–1594.
- (259) Wang, H.; Cui, L. F.; Yang, Y.; Sanchez Casalongue, H.; Robinson, J. T.; Liang, Y.; Cui, Y.; Dai, H. Mn<sub>3</sub>O<sub>4</sub>-Graphene Hybrid as a High-Capacity Anode Material for Lithium Ion Batteries. *J. Am. Chem. Soc.* **2010**, *132*, 13978–13980.
- (260) Kim, S.; Zhou, S.; Hu, Y.; Acik, M.; Chabal, Y. J.; Berger, C.; de Heer, W.; Bongiorno, A.; Riedo, E. Room-Temperature Metastability of Multilayer Graphene Oxide Films. *Nat. Mater.* **2012**, *11*, 544–549.
- (261) Dimiev, A. M.; Alemany, L. B.; Tour, J. M. Graphene Oxide. Origin of Acidity, Its Instability in Water, and a New Dynamic Structural Model. *ACS Nano* **2013**, *7*, 576–588.
- (262) Williams, G.; Seger, B.; Kamt, P. V. TiO<sub>2</sub>-Graphene Nanocomposites. UV-Assisted Photocatalytic Reduction of Graphene Oxide. *ACS Nano* **2008**, *2*, 1487–1491.
- (263) Salas, E. C.; Sun, Z.; Lüttge, A.; Tour, J. M. Reduction of Graphene Oxide *via* Bacterial

- Respiration. *ACS Nano* **2010**, *4*, 4852–4856.
- (264) Matsumoto, Y.; Koinuma, M.; Kim, S. Y.; Watanabe, Y.; Taniguchi, T.; Hatakeyama, K.; Tateishi, H.; Ida, S. Simple Photoreduction of Graphene Oxide Nanosheet under Mild Conditions. *ACS Appl. Mater. Interfaces* **2010**, *2*, 3461–3466.
- (265) Matsumoto, Y.; Koinuma, M.; Ida, S.; Hayami, S.; Taniguchi, T.; Hatakeyama, K.; Tateishi, H.; Watanabe, Y.; Amano, S. Photoreaction of Graphene Oxide Nanosheets in Water. *J. Phys. Chem. C* **2011**, *115*, 19280–19286.
- (266) Zhao, J.; Wang, Z.; White, J. C.; Xing, B. Graphene in the Aquatic Environment: Adsorption, Dispersion, Toxicity and Transformation. *Environ. Sci. Technol.* **2014**, *48*, 9995–10009.
- (267) Chowdhury, I.; Duch, M. C.; Mansukhani, N. D.; Hersam, M. C.; Bouchard, D. Colloidal Properties and Stability of Graphene Oxide Nanomaterials in the Aquatic Environment. *Environ. Sci. Technol.* **2013**, *47*, 6288–6296.
- (268) Wu, L.; Liu, L.; Gao, B.; Muñoz-Carpena, R.; Zhang, M.; Chen, H.; Zhou, Z.; Wang, H. Aggregation Kinetics of Graphene Oxides in Aqueous Solutions: Experiments, Mechanisms, and Modeling. *Langmuir* **2013**, *29*, 15174–15181.
- (269) Lanphere, J. D.; Luth, C. J.; Walker, S. L. Effects of Solution Chemistry on the Transport of Graphene Oxide in Saturated Porous Media. *Environ. Sci. Technol.* **2013**, *47*, 4255–4261.
- (270) Overbeek, T. DLVO Theory: Milestone of 20th Century Colloid Science- Preface. *Adv. Colloid Interface Sci.* **1999**, *83*, IX–XI.
- (271) Gregory, J. *Particles in Water : Properties and Processes*; IWA Pub., 2005.
- (272) Feriancikova, L.; Xu, S. Deposition and Remobilization of Graphene Oxide within Saturated Sand Packs. *J. Hazard. Mater.* **2012**, *235–236*, 194–200.
- (273) Liu, L.; Gao, B.; Wu, L.; Morales, V. L.; Yang, L.; Zhou, Z.; Wang, H. Deposition and Transport of Graphene Oxide in Saturated and Unsaturated Porous Media. *Chem. Eng. J.* **2013**, *229*, 444–449.
- (274) Zhou, X.; Zhang, Y.; Wang, C.; Wu, X.; Yang, Y.; Zheng, B.; Wu, H.; Guo, S.; Zhang, J. Photo-Fenton Reaction of Graphene Oxide: A New Strategy to Prepare Graphene Quantum Dots for DNA Cleavage. *ACS Nano* **2012**, *6*, 6592–6599.
- (275) Gengler, R. Y. N.; Badali, D. S.; Zhang, D.; Dimos, K.; Spyrou, K.; Gournis, D.; Miller, R. J. D. Revealing the Ultrafast Process behind the Photoreduction of Graphene Oxide. *Nat. Commun.* **2013**, *4*, 2560.

- (276) Koinuma, M.; Ogata, C.; Kamei, Y.; Hatakeyama, K.; Tateishi, H.; Watanabe, Y.; Taniguchi, T.; Gezuhara, K.; Hayami, S.; Funatsu, A.; *et al.* Photochemical Engineering of Graphene Oxide Nanosheets. *J. Phys. Chem. C* **2012**, *116*, 19822–19827.
- (277) Hou, W.-C.; Chowdhury, I.; Goodwin, D. G.; Henderson, W. M.; Fairbrother, D. H.; Bouchard, D.; Zepp, R. G. Photochemical Transformation of Graphene Oxide in Sunlight. *Environ. Sci. Technol.* **2015**, *49*, 3435–3443.
- (278) Kotchey, G. P.; Allen, B. L.; Vedala, H.; Yanamala, N.; Kapralov, A. A.; Tyurina, Y. Y.; Klein-Seetharaman, J.; Kagan, V. E.; Star, A. The Enzymatic Oxidation of Graphene Oxide. *ACS Nano* **2011**, *5*, 2098–2108.
- (279) Bai, H.; Jiang, W.; Kotchey, G. P.; Saidi, W. A.; Bythell, B. J.; Jarvis, J. M.; Marshall, A. G.; Robinson, R. A. S.; Star, A. Insight into the Mechanism of Graphene Oxide Degradation via the Photo-Fenton Reaction. *J. Phys. Chem. C* **2014**, *118*, 10519–10529.
- (280) Batley, G. E.; Kirby, J. K.; McLaughlin, M. J. Fate and Risks of Nanomaterials in Aquatic and Terrestrial Environments. *Acc. Chem. Res.* **2013**, *46*, 854–862.
- (281) Elimelech, M.; Phillip, W. A. The Future of Seawater and the Environment: Energy, Technology, and the Environment. *Science* **2011**, *333*, 712–718.
- (282) Zodrow, K. R.; Bar-Zeev, E.; Giannetto, M. J.; Elimelech, M. Biofouling and Microbial Communities in Membrane Distillation and Reverse Osmosis. *Environ. Sci. Technol.* **2014**, *48*, 13155–13164.
- (283) Li, Q.; Elimelech, M. Organic Fouling and Chemical Cleaning of Nanofiltration Membranes: Measurements and Mechanisms. *Environ. Sci. Technol.* **2004**, *38*, 4683–4693.
- (284) Nguyen, T.; Roddick, F. A.; Fan, L. Biofouling of Water Treatment Membranes: A Review of the Underlying Causes, Monitoring Techniques and Control Measures. *Membranes*, 2012, *2*, 804–840.
- (285) Ruiz-García, A.; Melián-Martel, N.; Nuez, I. Short Review on Predicting Fouling in RO Desalination. *Membranes*, 2017, *7*, 62–79.
- (286) Wu, S. *Polymer Interface and Adhesion*; M. Dekker, 1982.
- (287) Chang, I.-S.; Le Clech, P.; Jefferson, B.; Judd, S. Membrane Fouling in Membrane Bioreactors for Wastewater Treatment. *J. Environ. Eng.* **2002**, *128*, 1018–1029.
- (288) Lee, J.; Chae, H.-R.; Won, Y. J.; Lee, K.; Lee, C.-H.; Lee, H. H.; Kim, I.-C.; Lee, J. Graphene Oxide Nanoplatelets Composite Membrane with Hydrophilic and Antifouling Properties for Wastewater Treatment. *J. Memb. Sci.* **2013**, *448*, 223–230.

- (289) Mejías Carpio, I. E.; Santos, C. M.; Wei, X.; Rodrigues, D. F. Toxicity of a Polymer–graphene Oxide Composite against Bacterial Planktonic Cells, Biofilms, and Mammalian Cells. *Nanoscale* **2012**, *4*, 4746.
- (290) Krishnamoorthy, K.; Veerapandian, M.; Zhang, L.-H.; Yun, K.; Kim, S. J. Antibacterial Efficiency of Graphene Nanosheets against Pathogenic Bacteria via Lipid Peroxidation. *J. Phys. Chem. C* **2012**, *116*, 17280–17287.
- (291) Gurunathan, S.; Woong Han, J.; Abdal Daye, A.; Eppakayala, V.; Kim, J. Oxidative Stress-Mediated Antibacterial Activity of Graphene Oxide and Reduced Graphene Oxide in *Pseudomonas Aeruginosa*. *Int. J. Nanomedicine* **2012**, *7*, 5901.
- (292) Le-Clech, P.; Chen, V.; Fane, T. A. G. Fouling in Membrane Bioreactors Used in Wastewater Treatment. *J. Memb. Sci.* **2006**, *284*, 17–53.
- (293) Krishnan, S.; Weinman, C. J.; Ober, C. K. Advances in Polymers for Anti-Biofouling Surfaces. *J. Mater. Chem.* **2008**, *18*, 3405.
- (294) Chun, Y.; Mulcahy, D.; Zou, L.; Kim, I. S. A Short Review of Membrane Fouling in Forward Osmosis Processes. *Membranes*, 2017, *7*, 30–53.
- (295) Al-Amoudi, A.; Lovitt, R. W. Fouling Strategies and the Cleaning System of NF Membranes and Factors Affecting Cleaning Efficiency. *J. Memb. Sci.* **2007**, *303*, 4–28.
- (296) de Lannoy, C.-F.; Jassby, D.; Gloe, K.; Gordon, A. D.; Wiesner, M. R. Aquatic Biofouling Prevention by Electrically Charged Nanocomposite Polymer Thin Film Membranes. *Environ. Sci. Technol.* **2013**, *47*, 2760–2768.
- (297) Istanbulu, O.; Babauta, J.; Duc Nguyen, H.; Beyenal, H. Electrochemical Biofilm Control: Mechanism of Action. *Biofouling* **2012**, *28*, 769–778.
- (298) Sultana, S. T.; Babauta, J. T.; Beyenal, H. Electrochemical Biofilm Control: A Review. *Biofouling* **2015**, *31*, 745–758.
- (299) Mutamim, N. S. A.; Noor, Z. Z.; Hassan, M. A. A.; Yuniarto, A.; Olsson, G. Membrane Bioreactor: Applications and Limitations in Treating High Strength Industrial Wastewater. *Chem. Eng. J.* **2013**, *225*, 109–119.
- (300) Nielsen, P. H.; Jahn, A. Extraction of EPS. In *Microbial Extracellular Polymeric Substances*; Springer Berlin Heidelberg: Berlin, Heidelberg, 1999; pp. 49–72.
- (301) Chowdhury, I.; Duch, M. C.; Mansukhani, N. D.; Hersam, M. C.; Bouchard, D. Deposition and Release of Graphene Oxide Nanomaterials Using a Quartz Crystal Microbalance. *Environ. Sci. Technol.* **2014**, *48*, 961–969.
- (302) Park, S.; Lee, K.-S.; Bozoklu, G.; Cai, W.; Nguyen, S. T.; Ruoff, R. S. Graphene Oxide

- Papers Modified by Divalent Ions—Enhancing Mechanical Properties *via* Chemical Cross-Linking. *ACS Nano* **2008**, *2*, 572–578.
- (303) Becerril, H. A.; Mao, J.; Liu, Z.; Stoltenberg, R. M.; Bao, Z.; Chen, Y. Evaluation of Solution-Processed Reduced Graphene Oxide Films as Transparent Conductors. *ACS Nano* **2008**, *2*, 463–470.
- (304) Kotov, N. A.; Dékány, I.; Fendler, J. H. Ultrathin Graphite Oxide-Polyelectrolyte Composites Prepared by Self-Assembly: Transition between Conductive and Non-Conductive States. *Adv. Mater.* **1996**, *8*, 637–641.
- (305) Crittenden, J. C.; Trussell, R. R.; Hand, D. W.; Howe, K. J.; Tchobanoglous, G. *MWH's Water Treatment*; John Wiley & Sons, Inc.: Hoboken, NJ, USA, 2012.
- (306) Liu, Y.; Rosenfield, E.; Hu, M.; Mi, B. Direct Observation of Bacterial Deposition on and Detachment from Nanocomposite Membranes Embedded with Silver Nanoparticles. *Water Res.* **2013**, *47*, 2949–2958.
- (307) Adout, A.; Kang, S.; Asatekin, A.; Mayes, A. M.; Elimelech, M. Ultrafiltration Membranes Incorporating Amphiphilic Comb Copolymer Additives Prevent Irreversible Adhesion of Bacteria. *Environ. Sci. Technol.* **2010**, *44*, 2406–2411.
- (308) Chen, K. L.; Elimelech, M. Interaction of Fullerene (C60) Nanoparticles with Humic Acid and Alginate Coated Silica Surfaces: Measurements, Mechanisms, and Environmental Implications. *Environ. Sci. Technol.* **2008**, *42*, 7607–7614.
- (309) Chowdhury, I.; Duch, M. C.; Mansukhani, N. D.; Hersam, M. C.; Bouchard, D. Interactions of Graphene Oxide Nanomaterials with Natural Organic Matter and Metal Oxide Surfaces. *Environ. Sci. Technol.* **2014**, *48*, 9382–9390.
- (310) Buffle, J.; Wilkinson, K. J.; Stoll, S.; Filella, M.; Zhang, J. A Generalized Description of Aquatic Colloidal Interactions: The Three- Colloidal Component Approach. *Environ. Sci. Technol.* **1998**, *32*, 2887–2899.
- (311) Ang, W. S.; Elimelech, M. Protein (BSA) Fouling of Reverse Osmosis Membranes: Implications for Wastewater Reclamation. *J. Memb. Sci.* **2007**, *296*, 83–92.
- (312) Ribou, A. C.; Vigo, J.; Viallet, P.; Salmon, J. M. Interaction of a Protein, BSA, and a Fluorescent Probe, Mag-Indo-1, Influence of EDTA and Calcium on the Equilibrium. *Biophys. Chem.* **1999**, *81*, 179–189.
- (313) Poitras, C.; Tufenkji, N. A QCM-D-Based Biosensor for E. Coli O157:H7 Highlighting the Relevance of the Dissipation Slope as a Transduction Signal. *Biosens. Bioelectron.* **2009**, *24*, 2137–2142.

- (314) Silhavy, T.; Kahne, D.; Walker, S. The Bacterial Cell Envelope. *Cold Spring Harb. Perspect. Biol.* **2010**, 2, a000414.
- (315) Wingender, J.; Neu, T. R.; Flemming, H.-C. What Are Bacterial Extracellular Polymeric Substances? In *Microbial Extracellular Polymeric Substances*; Springer Berlin Heidelberg: Berlin, Heidelberg, 1999; pp. 1–19.
- (316) Evans, L. V. *Biofilms : Recent Advances in Their Study and Control.*; CRC Press, 2000.
- (317) Sheng, G.-P.; Yu, H.-Q.; Li, X.-Y. Extracellular Polymeric Substances (EPS) of Microbial Aggregates in Biological Wastewater Treatment Systems: A Review. *Biotechnol. Adv.* **2010**, 28, 882–894.
- (318) Donlan, R. M.; Costerton, J. W. Biofilms: Survival Mechanisms of Clinically Relevant Microorganisms. *Clin. Microbiol. Rev.* **2002**, 15, 167–193.
- (319) Eboigbodin, K. E.; Newton, J. R. A.; Routh, A. F.; Biggs, C. A. Bacterial Quorum Sensing and Cell Surface Electrokinetic Properties. *Appl. Microbiol. Biotechnol.* **2006**, 73, 669–675.
- (320) Pletnev, P.; Osterman, I.; Sergiev, P.; Bogdanov, A.; Dontsova, O. Survival Guide: Escherichia Coli in the Stationary Phase. *Acta Naturae* **2015**, 7, 22–33.
- (321) Chowdhury, I.; Cwiertny, D. M.; Walker, S. L. Combined Factors Influencing the Aggregation and Deposition of Nano-TiO<sub>2</sub> in the Presence of Humic Acid and Bacteria. *Environ. Sci. Technol.* **2012**, 46, 6968–6976.
- (322) Bouchard, D.; Zhang, W.; Powell, T.; Rattanaudompol, U. Aggregation Kinetics and Transport of Single-Walled Carbon Nanotubes at Low Surfactant Concentrations. *Environ. Sci. Technol.* **2012**, 46, 4458–4465.
- (323) Liu, H.; Du, Y.; Deng, Y.; Ye, P. D. Semiconducting Black Phosphorus: Synthesis, Transport Properties and Electronic Applications. *Chem. Soc. Rev.* **2015**, 44, 2732–2743.
- (324) Castellanos-Gomez, A. Black Phosphorus: Narrow Gap, Wide Applications. *J. Phys. Chem. Lett.* **2015**, 6, 4280–4291.
- (325) Li, L.; Yu, Y.; Ye, G. J.; Ge, Q.; Ou, X.; Wu, H.; Feng, D.; Chen, X. H.; Zhang, Y. Black Phosphorus Field-Effect Transistors. *Nat. Nanotechnol.* **2014**, 9, 372–377.
- (326) Du, Y.; Liu, H.; Deng, Y.; Ye, P. D. Device Perspective for Black Phosphorus Field-Effect Transistors: Contact Resistance, Ambipolar Behavior, and Scaling. *ACS Nano* **2014**, 8, 10035–10042.
- (327) Zhang, Z.; Li, L.; Horng, J.; Wang, N. Z.; Yang, F.; Yu, Y.; Zhang, Y.; Chen, G.; Watanabe, K.; Taniguchi, T.; *et al.* Strain-Modulated Bandgap and Piezo-Resistive Effect

- in Black Phosphorus Field-Effect Transistors. *Nano Lett.* **2017**, *17*, 6097–6103.
- (328) Kim, S.; Lee, J. Y.; Lee, C. H.; Lee, G. H.; Kim, J. Recovery of the Pristine Surface of Black Phosphorus by Water Rinsing and Its Device Application. *ACS Appl. Mater. Interfaces* **2017**, *9*, 21382–21389.
- (329) Illarionov, Y. Y.; Wai, M.; Rzepa, G.; Kim, J. S.; Kim, S.; Dodabalapur, A.; Akinwande, D.; Grasser, T. Long-Term Stability and Reliability of Black Phosphorus Field-Effect Transistors. *ACS Nano* **2016**, *10*, 9543–9549.
- (330) Wood, J. D.; Wells, S. A.; Jariwala, D.; Chen, K. S.; Cho, E.; Sangwan, V. K.; Liu, X.; Lauhon, L. J.; Marks, T. J.; Hersam, M. C. Effective Passivation of Exfoliated Black Phosphorus Transistors against Ambient Degradation. *Nano Lett.* **2014**, *14*, 6964–6970.
- (331) Ryder, C. R.; Wood, J. D.; Wells, S. A.; Yang, Y.; Jariwala, D.; Marks, T. J.; Schatz, G. C.; Hersam, M. C. Covalent Functionalization and Passivation of Exfoliated Black Phosphorus via Aryl Diazonium Chemistry. *Nat. Chem.* **2016**, *8*, 597–602.
- (332) Island, J. O.; Steele, G. A.; Van Der Zant, H. S. J.; Castellanos-Gomez, A. Environmental Instability of Few-Layer Black Phosphorus. *2D Mater.* **2015**, *2*, 011002.
- (333) Ziletti, A.; Carvalho, A.; Campbell, D. K.; Coker, D. F.; Castro Neto, A. H. Oxygen Defects in Phosphorene. *Phys. Rev. Lett.* **2015**, *114*, 26–29.
- (334) Kuntz, K. L.; Wells, R. A.; Hu, J.; Yang, T.; Dong, B.; Guo, H.; Woomer, A. H.; Druffel, D. L.; Alabanza, A.; Tománek, D.; *et al.* Control of Surface and Edge Oxidation on Phosphorene. *ACS Appl. Mater. Interfaces* **2017**, *9*, 9126–9135.
- (335) Batmunkh, M.; Bat-Erdene, M.; Shapter, J. G. Phosphorene and Phosphorene-Based Materials - Prospects for Future Applications. *Adv. Mater.* **2016**, *28*, 8586–8617.
- (336) Pumera, M. Phosphorene and Black Phosphorus for Sensing and Biosensing. *Trends Anal. Chem.* **2017**, *93*, 1–6.
- (337) Sun, C.; Wen, L.; Zeng, J.; Wang, Y.; Sun, Q.; Deng, L.; Zhao, C.; Li, Z. One-Pot Solventless Preparation of PEGylated Black Phosphorus Nanoparticles for Photoacoustic Imaging and Photothermal Therapy of Cancer. *Biomaterials* **2016**, *91*, 81–89.
- (338) Zhang, T.; Wan, Y.; Xie, H.; Mu, Y.; Du, P.; Wang, D.; Wu, X.; Ji, H.; Wan, L. Degradation Chemistry and Stabilization of Exfoliated Few-Layer Black Phosphorus in Water. *J. Am. Chem. Soc.* **2018**, DOI: 10.1021/jacs.8b02156.
- (339) Huang, X.; Jiang, P.; Tanaka, T. A Review of Dielectric Polymer Composites with High Thermal Conductivity. *IEEE Electr. Insul. Mag.* **2011**, *27*, 8–16.
- (340) Moore, A. L.; Shi, L. Emerging Challenges and Materials for Thermal Management of

- Electronics. *Mater. Today* **2014**, *17*, 163–174.
- (341) Anandan, S. S.; Ramalingam, V. Thermal Management of Electronics: A Review of Literature. *Therm. Sci.* **2008**, *12*, 5–25.
- (342) Chen, H.; Ginzburg, V. V.; Yang, J.; Yang, Y.; Liu, W.; Huang, Y.; Du, L.; Chen, B. Thermal Conductivity of Polymer-Based Composites: Fundamentals and Applications. *Prog. Polym. Sci.* **2015**, *59*, 41–85.
- (343) Idumah, C. I.; Hassan, A. Recently Emerging Trends in Thermal Conductivity of Polymer Nanocomposites. *Rev. Chem. Eng.* **2016**, *32*, 413–457.
- (344) Kim, S. J.; Choi, K.; Lee, B.; Kim, Y.; Hong, B. H. Materials for Flexible, Stretchable Electronics: Graphene and 2D Materials. *Annu. Rev. Mater. Res.* **2015**, *45*, 63–84.
- (345) Rim, Y. S.; Bae, S. H.; Chen, H.; De Marco, N.; Yang, Y. Recent Progress in Materials and Devices toward Printable and Flexible Sensors. *Adv. Mater.* **2016**, *28*, 4415–4440.
- (346) Kim, J.; Kumar, R.; Bandodkar, A. J.; Wang, J. Advanced Materials for Printed Wearable Electrochemical Devices: A Review. *Adv. Electron. Mater.* **2017**, *3*, 1600260.
- (347) Yarmolenko, P. S.; Moon, E. J.; Landon, C.; Manzoor, A.; Hochman, D. W.; Viglianti, B. L.; Dewhirst, M. W. Thresholds for Thermal Damage to Normal Tissues: An Update. *Int. J. Hyperth.* **2011**, *27*, 320–343.
- (348) Meng, W.; Huang, Y.; Fu, Y.; Wang, Z.; Zhi, C. Polymer Composites of Boron Nitride Nanotubes and Nanosheets. *J. Mater. Chem. C* **2014**, *2*, 10049–10061.
- (349) Jakus, A. E.; Rutz, A. L.; Shah, R. N. Advancing the Field of 3D Biomaterial Printing. *Biomed. Mater.* **2016**, *11*, 014102.
- (350) Wang, X.; Jiang, M.; Zhou, Z.; Gou, J.; Hui, D. 3D Printing of Polymer Matrix Composites: A Review and Prospective. *Compos. Part B Eng.* **2017**, *110*, 442–458.
- (351) Farahani, R. D.; Dube, M.; Therriault, D. Three-Dimensional Printing of Multifunctional Nanocomposites: Manufacturing Techniques and Applications. *Adv. Mater.* **2016**, *28*, 5794–5821.
- (352) Ramanathan, T.; Abdala, A. A.; Stankovich, S.; Dikin, D. A.; Herrera-Alonso, M.; Piner, R. D.; Adamson, D. H.; Schniepp, H. C.; Chen, X.; Ruoff, R. S.; *et al.* Functionalized Graphene Sheets for Polymer Nanocomposites. *Nat. Nanotechnol.* **2008**, *3*, 327–331.
- (353) Rao, C. N. R.; Ramakrishna Matte, H. S. S.; Maitra, U. Graphene Analogues of Inorganic Layered Materials. *Angew. Chemie - Int. Ed.* **2013**, *52*, 13162–13185.
- (354) Mosanenzadeh, S. G.; Khalid, S.; Cui, Y.; Naguib, H. E. High Thermally Conductive PLA

- Based Composites With Tailored Hybrid Network of Hexagonal Boron Nitride and Graphene Nanoplatelets. *Polym. Compos.* **2015**, 37, 2196–2205.
- (355) Boland, C. S.; Barwich, S.; Khan, U.; Coleman, J. N. High Stiffness Nano-Composite Fibres from Polyvinylalcohol Filled with Graphene and Boron Nitride. *Carbon N. Y.* **2016**, 99, 280–288.
- (356) Cui, X.; Ding, P.; Zhuang, N.; Shi, L.; Song, N.; Tang, S. Thermal Conductive and Mechanical Properties of Polymeric Composites Based on Solution-Exfoliated Boron Nitride and Graphene Nanosheets: A Morphology-Promoted Synergistic Effect. *ACS Appl. Mater. Interfaces* **2015**, 7, 19068–19075.
- (357) Lewis, J. A.; Ahn, B. Y. Three-Dimensional Printed Electronics. *Nature* **2015**, 518, 42–43.
- (358) García-Tuñón, E.; Barg, S.; Franco, J.; Bell, R.; Eslava, S.; D’Elia, E.; Maher, R. C.; Guitian, F.; Saiz, E. Printing in Three Dimensions with Graphene. *Adv. Mater.* **2015**, 27, 1688–1693.
- (359) Foster, C. W.; Down, M. P.; Zhang, Y.; Ji, X.; Rowley-Neale, S. J.; Smith, G. C.; Kelly, P. J.; Banks, C. E. 3D Printed Graphene Based Energy Storage Devices. *Sci. Rep.* **2017**, 7, 42233.
- (360) Pakdel, A.; Bando, Y.; Golberg, D. Nano Boron Nitride Flatland. *Chem. Soc. Rev.* **2014**, 43, 934–959.
- (361) Luo, W.; Wang, Y.; Hitz, E.; Lin, Y.; Yang, B.; Hu, L. Solution Processed Boron Nitride Nanosheets: Synthesis, Assemblies and Emerging Applications. *Adv. Funct. Mater.* **2017**, 27, 1701450.
- (362) Sichel, E. K.; Miller, R. E.; Abrahams, M. S.; Buiocchi, C. J. Heat Capacity and Thermal Conductivity of Hexagonal Pyrolytic Boron Nitride. *Phys. Rev. B* **1976**, 13, 4607–4611.
- (363) Ngo, I. L.; Jeon, S.; Byon, C. Thermal Conductivity of Transparent and Flexible Polymers Containing Fillers: A Literature Review. *Int. J. Heat Mass Transf.* **2016**, 98, 219–226.
- (364) Donnay, M.; Tzavalas, S.; Logakis, E. Boron Nitride Filled Epoxy with Improved Thermal Conductivity and Dielectric Breakdown Strength. *Compos. Sci. Technol.* **2015**, 110, 152–158.
- (365) Kemaloglu, S.; Ozkoc, G.; Aytac, A. Properties of Thermally Conductive Micro and Nano Size Boron Nitride Reinforced Silicon Rubber Composites. *Thermochim. Acta* **2010**, 499, 40–47.
- (366) Kim, K.; Ju, H.; Kim, J. Vertical Particle Alignment of Boron Nitride and Silicon Carbide

- Binary Filler System for Thermal Conductivity Enhancement. *Compos. Sci. Technol.* **2016**, *123*, 99–105.
- (367) Kim, K.; Kim, M.; Hwang, Y.; Kim, J. Chemically Modified Boron Nitride-Epoxy Terminated Dimethylsiloxane Composite for Improving the Thermal Conductivity. *Ceram. Int.* **2014**, *40*, 2047–2056.
- (368) Zhi, C.; Bando, Y.; Tang, C.; Kuwahara, H.; Golberg, D. Large-Scale Fabrication of Boron Nitride Nanosheets and Their Utilization in Polymeric Composites with Improved Thermal and Mechanical Properties. *Adv. Mater.* **2009**, *21*, 2889–2893.
- (369) Zeng, X.; Ye, L.; Yu, S.; Li, H.; Sun, R.; Xu, J.; Wong, C. Artificial Nacre-like Papers Based on Noncovalent Functionalized Boron Nitride Nanosheets with Excellent Mechanical and Thermally Conductive Properties. *Nanoscale* **2015**, 6774–6781.
- (370) Gao, T.; Yang, Z.; Chen, C.; Li, Y.; Fu, K.; Dai, J.; Hitz, E. M.; Xie, H.; Liu, B.; Song, J.; *et al.* Three-Dimensional Printed Thermal Regulation Textiles. *ACS Nano* **2017**, *11*, 11513–11520.
- (371) Jakus, A. E.; Rutz, A. L.; Jordan, S. W.; Kannan, A.; Mitchell, S. M.; Yun, C.; Koube, K. D.; Yoo, S. C.; Whiteley, H. E.; Richter, C.-P.; *et al.* Hyperelastic “Bone”: A Highly Versatile, Growth Factor-Free, Osteoregenerative, Scalable, and Surgically Friendly Biomaterial. *Sci. Transl. Med.* **2016**, *8*, 358ra127.
- (372) Jakus, A. E.; Koube, K. D.; Geisendorfer, N. R.; Shah, R. N. Robust and Elastic Lunar and Martian Structures from 3D-Printed Regolith Inks. *Sci. Rep.* **2017**, *7*, 44931.
- (373) Weng, Q.; Wang, B.; Wang, X.; Hanagata, N.; Li, X.; Liu, D.; Wang, X.; Jiang, X.; Bando, Y.; Golberg, D. Highly Water-Soluble, Porous, and Biocompatible Boron Nitrides for Anticancer Drug Delivery. *ACS Nano* **2014**, *8*, 6123–6130.
- (374) Xue, Q.; Zhang, H.; Zhu, M.; Wang, Z.; Pei, Z.; Huang, Y.; Huang, Y.; Song, X.; Zeng, H.; Zhi, C. Hydrothermal Synthesis of Blue-Fluorescent Monolayer BN and BCNO Quantum Dots for Bio-Imaging Probes. *RSC Adv.* **2016**, *6*, 79090–79094.
- (375) O’Neill, M. J. Measurement of Specific Heat Functions by Differential Scanning Calorimetry. *Anal. Chem.* **1966**, *38*, 1331–1336.
- (376) Mudunkotuwa, I. A.; Grassian, V. H. Biological and Environmental Media Control Oxide Nanoparticle Surface Composition: The Roles of Biological Components (Proteins and Amino Acids), Inorganic Oxyanions and Humic Acid. *Environ. Sci. Nano* **2015**, *2*, 429–439.
- (377) Kenry; Lim, C. T. Biocompatibility and Nanotoxicity of Layered Two-Dimensional Nanomaterials. *ChemNanoMat* **2017**, *3*, 5–16.

- (378) Fojtů, M.; Teo, W. Z.; Pumera, M. Environmental Impact and Potential Health Risks of 2D Nanomaterials. *Environ. Sci. Nano* **2017**, *4*, 1617–1633.
- (379) Tan, C.; Lai, Z.; Zhang, H. Ultrathin Two-Dimensional Multinary Layered Metal Chalcogenide Nanomaterials. *Adv. Mater.* **2017**, *29*, 1701392.
- (380) Boukhvalov, D.; Gürbulak, B.; Duman, S.; Wang, L.; Politano, A.; Caputi, L.; Chiarello, G.; Cupolillo, A. The Advent of Indium Selenide: Synthesis, Electronic Properties, Ambient Stability and Applications. *Nanomaterials* **2017**, *7*, 372.
- (381) Huang, S.; Ling, X. Black Phosphorus: Optical Characterization, Properties and Applications. *Small* **2017**, *13*, 1700823.
- (382) Ye, Y.; Guo, Q.; Liu, X.; Liu, C.; Wang, J.; Liu, Y.; Qiu, J. Two-Dimensional GeSe as an Isostructural and Isoelectronic Analogue of Phosphorene: Sonication-Assisted Synthesis, Chemical Stability, and Optical Properties. *Chem. Mater.* **2017**, *29*, 8361–8368.
- (383) Li, Z.; Qiao, H.; Guo, Z.; Ren, X.; Huang, Z.; Qi, X.; Dhanabalan, S. C.; Ponraj, J. S.; Zhang, D.; Li, J.; *et al.* High-Performance Photo-Electrochemical Photodetector Based on Liquid-Exfoliated Few-Layered InSe Nanosheets with Enhanced Stability. *Adv. Funct. Mater.* **2017**, 1705237.
- (384) Zhang, H.; Ji, Z.; Xia, T.; Meng, H.; Low-Kam, C.; Liu, R.; Pokhrel, S.; Lin, S.; Wang, X.; Liao, Y.-P.; *et al.* Use of Metal Oxide Nanoparticle Band Gap To Develop a Predictive Paradigm for Oxidative Stress and Acute Pulmonary Inflammation. *ACS Nano* **2012**, *6*, 4349–4368.

## CURRICULUM VITAE

**Linda M. Guiney**

lindaguiney@gmail.com

7450 N Claremont Ave. Chicago, IL 60645

(617) 688-2946

### ***Education***

---

**Northwestern University**, Evanston, IL

Ph.D June 2018, Materials Science and Engineering

Advisor: Prof. Mark C. Hersam

**Wellesley College**, Wellesley, MA

B.A. June 2009, Double major in Chemistry and French

*Distinctions:* Cum Laude, Departmental Honors in Chemistry, Sigma Xi

Study Abroad: **Université de Provence Aix-Marseille**, Aix-en-Provence, France, Spring 2008

### ***Research Experience***

---

**Northwestern University, Department of Materials Science and Engineering, Evanston, IL**

*Graduate Research Assistant with Prof. Mark Hersam, October 2012-present*

- Develop biocompatible methods for dispersing and handling 2D nanomaterials
- Incorporate functional 2D nanomaterials into 3D printable inks for biomedical applications
- Investigate the structure/activity relationship of 2D nanomaterials as it relates to toxicity and aqueous transport

**Semprus BioSciences, Cambridge, MA**

*Associate Analytical Scientist, November 2010-May 2012*

- Performed analysis and characterization of new surface modifications, polymer formulations, raw materials, and process intermediates
- Developed new analytical methods and wrote test methods and standard operating procedures

**Vertex Pharmaceuticals, Inc., Cambridge, MA**

*Scientific Associate II, October 2009-November 2010*

- Characterized and developed formulations for discovery phase active pharmaceutical ingredients

**Wellesley College, Department of Chemistry, Wellesley, MA**

*Undergraduate Research Assistant with Prof. Nolan Flynn, January 2006-June 2009*

- Synthesized and characterized macromolecular release from thermoresponsive hydrogels
- Developed a method for the synthesis of pH-responsive metal-oxide microspheres

### ***Honors and Awards***

---

Hierarchical Materials Cluster Fellowship, 2013

National Science Foundation Graduate Research Fellowship Program, Honorable Mention, 2013

### ***Activities***

**Chicago North Shore Women's Rugby Football Club**, 501(c)(3), Chicago, IL, Fall 2012-Present  
President (2014-2016), Community Agent (2013-2014), Board of Directors (2013-present), Active Player (2012-present)

### ***Patents***

[Inventors] Zhang, Z.; Cook, A.; Schultz, K. A.; Li, J.; Skinner, M.; Weinstock, A.; **Guiney, L. M.**; Wang, H.; Loose, C.; Coury, A. Patent number 20130155370 A1 "Surface Modified Contact Lenses,"; 20 Jun 2013.

[Inventors] Nel, A. E.; Xia, T.; Li, R.; Mansukhani, N. D.; **Guiney, L. M.**; Hersam, M. C. "Identification and Optimization of Carbon Radicals on Hydrated Graphene Oxide for Ubiquitous Antibacterial Coatings,"; *filed January 2017*.

### ***Presentations***

American Chemical Society National Meeting, Chicago, IL, March 2007

"Macromolecular Release of Thermoresponsive Cationic Hydrogels," *poster*

American Chemical Society National Meeting, Salt Lake City, UT, March 2009

"Synthesis of pH-Responsive Metal-Oxide Microspheres," *poster*

UC CEIN Nano EH&S Forum, UCLA, Los Angeles, CA, May 2013

"Investigating the Toxicity and Environmental Fate of Carbon-Based Nanomaterials," *poster*

American Chemical Society National Meeting, San Francisco, CA, August 2014

"Investigating the Toxicity and Environmental Fate of Graphene Nanomaterials," *oral presentation*

Gordon Research Seminar, Mount Snow, West Dover, VT, June 2015

"Aqueous, High Concentration Dispersions of MoS<sub>2</sub> in Biocompatible Block Copolymers," *oral presentation*

American Chemical Society National Meeting, Boston, MA, August 2015

"Toxicological Potential and Environmental Fate of Molybdenum Disulfide (MoS<sub>2</sub>), a Post-Graphene 2D Material," *oral presentation*

The John E. Hilliard Symposium, Northwestern University, Evanston, IL, May 2017

"Three-dimensional Printing of Hexagonal Boron Nitride for Biomedical and Electronic Applications," *oral presentation*

### ***Publications***

**Guiney, L. M.**; Agnello, A. D.; Thomas, J. C.; Takatori, K.; Flynn, N. T. Thermoresponsive Behavior of Charged N-Isopropylacrylamide-Based Hydrogels Containing Gold Nanostructures. *Colloid Polym. Sci.* **2009**, 287, 601–608.

Weinstock, B. A.; **Guiney, L. M.**; Loose, C. Rapid, Nondestructive Estimation of Surface Polymer Layer Thickness Using Attenuated Total Reflection Fourier Transform Infrared (ATR FT-IR) Spectroscopy and Synthetic Spectra Derived from Optical Principles. *Appl. Spectrosc.* **2012**, 66, 1311–1319.

Zhang, Z.; Borenstein, J.; **Guiney, L.**; Miller, R.; Sukavaneshvar, S.; Loose, C. Polybetaine Modification of PDMS Microfluidic Devices to Resist Thrombus Formation in Whole Blood. *Lab Chip* **2013**, 13, 1963–1968.

Lanphere, J. D.; Luth, C. J.; **Guiney, L. M.**; Mansukhani, N. D.; Hersam, M. C.; Walker, S. L. Fate and Transport of Molybdenum Disulfide Nanomaterials in Sand Columns. *Environ. Eng. Sci.* **2015**, 32, 163–173.

- Wang, X.; Mansukhani, N. D.; **Guiney, L. M.**; Ji, Z.; Chang, C. H.; Wang, M.; Liao, Y. P.; Song, T. Bin; Sun, B.; Li, R.; et al. Differences in the Toxicological Potential of 2D versus Aggregated Molybdenum Disulfide in the Lung. *Small* **2015**, *11*, 5079–5087.
- Chowdhury, I.; Mansukhani, N. D.; **Guiney, L. M.**; Hersam, M. C.; Bouchard, D. Aggregation and Stability of Reduced Graphene Oxide: Complex Roles of Divalent Cations, pH, and Natural Organic Matter. *Environ. Sci. Technol.* **2015**, *49*, 10886–10893.
- Mansukhani, N. D.; **Guiney, L. M.**; Kim, P. J.; Zhao, Y.; Alducin, D.; Ponce, A.; Larios, E.; Yacaman, M. J.; Hersam, M. C. High-Concentration Aqueous Dispersions of Nanoscale 2D Materials Using Nonionic, Biocompatible Block Copolymers. *Small* **2016**, *12*, 294–300.
- Wang, X.; Mansukhani, N. D.; **Guiney, L. M.**; Lee, J.-H.; Li, R.; Sun, B.; Liao, Y.-P.; Chang, C. H.; Ji, Z.; Xia, T.; et al. Toxicological Profiling of Highly Purified Metallic and Semiconducting Single-Walled Carbon Nanotubes in the Rodent Lung and *E. Coli*. *ACS Nano* **2016**, *10*, 6008–6019.
- Li, R.; Mansukhani, N. D.; **Guiney, L. M.**; Ji, Z.; Zhao, Y.; Chang, C. H.; French, C. T.; Miller, J. F.; Hersam, M. C.; Nel, A. E.; et al. Identification and Optimization of Carbon Radicals on Hydrated Graphene Oxide for Ubiquitous Antibacterial Coatings. *ACS Nano* **2016**, *10*, 10966–10980.
- Chen, K.-S.; Xu, R.; Luu, N. S.; Secor, E. B.; Hamamoto, K.; Li, Q.; Kim, S.; Sangwan, V. K.; Balla, I.; **Guiney, L. M.**; Seo, J.-W. T.; Yu, X.; Liu, W.; Wu, J.; Wolverton, C.; Dravid, V. P.; Barnett, S. A.; Lu, J.; Amine, K.; Hersam, M. C. Comprehensive Enhancement of Nanostructured Lithium-Ion Battery Cathode Materials via Conformal Graphene Dispersion. *Nano Lett.* **2017**, *17*, 2539–2546.
- Mansukhani, N. D.; **Guiney, L. M.**; Wei, Z.; Roth, E. W.; Putz, K. W.; Luijten, E.; Hersam, M. C. Optothermally Reversible Carbon Nanotube-DNA Supramolecular Hybrid Hydrogels. *Macromol. Rapid Commun.*, **2018**, *39*, 1700587.
- Li, R.; **Guiney, L. M.**; Chang, C. H.; Mansukhani, N. D.; Ji, X.; Wang, X.; Liao, Y.-P.; Jiang, W.; Sun, B.; Hersam, M. C.; Nel, A. E.; Xia, T. The Surface Oxidation of Graphene Oxide Determines Membrane Damage, Lipid Peroxidation, and Cytotoxicity in Macrophages in a Pulmonary Toxicity Model. *ACS Nano*, **2018**, *12*, 1390–1402.
- Wang, X.; Lee, J.-H.; Li, R.; Liao, Y.-P.; Kang, J.; Chang, C. H.; **Guiney, L. M.**; Mirshafiee, V.; Li, L.; Lu, J.; Xia, T.; Hersam, M. C.; Nel, A. E. Toxicological Profiling of Highly-Purified Single-Walled Carbon Nanotubes with Different Lengths in the Rodent Lung and *E. coli*. *Small*, **2018**; in press.

### ***Manuscripts in Preparation***

- Guiney, L. M.**; Mansukhani, N. D.; Jakus, A. E.; Wallace, S. G.; Shah, R. N.; Hersam, M. C. Three-Dimensional Printing of Biocompatible, Thermally Conductive Hexagonal Boron Nitride Nanocomposites. *Nano Lett.*, under review
- Guiney, L. M.**; Wang, X.; Xia, T.; Nel, A.; Hersam, M. C. Assessing and Mitigating the Hazard Potential of Two-Dimensional Nanomaterials Beyond Graphene. *ACS Nano*, under review
- Alam, I.; **Guiney, L. M.**; Hersam, M. C.; Chowdhury, I. Antifouling Properties of Two-Dimensional Graphene Oxide and Molybdenum Disulfide. *Environ. Sci. Nano*, under review
- Shams, M.; **Guiney, L. M.**; Ramesh, M.; Hersam, M. C.; Chowdhury, I. Influence of Functional Groups on the Direct Photolysis of Graphene Oxide. *Environ. Sci. Technol.*, under review
- Guiney, L. M.**; Ramesh, M.; Kang, J.; Sponenburg, R. A.; MacRenaris, K.; Hersam, M. C. Stability of solution-processed black phosphorus in aqueous and biologically relevant environments. in preparation

- Chen, X.; Jiang, W.; Ahmed, A.; **Guiney, L. M.**; Wang, X.; Jiang, J.; Lu, J.; Liu, X.; Xu, I.; Chang, C. H.; Sun, B.; Ji, Y.; Hersam, M. C.; Nel, A. E.; Xia, T. Oxidative State and Lateral Size of Graphene Oxide Determine Differential Cell Death Mechanisms and Pro-inflammatory Responses in Three Liver Cell Types. in preparation
- Alam, I.; **Guiney, L. M.**; Hersam, M. C.; Chowdhury, I. Application of External Voltage for fouling mitigation from Graphene Oxide-PPy and Molybdenum Disulfide-PPy. in preparation
- Story, S. D.; Boggs, S.; **Guiney, L. M.**; Ramesh, M.; Hersam, M. C.; Brinker, J.; Walker, S. L. Aggregation Morphology of Planar Engineered Nanomaterials. in preparation

### ***Scientific Laboratory Techniques***

---

- |   |  |
|---|--|
| • Atomic force microscopy                 | • High-performance liquid chromatography       |
| • Cell culture                            | • Inductively coupled plasma-mass spectrometry |
| • Confocal microscopy                     | • Raman spectroscopy                           |
| • Contact angle goniometry                | • Scanning electron microscopy                 |
| • Differential scanning calorimetry       | • Thermogravimetric analysis                   |
| • Dynamic light scattering                | • UV-visible spectroscopy                      |
| • Fluorescence spectroscopy               | • X-ray photoelectron spectroscopy             |
| • Fourier-transform infrared spectroscopy | • X-ray powder diffraction                     |